



HAL
open science

Contributions to the study of Switched reluctance machine for automotive integrated starter-alternator application

Mihai Valentin Zaharia

► **To cite this version:**

Mihai Valentin Zaharia. Contributions to the study of Switched reluctance machine for automotive integrated starter-alternator application. Other. Ecole Centrale de Lille, 2016. English. NNT : 2016ECLI0022 . tel-01943737

HAL Id: tel-01943737

<https://theses.hal.science/tel-01943737v1>

Submitted on 4 Dec 2018

HAL is a multi-disciplinary open access archive for the deposit and dissemination of scientific research documents, whether they are published or not. The documents may come from teaching and research institutions in France or abroad, or from public or private research centers.

L'archive ouverte pluridisciplinaire **HAL**, est destinée au dépôt et à la diffusion de documents scientifiques de niveau recherche, publiés ou non, émanant des établissements d'enseignement et de recherche français ou étrangers, des laboratoires publics ou privés.

N° d'ordre : 312

CENTRALE LILLE

THÈSE

présentée en vue
d'obtenir le grade de

DOCTEUR

en

Spécialité : Génie électrique

par

Mihai Valentin **ZAHARIA**

**DOCTORAT DELIVRE CONJOINTEMENT PAR CENTRALE LILLE ET L'UNIVERSITÉ
TECHNIQUE DE CLUJ-NAPOCA (UTC-N), ROUMANIE DANS LE CADRE D'UNE
COTUTELLE INTERNATIONALE DE THESE**

Titre de la thèse :

Contributions à l'étude des machines à reluctance variable pour application alterno-démarrreur automobile

Thèse soutenue le 15 décembre 2016 devant le jury d'examen :

Président	Radu MUNTEANU , <i>Professeur des universités, UTC-N, Roumanie</i>
Rapporteur	Maria IMECS , <i>Professeur des universités, UTC-N, Roumanie</i>
Rapporteur	Mohamed GABSI , <i>Professeur des universités, Ecole Normale Supérieure de Cachan, France</i>
Examineur	Mohamed KETATA , <i>Professeur des universités, Université de Rouen, Mont-saint Aignan, France</i>
Co-directeurs de thèse	Frédéric GILLON , <i>Maître de conférences, HDR, L2EP – Centrale Lille, France</i> Mircea M. RADULESCU , <i>Professeur des universités, UTC-N, Roumanie</i>
Membre	Stéphane BRISSET , <i>Maître de conférences, HDR, L2EP – Centrale Lille, France</i>

Acknowledgments

The research work of this thesis was realized within an international collaboration between Technical University of Cluj-Napoca, Romania and Ecole Centrale de Lille, France

The thesis was elaborated within the Special Electric Machines and Light Electric Traction (SEMLET) Research Laboratory, Technical University of Cluj-Napoca and the Laboratory of Electrical Engineering and Power Electronics (L2EP), Ecole Centrale de Lille.

I want to express my deep gratitude to Professor *Mircea M. Radulescu*, co-supervisor of my thesis from the Technical University of Cluj-Napoca, for all the scientific and moral support which he offered me during the entire period of my PhD research. His encouraging throughout these years was of great help.

I particularly want to thank MdC *Frédéric Gillon*, co-supervisor of my thesis from Ecole Centrale de Lille, for having given me the opportunity to be a member of the optimization team. His dedication and his optimism along with all the scientific advices were likewise of great help in the developing of this PhD thesis.

I would like to thank the referees and members of the jury of this thesis, Professors *Maria Imecs* from the Technical University of Cluj-Napoca, Romania, *Mohamed Gabsi* from the Ecole Normale Supérieure de Cachan, France, MdC *Stéphane Brisset* from Ecole Centrale de Lille, France, Professors *Radu Munteanu* from the Technical University of Cluj-Napoca, Romania and *Mohamed Ketata* from the Université de Rouen, Mont-saint Aignan, France, for their valuable comments and suggested improvements.

I would also like to thank Professors Teodor Pana, Calin Rusu and Iulian Birou, from the Faculty of Electrical Engineering, UTC-N, who have evaluated my doctoral reports.

As well, I would like to thank my colleagues from the both laboratories SEMLET (*Stefan, Mihai, Marius* and all the others) and L2EP (*Xavier, Mathieu, Maxime, Patricio, Florent* and all the others). Thanks for all the help and good moments.

Finally I will be always grateful to my family, in particularly to my wife *Andreea* who has been very supportive and understanding with me at each moment, but also to my parents and my sister for their encouraging throughout all my years of study.

Cluj-Napoca, December 2016

Mihai Valentin ZAHARIA

Table of contents

Notations and definitions.....	5
General introduction.....	9
Ch. 1 Switched reluctance machine as integrated starter-alternator.....	11
1.1 Introduction.....	12
1.2 Main features of switched reluctance machines.....	13
1.3 SR machine as integrated starter-alternator.....	15
1.4 Conclusions.....	18
Selected references.....	19
Ch. 2 Modeling and simulation of the switched reluctance machine.....	21
2.1 Introduction.....	22
2.2 Topologies of switched reluctance machine and associated power electronic converter.....	22
2.2.1 Classical SR machine topologies.....	22
2.2.2 Novel SR machine topologies.....	23
2.2.3 Topologies of SR machine associated power electronic converters.....	24
2.2.3.1 Three-phase asymmetric half-bridge power converter.....	24
2.2.3.2 Miller power converter.....	26
2.2.3.3 Three-phase full bridge power converter.....	26
2.2.4 SR machine prototype under study.....	27
2.3 Analytical modeling of the SR machine prototype.....	28
2.3.1 Analysis of voltage equations.....	29
2.3.2 Instantaneous electromagnetic torque.....	30
2.3.3 Phase inductance vs. rotor position.....	31
2.3.3.1 Analytical calculation of the phase inductance for aligned rotor position	33
2.3.3.2 Analytical calculation of the phase inductance for unaligned rotor position.....	36
2.4 Validation of the analytical model by finite-element magnetic field analysis.....	45
2.4.1 Finite element software used for validation.....	45

2.4.2	Comparative FE-computed and analytical results.....	45
2.4.2.1	Validation of the voltage equations.....	46
2.4.2.2	Validation of electromagnetic torque equations.....	47
2.4.2.3	Phase inductance validation.....	48
2.5	Simulations of the SR machine model.....	50
2.5.1	MATLAB/Simulink model.....	50
2.5.2	Influence of commutation angles.....	51
2.5.2.1	Simulations with theoretical angle.....	51
2.5.2.2	Simulations when commutation angles change.....	53
2.6	Conclusions.....	55
	Selected references.....	56
Ch. 3	Optimization of switched reluctance machine using space mapping technique.....	59
3.1	Introduction.....	60
3.2	General aspects of optimization.....	60
3.2.1	Optimization.....	61
3.2.2	Design provided by optimization.....	62
3.2.3	Space mapping method.....	63
3.3	Space mapping at the output level.....	66
3.3.1	Space mapping function.....	66
3.3.2	Optimization using a mathematical model.....	67
3.3.2.1	Optimization on the fine model.....	68
3.3.3	Output space mapping proportional.....	70
3.3.3.1	General function calculation.....	70
3.3.3.2	Mathematical based problem.....	72
3.3.4	Manifold mapping.....	75
3.3.4.1	Mathematical problem.....	77
3.3.5	Comparison between the OSMP and MM methods applied to the mathematical model.....	78
3.4	Optimization of the SR machine by using SM technique.....	81
3.4.1	Description of the parameter control optimization.....	81
3.4.2	Approach used in fine and coarse models selection.....	82

3.4.3	Output space mapping proportional applied to machine optimization.....	87
3.4.4	Manifold mapping applied to SR machine optimization.....	89
3.4.5	Comparative optimal results.....	90
3.5	Space mapping technique applied to design and control optimization of SR machine for ISA applications.....	92
3.5.1	Optimization problem description.....	92
3.5.2	Selection of the fine and coarse models.....	93
3.5.3	Output space mapping proportional applied to SR machine optimization.....	95
3.5.4	Manifold mapping applied to SR machine optimization.....	95
3.5.5	Comparative optimal design.....	96
3.6	Simulation of the optimally-designed SR machine used in ISA application.....	97
3.7	Conclusions.....	101
	Selected references.....	102
Ch. 4	Experimental study and control of a three-phase 6/8 SR machine.....	105
4.1	Introduction.....	106
4.2	Experimental test bench.....	106
4.2.1	Hardware components.....	107
4.2.1.1	Three-phase half-bridge inverter.....	107
4.2.1.2	Testing equipment dSpace 1104.....	109
4.2.1.3	Auxiliary equipment.....	110
4.2.2	Software components.....	111
4.2.2.1	Real-time control software.....	112
4.2.2.2	Real-time software.....	117
4.3	Steady-state tests for motor and generator operation modes of the studied SR machine and dynamic tests for a part of ISA driving cycle.....	119
4.3.1	Phase inductance measurement.....	119
4.3.2	Commutation angles validation for motor operation mode.....	120
4.3.3	Steady-state tests under motor and generator operation mode.....	121
4.3.3.1	Motor operation mode.....	121

4.3.3.2	Generator operation mode.....	122
4.3.4	SR machine tests as part of automotive ISA operation cycle.....	123
4.4	Conclusions.....	125
4.5	Selected references.....	126
General conclusions, original contributions and prospects.....		127
Appendix 2.A	Detailed voltage calculation.....	131
Appendix 2.B	Analytical calculation of the phase inductance for aligned and unaligned rotor position.....	133
Appendix 3.A	Matlab implementation of the OSMP technique.....	139
Appendix 3.B	Matlab implementation of the MM technique.....	143
Appendix 3.C	VBScript used to automatically draw the SR machine.....	147
Appendix 4.A	Datasheet Semikron Semiteach –IGBT.....	153
Appendix 4.B	Datasheet position sensor BaumerIVO GI321.....	154
Appendix 4.C	Datasheet torque transducer.....	156
Curriculum Vitae.....		159
Publications		163
Résumé étendu.....		181
Abstract.....		191

Notations and definitions

A_g	Air-gap area
A_{Rp}	Rotor tooth area
A_{Ry}	Rotor yoke area
A_{Sp}	Stator tooth area
A_{Sy}	Stator yoke area
B	Magnetic flux density
D_{Rext}	Rotor outer diameter
D_{Rint}	Rotor inner diameter
D_{Sext}	Stator outer diameter
D_{Sint}	Stator inner diameter
e	Induced electromotive force
ε	Tolerance
g	Airgap
H	Magnetic field strength
h_R	Height of rotor tooth
h_S	Height of stator tooth
ICE	Internal combustion engine
IM	Induction machine
i_{ph}	Phase current
IPM	Internal permanent magnet machine
i_{ref}	Reference current
J_R	Rotor jug width
J_S	Stator jug width
k	Correction coefficient
l_a	Machine axial length
L_a	Aligned inductance
l_g	Length of air-gap
L_M	Maximum inductance
L_m	Minimum inductance
L_{ph}	Phase inductance
l_{Rp}	Length of rotor tooth
l_{Ry}	Length of rotor yoke
l_{Sp}	Length of stator tooth

l_{Sy}	Length of stator yoke
L_u	Unaligned inductance
MM	Manifold mapping
N_p	Number of pole pairs per phase
N_R	Number of rotor teeth
N_S	Number of stator teeth
N_{sp}	Number of turns per phase
OSMP	Output space mapping proportional
P	Mapping function
p_i	Input power
q	Number of phases
R	Phase resistance
R_g	Reluctance of air-gap
R_{Rp}	Reluctance of rotor pole
R_{Ry}	Reluctance of stator yoke
R_{Sp}	Reluctance of stator pole
R_{Sy}	Reluctance of stator yoke
RTI	Real time interface
SM	Space mapping
SRM	Switched reluctance machine
T_{av}	Average value of electromagnetic torque
T_e	Electromagnetic torque
T_{emax}	Maximum value of electromagnetic torque
T_{emin}	Minimum value of electromagnetic torque
T_l	Load
u_{ph}	Stator phase voltage
V_{dc}	Supply voltage
W_c	Magnetic co-energy
W_d	Energy returned to supply
W_f	Stored field energy
W_{md}	Energy converted into mechanical work
W_{mt}	Converted energy
w_R	Rotor pole thickness
w_{Ry}	Rotor yoke thickness

w_s	Stator pole thickness
w_{sy}	Stator yoke thickness
β_R	Rotor pole arc
β_{Ropen}	Rotor arc opening
β_s	Stator pole arc
η	Machine efficiency
θ	Angular position
θ_{off}	Theta off
θ_{on}	Theta on
θ_R	Rotor Position
θ_{rp}	Rotor pole pitch
Ψ_a	Phase flux at aligned position
Ψ_u	Phase flux at unaligned position
Ω	Machine rotational speed

General introduction

The research work is realized within an international collaboration between Technical University of Cluj-Napoca, Romania and Ecole Centrale de Lille, France. The presented thesis is focused on the optimization of a three-phase 6/8 SR machine.

The switched reluctance machine has a simple construction making it cheaper in execution but one of the drawbacks of this machine is the torque ripple. This thesis had as first target, the usage of an optimization tool to calculate the best control parameters to correct this major drawback of the SR machine in motor and generator operation modes. Hence, an analytical model that takes into account the machine geometry and that is able to be simulated in both operation modes by adjusting the commutation angles was provided and implemented in a calculation environment. Furthermore, a mathematical optimization was launched for the control parameters calculation, but in order to have good results the optimization must be very accurate, hence, it will be very slow. As a result, the second objective of this work was to investigate a method to reduce the optimization time without lowering the accuracy of the results. But during the investigation process regarding the optimization strategy, it was discovered that a very important role in defining the optimal results is played by the fast model, because in order to have a smooth convergence this model and the accurate one need to have almost the same tendency; therefore, the modality of choosing these models was also provided in the thesis.

The strategy used in the optimization process is known in literature as the space mapping technique, more precisely for this thesis output space mapping proportional and manifold mapping were studied. After testing them on a mathematical model it was possible to continue the investigation on defining the optimal control parameters of a three-phases 6/8 SR machine prototype, being able that further to use this strategy in a much complicated process, i.e. defining the right geometry and control of a SR machine to be used in automotive integrated starter alternator systems. The final target of the thesis was to conduct experiments and tests on the existing prototype in order to partially validate the results of the optimization process.

It is now possible to provide the main objective of the present thesis, which are to (i) search for optimization tools to reduce the torque ripple of the SR machine in ISA applications; (ii) apply the space mapping technique for shortening the optimization time without lowering the accuracy of optimization results and (iii) conduct relevant experiments and tests on the existing SR machine prototype in order to validate the results of the optimization process

The thesis is structured in five chapters, which are briefly described below.

Chapter 1 outlines the main features of SR machine in view of its ISA application in automotive industry, thus justifying the thesis research.

Different topologies of SR machine and of associated power electronic converter are first presented in **chapter 2**. The analytical model of the three-phase SR machine with six-stator-poles and eight-rotor-teeth, is then developed and validated by finite-element field analysis. The entire system implemented in MATLAB/Simulink for steady-state simulations of SR machine operation is also presented. Finally, the SR machine prototype under study is introduced, and the importance of commutation angles in torque ripple minimization is emphasized.

The space mapping optimization technique used in this thesis is described in detail at the beginning of **chapter 3**. A mathematical model is used for validation of this technique to be applied in finding the best control of SR machine prototype, in both motor and generator operation modes. At the end of the chapter, the optimization problem is upgraded, by adding also the sizing parameters besides the control, in order to obtain the best geometry and control for the SR machine in ISA applications. Steady-state and dynamic simulations for a small speed cycle using the optimized control and geometry of the SR machine are also provided.

Chapter 4 is used to experimentally validate the optimization results for the SR machine prototype. Detailed presentation of the test bench with all hardware components and the software used for machine control is made. Steady-state and dynamic test results, in motor and generator operation modes of the SR machine prototype, are provided and compared with simulation results.

In the **last chapter**, general conclusions of the research are drawn, and the main contributions of the thesis are highlighted.

Chapter 1

Switched reluctance machine as integrated starter-alternator

1.1. Introduction

The motivation of this thesis is linked to the keen interest of the European Government Agency in developing an alternative for the classical internal combustion engines (ICEs) in order to minimize the carbon dioxide emissions. Several reports have been issued by the European Union agency concerning the impact of the transportation sector upon global energy-related carbon-dioxide emissions [1]. Considering, for example, the emissions recorded in 2013 (fig. 1.1), they mainly originate from heat generation and transport sectors, accounted for 42% for the first sector, and 23% for the second one.

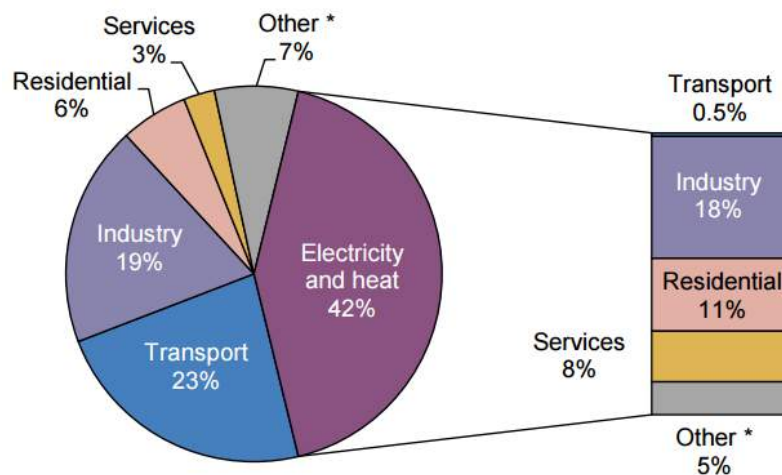


Fig. 1.1 World carbon-dioxide emissions by sectors, in 2013 [2]

The advantages of using electric-powered engines instead of an internal combustion engine are:

- Improved efficiency
- Reduction in the total mass
- High starting torque
- Elimination of the CO₂ emissions
- Energy saving in the braking mode
- Noise reduction

In recent years the research on electrical machines increased, due to the vast number of industrial applications and processes in which these electromechanical energy converters operate. Moreover these are often critical components for the systems in which they operate.

For this thesis robust electrical machines are targeted to automotive, where they either directly replace the mechanical systems, or are used as auxiliaries of mechanical systems [3]. However, for this thesis integrated starter alternator systems are targeted and for this application

the motor and also generator operations mode should be covered when designing the electrical machine.

A motor is an electrical machine that converts electrical energy into mechanical energy. When a conductor carrying current is placed into a magnetic field, it can experience mechanical force, which is practically the basic principle behind the motor action (Laplace force or Lorentz force [4]). A generator on the other hand converts the mechanical energy into electrical energy and requires a prime mover such as water/wind/steam turbines etc. to be engaged in motion, or even an internal combustion engine (ICE) or similar other sources. Its main principle is that whenever a conductor moves in a magnetic field, an electromotive force gets induced (Faraday's law [5]).

1.2. Main features of switched reluctance machines

The *switched reluctance (SR) machine* falls in two categories of special electric machines: (i) the first one comprises the doubly-salient variable-reluctance machines, for which by energizing stator-pole concentrated windings, reluctance torque is produced due to the tendency of rotor teeth to move to a position where the air-gap reluctance is minimized, i.e. the position where the rotor teeth are aligned with the energized stator poles; (ii) the second category is represented by the electronically-commutated (brushless) machines, which operate only in conjunction with specific electronic power converter and switching control, so that the stator-pole windings are sequentially energized with DC currents in synchronism with the rotor position, thus producing continuous electromagnetic (reluctance) torque [6] [7].

The basic operating principle of the SR machine is easily visualized in the single-phase SR machine illustrated in fig. 1.2. If the stator winding is supplied by constant DC voltage, unidirectional electric current flows through the winding, thus creating magnetic flux in stator poles U and U' with the tendency of pulling the rotor teeth R and R' towards the alignment position with corresponding stator poles.

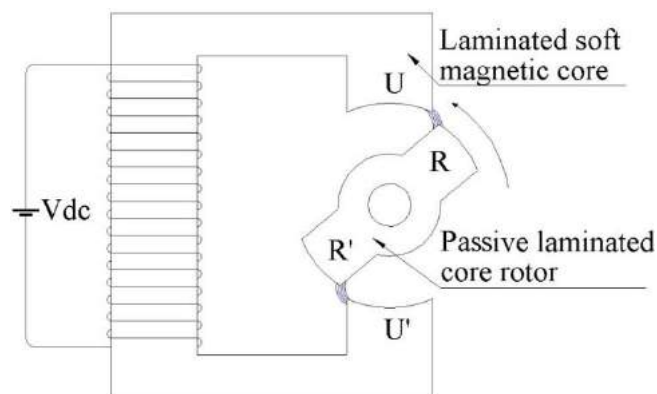


Fig. 1.2 Illustration of the single-phase SR machine operating principle

The simple single-phase SR machine in fig. 1.2 is able to produce torque over only half of its electrical cycle. Hence, practical applications of SR machines entail higher numbers of stator poles and rotor teeth, with the stator poles wound and connected in several phase windings. For example, the 6 stator-poles, 8 rotor-teeth, topology used for three-phase SR machines, has each stator-phase winding consisting of two concentrated coils series-connected and energized simultaneously. Self-starting in either direction of SR machine requires at least three stator phases.

For understanding the electromechanically energy conversion, a nonlinear analyze of the circuit that take in to account saturation must be realized. However this analyze is based on the magnetization curve. This curve is characterized to be the magnetization curve of the flux-linkage versus current for each specific rotor position. The graphically representation of the stored magnetic energy (W_f) and the co-energy (W_c) is represented in fig. 1.3 and the mathematical expression of the both is realized with equation 1.1.

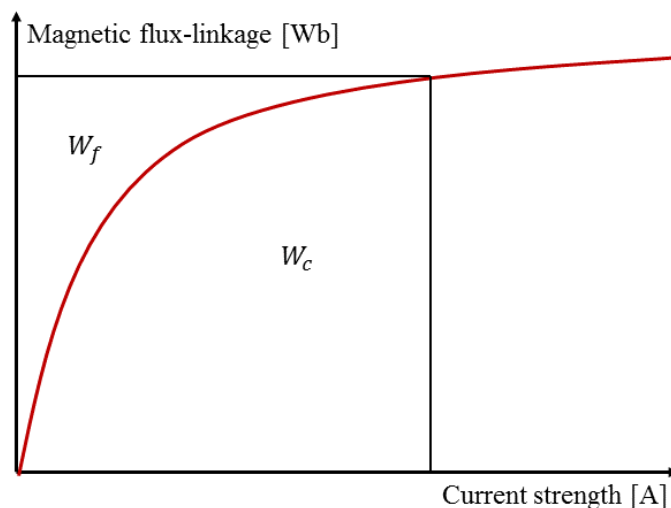


Fig.1.3 Stored field energy and co-energy definition

$$W_f = \int i d\Psi \text{ respectively } W_c = \int \Psi di \quad (1.1)$$

In the case of rotational electrical machines, where the rotor position is constantly changing, the mechanical energy in terms of electromagnetic torque can be obtained from equation 1.2.

$$\delta W_m = T_e \delta \theta \quad (1.2)$$

According to [7] the energy ratio for a switched reluctance machine with saturation flux linkage can be up to 0.65.

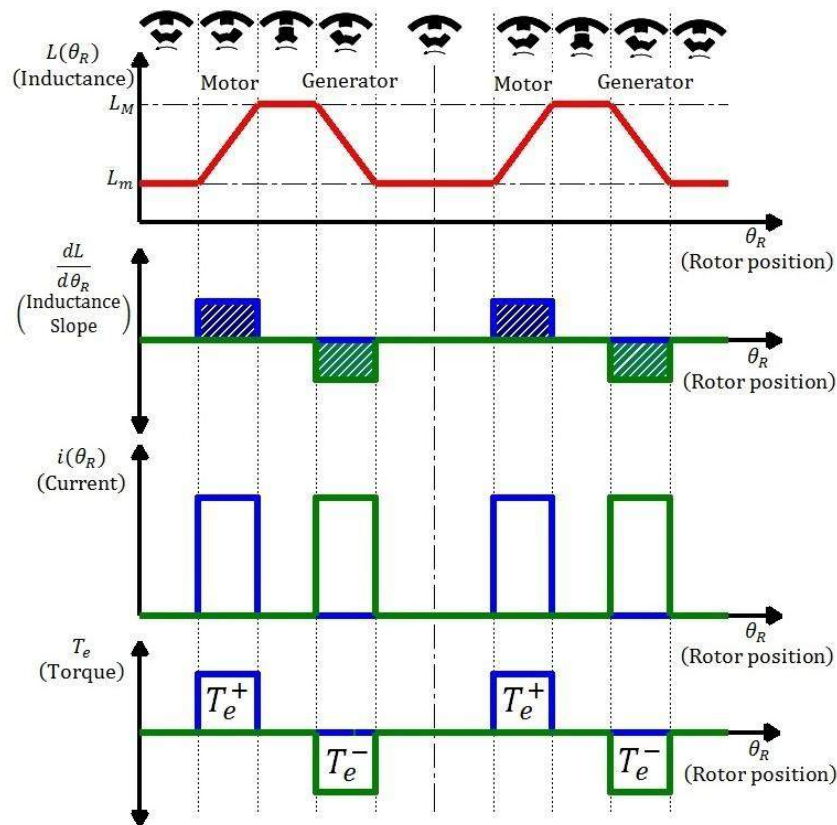


Fig.1.4 Idealized waveforms of the main electromagnetic quantities for a stator phase of SR machine.

The idealized waveforms of the main electromagnetic quantities for a stator phase of SR machine, are shown in fig. 1.4. It can be seen, that the phase inductance changes with rotor position, from a minimum (L_m) to a maximum value (L_M). If the stator phase is energized during the positive-slope variation of phase inductance, when the rotor teeth are not aligned with the corresponding energized stator poles, the phase developed electromagnetic (reluctance) torque T_e is positive (active torque). Conversely, if the stator phase is energized during the negative-slope variation of phase inductance, when the rotor teeth are starting to come out from the aligned position with corresponding energized stator poles, the phase developed torque is negative (resistant or braking torque).

1.3. SR machine as integrated starter-alternator

In conventional gasoline-powered ICE-based automotive vehicles, the functions of the electric starter to spin-up the engine, and of the electric generator to convert mechanical energy to electric energy for charging the battery and running onboard electrical accessories, are performed separately. If the functions of the starting engine and generating electric power are performed by single electric machine, it is named *integrated starter-alternator* (ISA), and the automotive vehicle gets the so-called mild hybrid-electric vehicle configuration [8] (fig.1.5).

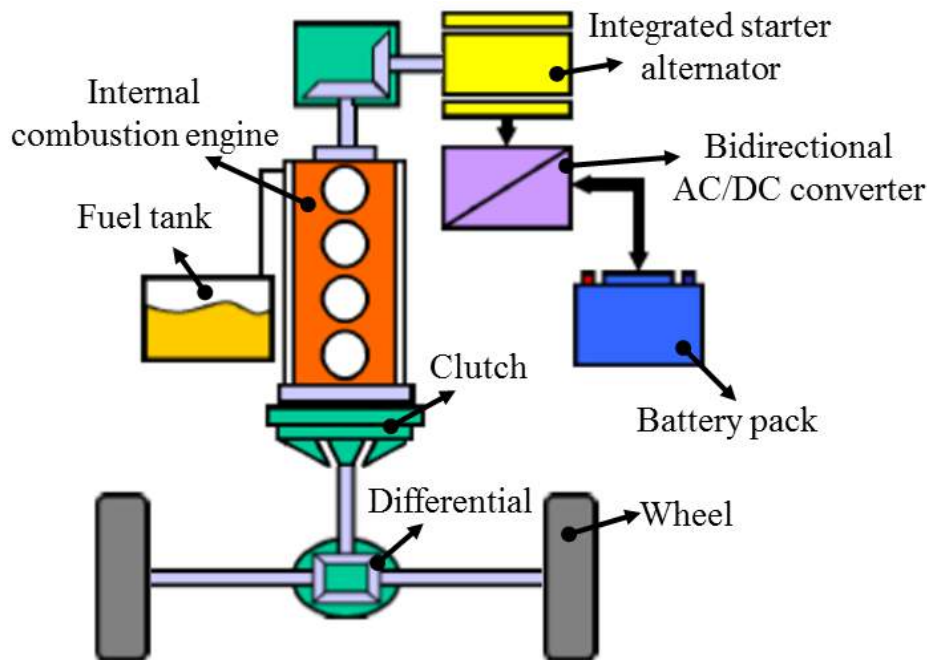


Fig.1.5 Schematic configuration of the mild hybrid-electric vehicle with integrated starter-alternator

ISA allows the engine to instantly start after the idle stop, when the engine shuts down to save fuel and emissions. ISA can help to decelerate the vehicle by regenerative electric braking. By producing electric power for battery charging, the fuel consumption is reduced. Moreover, some provision can be made for accessories, such as air conditioning devices, which can continue to run on electric power when the engine is off.

There are many advantages in using ISA, some of them being listed below [9] [10]:

- The combination between ICE and the electric machine leads in augmentation of the system power, and by enabling a start-stop feature a small ICE can be used without reducing performances.
- The start-stop and the recuperative braking capability together with the high voltage and increased size make the ISA more efficient than a conventional generator, this leads to a minimization with 20% of fuel consumption and a reduction of CO₂ typically with 10% to 25%.
- By using ISA, for ICE starting moment no fuel is necessary, so that starting emissions are considerably lower, especially during the cold cranking period.
- For urban traffic, when normally the engine is idling, it can be shut-down completely.
- ISA can be integrated in most of automotive vehicle models, therefore there is no need to develop new models or to add significant changes in the existing models for integrating ISA.
- With ISA the starting of ICE is possible even at low temperatures.

Currently two types of connections for ISA are used in automotive industry: in the first one, ISA is linked to the ICE through a belt, whereas in the second one, crankshaft is used between the ICE, ISA and gear box (Fig.1.6).

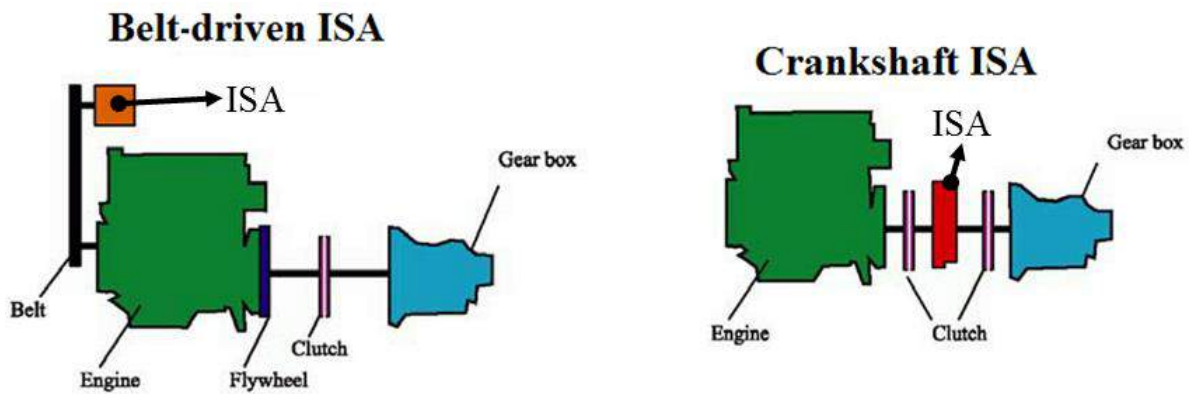


Fig.1.6 ISA connections to the ICE [11]

To avoid the cost and complexity of the belt coupling, the crankshaft is preferred for ISA applications. However, since ISA is directly connected to the crankshaft, it requires much stronger and stable electric current than conventional starter [8]. But for normal batteries, it is hard to handle high power cycle for long time without damaging. Hence, supercapacitor is helpful for reducing the battery pack cost, and improving the overall system efficiency.

SR machine is a valid candidate for ISA applications in automotive industry. If compared to other types of electric machine, SR machines offer an excellent balance between reliability and power density [12]. The absence of windings and permanent magnets on the rotor helps to reduce the inertia and as the major losses are kept within the stator, these aspects makes the SR machine a viable contender for high-speed and high-temperature applications. When operating in generator operation mode, the SR machine provides good electric power quality, high power density and unique fault tolerance [12]. Despite of all these advantages, SR machines engender high torque ripple, high acoustic noise and require costly power electronic converters with high volt-amperes.

In order to justify the choice of switched reluctance machine for integrated starter alternator application a comparison between three electric-machine candidates for ISA applications, i.e. the interior permanent-magnet synchronous (IPMS) machine, the cage induction (CI) machine and the SR machine, is presented in Table 1.1 [13], in terms of weight and cost of their main components [14].

Table 1.1 Comparison between three electric-machine candidates for ISA applications [13]

	Cost/Weight [\$/kg]	Laminated Steel <i>1.6 \$/kg</i>	Copper <i>8 \$/kg</i>	Neodymium Iron Boron <i>100 \$/kg</i>	Total	Cost/Weight [\$/kg]
IPMS machine	<i>Weight</i>	23.87	5.99	1.3	31.16 kg	6.94
	<i>Cost</i>	38.192	47.92	130	216.112	
CI machine	<i>Weight</i>	18.01	18.24	0	36.25 kg	4.82
	<i>Cost</i>	28.816	145.92	0	174.736	
SR machine	<i>Weight</i>	19.27	7.44	0	26.71 kg	3.38
	<i>Cost</i>	30.832	59.52	0	90.352	

Switched reluctance machine has a simple construction making it cheaper in execution but one of the drawbacks of this machine is the torque ripple. Since the IPMS machine has the highest cost due to its expensive Nd-Fe-B rotor magnets, and the CI machine design requires high manufacturing cost of its cage rotor, the choice of SR machine for ISA applications is justified.

It is the aim of this thesis to design and optimize SR machine capable to operate under high starting torque in motor mode (to provide mechanical power to the ICE during start-up), and also to perform as generator at high speed, for ISA applications.

When using the optimization of electric machines, the objective is the maximization or minimization of some quantities. For example, the optimization of SR machine can be done to minimize the torque ripple and/or to maximize the average developed electromagnetic torque.

The many requirements of electrical machines are in contradiction one with each other, therefore finding the optimal geometry and control of a machine can be overwhelming due to the increased number of parameters, model evaluations and time required to finalize the optimization. Hence, one of the objectives of this thesis is to reduce the optimization computation time.

1.4. Conclusions

This chapter briefly reviews the importance of fuel consumption diminution for CO₂ minimization. The operation principle of switched reluctance machine in both motor and generator is also described in this part. The connection possibilities for integrated starter alternator system together with some advantages of using ISA in the automotive industry, are also provided and described in this chapter.

The link between the electrical machine and the ICE is also detailed in this chapter. To justify the choice of SR machine for ISA applications a comparison in terms of costs is realized in this part of the thesis. It is possible to conclude that due to its simple rotor the SR machine proved to be the cheapest one.

Selected references

- [1] Anwar M. N. Teimor M. Swales S., "Switched Reluctance Machine Converter Design for ISA Applications from Engine Cranking Perspectives," in *IEEE International Conference on Electric Machines and Drives*, San Antonio, TX, 2005, pp. 219 - 226.
- [2] IEA Statistics. (2015) International Energy Agency. [Online]. www.iea.org
- [3] Gerada D. Mebarki A., Brown N. L., Gerada C., Cavagnino A. Boglietti A., "High-Speed Electrical Machines: Technologies, Trends, and Developments," *IEEE Transactions on Industrial Electronics*, vol. Volume:61, no. June 2014, pp. 2946 - 2959, December 2013.
- [4] Wikipedia. [Online]. <https://en.wikipedia.org>
- [5] Wikipedia. [Online]. <https://en.wikipedia.org>.
- [6] R. Krishnan, *SWITCHED RELUCTANCE MOTOR DRIVES Modeling, Simulation, Analysis, Design, and Applications*. United States of America: CRC Press LLC, 2001.
- [7] Miller T. J. E. (Ed.), *Electronic control of switched reluctance machines*. Newnes. Oxford, UK, 2001.
- [8] I. Boldea, "Starter/alternator system for HEV and their control: a review," *KIEE International Trans. on EMECS*, vol. 4-B, pp. 157-169, July 2004.
- [9] Jain A. K. Mathapati S., Ranganathan V. T. Narayanan V. A. N. V. , "Integrated Starter Generator for 42-V Powernet Using Induction Machine and Direct Torque Control Technique," *IEEE TRANSACTIONS ON POWER ELECTRONICS*, vol. 21, no. 3, pp. 701 - 710, May 2006.
- [10] Zhang P. Williamson S. S., "Recent Status and Future Prospects of Integrated Starter-Generator Based Hybrid Electric Vehicles," in *IEEE Vehicle Power and Propulsion Conference (VPPC)*, Harbin, China, 2008, pp. 1-8.
- [11] Viorel I. A. Szabó L., Lowenstein L. STET C., "INTEGRATED STARTER-GENERATORS FOR AUTOMOTIVE APPLICATIONS," in *Conferința anuală de acționări electrice CNAE*, Cluj-Napoca, 2004, pp. 251-254.
- [12] Sun J. Kuang Z., Wu H., Wang S. Ning G., "Implementation of a high-speed switched reluctance starter/generator system. ," in *Electrical Machines and Systems (ICEMS)*, 2011, pp. 1-5.

- [13] Dorrell D. G. Knight A. M., Popescu M., Evans L., Staton D. A., "Comparison of different motor design drives for hybrid electric vehicles," in *IEEE Energy Conversion Congress and Exposition*, Atlanta, GA, 2010, pp. 3352 - 3359.
- [14] Tianjin Shunxin Steelplate Co. [Online]. www.alibaba.com

Chapter 2

Modeling and simulation of the switched reluctance machine

2.1. Introduction

As mentioned in the first chapter this thesis studies the SR rotating machine with radial flux [1]. As name implies the functioning of the machine is linked to a commutation sequence, provided through a full-bridge or half-bridge inverter. Because one of the aspects of this thesis is based on optimizing the SR machine an analytical model that considers the saturation effect and the machine geometry must be provided. Therefore, in this chapter the analytical model of this machine is developed along with a modality of computing the maximum and minimum inductance based on the magnetic flux lines. Finally the entire system implemented in Matlab/Simulink environment is presented together with the importance of the commutation angles.

2.2. Topologies of switched reluctance machine and associated power electronic converter

2.2.1. Classical SR machine topologies

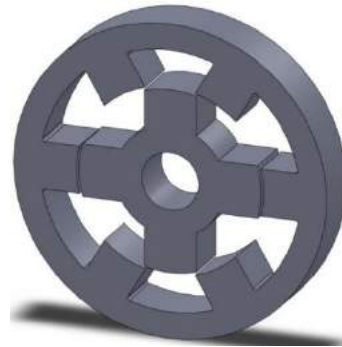
For SR machine the number of stator poles and rotor teeth is chosen so that the sum of electromagnetic torque produced by each phase is never zero. Hence, the number of stator and rotor poles will never be equal and they can be calculated as follows:

$$N_S = q \cdot 2 \cdot N_p \text{ and } N_R = N_S - 2 \cdot N_p \quad (2.1)$$

where q represents the number of phases and N_p is the number of pole pairs per phase.



$$q = 2, k = 1 \text{ then } N_S = 4 \text{ and } N_R = 2$$



$$q = 3, k = 2 \text{ then } N_S = 6 \text{ and } N_R = 4$$



$q = 4, k = 3$ then $N_S = 8$ and $N_R = 6$

$q = 5, k = 4$ then $N_S = 10$ and $N_R = 8$

Fig.2.1 3D view of different SR machine topologies

Over the years several configurations have been proposed in literature; 3D views of different configurations with an increased number of stator teeth are presented in fig. 2.1. In general, multiphase SR machine benefits by reduction of the ripple torque, but exhibits higher manufacturing costs, since it requires a larger amount of electronic switching devices in the associated power converter for its operation. In order to have the guaranty for starting in both motion directions, at least three phases are required [2].

2.2.2. Novel SR machine topologies

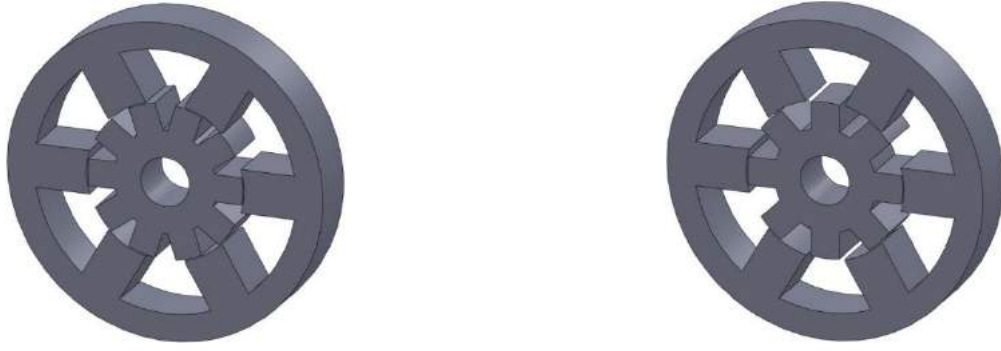
For the SR machine topologies in which the number of rotor teeth are greater than the number of stator poles [3], it is possible to introduce a new relationship, i.e.

$$N_R = 2N_S - 2 \quad (2.2)$$

when $N_S > 4$.

One results the configuration of fig. 2.2 (left side) with 6 stator poles and 10 rotor teeth. For this configuration the operation principle is simple and similar to classical topologies. In this case, if one rotor tooth is at 12° away and another is at 24° away, the one that is nearest with the energized stator pole will be attracted. Therefore the rotation will be continuous and without dead zones. According to [4] and [5] this configuration exhibits increased electromagnetic torque density and smaller torque pulsations.

The three-phase SR machine having the configuration inspired from [6] and presented in fig. 2.2 (right side), i.e. 6 stator and 8 rotor teeth will be the SR machine topology studied in this thesis. The reasons for this choice are the advantages of larger available stator-windings space, higher average electromagnetic torque, and lower ripple torque due to the increased number of strokes compared to the 6 stator-pole /4 rotor-tooth topology [7].



$q = 3, k = 5$ then $N_S = 6$ and $N_R = 10$

$q = 3, k = 4$ then $N_S = 6$ and $N_R = 8$

Fig.2.2 3D view of different non-conventional SR machine topologies

2.2.3. Topologies of SR machine associated power electronic converters

2.2.3.1. Three-phase asymmetric half-bridge power converter

The commonly used power electronic converter associated to SR machine is of three-phase half-bridge topology (fig. 2.3). A bridge of this converter is based on two controllable IGBTs and two diodes used for demagnetization.

This type of converter provides the most control flexibility and fault tolerance. Using this converter, each phase can be supplied independently with positive and negative DC voltage. This independence between phases makes the converter reliable during fault conditions. If the machine works in motor operation mode during regenerative braking the converter provides a maximum capacity of energy recovery [8].

When a three phase SR machine with 6 stator poles and 8 rotor teeth (6/8 SR machine) is considered, the electronic commutation pattern is that presented in the right part of fig. 2.3. Considering that the rotor is aligned with *stator phase C*, the operating principle is simple, as it is done on the positive slope of phase inductance (motor operation mode). In this case, *stator phase A* is in conduction, and transistors T_1 and T_2 are conducting; when the rotor reaches the aligned position, transistors T_1 and T_2 are blocked, and demagnetization is realized through diodes D_1 and D_2 . The advantage of using this power electronic converter in this case is given by the possibility of prolonging the excitation of *phase A* more than one period ($\theta_{period} = 2\pi/q \cdot N_R$) or continuing the supply of the second phase before rotor reaches the aligned position due to the phase independence.

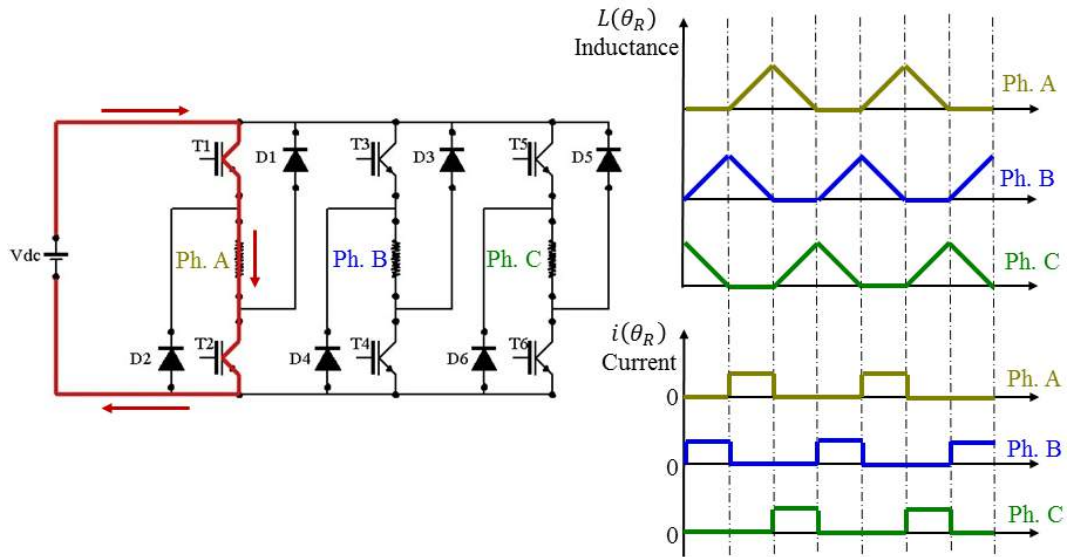


Fig.2.3 Three-phase asymmetric half-bridge power converter and phase conduction intervals in motor operation mode of SR machine

When the phase is energized during the negative slope variation of phase inductance (generator operation) from an external DC voltage (V_{dc}) via the transistors T_1 and T_2 (fig 2.4 excitation period) and when the SR machine generated voltage exceeds the V_{dc} value, conducting diodes D_1 and D_2 switch on and the flow of the current is the one presented in fig. 2.4 generation period. As it can be seen from the figure the direction of the current in the phase is always the same during the excitation and the generation period.

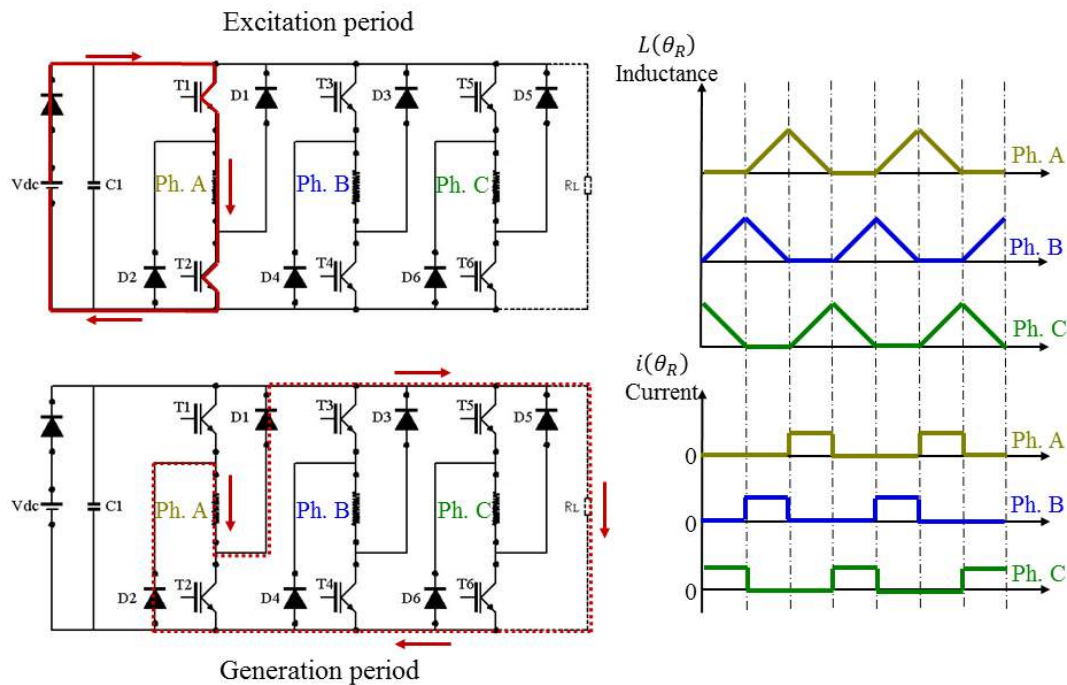


Fig.2.4 Three-phase asymmetric half-bridge power converter and phase conduction intervals in generator operation mode of SR machine

2.2.3.2. Miller power converter

Another power converter topology associated to SR machine is Miller converter (fig.2.5). It has the advantage of requiring less (only four) power devices compared to the three-phase half-bridge asymmetric converter.

Its structure is built starting from a three-phase half-bridge inverter, the lower part being kept and the upper part being replaced by only one IGBT. The phase conduction period is provided by transistors T_2 to T_4 (fig.2.5), therefore if *phase A* is to be energized, one will have three operating stages:

- magnetization stage when T_1 and T_2 are in conduction
- demagnetization when T_1 and T_2 are closed to the current flow, in which case the current in phase decreases fast through the phase diode and the commune diode
- period of freewheeling when T_1 is in conduction and T_2 is not, hence the phase current in this case is decreasing slowly

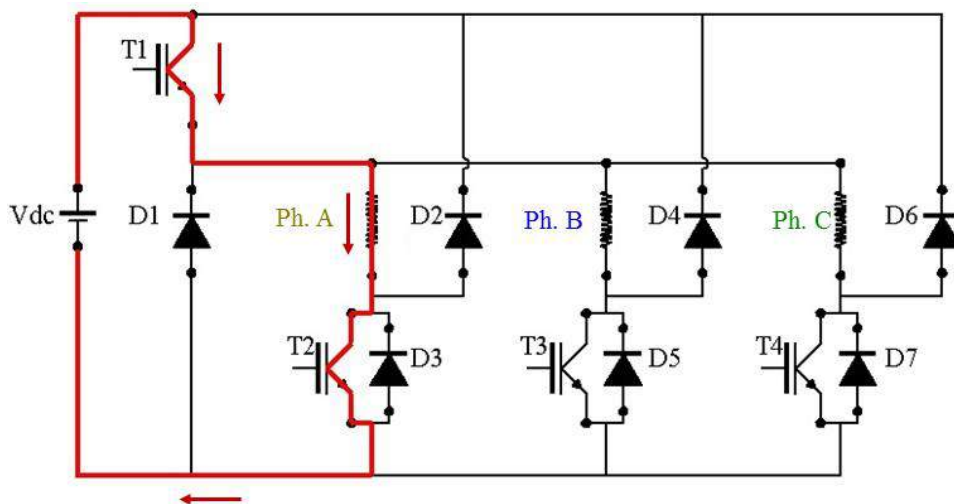


Fig.2.5 Miller power converter associated to SR machine

Miller power converter is disadvantageous when two phases are supplied in the same time, since in the conduction time the voltage of each phase will be half of the supplied DC-bus voltage [9].

2.2.3.3. Three-phase full bridge power converter

The three-phase full-bridge power converter is becoming common solution for many manufacturers, which offer the power module with the driver and protection circuits, as for three-phase AC machines. Given the fact that the price is less than for the above topologies, many authors have studied the electronic commutation and control of SR machines via such three-phase full-bridge power converters [10].

A three-phase star-connected 6/8 SR machine with ideal waveforms of phase inductance and current is presented in fig. 2.6. The three-phase full-bridge power converter entails three operating stages:

- if transistors T_3 and T_2 are conducting, the current in phase B is positive and in phase A is negative
- when T_3 is blocked, the phase current decreases slowly through diode D_3 and transistor T_4
- if both transistors T_3 and T_4 are blocked, the phase current decreases fast thanks to the negative voltage applied via diodes D_3 and D_4

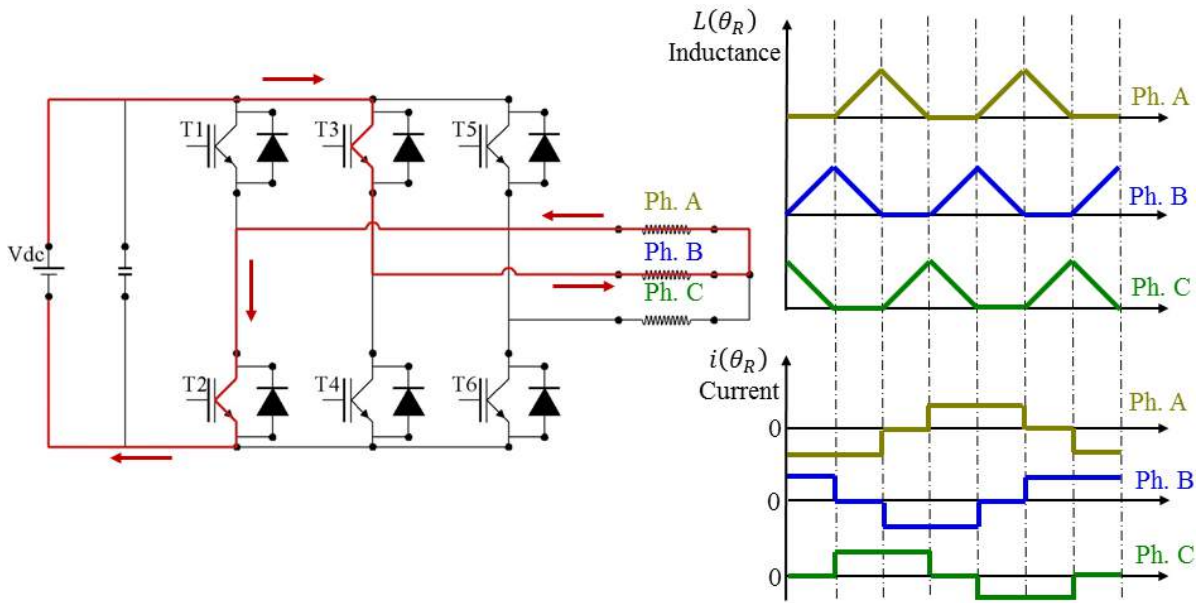


Fig.2.6 Three-phase full-bridge power converter associated to SR machine with corresponding stator phase inductance and current waveforms

As pointed out in [9] the major advantage of using three-phase full-bridge power converter associated to SR machines is justified by the low overall cost. By using this converter the number of switching pulses is reduced, therefore the switching losses are decreasing.

2.2.4. SR machine prototype under study

The SR machine studied in this thesis is of three-phase 6/8 topology with the expedient features of more machine-sizing flexibility, larger available stator-winding space, lesser mass for stator and rotor laminations, higher average electromagnetic torque and lower torque ripple due to increased number of strokes, and hence faster rate of change of the stator phase-winding inductance, when compared to conventional 6/4 and 12/8 SR machine topologies with similar volume constraints [3] [4] [5]. A detailed view in SolidWorks environment of the studied SR machine is presented in fig. 2.7.

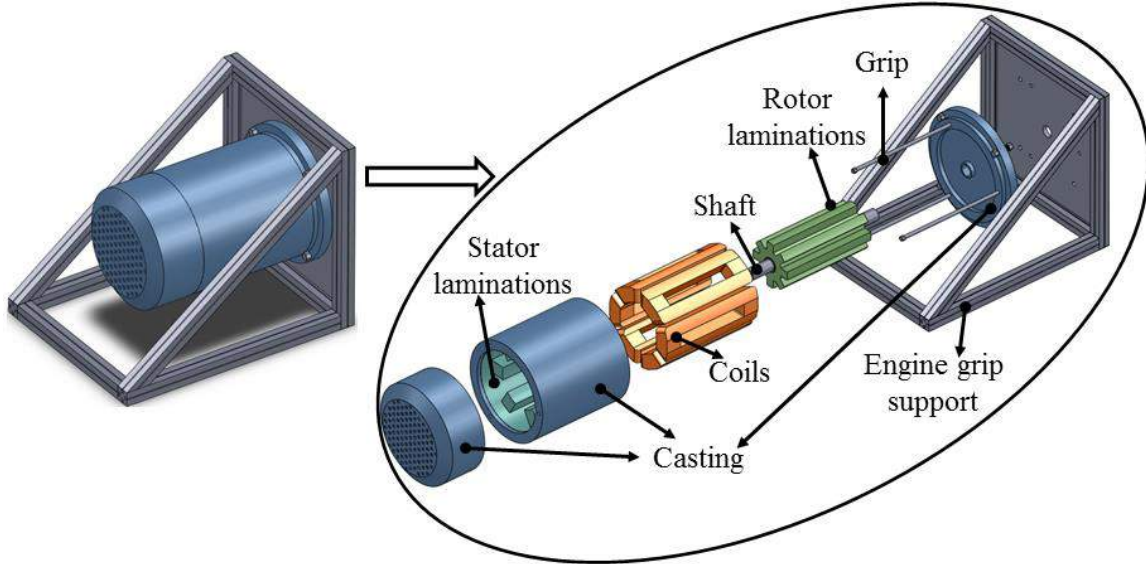


Fig.2.7 Isometric view of the SR machine prototype under study

This SR machine topology is used to validate by numerical simulations and experimental tests the optimization process developed in this thesis. Table 2.1 introduces some design data, more detailed description of design and materials used for the SR machine prototype being found in [9].

Table 2.1 Main design data of the SR machine prototype under study

Signification	Symbols	Value	Units
Number of stator teeth	N_S	6	-
Number of rotor teeth	N_R	8	-
Stator outer diameter	$D_{S_{ext}}$	116.6	[mm]
Stator inner diameter	$D_{S_{int}}$	58.25	[mm]
Stator pole width	w_S	16	[mm]
Stator yoke width	J_S	10	[mm]
Rotor outer diameter	$D_{R_{ext}}$	56.55	[mm]
Rotor inner diameter	$D_{R_{int}}$	38	[mm]
Rotor pole width	w_R	10.5	[mm]
Rotor yoke width	J_R	10	[mm]
Airgap	g	0.85	[mm]
Machine axial length	l_a	118	[mm]

The number of turns per stator phase is $N_{sp} = 156$, and the electrical resistance of each phase is $R = 3.1 \Omega$. The maximum admissible temperature of the phase windings is 155°C . The SR machine is equipped with Baumer IVO GI321-type encoder having resolution of 600 pulses for recording the rotor position and speed.

2.3. Analytical modeling of the SR machine prototype

The analytical model is applied for a three-phase 6/8 switched reluctance machine topology, i.e having $N_S = 6$ stator poles and $N_R = 8$ rotor poles that means that the angle between aligned and unaligned position is 22.5° . This value is deduced to be half of one period

$(2\pi/N_R)$ that in this particular case is 45° . The aligned and unaligned positions (fig.2.8) are characterized as follows [11]:

- when the axis of rotor pole and stator excited pole are in the same direction it means that the rotor and stator teeth are aligned (we consider this position $\theta = 0^\circ$ in future simulations) (fig.2.8 left)
- when the axis of two rotor poles is in the same direction with the axis of one excited stator pole that means the rotor and stator teeth are unaligned (we consider this position $\theta = 22.5^\circ$ in future simulations) (fig.2.8 right)

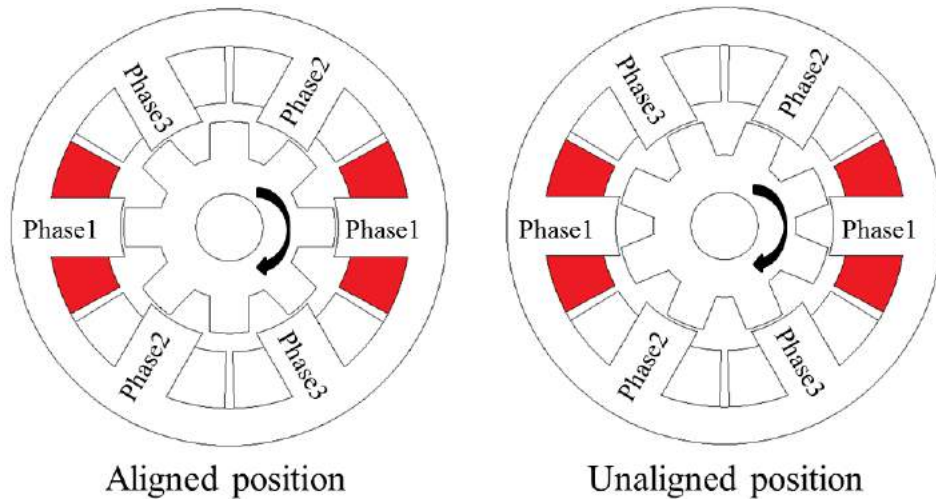


Fig.2.8 Different rotor positions for the SR machine prototype

2.3.1. Analysis of voltage equations

For the simplification when writing the voltage equations we neglect the mutual inductance between phases, this being justified by its lower value, verified by finite elements analyze and measurements on the prototype. We also neglect the effect of fringing flux around the corners and we assume that the flux lines cross the airgap in the radial direction. Instead we consider the material magnetic saturation. Therefore the general stator phase-winding voltage equation of the three-phase 6/8 SR machine under study can be written as shown in eq. 2.3.

$$u_{ph} = R \cdot i_{ph} + \frac{d\Psi_{ph}(i_{ph}, \theta)}{dt} \quad (2.3)$$

The leakage flux per phase is given by $\Psi_{ph} = L(i_{ph}, \theta) \cdot i_{ph}$, with L being the phase inductance, which is dependent on the current and rotor position. On this basis, the voltage equation becomes:

$$u_{ph} = R \cdot i_{ph} + \frac{d(L(i_{ph}, \theta)i_{ph})}{dt} =$$

$$= R \cdot i_{ph} + \left(L(i_{ph}, \theta) + i_{ph} \frac{\partial (L(i_{ph}, \theta))}{\partial i_{ph}} \right) \frac{di_{ph}}{dt} + i_{ph} \cdot \Omega \frac{\partial (L(i_{ph}, \theta))}{\partial \theta} \quad (2.4)$$

The last term in the above equation is the motional phase back-emf developed in the SR machine, which opposes the increase of stator-phase current during motoring, whereas contributes to the increase of stator-phase current in generating mode of operation. The relation is deduced from the switched reluctance machine's one phase equivalent circuit (fig.2.9).

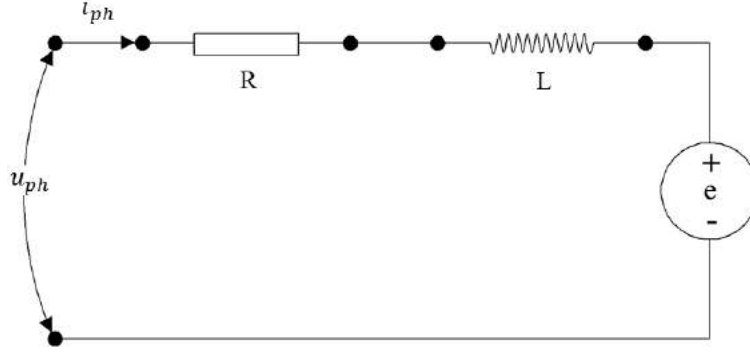


Fig.2.9 Stator-phase equivalent circuit

By neglecting the nonlinear effects of saturation, i.e. assuming magnetic linearity, the SR motor/generator voltage eq. 2.4 can be simplified as:

$$u_{ph} = R \cdot i_{ph} + L(\theta) \frac{di_{ph}}{dt} + i_{ph} \cdot \Omega \frac{\partial L(\theta)}{\partial \theta} \quad (2.5)$$

All equations for voltage computation are written for one phase only, for the other phases the same equation is applied. The mathematical computation of the voltage equation can be found in *Appendix 2.A*.

2.3.2. Instantaneous electromagnetic torque

The instantaneous electric power (P_i) is given by multiplying the voltage equation with the current, therefore when saturation is considered the equation can be written as:

$$P_{i,ph} = u_{ph} \cdot i_{ph} = R \cdot i_{ph}^2 + L(\theta) \cdot i_{ph} \cdot \frac{di_{ph}}{dt} + i_{ph}^2 \cdot \Omega \cdot \frac{dL(\theta)}{d\theta} \quad (2.6)$$

At any instant the magnetic stored energy change is given by eq. 2.7.

$$\begin{aligned} \frac{d}{dt} \left(\frac{1}{2} L(\theta) \cdot i_{ph}^2 \right) &= \frac{1}{2} i_{ph}^2 \frac{dL(\theta)}{dt} + L(\theta) \cdot i_{ph} \frac{di_{ph}}{dt} \\ &= \frac{1}{2} i_{ph}^2 \cdot \Omega \cdot \frac{dL(\theta)}{d\theta} + L(\theta) \cdot i_{ph} \frac{di_{ph}}{dt} \end{aligned} \quad (2.7)$$

The airgap or mechanical power conversion according to energy conversion law $P = \Omega \cdot T_e$, is what's left after resistive losses $R \cdot i_{ph}^2$ and from the input power we can withdraw the magnetic stored energy, with T_e being the instantaneous electromagnetic torque. According to [12] it is possible to write:

$$T_{e,ph} = \frac{1}{2} i_{ph}^2 \frac{dL}{d\theta} \quad (2.8)$$

It should be noted that $dL/d\theta$ is the inductance slope presented in chapter 1.

When the nonlinear effect of saturation is considered, the electromagnetic torque developed by the three-phase 6 stator and 8 rotor teeth machine can be expressed in terms of phase magnetic co-energy (presented in chapter 1) as:

$$T_{e,ph}(i_{ph}, \theta) = \left. \frac{\partial W_{c,ph}}{\partial \theta} \right|_{i_{ph}=cte} = \left. \frac{\partial \int_0^{i_{ph}} L(i_{ph}, \theta) \cdot i_{ph} \cdot di}{\partial \theta} \right|_{i_{ph}=cte} \quad (2.9)$$

During motoring operation, the SR machine produces positive phase electromagnetic torque for the positive phase self-inductance slope at rotor angles between unaligned and the next aligned pole position in the direction of rotation. In generating mode, due to the negative slope of the phase-winding inductance from aligned to unaligned pole position in the direction of rotation, negative phase electromagnetic torque is produced.

2.3.3. Phase inductance vs. rotor position

The motional phase back-emf depends on the slope of the phase-winding self-inductance profile with reference to rotor position, which has the ideal shape shown in fig. 2.10. The self-inductance corresponds for one phase when material magnetic saturation and fringe effect are neglected, a representation of it being exemplified in the below figure. This inductance changes with the changing of the number of rotor poles and the width of the stator and rotor teeth. Before computing the angles θ_1 to θ_5 we need to compute the rotor arc opening β_{Ropen} .

$$\beta_{Ropen} = \frac{2\pi - N_R \cdot \beta_R}{N_R} \quad (2.10)$$

$$\theta_1 = \frac{\beta_S - \beta_{Ropen}}{2} \quad (2.11 \text{ a})$$

$$\theta_2 = \beta_R - \theta_1 \quad (2.11 \text{ b})$$

$$\theta_3 = \theta_2 + (\beta_S - \beta_R) \quad (2.11 \text{ c})$$

$$\theta_4 = \theta_3 + (\beta_{Ropen} + \beta_R - \beta_S) \quad (2.11 d)$$

$$\theta_5 = \theta_4 + \theta_1 = \frac{2\pi}{N_R} \quad (2.11 e)$$

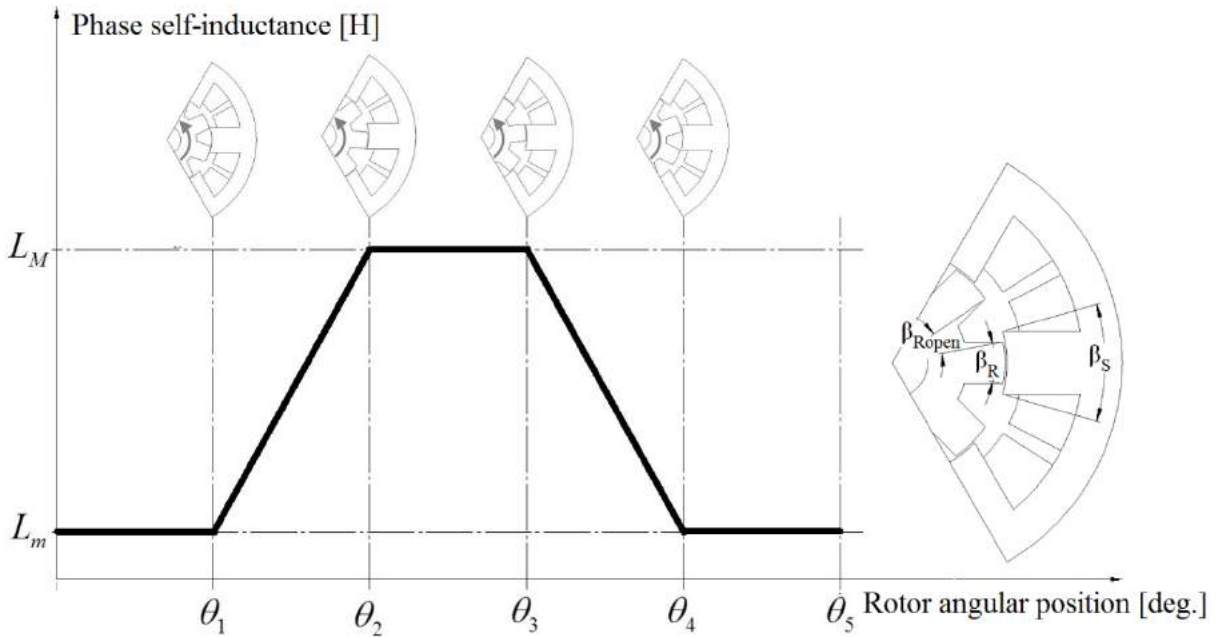


Fig.2.10 Idealized stator-phase inductance profile vs. rotor position for the three-phase 6/8 SR machine prototype

Fig. 2.10 points out four distinct regions:

- $0 \rightarrow \theta_1$ and $\theta_4 \rightarrow \theta_5$: For the prototype under the study, having an increased number of rotor teeth in respect with stator, a small overlap between rotor and stator teeth appears (see fig. 2.8 Unaligned), this means that the flux lines will be concentrated in the overlap area. Considering that the area of overlapping is small, the torque production between $0 \rightarrow \theta_1$ and $\theta_4 \rightarrow \theta_5$ will be small. The inductance in this region is known as unaligned inductance L_u .
- $\theta_1 \rightarrow \theta_2$: The area of overlapping increases, that means that the flux path is mainly through the stator and rotor laminations. The linear increasing of the overlap area leads to an increase of the inductance, giving it a positive slope. By applying a current in the windings in this period, a positive torque will be produced, i.e motor operation mode. The inductance increase period ends when the overlap is complete.
- $\theta_2 \rightarrow \theta_3$: During this interval the area of overlapping is constant, that means that the path of the dominant flux is the same, leading to a constant maximum inductance, being known as aligned inductance L_a . For this interval the torque

generation is zero even if remnant current may be found in the phase during this area. This interval provides the necessary time for the current to decrease.

- $\theta_3 \rightarrow \theta_4$: In this interval the area of overlapping starts to decrease, i.e the rotor teeth are starting to come out from the aligned position. This area is similar with the region $\theta_1 \rightarrow \theta_2$ but opposite, meaning that the inductance starts to decrease having a negative slope. When applying a current in this area the electromagnetic torque produced will be negative i.e SR machine works in generator operation mode.

The representation from fig. 2.10 is pure informative, because in reality the phase inductance does not have this ideal form due to the saturation effect, which rounds the inductance curve near the top. The values of the angles θ_1 to θ_5 applied for this prototype can be found in *Appendix 2.B*.

The analytical procedure for calculating the aligned and unaligned inductance for this specific configuration is done by determining the flux path in the two rotor position, when the tooth is aligned and when the rotor is perfectly unaligned with the stator excited one. The next paragraph presents step by step the calculation of the inductance profile.

2.3.3.1. Analytical calculation of the phase inductance for aligned rotor position

The computation of the inductance in the aligned position is simple due to the majority of the flux lines, 90% to 98% of them crossing the airgap in the radial direction [13]. Considering the flux plot for the three-phase six stator eight rotor teeth SR machine shown in fig. 2.11, it can be seen that the majority of the flux lines follow path 1 and one small part follow path 2.

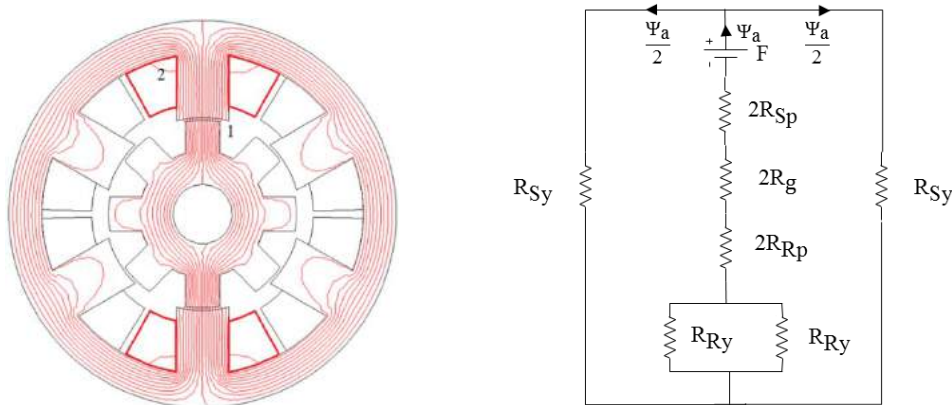


Fig.2.11 Magnetic flux path (left) and equivalent circuit (right) for analytical calculation of the phase inductance for aligned rotor position

The flux density calculated in all machine parts is used to determine the intensities of the magnetic field extracted from the B-H characteristics. First is realized the calculation of the length and area of the cross section for the flux path1 in each segment as follows:

- *Air-gap path1*

$$l_{g1} = g \quad (2.12)$$

$$A_{g1} = \frac{\beta_S \frac{D_{Sint}}{2} l_a + \beta_R \left(\frac{D_{Sint}}{2} - g \right) l_a}{2} \quad (2.13)$$

- *Stator tooth path1*

$$l_{Sp1} = h_S \quad (2.14)$$

$$A_{Sp1} = \beta_S \frac{D_{Sint}}{2} l_a \quad (2.15)$$

- *Rotor tooth path1*

$$l_{Rp1} = h_R \quad (2.16)$$

$$A_{Rp1} = \beta_R \left(\frac{D_{Sint}}{2} - g \right) l_a \quad (2.17)$$

- *Stator yoke path1*

$$l_{Sy1} = \frac{\pi(D_{Sint} + h_S + w_{Sy})}{2} \quad (2.18)$$

$$A_{Sy1} = w_{Sy} \cdot l_a \quad (2.19)$$

- *Rotor yoke path1*

$$l_{Ry1} = \frac{\pi}{2} \left(\frac{D_{Sint}}{4} - g - h_R + \frac{D_{Rint}}{2} \right) \quad (2.20)$$

$$A_{Ry1} = \left(\frac{D_{Sint}}{2} - g - h_R \right) l_a \quad (2.21)$$

Having the equations that allow to compute the length and area for each segment in the flux path1 next we can calculate the reluctance for all segments.

$$R_{g1} = \frac{l_{g1}}{\mu_0 A_{g1}} \quad (2.22)$$

$$R_{Sp1} = \frac{H_{Sp1} l_{Sp1}}{B_{Sp1} A_{Sp1}} \quad (2.23)$$

$$R_{Rp1} = \frac{H_{Rp1} l_{Rp1}}{B_{Rp1} A_{Rp1}} \quad (2.24)$$

$$R_{Sy1} = \frac{H_{Sy1} l_{Sy1}}{B_{Sy1} A_{Sy1}} \quad (2.25)$$

$$R_{Ry1} = \frac{H_{Ry1} l_{Ry1}}{B_{Ry1} A_{Ry1}} \quad (2.26)$$

With the reluctance in each segment one can easily calculate the flux and inductance in path1 as follows:

$$\Psi_{a1} = \frac{N_{sp} \cdot i_{ph}}{2(R_{Sp1} + R_{g1} + 2R_{Rp1}) + \frac{1}{2}R_{Ry1} + \frac{1}{2}R_{Sy1}} \quad (2.27)$$

$$L_{a1} = \frac{N_{sp} \Psi_{a1}}{i_{ph}} \quad (2.28)$$

The length and area of the flux path2 is calculated as shown below, for which the magnetic flux density is concentrated at a radius of $h_s/4$ and an angle of $\pi/2$.

- *Air-gap path2*

$$l_{g2} = \frac{3h_s \pi}{4} \frac{\pi}{2} \quad (2.29)$$

$$A_{g2} = \frac{3h_s}{4} l_a \quad (2.30)$$

- *Stator tooth path2*

$$l_{sp2} = \frac{1}{2} \frac{3h_s}{4} + \frac{w_{sy}}{2} \quad (2.31)$$

$$A_{sp2} = \frac{1}{2} \left(\frac{3h_s}{4} l_a \right) \quad (2.32)$$

- *Stator yoke path2*

$$l_{sy2} \cong l_{sp2} \quad (2.33)$$

$$A_{sy2} = w_{sy} \cdot l_a \quad (2.34)$$

In these segments the reluctance can be calculated as shown in eqs. 2.22, 2.23 and 2.25 applied for their specific lengths and areas calculated above. The flux and inductance is obtained as follows:

$$\Psi_{a2} = \frac{\frac{3}{4} N_{sp} \cdot i_{ph}}{R_{Sp2} + R_{g2} + R_{Sy2}} \quad (2.35)$$

$$L_{a2} = 4 \left[\frac{\frac{3}{4} N_{sp} \cdot i_{ph}}{i_{ph}} \right] = \frac{3N_{sp} \Psi_{a2}}{i_{ph}} \quad (2.36)$$

The total aligned inductance known as maximum inductance derives from:

$$L_M = L_{a1} + L_{a2} \quad (2.37)$$

2.3.3.2. Analytical calculation of the phase inductance for unaligned rotor position

For the fully unaligned inductance we take the position when the axes of the two rotor teeth are identical with the axes of the stator tooth excited. As for the aligned position the reluctance in different segments is calculated R_{Sp} , R_{Sy} , R_{Ry} and R_g for the different flux paths as shown in fig. 2.12.

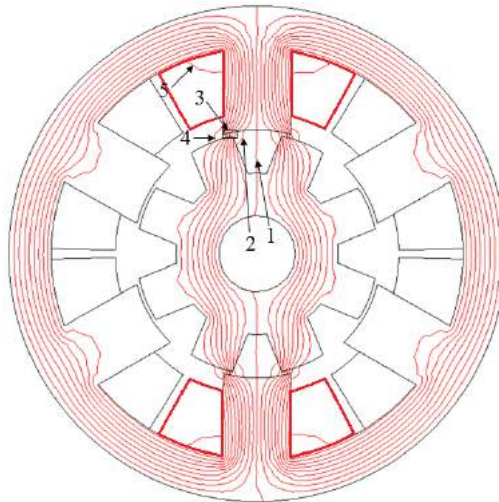


Fig.2.12 Identification of magnetic flux paths for analytical calculation of the phase inductance for unaligned rotor position

The area and the length of the flux path1 are calculated as one quarter of the stator pole arc. Fig. 2.13 shows the first flux path and fig. 2.14 presents the equivalent circuit for the path1 for the fully unaligned position.

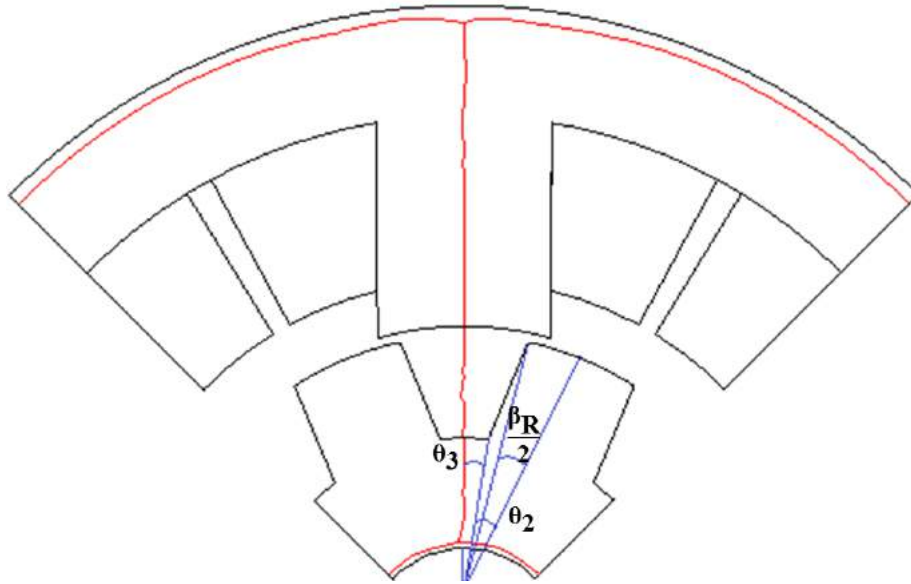


Fig.2.13 Magnetic flux path1 for unaligned rotor position

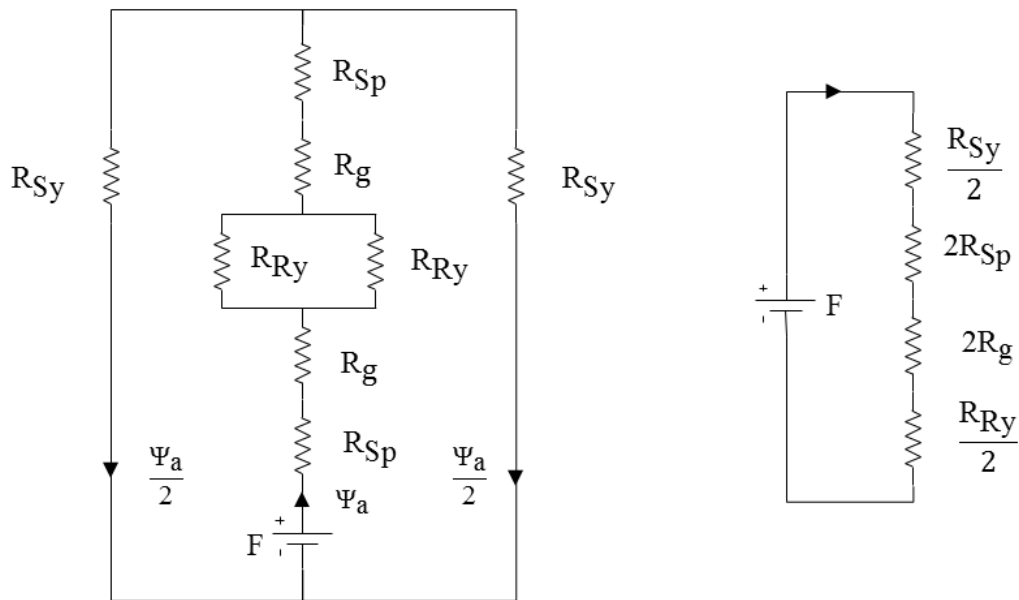


Fig.2.14 Equivalent circuit and simplified circuit of the magnetic flux path1 for unaligned rotor position

- *Air-gap path1*

$$l_{g1} = \frac{D_{Sint}}{2} - g - h_R \quad (2.38)$$

$$A_{g1} = 2 \cdot \theta_3 \left(\frac{D_{Sint}}{2} - g - h_R \right) l_a \quad (2.39)$$

Where θ_3 can be calculated as shown in eq. 2.40 assuming that the rotor tooth width is constant throughout the length.

$$\theta_3 = \frac{1}{2} \left(\frac{2\pi}{N_R} \right) - \theta_2 \quad (2.40)$$

$$\theta_2 = \frac{\frac{\beta_R \left(\frac{D_{Sint}}{2} - g \right)}{2}}{\left(\frac{D_{Sint}}{2} - g - h_R \right)} \quad (2.41)$$

- *Stator tooth path1*

$$l_{Sp1} = h_S \quad (2.42)$$

$$A_{Sp1} = \frac{1}{4} \left(\frac{D_{Sint}}{2} \beta_S \cdot l_a \right) \quad (2.43)$$

- *Stator yoke path1*

$$l_{Sy1} = \frac{\pi(D_{Sint} + 2h_S + w_{Sy})}{2} \quad (2.44)$$

$$A_{Sy1} = w_{Sy} \cdot l_a \quad (2.45)$$

- *Rotor yoke path1*

$$l_{Ry1} = \pi \left(\frac{D_{Rint}}{4} + \frac{D_{Sint}}{4} - \frac{g}{2} - \frac{h_R}{2} \right) \quad (2.46)$$

$$A_{Ry1} = \left(\frac{D_{Sint}}{2} - g - h_R - \frac{D_{Rint}}{2} \right) l_a \quad (2.47)$$

In these segments the reluctance can be calculated as shown in eqs. 2.22, 2.23 and 2.25 applied for their specific length and areas determined above. The flux and inductance result:

$$\Psi_{u1} = \frac{N_{sp} \cdot i_{ph}}{2R_{Sp1} + 2R_{g1} + \frac{R_{Sy1}}{2} + \frac{R_{Ry1}}{2}} \quad (2.48)$$

$$L_{u1} = \frac{N_{sp} \Psi_{u1}}{i_{ph}} \quad (2.49)$$

In the calculation of the flux path in path2 it is assumed that the flux lines come out from the stator teeth at $\frac{5}{64} \beta_S$ and enter in the rotor tooth at $\frac{h_R}{4}$, therefore the arc of the flux path is considered to be $\frac{3}{48} \beta_S$. The magnetic equivalent circuit of the flux path2 is presented in fig. 2.15 right and fig. 2.15 left presents the flux line in path2.

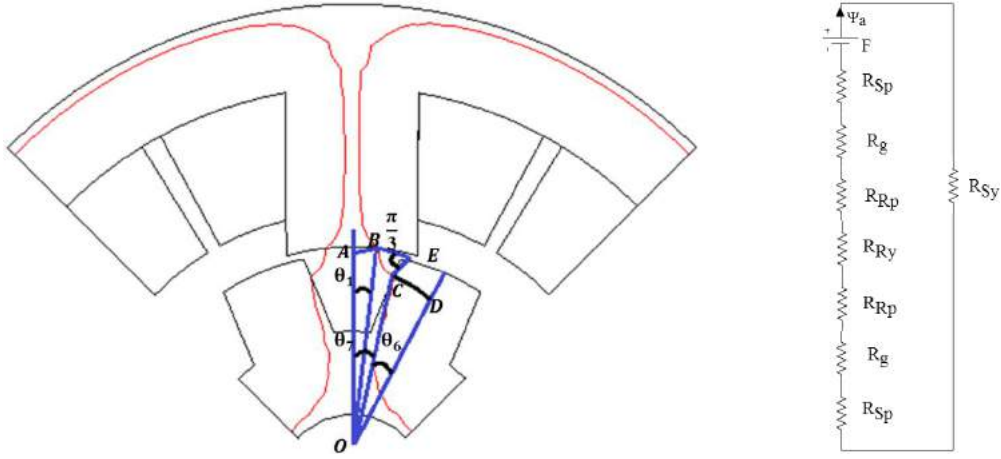


Fig.2.15 Magnetic flux path2 (left) and equivalent (right) circuit for unaligned rotor position

- *Air-gap path2*

$$OD = \left(\frac{D_{Sint}}{2} - g - \frac{h_R}{4} \right) \quad (2.50)$$

$$CD = \left(\frac{D_{Sint}}{2} - g \right) \frac{\beta_R}{2} \quad (2.51)$$

$$OB = \frac{D_{Sint}}{2} \quad (2.52)$$

$$\theta_1 = \left(\frac{\beta_S}{2} - \frac{5}{64} \beta_S \right) \quad (2.53)$$

$$\theta_6 = \frac{CD}{OD} \quad (2.54)$$

$$\theta_7 = \theta_{rp} - \theta_6 \quad (2.55)$$

The coordinates of B and C can be calculated with eqs. 2.56 and 2.57 respectively.

$$B = (x_1, y_1) = [(OB)\sin\theta_1, (OB)\cos\theta_1] \quad (2.56)$$

$$C = (x_2, y_2) = [(OD)\sin\theta_7, (OD)\cos\theta_7] \quad (2.57)$$

$$BC = \sqrt{(x_2 - x_1)^2 + (y_2 - y_1)^2} \quad (2.58)$$

$$l_{g2} = BC \left(\frac{\pi}{3} \right) \quad (2.59)$$

$$A_{g2} = \frac{1}{2} (A_{Rp2} + A_{Sp2}) \quad (2.60)$$

- *Stator tooth path2*

$$l_{Sp2} \cong h_S \quad (2.61)$$

$$A_{Sp2} = \frac{3}{48} \beta_S \frac{D_{Sint}}{2} l_a \quad (2.62)$$

- *Rotor tooth path2*

$$l_{Rp2} \cong \frac{3}{4} h_R \quad (2.63)$$

$$A_{Rp2} = \frac{h_R}{4} l_a \quad (2.64)$$

- *Stator yoke path2*

$$l_{Sy2} \cong l_{Sy1} \quad (2.65)$$

$$A_{Sy2} \cong A_{Sy1} \quad (2.66)$$

- *Rotor yoke path2*

$$l_{Ry2} \cong l_{Ry1} \quad (2.67)$$

$$A_{Ry2} \cong A_{Ry1} \quad (2.68)$$

$$\Psi_{u2} = \frac{N_{sp} \cdot i_{ph}}{2(R_{Sp2} + R_{g2} + R_{Rp2}) + R_{Sy2} + R_{Ry2}} \quad (2.69)$$

$$L_{u2} = 2 \frac{N_{sp} \Psi_{u2}}{i_{ph}} \quad (2.70)$$

When calculating the flux path3, the considerations are like in aligned position because one small part of the rotor tooth overlaps the stator. Fig. 2.16 represents the flux lines that cross the stator and the rotor in the overlapped segment.

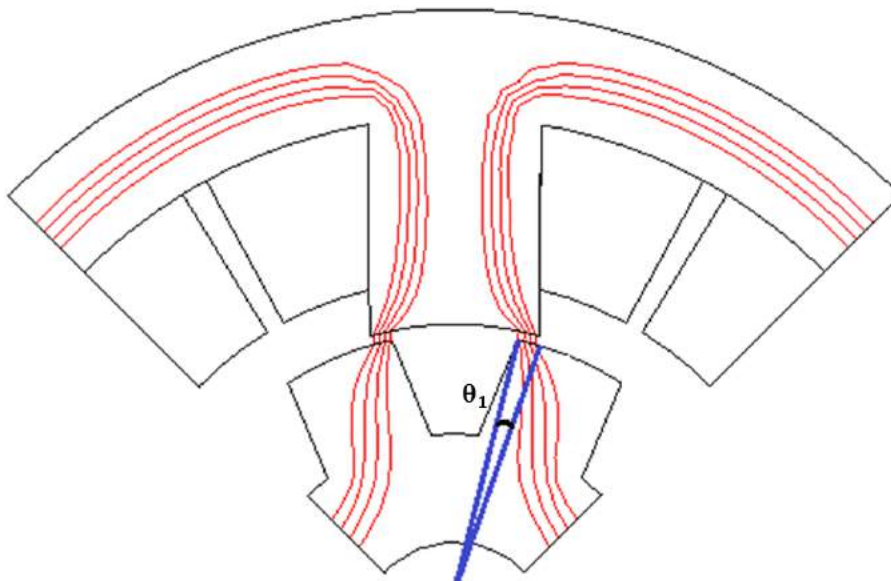


Fig.2.16 Magnetic flux path3 for unaligned rotor position

- *Air-gap path3*

$$l_{g3} = g \quad (2.71)$$

$$\theta_1 = \frac{\beta_S - \beta_{\text{Ropen}}}{2} \quad (2.72)$$

$$A_{g3} = \frac{\theta_1 \frac{D_{\text{Sint}}}{2} l_a + \theta_1 \left(\frac{D_{\text{Sint}}}{2} - g \right) l_a}{2} \quad (2.73)$$

- *Stator tooth path3*

$$l_{Sp3} = h_S \quad (2.74)$$

$$A_{Sp3} = \theta_1 \frac{D_{\text{Sint}}}{2} l_a \quad (2.75)$$

- *Rotor tooth path3*

$$l_{Rp3} = h_R \quad (2.76)$$

$$A_{Rp3} = \theta_1 \left(\frac{D_{\text{Sint}}}{2} - g \right) l_a \quad (2.77)$$

- *Stator yoke path3*

$$l_{Sy3} \cong l_{Sy1} \quad (2.78)$$

$$A_{Sy3} \cong A_{Sy1} \quad (2.79)$$

- *Rotor yoke path3*

$$l_{Ry3} \cong l_{Ry1} \quad (2.80)$$

$$A_{Ry3} \cong A_{Ry1} \quad (2.81)$$

$$\Psi_{u3} = \frac{N_{sp} \cdot i_{ph}}{2(R_{Sp3} + R_{g3} + R_{Rp3}) + R_{Sy3} + R_{Ry3}} \quad (2.82)$$

$$L_{u3} = 2 \frac{N_{sp} \Psi_{u3}}{i_{ph}} \quad (2.83)$$

For flux path4 is considered that the path when flux exits the stator tooth has a width of $\frac{3}{4} \left(\frac{h_S}{4} \right)$. The flux path4 is depicted in fig. 2.17 and the calculation for each segment is detailed below.

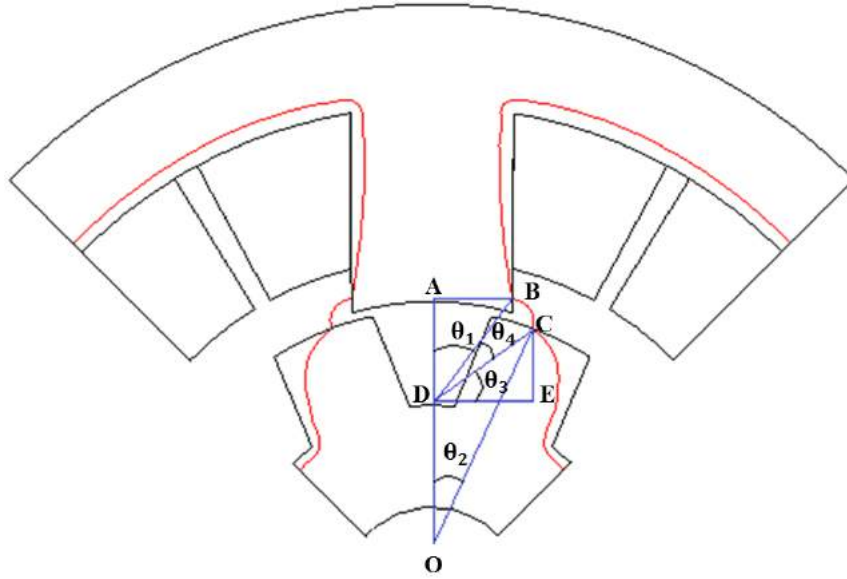


Fig.2.17 Magnetic flux path4 for unaligned rotor position

- *Air-gap path4*

$$x_1 = AB = \frac{D_s \sin t}{2} \sin\left(\frac{\beta_s}{2}\right) \quad (2.84)$$

$$y_1 = OA = \frac{D_s \sin t}{2} \cos\left(\frac{\beta_s}{2}\right) + h_s \quad (2.85)$$

The coordinates of B can be calculated as follows:

$$B = (x_1, y_1) \quad (2.86)$$

$$\theta_1 = \tan^{-1}\left(\frac{x_1}{AD}\right) = \tan^{-1}\left(\frac{x_1}{y_1 - \left(\frac{D_s \sin t}{2} - g - h_R\right)}\right) \quad (2.87)$$

$$OC = \left(\frac{D_s \sin t}{2} - g\right) \quad (2.88)$$

$$\theta_2 = \left(\frac{\theta_{rp}}{2} - \frac{5}{64}\beta_R\right) \quad (2.89)$$

Further the coordinates of C and D can be calculated with the help of eqs. 2.90 and 2.91

$$C = (x_2, y_2) = [(OC) \sin(\theta_2), (OC) \cos(\theta_2)] \quad (2.90)$$

$$D = (x_3, y_3) = \left[0, \left(\frac{D_s \sin t}{2} - g - h_R\right)\right] \quad (2.91)$$

$$DC = \sqrt{(x_3 - x_2)^2 + (y_3 - y_2)^2} \quad (2.92)$$

$$DB = \sqrt{(x_3 - x_1)^2 + (y_3 - y_1)^2} \quad (2.93)$$

$$\theta_3 = \tan^{-1} \left(\frac{CE}{DE} \right) = \tan^{-1} \left(\frac{y_2 - y_3}{x_2} \right) \quad (2.94)$$

$$\theta_4 = \frac{\pi}{2} - \theta_3 - \theta_1 \quad (2.95)$$

$$l_{g4} = \frac{1}{2} (DB + DC) \theta_4 \quad (2.96)$$

$$A_{g4} = \frac{1}{2} (A_{Sp4} + A_{Rp4}) \quad (2.97)$$

- *Stator tooth path4*

$$l_{Sp4} = h_S \quad (2.98)$$

$$A_{Sp4} = \frac{3}{4} \frac{h_S}{4} l_a \quad (2.99)$$

- *Rotor tooth path4*

$$l_{Rp4} = h_R \quad (2.100)$$

$$A_{Rp4} = \left(\frac{D_{Sint}}{2} - g \right) \frac{\beta_R}{8} l_a \quad (2.101)$$

- *Stator yoke path4*

$$l_{Sy4} \cong l_{Sy1} \quad (2.102)$$

$$A_{Sy4} \cong A_{Sy1} \quad (2.103)$$

- *Rotor yoke path4*

$$l_{Ry4} \cong l_{Ry1} \quad (2.104)$$

$$A_{Ry4} \cong A_{Ry1} \quad (2.105)$$

$$\Psi_{u4} = \frac{N_{sp} \cdot i_{ph}}{2(R_{Sp4} + R_{g4} + R_{Rp4}) + R_{Sy4} + R_{Ry4}} \quad (2.106)$$

$$L_{u4} = 2 \frac{N_{sp} \Psi_{u4}}{i_{ph}} \quad (2.107)$$

The flux path5 is the one represented in fig. 2.18 the center being situated in point A and the radius of the flux path is $\left(\frac{h_S}{4}\right)$ with an angle of $\left(\frac{\pi}{2}\right)$. The flux path is found in the stator pole and yoke and in the air-gap. Fig. 2.18 right represents the magnetic equivalent circuit of the flux path5.

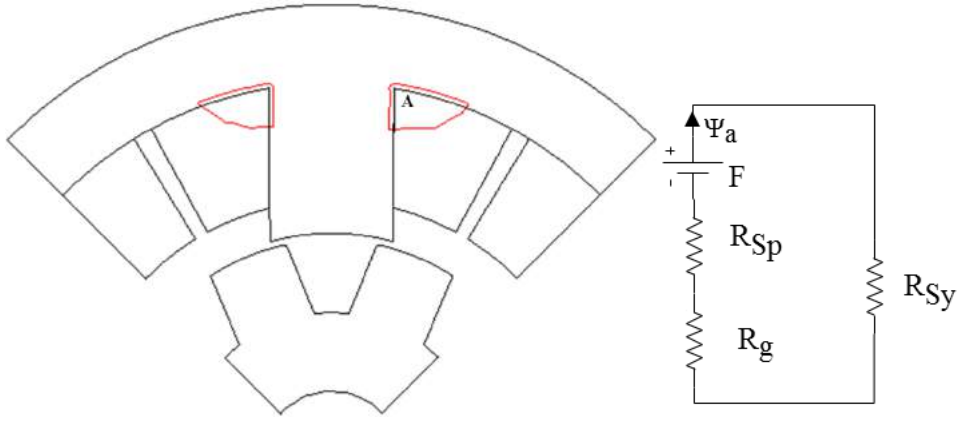


Fig.2.18 Magnetic flux path5 and magnetic equivalent circuit for unaligned position

- *Air-gap path5*

$$l_{g5} = \frac{h_S \pi}{4 \cdot 2} \quad (2.108)$$

$$A_{g5} = A_{Sp5} \quad (2.109)$$

- *Stator tooth path5*

$$l_{Sp5} = \frac{h_S}{4} \quad (2.110)$$

$$A_{Sp5} = \frac{h_S}{2} l_a \quad (2.111)$$

- *Stator yoke path5*

$$l_{Sy5} \cong \frac{h_S}{4} + \frac{w_{Sy}}{4} \quad (2.112)$$

$$A_{Sy5} = A_{Sy1} \quad (2.113)$$

$$\Psi_{u5} = \frac{N_{Sp} \cdot i_{ph}}{2R_{Sp5} + R_{g5} + R_{Sy5}} \quad (2.114)$$

$$L_{u5} = 2 \frac{N_{Sp} \Psi_{u5}}{i_{ph}} \quad (2.115)$$

The unaligned inductance known as the minimum inductance represents the sum of all inductances calculated for each flux path

$$L_m = \sum_{j=1}^5 L_{uj} \quad (2.116)$$

The entire calculation of the maximum and minimum inductance applied for the nominal current of the SR machine prototype (4A) can be found in *Appendix 2.B*. Yet, a

comparison in terms of results obtained analytically and FE computation of the aligned and unaligned inductance can be found in the next paragraphs.

2.4. Validation of the analytical model by finite-element magnetic field analysis

Validation by finite element (FE) field analysis is useful in order to predict the accuracy of the analytical model. The current in phase when applying a constant DC voltage, the electromagnetic torque when supplying one phase and rotate the machine at a constant speed as well as the phase inductances for aligned and unaligned rotor positions are validated by means of FE software.

2.4.1. Finite element software used for validation

The finite element software used for validation is JMAG Designer, this is a FE software at the core of JMAG that is used to develop and design electrical components. The first appearance of JMAG was in 1983, built to support the design of the devices such as motors, actuators and circuits. Many versions appeared over the time, the last one is JMAG Designer 15.1 released in 2016 [14]. Many features were improved over the years such as: parallel solver performance, some practical functions were added, etc.

2.4.2. Comparative FE-computed and analytical results

By using the JMAG-Designer software, several magnetic field FE analyses in the cross-section of the three-phase 6/8 SR machine (fig. 2.19) have been carried out in order to plot the stator phase-winding self-inductance variation and electromagnetic torque in respect of rotor angular position for different phase current strengths. When implementing the geometry in FE software the parameters used were those from table 2.1 and copper was set as material for the coils whilst for the stator and rotor the material curve is the one presented in [9].

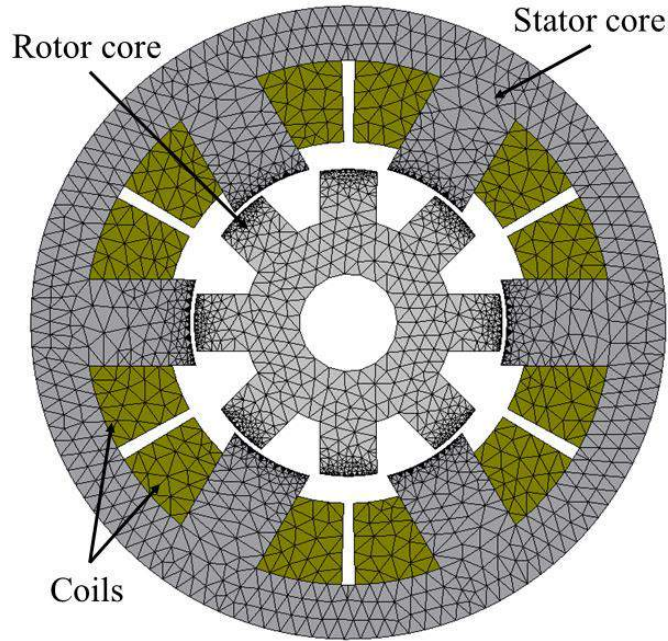


Fig.2.19 FE-discretized cross-section geometry of the three-phase 6/8 SR machine under study

A cartography map of the inductance evolution with the rotor position for different values of phase current strength is presented in fig. 2.20. These waveforms were realized in FE software by supplying one phase with constant current for different values and engaging the rotor in motion at constant speed for one mechanical period ($2\pi/N_R$).

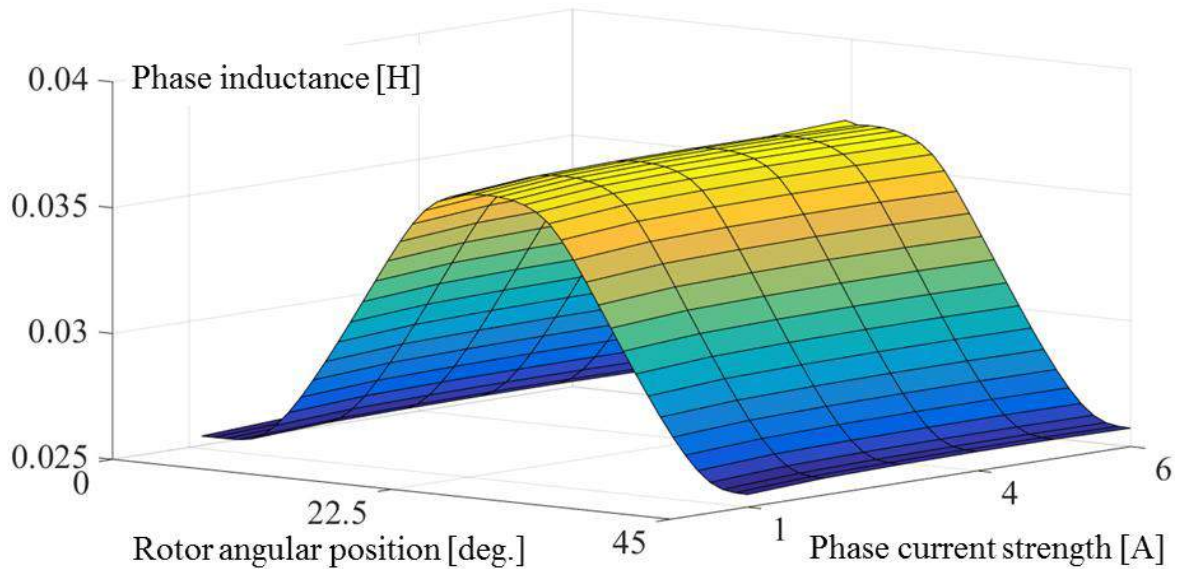


Fig.2.20 Stator-phase self-inductance of the three-phase 6/8 SR machine as a function of stator-phase current strength and rotor angular position.

2.4.2.1. Validation of the voltage equations

By solving the SRM/G phase-voltage eq. 2.4, one obtains the time-variation of the phase current strength. When calculating eq. 2.4 the evolution of the phase inductance with the rotor position and current was taken the one from fig. 2.20. Fig. 2.21 displays comparative FE-

computed and analytically-calculated results for the time-variation of the stator-phase current strength in the steady-state of the three-phase 6/8 SR machine under study, at constant rotor speed and for two values of the energizing DC-link voltage, i.e. 8V and 15V, respectively. As assessed outcome of this comparison, the average value of the phase current strength obtained from FE-computed results is with 1.1% lower than that determined analytically, for the case of 8V and 15V energizing DC-link voltage.

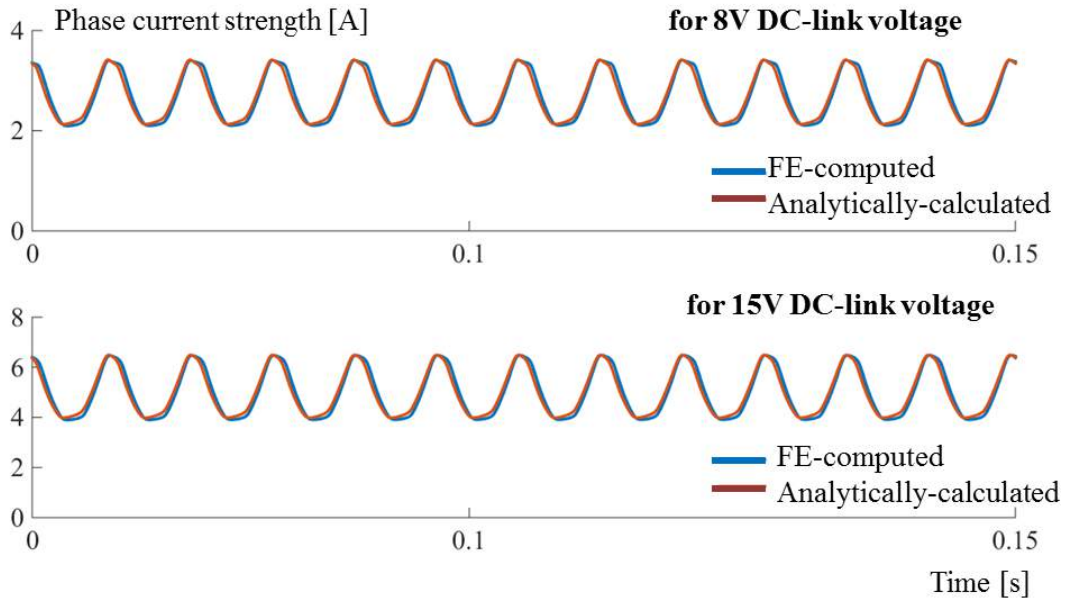


Fig.2.21 Comparative FE-computed and analytically-calculated results for the time-variation of the stator-phase current strength in the steady-state of the three-phase 6/8 SR machine, for constant rotor speed and two values of DC-link voltage

When obtaining the waveforms of fig. 2.21, one phase was energized with constant DC voltage and the rotor was engaged in motion at constant speed. The increase and decrease of the current in the phase is given by the evolution of the inductance as a function of the rotor position, i.e. in the positive slope of the inductance the phase current decreases and in the negative slope of the inductance the phase current increases.

2.4.2.2. Validation of electromagnetic torque equations

By solving eq. 2.9, time variation of the electromagnetic torque in both motor and generator operation mode is displayed. Fig. 2.22 highlights comparative evolution of the electromagnetic torque analytically calculated and FE computed.

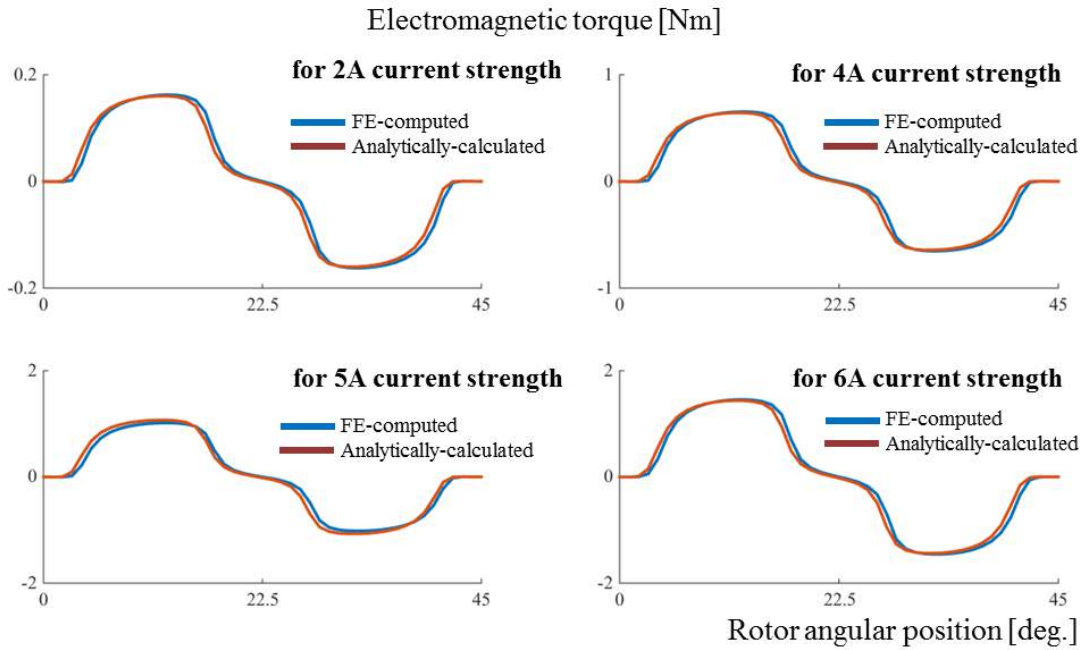


Fig.2.22 Comparative FE-computed and analytically-calculated results for time variation of electromagnetic torque in steady-state, for constant rotor speed and different values of phase current

The comparison was realized by imposing a constant rotor speed and one phase was energized over one mechanical period. The both alternation of electromagnetic torque indicates that the machine, depending on the rotor position, is able to operate in both motor and generator mode. Therefore when the rotor is starting to come into aligned position with the stator energized one, the electromagnetic torque produced by the machine is positive, i.e. SR machine functions in motor operation mode and when the aligned position is overcome and the stator phase is still energized the electromagnetic torque produced by the machine is negative, i.e. SR machine functions in generator mode.

2.4.2.3. Phase inductance validation

The phase inductance of the studied SR machine changes, its variation depending on the rotor position, but the value of the inductance depends on the geometry of the machine and phase current. For this thesis, the modality of aligned and unaligned inductance calculation detailed in [13], was adapted here for an increased number of rotor teeth. Therefore eqs. 2.12 - 2.116 present in a detailed fashion, the aligned and unaligned inductance determination from the magnetic flux lines paths for a configuration with an increased number of rotor teeth.

Starting from a known geometry, finite elements validation was realized to determine the accuracy of the analytical model. Fig. 2.23 and table 2.2 presents the comparison between FE-computation and analytically-calculated inductances for the aligned and unaligned rotor positions, when changing the current in phase.

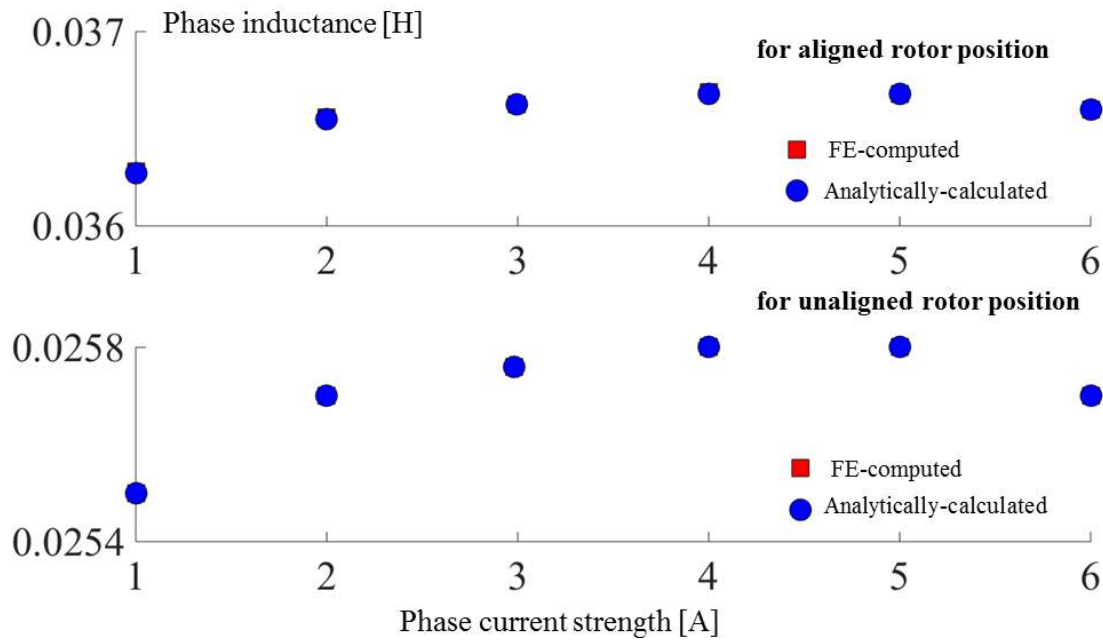


Fig.2.23 Comparative FE-computed and analytically-calculated maximum and minimum values of the stator-phase self-inductance of the three-phase 6/8 SR machine

Table 2.2 Comparative FE-computed and analytically-calculated maximum and minimum values of the stator-phase self-inductance for multiple phase current strength

Phase current strength [A]	Rotor position	Analytically calculated inductance [H]	FE computed inductance [H]
1	Aligned	0.03627	0.03628
	Unaligned	0.0255	0.0255
2	Aligned	0.03655	0.03656
	Unaligned	0.0257	0.0257
3	Aligned	0.03666	0.03666
	Unaligned	0.02574	0.02574
4	Aligned	0.03668	0.03669
	Unaligned	0.0258	0.0258
5	Aligned	0.03668	0.03668
	Unaligned	0.0258	0.0258
6	Aligned	0.03666	0.03666
	Unaligned	0.0257	0.0257

For both of the rotor positions (aligned and unaligned) the inductance was computed by FE software and analytically for different values of phase current strength. If we take in consideration the values of inductance computed for a phase current strength of 4A, the difference between the values computed by FE analyze and analytically calculated is less than 1%. Given the fact that in computation time the analytical calculation is faster, this approach will be used further in the optimization process. The proximity between the values of the inductances computed by means of FE-computation and analytically calculated is due to the fact that the values of the magnetic field (H) and flux density (B) were chosen from the material magnetization curve and used for the analytical calculation in order to ensure a minimum discrepancy between both computations.

2.5. Simulations of the SR machine model

In this subchapter the analytical model presented above is implemented in MATLAB/Simulink, where simulations will be launched for the three-phase six stator and eight rotor teeth SR machine. The operation mode as motor as well as generator will be covered in this subchapter.

2.5.1. MATLAB/Simulink model

The SR motor and generator simulation model has been developed and implemented in MATLAB/Simulink environment with the block diagram shown in fig. 2.24. It should be pointed that in motor operation mode a speed control was realized and in generator operation mode a torque control provides the reference current for a given speed.

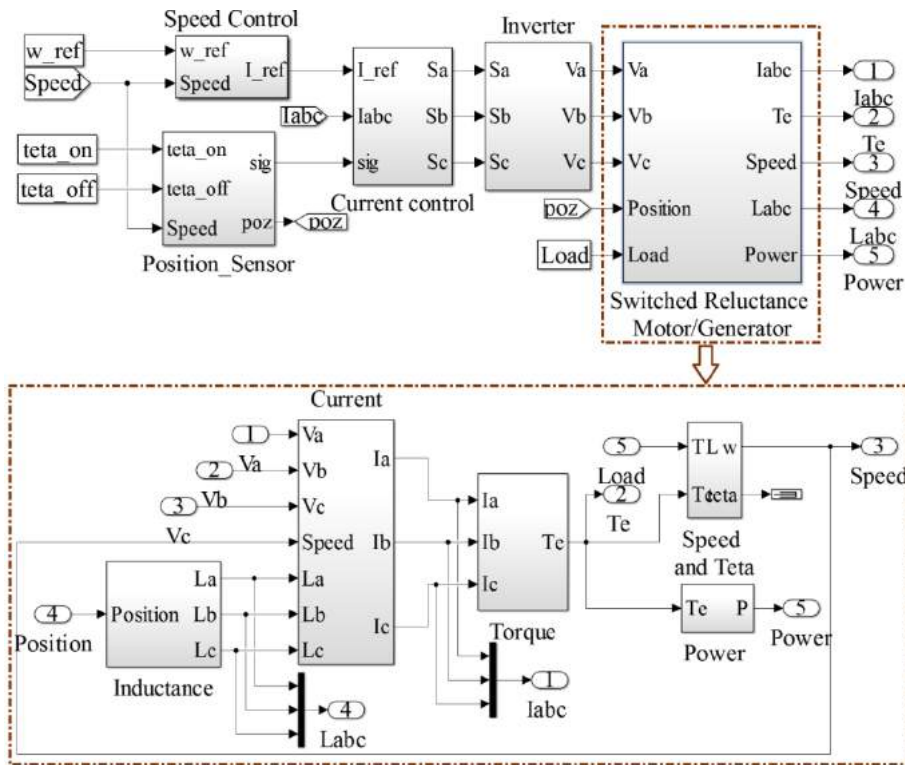


Fig.2.24 MATLAB/Simulink model of the three-phase 6/8 SR machine for motor and generator operation modes

The simulation modules are the three-phase 6/8 SR machine model, the current control block which realizes a stator current control by hysteresis, considering the reference current provided by the speed control block, inside of which a PI rotor-speed regulation is done. The position sensor block provides the rotor position information for electronic commutation of stator phase currents; this is used for determining the ON and OFF signals to be applied to each specific bridge of the three-phase half-bridge asymmetrical power converter.

A more detailed view of the switched reluctance motor/generator block is pointed in the below part of the figure. The first part presented above incorporates the control of the SR machine and the SRM/G block contains the electrical, electromagnetic and mechanical equations. The data used to realize fig. 2.20 is implemented in a Lookup table and depending on the rotor position and current it provides the real shape of the inductance. Eqs. 2.4 and 2.9 are implemented in the current block respectively torque block. The outputs of the SR machine simulation block are the stator phase currents, the developed electromagnetic torque, the rotor speed and the generated power.

Further application of dynamic simulations using MATLAB/Simulink model together with FE magnetic field analyses enables the control/design of the three-phase 6/8 SR machine to be optimized for motoring and generating operation.

2.5.2. Influence of commutation angles

Studies show that the commutation angles have a great impact in SR machine's efficiency and the adjustment of the commutation angles can lead to an increased efficiency for this type of machine. A part of the studies in this thesis is dedicated to the effect of the commutation angles on the torque ripple and on the value of mean electromagnetic torque $\langle T_e \rangle$.

2.5.2.1. Simulations with theoretical angle

For the first set of simulations in motor operation mode, if we consider fig. 2.8 when rotor teeth are aligned with phase1 and we keep the rotation direction, phase3 should be supplied in order for the machine to produce positive torque. For this particular case we can consider $\theta_{on} = 0^\circ$ and θ_{off} can be calculated with eq. 2.117.

$$\theta_{off} = \frac{2\pi}{N_R \cdot q} \quad (2.117)$$

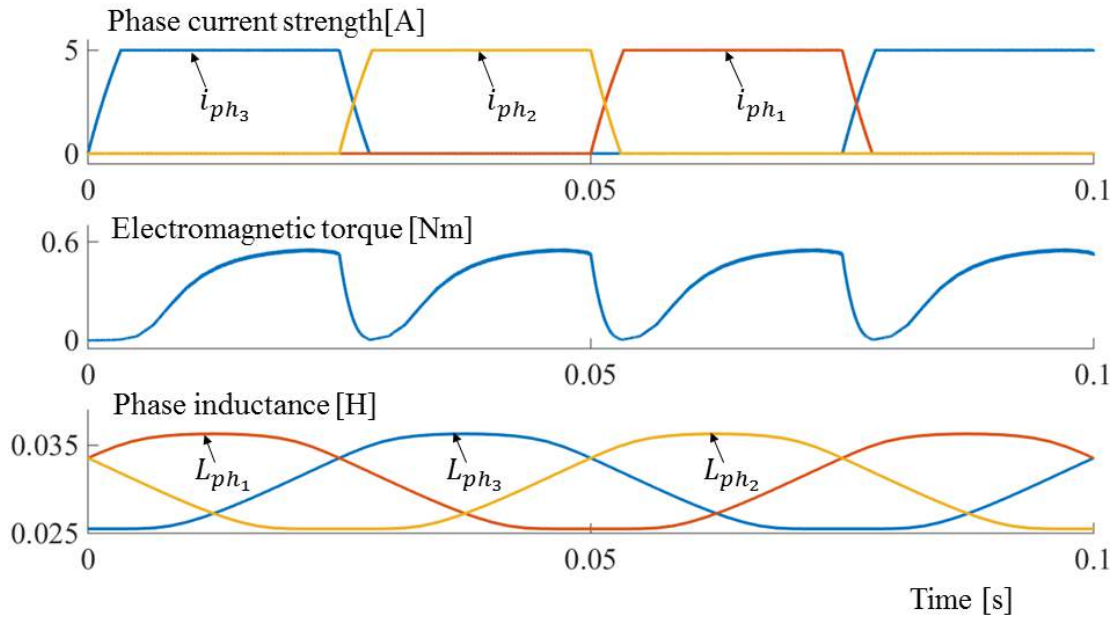


Fig.2.25 Simulated steady-state responses in current, electromagnetic torque and inductance of the three-phase 6/8 SR machine, for motor operation mode

Fig. 2.25 represents the waveforms of the current, electromagnetic torque and inductance of the three-phase 6 stator and 8 rotor teeth switched reluctance machine working in motor operation mode with $\theta_{on} = 0^\circ$ and $\theta_{off} = 15^\circ$. As it can be remarked the machine phases are independent to one another and are in conduction during the positive slope of the inductance, i.e. the moment in which the rotor starts to come into aligned position with the stator excited phase.

By shifting the excitation in the negative slope of the inductance, i.e. rotor teeth are starting to come out from aligned position with the stator excited phase, SR machine will produce negative torque. For the next set of simulations we want to define the angles θ_{on} and θ_{off} so that the excitation of the phase to be found in the negative slope of inductance. Therefore in the calculation of the theoretical angles for the generator operation mode eqs. 2.118 and 2.119 are used.

$$\theta_{on} = \frac{2\pi}{N_R} \left(1 - \frac{1}{q}\right) \quad (2.118)$$

$$\theta_{off} = \frac{2\pi}{N_R} \quad (2.119)$$

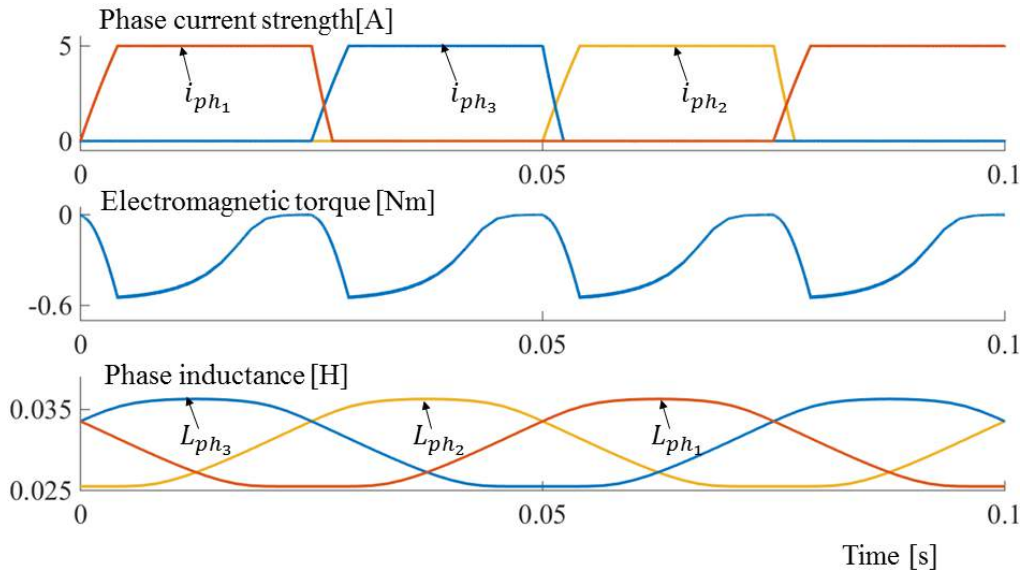


Fig.2.26 Simulated steady-state responses in current, electromagnetic torque and inductance of the three-phase 6/8 SR machine, for generator operation mode

Fig. 2.26 displays the evolution of current, electromagnetic torque and inductance for the three-phase 6/8 SR machine under study in generator operation mode with $\theta_{on} = 30^\circ$ and $\theta_{off} = 45^\circ$.

To be noted that in the realization of the above figures, the current control by hysteresis was done with a hysteresis band of 0.05A, for a reference current of 5A and the rotor was engaged in motion at constant speed of 100 rpm. The MATLAB/Simulink model used for the above simulations is the one presented in fig. 2.24, but without the speed control block, the reference current being given as a constant value.

2.5.2.2. Simulations when commutation angles change

Having an analytical model of the three-phase 6/8 SR machine implemented in MATLAB/Simulink that is able to be simulated in motor and generator operation mode by changing the commutation angles, next we can try to minimize the torque oscillation and in the same time to increase the mean electromagnetic torque by adjusting the commutation angles for both operation modes (motor and generator).

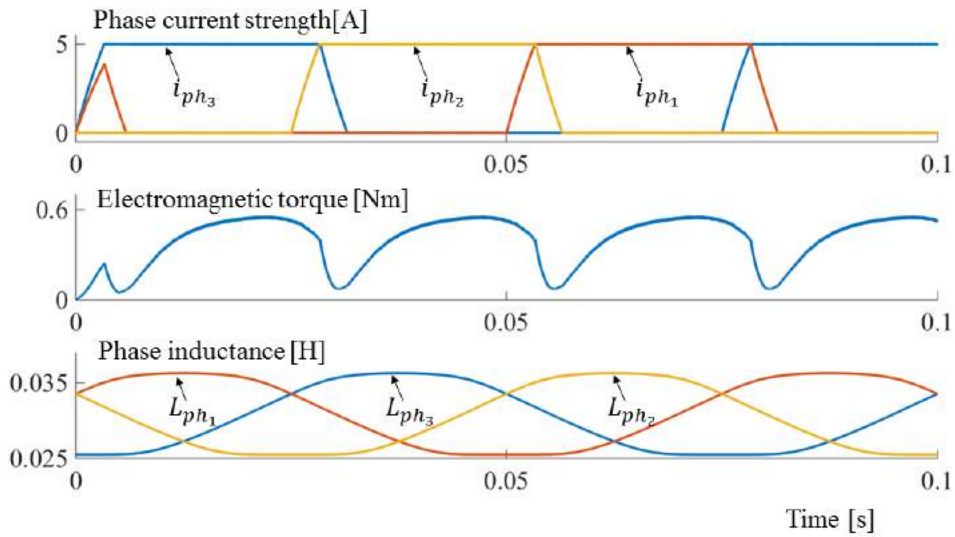


Fig.2.27 Simulated steady-state responses in current, electromagnetic torque and inductance of the three-phase 6/8 SR machine, for motor operation mode and shifted angle θ_{off}

Further simulations are based on changing θ_{off} angle by increasing the excitation period of the phase. If the motor operation mode is considered for the 6/8 SR machine, with the rotor position and direction of rotation as presented in fig. 2.8 (aligned), after phase3 finishes its conduction period at $\theta_{off} = 15^\circ$ (fig. 2.25), the current in this phase decreases whilst phase2 becomes energized. However, a certain rising time is required by the phase2 current to reach its maximum value, which leads to oscillations in the electromagnetic torque waveform. To overcome this, it has been observed that with an overlap of the phase currents the variations in the torque's shape are greatly diminished by simply shifting the θ_{on} and θ_{off} angles, as noticeable in fig. 2.27. In order to see the impact of this shift, table 2.3 comprises the average values of the electromagnetic torque and ripple torque when one angle is shifted. Eq. 2.120 is used to calculate the ripple torque.

$$T_{rip} = T_{max} - T_{min} \quad (2.120)$$

Table 2.3 Comparative results for different commutation angles of the studied SR machine, in motor operation mode

Commutation angle [deg.]	Ripple torque [Nm]	Mean electromagnetic torque [Nm]
$\theta_{on} = 0^\circ$ $\theta_{off} = 15^\circ$	0.56	0.35
$\theta_{on} = 0^\circ$ $\theta_{off} = 17^\circ$	0.51	0.4
$\theta_{on} = 0^\circ$ $\theta_{off} = 19^\circ$	0.5	0.43

As for the motor operation mode, in the generator mode the same idea of angle shifting is kept. Fig. 2.28 points the evolution of current, electromagnetic torque and inductance of SR machine under study with $\theta_{on} = 27^\circ$ and $\theta_{off} = 45^\circ$.

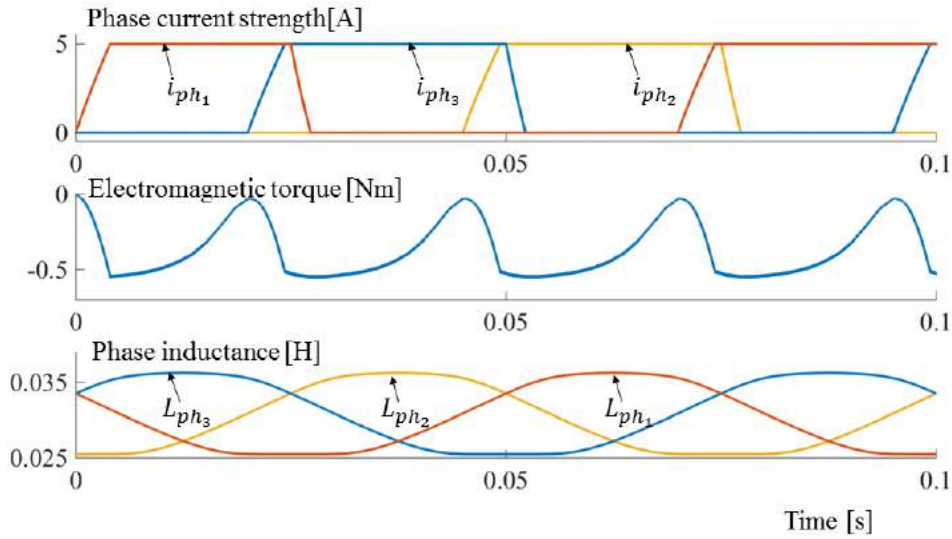


Fig.2.28 Simulated steady-state responses in current, electromagnetic torque and inductance of the three-phase 6/8 SR machine, for generator operation mode and shifted angle θ_{on}

As can be seen from table 2.4 when shifting at least one of the commutation angles the torque oscillations decrease and the value of mean electromagnetic torque increases.

Table 2.4 Comparative results for different commutation angles of the studied SR machine in generator operation mode

Commutation angle [deg.]	Ripple torque [Nm]	Mean electromagnetic torque [Nm]
$\theta_{on} = 30^\circ$ $\theta_{off} = 45^\circ$	0.56	-0.28
$\theta_{on} = 27^\circ$ $\theta_{off} = 45^\circ$	0.53	-0.37
$\theta_{on} = 25^\circ$ $\theta_{off} = 45^\circ$	0.5	-0.41

From table 2.3 and 2.4 it can be pointed out that when increasing the period of current in phase the values of average electromagnetic torque increase and a minimization of the torque pulsations can be noticed. Given the fact that the values of commutation angles chosen for the simulations are random and improvement is still noticeable, if an optimization were to be applied on the commutation angles a greater improvement should be observed.

2.6. Conclusions

The second chapter is dedicated to the analytical approach of the three-phase six stator and eight rotor teeth switched reluctance machine. The electric and electromagnetic points of view for this machine are studied in this chapter. This analytical modeling will be further used

in an optimization process to obtain the best commutation angles and reference current of the existing prototype. Furthermore the complexity of the optimization problem will be increased by adding the machine design along with the control, to obtain the best size and control of the SR machine to be used in ISA applications.

As the main issue of this machine is the torque ripple, many studies in literature have tried to reduce this problem by various methods. One method applied in this thesis as well is increasing the rotor teeth in order for the machine to produce continuous rotation without any dead zones, in this way a minimization in ripple torque is noticeable.

A big influence in SRM has the inverter used to supply the machine; this chapter presents three types of inverters that can be used for phase supplying. Furthermore in this chapter one can find SR machine voltage equations and electromagnetic torque written for the case when the magnetic material saturation is considered and in the case in which it is not considered.

One of the challenges when studying this machine is the inductance evolution. In this chapter an ideal evolution of inductance and the calculation at each step of the corresponding angle for an increased number of rotor teeth is also provided. When optimizing the size of machine is useful, for time consuming reasons, to have an analytical calculation of the maximum and minimum inductance. This chapter starting from a calculation of the aligned and unaligned inductance applied for an 8 stator and 6 rotor teeth machine, details a new approach of inductance calculation applied for a three-phase 6 stator and 8 rotor teeth SR machine. The difficulty of this approach resides in unaligned position where an overlap between stator and rotor teeth exists. As known, the flux lines have the tendency of crossing the stator teeth towards rotor in the area where the distance between them is smaller.

Validation by finite element method is realized in this chapter for the voltage and electromagnetic torque, as well as validation of the maximum and minimum inductance calculated with the presented approach.

One step was achieved in the reduction of torque oscillations when a configuration with an increased number of rotor teeth was chosen. Not necessary a reduction of ripple torque but rather an increase in the mean electromagnetic torque is possible by adjusting the commutation angles. The last part of this chapter presents the influence of θ_{on} and θ_{off} on the mean electromagnetic torque and on torque oscillations.

Selected references

- [1] Lee B. S. Bae H. K. Vijayraghavan P. Krish, "Design of a linear switched reluctance machine," *IEEE Transactions on Industry Applications*, vol. 4, pp. 2267-2274, November/December 2000.
- [2] M. T. DiRenzo, "Switched reluctance motor control—basic operation and example using the tms320f240," in *Texas Instruments, Digital Signal Processing Solutions*, 2000.
- [3] Desai P. C. Krishnamurthy M. Schofield N., "Novel switched reluctance machine configuration with higher number of rotor poles than stator poles: concept to implementation," *IEEE Transactions on Industrial Electronics*, vol. 57(2), pp. 649-659, 2010.
- [4] Emadi A. Krishnamurthy M. Bilgin B., "Design considerations for switched reluctance machines with a higher number of rotor poles," *IEEE transactions on Industrial Electronics*, vol. 59(10), pp. 3745-3756, 2012.
- [5] Bilgin B. Emadi A. Krishnamurthy M., "Comprehensive evaluation of the dynamic performance of a 6/10 SRM for traction application in PHEVs," *IEEE Transactions on Industrial Electronics*, vol. 60(7), pp. 2564-2575, 2013.
- [6] Ilea D. Radulescu M. M., Gillon F. Brochet P., "Dynamic model of a three-phase full-bridge inverter-fed Switched Reluctance Motor for optimization purposes," *International Aegean Conference on Electrical Machines and Power Electronics and Electromotion*, pp. 260-265, 2011.
- [7] **M. V. Zaharia** M.M. Radulescu F. Gillon, "Design optimization of a switched reluctance machine-based integrated starter/alternator for automotive applications," *International Conference on Electrical Machines (ICEM), 2016, IEEE*.
- [8] Chancharoensook P. Rahman M. F., "Control of a four-phase switched reluctance generator: experimental investigations," in *Electric Machines and Drives IEMDC'03*, 2003, pp. 842-848.
- [9] Dan Ilea, *Conception optimale des moteurs à réluctance variable à commutation électronique pour la traction des véhicules électriques légers.*: École centrale de Lille, France and Technical university of Cluj-Napoca, Roumanie, 2011.
- [10] Somsiri P. Tungpimonrut K. Aree P., "Three-phase full-bridge converters applied to switched reluctance motor drives with a modified switching strategy," in *Electrical Machines and Systems ICEMS*, Seoul, Korea, 2007, pp. 1563-1568.

- [11] Rafajdus P. Zrak I. Hrabovcová V., "Analysis of the switched reluctance motor (SRM) parameters," *JOURNAL OF ELECTRICAL ENGINEERING-BRATISLAVA*, vol. 55(7/8), pp. 195-200, 2004.
- [12] T. J. E. (Ed.) Miller, *Electronic control of switched reluctance machines*. Newnes. Oxford, UK, 2001.
- [13] R. Krishnan, *SWITCHED RELUCTANCE MOTOR DRIVES Modeling, Simulation, Analysis, Design, and Applications*. United States of America: CRC Press LLC, 2001.
- [14] JMAG. [Online]. <https://www.jmag-international.com>

Chapter 3

Optimization of switched reluctance machine using space mapping technique

3.1. Introduction

In the previous chapter the analytical model of the SR machine was detailed. The objective of this chapter is there forth to use that analytical model in an optimization process. The difficulty of this chapter is the exploitation of this model in an optimization process, this is due to the increased number of evaluations required by the optimization method.

The analytical model is quite fast, but due to the simulation step combined with the differential equations used for current computation and the controls used in simulation, the speed of this model decreases. Therefore, this chapter stands to present time reducing methods that can be used in an optimization process in order to obtain optimal results in the shortest time possible.

In the first part of this chapter a comparison between local minimum and global minimum is realized. Afterwards, time reducing techniques are presented and validated with the help of a mathematical model in the following section. Having the optimization algorithm (SQP - sequential quadratic programing), the method (Multistart fmincon) and the strategy of optimization (output space mapping), it is now possible to pass to the optimization of the SR machine. But in order to ensure that this approach works properly for this machine, simulation and experimental validations (chapter 4) are realized, based on the inputs and outputs obtained after the optimization; following that this approach to be used in a much complex problem, namely, finding the best size and control of a three-phase 6/8 SR machine for automotive ISA applications.

3.2. General aspects of optimization

In most elemental terms, optimization is a mathematical discipline that focuses on finding an extreme (minimum or maximum) of a function. Optimization finds simultaneously, the best output and input from a predefined band [1].

Usually, optimization stands in terms of minimization, although it is possible for the objective function to have multiple local minima. It is viable to say that a local minimum is the region around which all of the function values are greater than or equal to the function value. In many circumstances the local minima is not necessary the global minima. Therefore, it is possible to affirm that a local minimum is as good as any nearby points, but a global minimum is as good as every feasible point [2].

$$f: x \in [-2,2] \rightarrow y_f \in \mathbb{R}^2$$

$$y_f = \left(\sin(x) - \frac{\sin(5x)}{5} + \frac{\sin(3x)}{3} + \frac{\cos(4x)}{4} + \frac{\cos(7x)}{7} + 7 \right) \frac{x^2}{x+1} \quad (3.1)$$

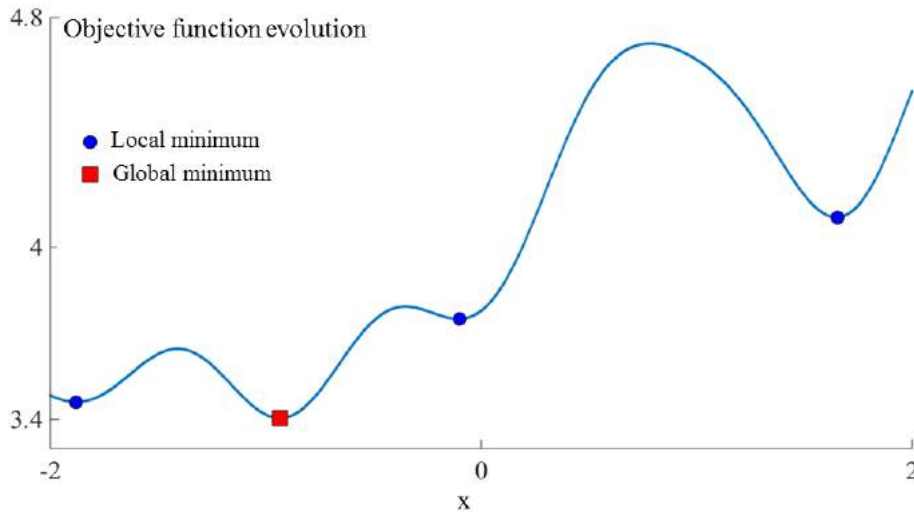


Fig.3.1 Objective function for both local and global minimum

Let's consider a simple objective function with multiple local minimum and one global minimum (eq. 3.1), fig. 3.1 reproduces the function evolution for the x band as pointed in eq. 3.1. The mathematical optimization process needs to determine the minimum point that is good for every feasible point.

$$\hat{x} = \arg_{x \in \mathbb{R}} \min f_{obj} \quad (3.2)$$

Eq. 3.2 represents the objective function applied to an optimization process that is to find the best \hat{x} that gives the minimum value of y_f .

3.2.1. Optimization

Investigating from the perspective of objective numbers, optimization can be categorized as: mono-objective and multi-objective optimization. The output of the mono-objective optimization is a scalar with a single vector for the input. Instead the multi-objective optimization is a population of non-dominant solutions, which belongs to a Pareto front. The output of this multi-objective optimization is a set of scalar and a set of inputs vector.

Over the years many intelligent optimization algorithms were developed such as: genetic algorithm (GA) [3], particle swarm optimization (PSO) [4], branch and bound (BB), etc. The optimization problem can be solved by means of finite element method combined with one optimization algorithm. The accuracy and complexity of the geometrical structure along with the applicability to nonlinear problems, makes FE-computation a feasible solution when designing an electrical machine. Despite all these advantages is hard to use FEM in an optimization process because of the increased computation time. Therefore, in an optimization process a much faster model (coarse model) can be used instead of FEM. Usually one can use as coarse model an analytical or a reluctance network model. However, this model is fast but

not so accurate in results, hence more authors tried to reduce this main drawback by refining it through a correction calculated based on the accurate model.

3.2.2. Design provided by optimization

Despite of the optimization methods developed over the years, the concept of design by optimization of electrical machines and systems has always been a focus in engineering field. When applied to electrical machines design, optimization problem is more likely to be a multi-objective due to the many objectives that can be defined depending on the application. For example, the electrical motors used for washing machines and refrigerators, the most important features are the price and output power, while for traction motors the features that must be considered when designing are the volume, power density and torque ripple [5].

The design by optimization in electrical machines consists of two main parts: the first part is represented by the electric machine's design and the second one by the optimization. The procedure when using design optimization of an electrical machine is described below:

- First of all, a design analysis needs to be realized, by including the application domain, followed by the type and configuration of the electrical machine as well as the types of materials going to be used.
- The design analysis is followed by the optimization model, where one must define the quantity/quantities to be optimized, the constraints that need to be respected during the optimization and the design parameters for which the optimization is effected
- The third step corresponds to establishing the optimization strategy. Many strategies exist in literature, though many studies are focused on optimizing directly the accurate model. However this thesis is not based on this approach because one of the focuses is to also reduce the optimization computing time.
- Finally, having the optimized machine model, validations in terms of experimental results compared with simulations are necessary.

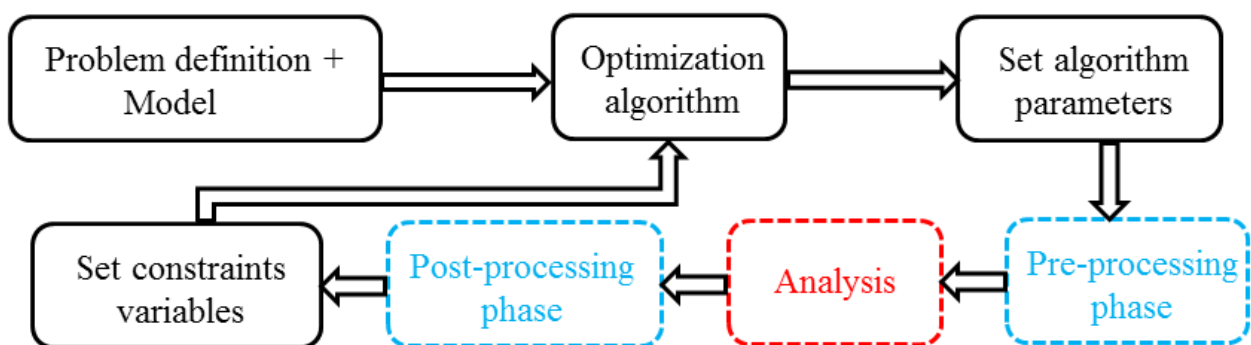


Fig.3.2 Workflow for optimization based on FE-computation [6]

If considered a FE model analysis, fig. 3.2 emphasizes the workflow of the optimization process. The above diagram can be described in the following steps: first the optimization is generating the design parameters from the imposed bands, upon which the machine model is drawn, next the FE model extracts the performance quantities after evaluating the model and the loop is closed with the constraints calculation and passing them to the optimization algorithm.

The main drawback of this workflow is the modality of machine performance analysis, because when using FE computation, in order to have accurate results, time consuming simulations are required and to obtain feasible design solutions a rather large number of evaluations is required, therefore a much faster model should be employed. Although, a faster model depreciates the accuracy of results, hence this thesis proposes to combine the accuracy of the FE-modeling with the velocity of the analytical model, to obtain the best parameters and control of a switched reluctance machine to be used in an integrated starter alternator system. The method used in literature and in this thesis for this type of approach is called space mapping (SM).

3.2.3. Space mapping method

The original space mapping technique was introduced by Bandler in 1995 [7]. This technique is an optimization method that provides a solution to reduce the optimization time. It requires two models: one fast in computation time (coarse model) on which optimization is launched and one accurate (fine model) by means of which the coarse model is refined. According to [8] space mapping based optimization technique contains four steps:

- Step 1. Simulation check on the fine model
- Step 2. Parameter extraction for the coarse model
- Step 3. Update of the coarse model
- Step 4. Re-optimization of the coarse model

In order to accomplish this optimization technique is necessary to have four elements:

- A *coarse model* whose best feature should be high velocity in computation time, because the entire machine optimization is based on it, while its accuracy is not an important aspect.
- The *fine model* is used as a reference to refine the coarse model, whose main aspect is the precision of its results. Usually, for this type a FE model is used.
- The *mapping function* is a mathematical transformation used for coarse model refining, having as benchmark the fine model.

- Finally, the *optimization algorithm* is the technic used to define the best configuration using the coarse model and the SM function.

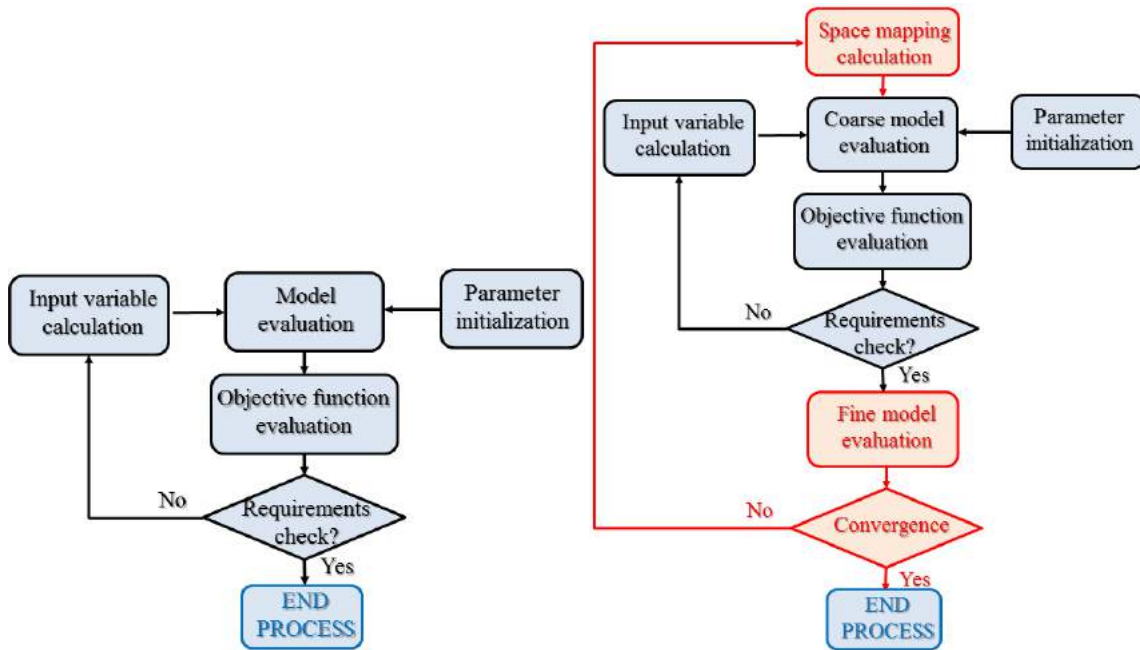


Fig.3.3 Space mapping optimization workflow [9]

Fig. 3.3 left emphasizes a classical optimization chart, while the right part of the figure highlights the optimization process with space mapping technique. As it can be remarked, the classical optimization process is kept and only an addition loop is added to correct the fast model in respect to the accurate one. The coarse model may result from the degradation of the fine model. The condition that must be respected by the coarse model is that it should be fast in computation time.

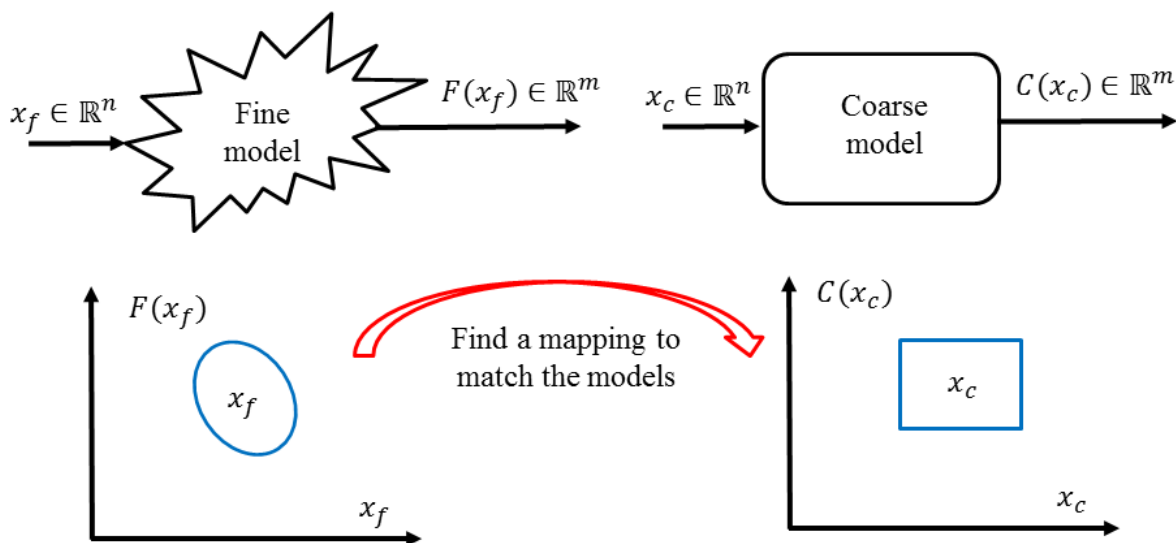


Fig.3.4 Definition of the fine and coarse model

The fine and coarse models can be written as: $F: x_f \in \mathbb{R}^n \rightarrow y_f \in \mathbb{R}^m$ respectively $C: x_c \in \mathbb{R}^n \rightarrow y_c \in \mathbb{R}^m$ where n is the number of design variables and m is the number of objective functions.

$$x_c = \begin{pmatrix} x_{c_1} \\ x_{c_2} \\ \dots \\ x_{c_n} \end{pmatrix}; x_f = \begin{pmatrix} x_{f_1} \\ x_{f_2} \\ \dots \\ x_{f_n} \end{pmatrix}; y_c = C(x_c) = \begin{pmatrix} C_1 \\ C_2 \\ \dots \\ C_m \end{pmatrix} \text{ and } y_f = F(x_f) = \begin{pmatrix} F_1 \\ F_2 \\ \dots \\ F_m \end{pmatrix} \quad (3.3)$$

The general optimization problem written from the perspective of space mapping can be expressed as follows:

$$\hat{x} = \arg_{x \in \mathbb{R}^n} \min \|k(F(x_f), C(x_c), x_f, x_c) - \bar{y}\| \quad (3.4)$$

where $k: \mathbb{R}^m \rightarrow \mathbb{R}^m$ is the mapping function related to the fine and coarse models (fig. 3.4). It must be specified that eq. 3.4 is used only for the case in which a distance is minimized.

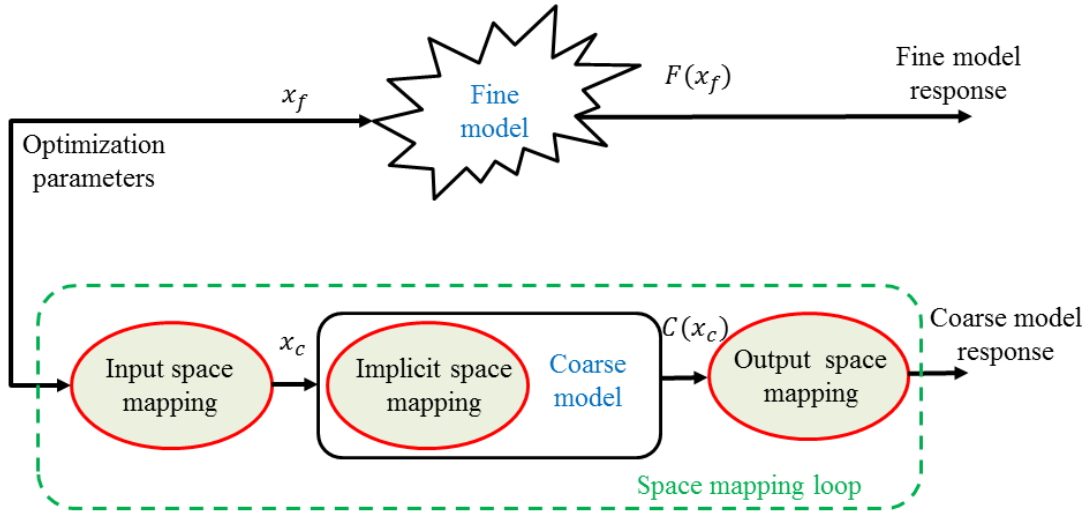


Fig.3.5 Different approaches of space mapping

When refining the coarse model in respect to the fine one is possible to have three main approaches, different from one another. The first one is input space mapping. This technique realizes the correction of the coarse model at the input level [10]. The implicit space mapping is the second one. In this approach, the design parameters are mapped linear through the mapping parameters. Here the parameter extraction is optimized to match the coarse model to a given fine model data [11]. The third possibility is output space mapping. For this one the output parameters of the coarse model are corrected iteratively to match the parameters of the fine model [12]. A workflow of all these approaches is represented in fig. 3.5.

3.3. Space mapping at the output level

The output space mapping strategy (OSM) is used to obtain a precise result in a fast manner with a minimum of fine model evaluations. This technique is based on using the coarse model in an optimization loop, while the fine one is used to gradually verify the correctness of the results. By reason of the difference between both models, towards minimization of the discrepancy between them, a correction is calculated iteratively based on the results obtained with a coarse corrected and the fine model. Thereafter, this corrected model is able to search for the optimal solution \hat{x} .

3.3.1. Space mapping function

In this thesis, space mapping at the output level is studied based on the correction of the both models at the output level. Here we make the assumption that, the number of inputs is identical for each model and the parameters of the inputs are the same $x_f \equiv x_c$.

$$k\text{CoC}(x) = F(x) \quad (3.5)$$

In eq. 3.5 k depends on the outputs of the both fine and coarse models.

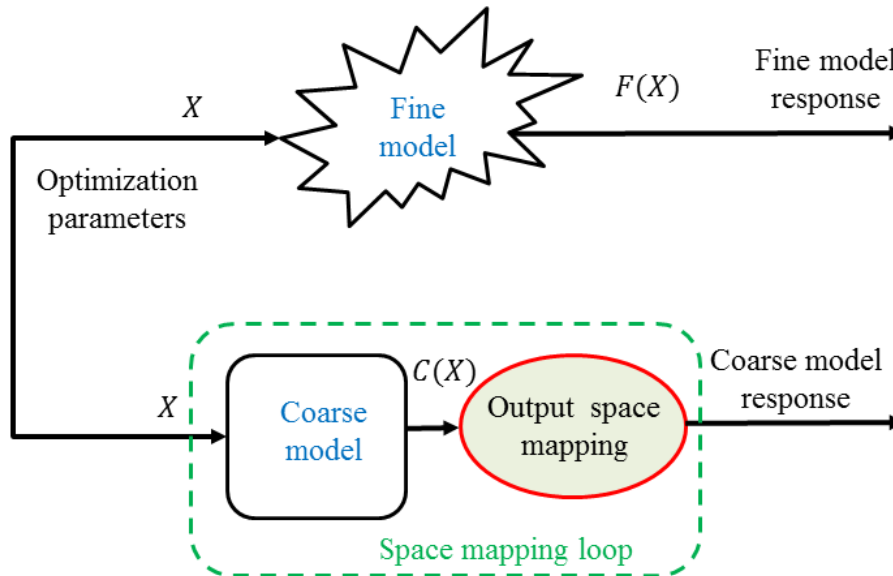


Fig.3.6 Space mapping applied at the output level

Fig. 3.6 represents the workflow of the output space mapping. When realizing the refining at the output level, correction k is calculated independently and iteratively for each output. According to the requirements of the optimized device the target is known, therefore is possible to consider for all of the device specifications a vector \bar{y} that contains the target for each required parameter. Thereupon the optimization problem for the OSM can be written as shown in eq. 3.6.

$$\hat{x} = \arg_{x \in \mathbb{R}^n} \min \|k_o C(x) - \bar{y}\| \quad (3.6)$$

Output space mapping can be divided into output space mapping proportional (OSMP), aggressive output space mapping (AOSM) and manifold mapping (MM). For the OSMP when calculating the correction coefficient a simple equation is used based on the ratio between the outputs of the fine model respect to the coarse ones. Instead, when using AOSM and MM to refine the coarse model one should appeal to the Jacobian matrix [13].

3.3.2. Optimization using a mathematical model

In this thesis OSMP and MM are studied. Before using these techniques in switched reluctance machine optimization, a verification of these techniques is realized by means of a mathematical model. Eqs. 3.7 and 3.8 emphasize the mathematical model for the fine respectively coarse models.

$$f: x \in [-2,2] \rightarrow y_f \in \mathbb{R}^2: \begin{cases} y_{f_1} = x^4 - x^3 - x^2 - x + 3 \\ y_{f_2} = -\frac{1}{2}x^3 \end{cases} \quad (3.7)$$

$$c: x \in [-2,2] \rightarrow y_c \in \mathbb{R}^2: \begin{cases} y_{c_1} = \frac{x^4}{2} + \frac{1}{2} \\ y_{c_2} = \frac{4}{5}x + 2 \end{cases} \quad (3.8)$$

The mathematical functions were chosen so as to be a difference between the fine and the coarse models. Because both of them are mathematical functions the computation time is the same in this case.

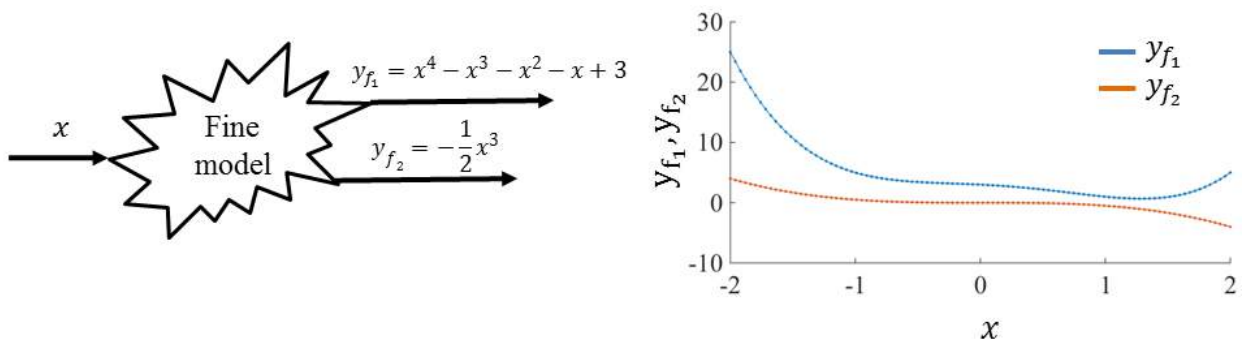


Fig.3.7 Variation of the fine model as a function of inputs

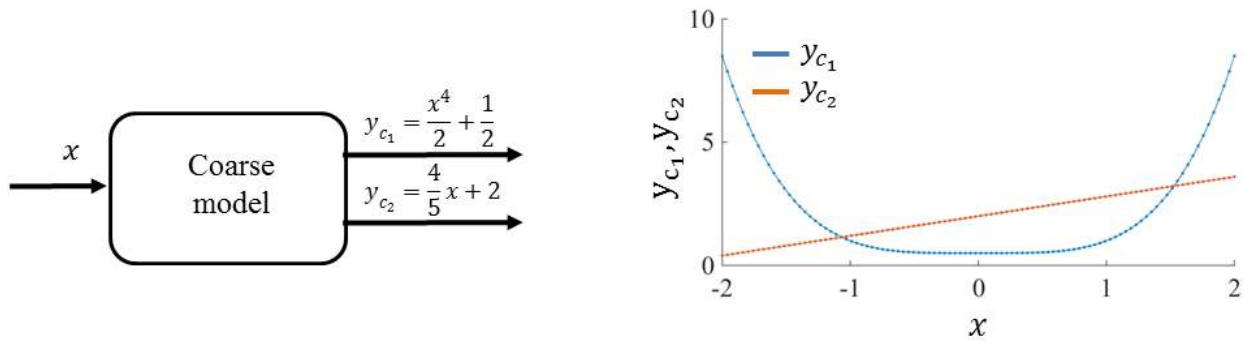


Fig.3.8 Variation of the coarse model as a function of inputs

When calculating the both fine and coarse models for 100 values of x in the band $[-2, 2]$, one can obtain the variation of the both models as illustrated in figs. 3.7 and 3.8. We consider that the fine model emphasizes a phenomenon in a much accurate manner. From fig. 3.9 we can observe that the fine model y_{f1} and the coarse model y_{c1} have the same tendency for $x < -0.5$.

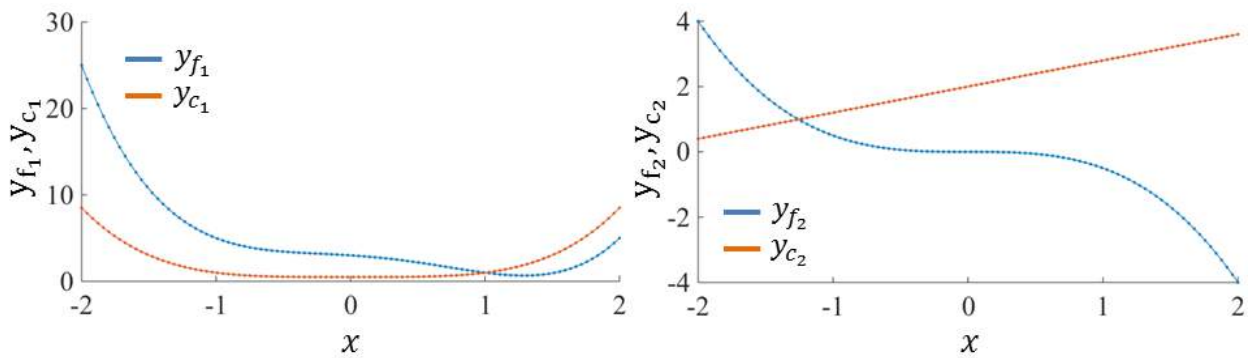


Fig.3.9 Comparison between fine and coarse mathematical function outputs

3.3.2.1. Optimization on the fine model

Starting from the above presented model, first is realized an optimization strictly on the fine model. The mathematical formulation of the objective function can be written as follows:

$$\hat{x} = \arg_{x \in \mathbb{R}} \min f_{obj} \quad (3.9)$$

with

$$f_{obj} = \|f(x) - \bar{y}\| \quad (3.10)$$

Optimization performed on the fine model minimizes the distance between the output function and a reference point (\bar{y}). In the first case a feasible solution is imposed and for the second optimization a non-feasible solution is chosen.

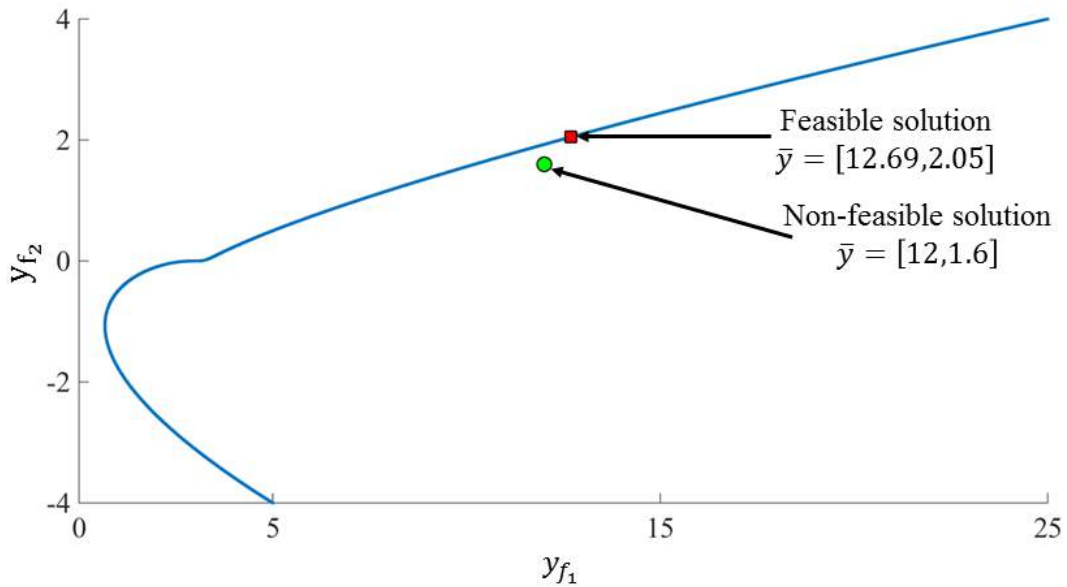


Fig.3.10 Fine model output variation

Fig. 3.10 highlights the fine model output variation, this figure also presenting both of the targeted solutions. The first solution that we are interested to obtain is $\hat{x} = -1.6$.

When calculating the objective function presented in eq. 3.10 for the feasible solution ($\bar{y} = [12.69, 2.05]$) one can obtain the variation of the fine model in function of the input x . Fig. 3.11 represents the best solution obtained with fine model for a feasible point and the variation of the objective function respect to the input x .

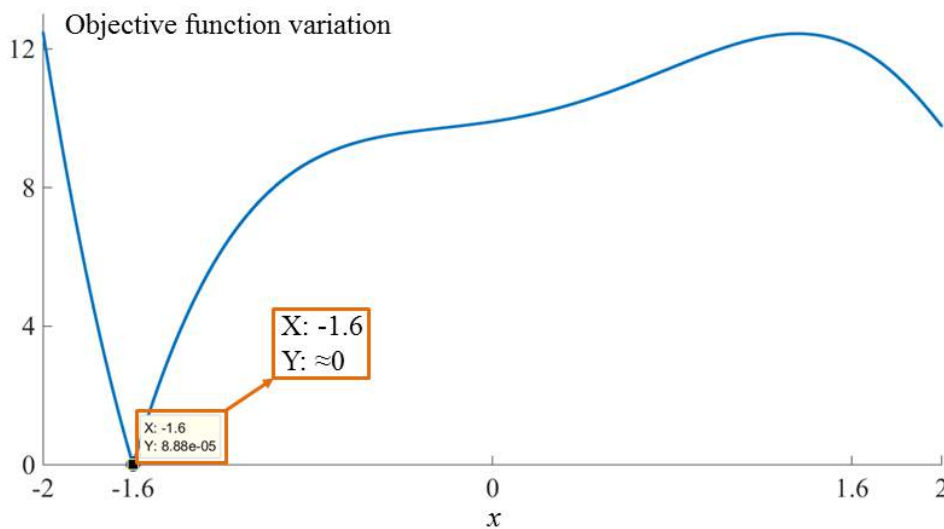


Fig.3.11 Objective function variation as a function of x

When considering a non-feasible solution ($\bar{y} = [12, 1.6]$), the best point found by the optimization is $\hat{x} = -1.565$ and $f_{obj}(\hat{x}) = 0.3208$. Fig. 3.12 represents the evolution of the objective function when considering a non-feasible solution and the answer obtained with the fine model.

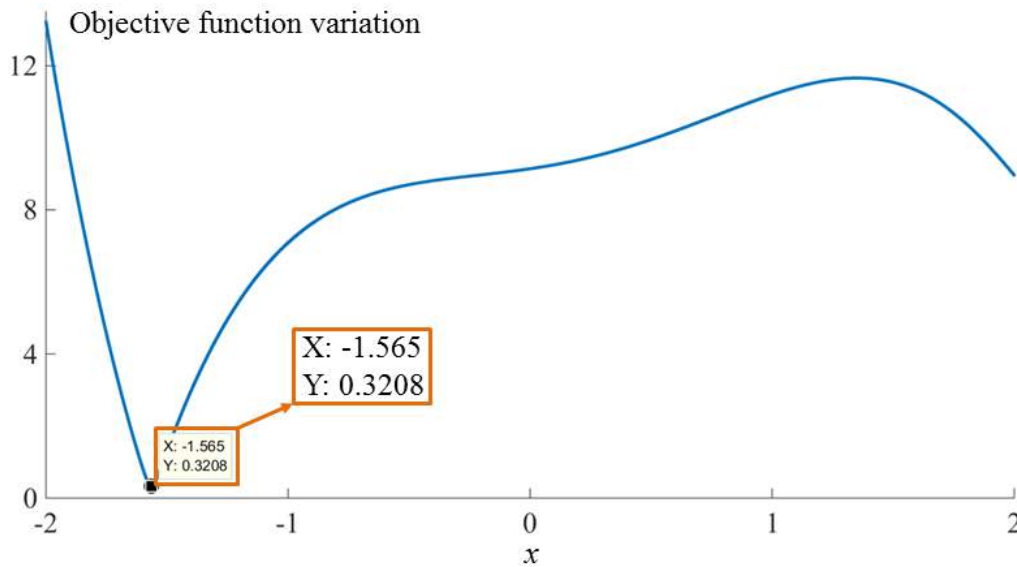


Fig.3.12 Objective function variation for a non-feasible solution as a function of input x

From the obtained solution it is clear that the distance between function and the reference point is not zero. This is normal due to the fact that for the model is impossible to take values 12 and 1.6 in the same time. Instead when the solution was feasible the point that the model could take was -1.6 and the distance in this case is null.

Having as a benchmark the results obtained with the fine model for the two references, next we can implement the output space mapping proportional and manifold mapping on the coarse model and iteratively correct this model to obtain the results achieved strictly with the fine model.

3.3.3. Output space mapping proportional

The OSMP is simply to implement, the main principle of this technique is to correct locally the fast model taking as benchmark the fine model [14]. The correction is calculated based on the output of the coarse model compared with the outputs of the fine model at the previous iteration.

3.3.3.1. General function calculation

The OSMP evolution can be synthesized as shown in fig. 3.13, a description of the working principle can be expressed as follows: first the optimization is launched on the coarse model, when the optimization loop finishes the inputs vector (\hat{X}_i) at iteration i is implemented to the fine model and the outputs of the both models ($F(\hat{X}_i)$ respectively $C(\hat{X}_i)$) are compared. If the difference between them is bigger than an imposed tolerance (ϵ), a correction k is calculated based on the results obtained with both fine and coarse models. Further this correction is applied to the coarse model at iteration $i+1$ and the process repeats itself.

Iteratively, the difference between the models decreases and when the tolerance is respected the optimization stops.

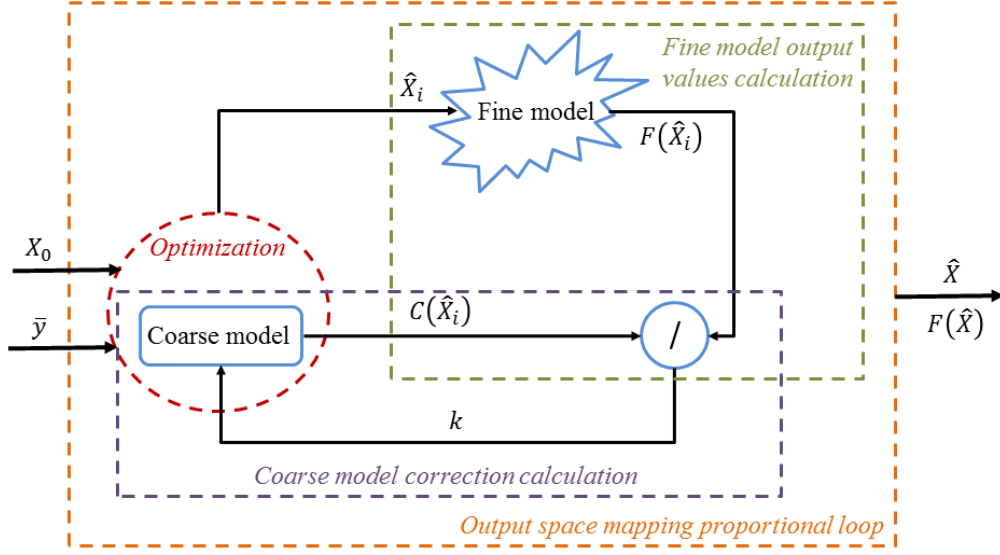


Fig.3.13 Interaction between the two models when using output space mapping proportional loop

All the above explaining can be synthetized in six steps:

Step 1: Definition of the optimization problem:

$$\hat{x}_i = \arg_{X \in \mathbb{R}} \min \|k_{i-1} \circ C(x) - \bar{y}\| \quad (3.11)$$

Step 2: Optimization of the coarse model to reach the optimal \hat{X}_i and evaluation of the coarse model $C(\hat{X}_i)$ with the optimal found \hat{X}_i

Step 3: Evaluation of the fine model $F(\hat{X}_i)$ with the optimal found \hat{X}_i

Step 4: Update of the mapping function as follows:

$$k_i = \frac{F(\hat{X}_i)}{C(\hat{X}_i)} = \left(\frac{F_1(\hat{X}_i)}{C_1(\hat{X}_i)}, \frac{F_2(\hat{X}_i)}{C_2(\hat{X}_i)}, \dots, \frac{F_m(\hat{X}_i)}{C_m(\hat{X}_i)} \right) \quad (3.12)$$

with $F(\hat{X}_i)$ and $C(\hat{X}_i)$ being the outputs of the fine respectively coarse models at the point \hat{X}_i .

Step 5: Stop if:

$$i > N_{\text{itermax}}$$

or

$$\frac{\|\hat{X}_i - \hat{X}_{i-1}\|}{\|\hat{X}_{i-1}\|} < \varepsilon_1 \quad (3.13)$$

$$\frac{\|F(\hat{X}_i) - F(\hat{X}_{i-1})\|}{\|F(\hat{X}_{i-1})\|} < \varepsilon_2 \quad (3.14)$$

Step 6: If stopping criteria is not satisfied go to step 2.

3.3.3.2. Mathematical based problem

- Search for a feasible solution: $\bar{y} = [12.69, 2.05]$ i.e. $\hat{x} = -1.6$

The objective function is written in terms of distance minimization (eq. 3.15). The OSMP technique is applied to the coarse model in order to obtain as much as possible the results presented in subchapter 3.2.2 when optimization was launched on the fine model.

$$\hat{x}_i = \arg_{x \in \mathbb{R}} \min \left\| koC(x) - \begin{bmatrix} 12.69 \\ 2.05 \end{bmatrix} \right\| \quad (3.15)$$

When computing the problem, x can take values in the band $[-2, 2]$, at the first iteration the correction coefficient is set to 1 ($k = [1, 1]$) and the stopping criteria is chosen $\varepsilon_1 = \varepsilon_2 = 10^{-4}$.

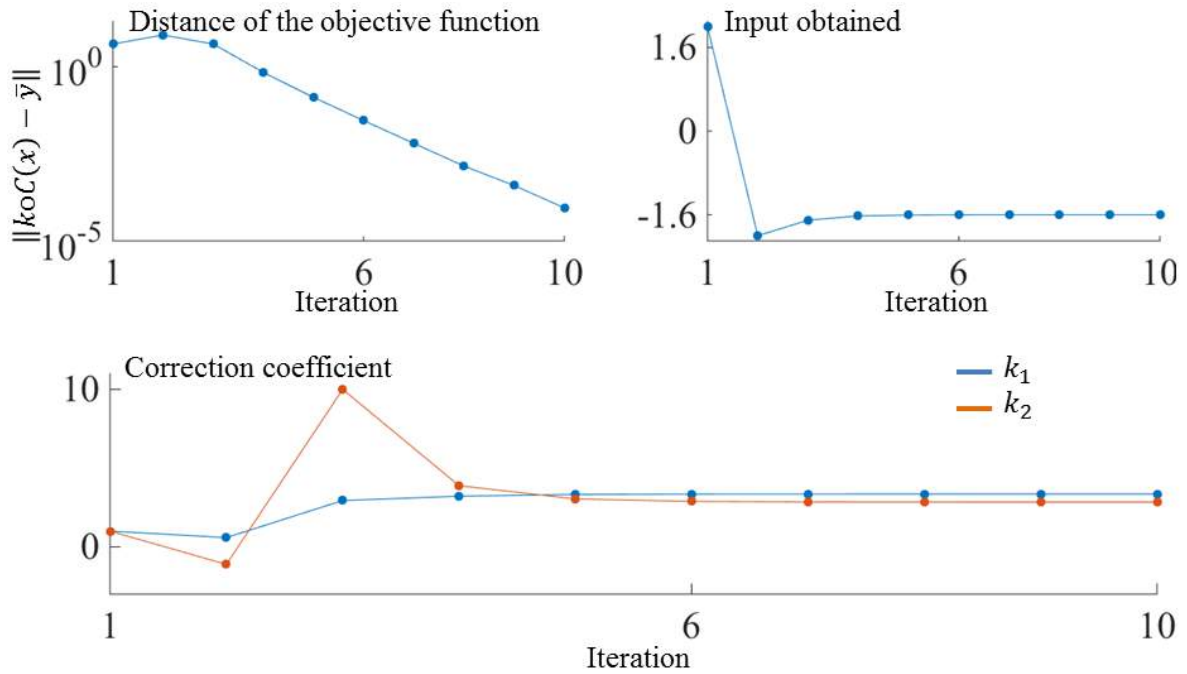


Fig.3.14 Distance of the objective function in respect to the target, best input obtained and correction coefficient

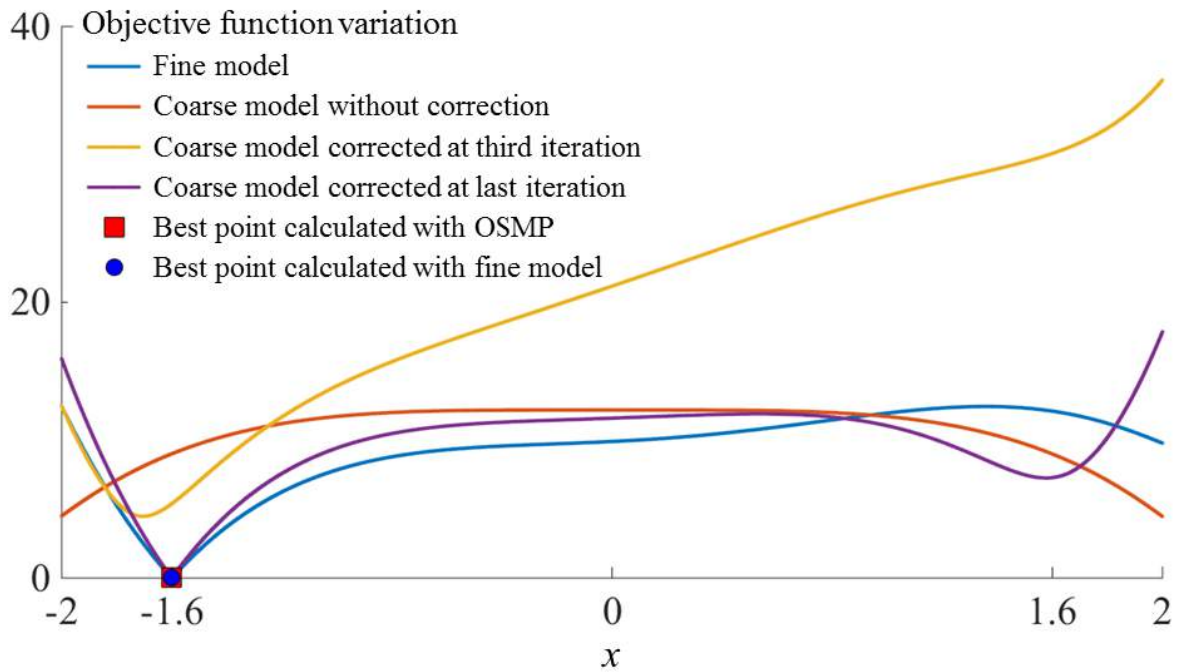


Fig.3.15 Objective function variation as a function of input x for different iterations

It is noticeable that by performing the optimization on the coarse model and iteratively correcting it with the help of the fine one, is possible to obtain the same results as if the optimization would have been done right on the fine model. When realizing the OSMP calculation, the maximum number of iterations was set to 40, however at iteration 10 the model finds the result that satisfies the constraints. In fig. 3.14 a representation of the objective function distance is given together with the best input calculated with the OSMP iteratively and the correction of the two coarse models which is updated after each iteration.

Fig. 3.15 represents the variation of the fine and coarse models according to the input x . From this figure one can observe that when the coarse model is not corrected, its minimum is quite different respect to the one of the fine model, anyhow iteratively the coarse model changes to meet the minimum of the fine model.

➤ Search for a non-feasible solution: $\bar{y} = [12, 1.6]$

For the second set of calculation the target is changed to: $\bar{y} = [12, 1.6]$, nonetheless the stopping criteria is kept at: $\varepsilon_1 = \varepsilon_2 = 10^{-4}$ and the first iteration starts with a correction equal to one. The new objective function can be written as show in eq. 3.16.

$$\hat{x}_i = \arg_{x \in \mathbb{R}} \min \left\| kOC(x) - \begin{bmatrix} 12 \\ 1.6 \end{bmatrix} \right\| \quad (3.16)$$

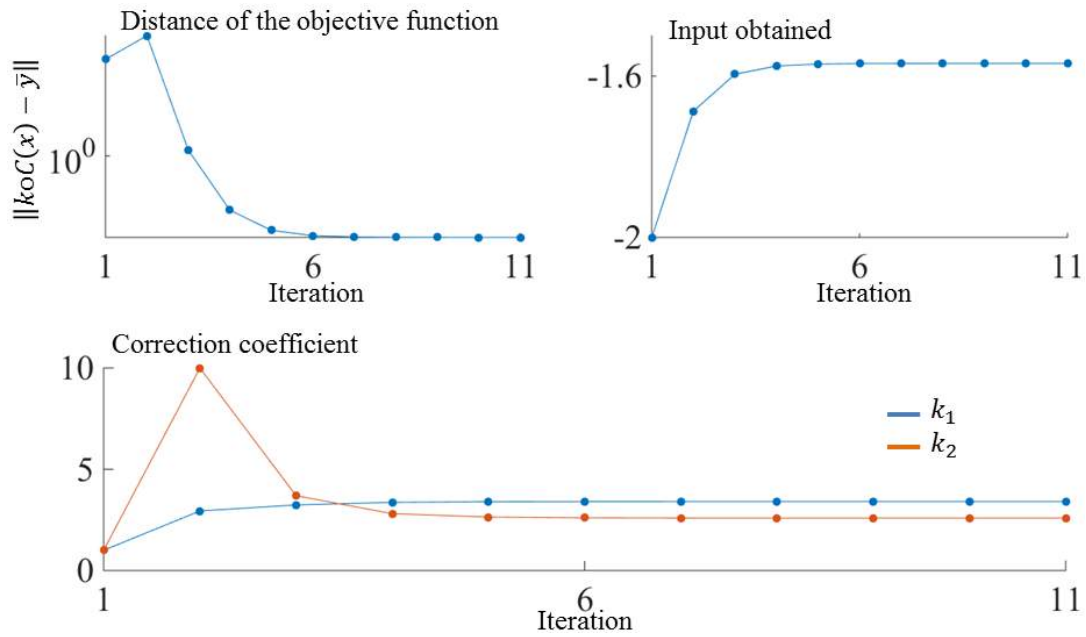


Fig.3.16 Distance of the objective function in respect to the target, best input obtained and correction coefficient

When calculating for a non-feasible point after a certain number of iterations the distance of the objective function is not decreasing any more, in this case from iteration 11. The solution obtained with the fine model is: $X = -1.565$ and $Y = 0.32$ (fig. 3.12) and the solution obtained with the coarse model using OSMP is: $X = -1.569$ and $Y = 0.33$. As it can be seen, the solution obtained with the coarse model is near the reference solution. Fig. 3.16 points iteratively the distance of the objective function, the obtained input and correction coefficient when using output SM proportional for the calculation of a non-feasible point.

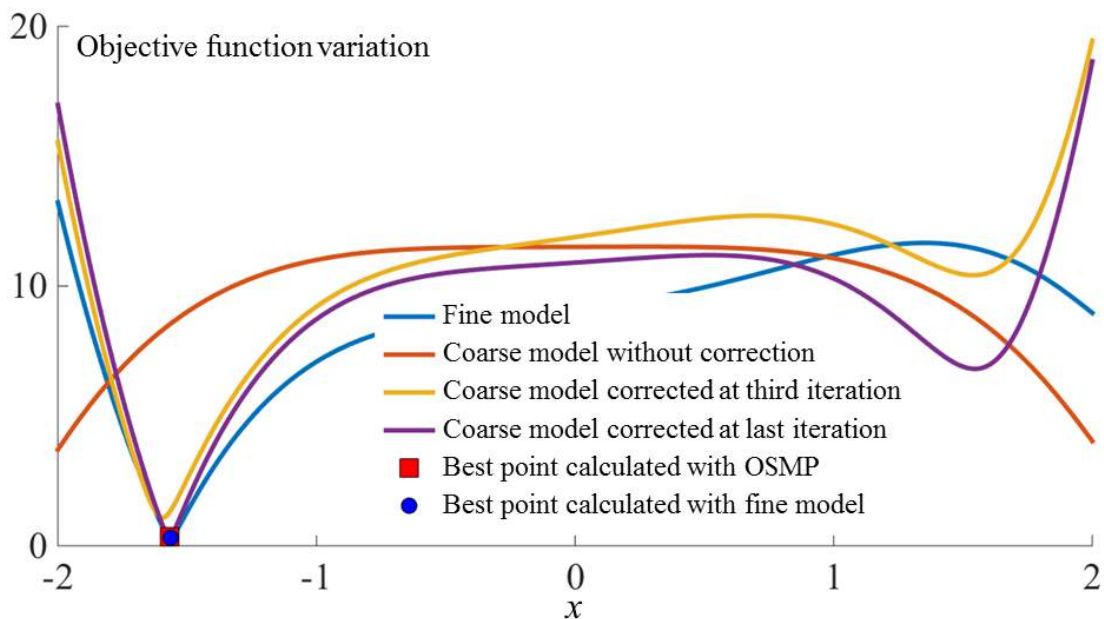


Fig.3.17 Objective function variation as a function of input x for different iterations when considering a non-feasible point

The objective function variation of the fine and coarse models for multiple values of x is represented in fig. 3.17. Here is pointed the evolution of the coarse model in function of the correction applied.

The entire Matlab script with the output space mapping proportional implementation for the specified mathematical model is given in *Appendix 3.A*.

3.3.4. Manifold mapping

Like output space mapping proportional, manifold mapping also adjusts the outputs of the coarse model to meet those of the fine one [15]. However the MM technique uses a much complicated relation to correct the coarse model. This method relies on two actions: a translation and a rotation of the fast model [16].

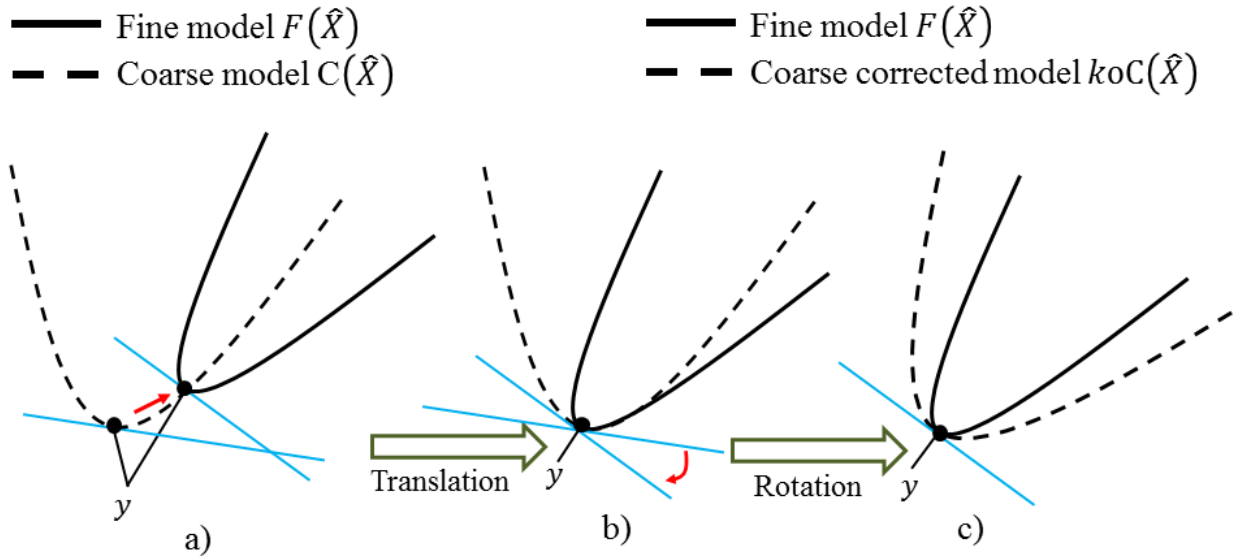


Fig.3.18 Manifold mapping model alignment steps

In fig. 3.18a the original fine and coarse models are represented, as mentioned above the technique first performs a translation of the coarse model (fig. 3.18b) and after this step is accomplished a rotation of the fast model is realized (fig. 3.18c).

The original MM problem can be written as shown in eq. 3.17.

$$K_{i-1}C(\hat{x}) = F(\hat{x}_{i-1}) + k_{i-1}(C(x) - C(\hat{x}_{i-1})) \quad (3.17)$$

where $k_{i-1} = J_f(\hat{x}_{i-1}) \cdot J_c^\dagger(\hat{x}_{i-1})$

The correction is calculated by computing the Jacobian matrix of the fine ($J_f(\hat{x}_{i-1})$) and coarse ($J_c^\dagger(\hat{x}_{i-1})$) models at the previous iteration ($i - 1$). Here with \dagger is noted the pseudo-inverse operator of the Jacobian matrix.

The calculation of the Jacobian matrix is useful as it provides information about the local variation tendency for the models outputs in function of inputs. In vector calculus,

the Jacobian matrix is the matrix of all first-order partial derivatives of a vector-valued function. When the matrix is a square matrix, both the matrix and its determinant are referred to as the Jacobian in literature [13]. The Jacobian matrix calculated for the fine and coarse model can be written as shown in eq. 3.18.

$$J_f = \begin{pmatrix} \frac{dF_1}{dx_1} & \dots & \frac{dF_1}{dx_n} \\ \vdots & \ddots & \vdots \\ \frac{dF_m}{dx_1} & \dots & \frac{dF_m}{dx_n} \end{pmatrix} \text{ and } J_c = \begin{pmatrix} \frac{dC_1}{dx_1} & \dots & \frac{dC_1}{dx_n} \\ \vdots & \ddots & \vdots \\ \frac{dC_m}{dx_1} & \dots & \frac{dC_m}{dx_n} \end{pmatrix} \quad (3.18)$$

The computation of the optimal point \hat{x}_i is realized for each iteration i . Therefore the Jacobian approaches for the both models $J_f(\hat{x}_i)$ and $J_c(\hat{x}_i)$ can be written respect to the previous iteration as follows:

$$J_f(\hat{x}_i) = \begin{pmatrix} \frac{F_1(\hat{x}_i) - F_1(\hat{x}_{i-1})}{\hat{x}_{i_1} - \hat{x}_{i-1_1}} & \dots & \frac{F_1(\hat{x}_i) - F_1(\hat{x}_{i-1})}{\hat{x}_{i_n} - \hat{x}_{i-1_n}} \\ \vdots & \ddots & \vdots \\ \frac{F_m(\hat{x}_i) - F_m(\hat{x}_{i-1})}{\hat{x}_{i_1} - \hat{x}_{i-1_1}} & \dots & \frac{F_m(\hat{x}_i) - F_m(\hat{x}_{i-1})}{\hat{x}_{i_n} - \hat{x}_{i-1_n}} \end{pmatrix} \quad (3.19)$$

$$J_c(\hat{x}_i) = \begin{pmatrix} \frac{C_1(\hat{x}_i) - C_1(\hat{x}_{i-1})}{\hat{x}_{i_1} - \hat{x}_{i-1_1}} & \dots & \frac{C_1(\hat{x}_i) - C_1(\hat{x}_{i-1})}{\hat{x}_{i_n} - \hat{x}_{i-1_n}} \\ \vdots & \ddots & \vdots \\ \frac{C_m(\hat{x}_i) - C_m(\hat{x}_{i-1})}{\hat{x}_{i_1} - \hat{x}_{i-1_1}} & \dots & \frac{C_m(\hat{x}_i) - C_m(\hat{x}_{i-1})}{\hat{x}_{i_n} - \hat{x}_{i-1_n}} \end{pmatrix} \quad (3.20)$$

But the Jacobian matrix can be simplified as follows:

$$\Delta F_i = [F(\hat{x}_i) - F(\hat{x}_{i-1}) \dots F(\hat{x}_i) - F(\hat{x}_{\min(i-1,n)})] \quad (3.21)$$

$$\Delta C_i = [C(\hat{x}_i) - C(\hat{x}_{i-1}) \dots C(\hat{x}_i) - C(\hat{x}_{\min(i-1,n)})] \quad (3.22)$$

The correction k_i can be written as:

$$k_i = \Delta F_i \cdot \Delta C_i^\dagger \quad (3.23)$$

If the calculation of k_{i-1} is not realized then the mapping function can be written as shown in eq. 3.24.

$$K_{i-1}(C(x)) = C(x) + (F(\hat{x}_{i-1}) - C(\hat{x}_{i-1})) \quad (3.24)$$

A much simple way of implementing the MM algorithm is expressed by eq. 3.25.

$$\hat{x}_i = \arg_{x \in \mathbb{R}} \min \|C(x) - \bar{y}_i\| \quad (3.25)$$

where

$$\bar{y}_i = C(\hat{x}_{i-1}) - k_{i-1}^{-1}(F(\hat{x}_{i-1}) - \bar{y}) \quad (3.26)$$

and

$$k_{i-1}^{-1} = J_c(\hat{x}_{i-1}) \cdot J_f^\dagger(\hat{x}_{i-1}) \quad (3.27)$$

The manifold mapping algorithm can be synthesized in six steps:

Step 1: Parameter initialization. Here the stopping criteria is set, together with all the initial values

Step 2: Calculation of the optimized problem (eq. 3.25)

Step 3: If tolerance is satisfied model stops, if not go to step 4

Step 4: Calculation of the Jacobian matrix of the fine and coarse models

Step 5: Update k_i and set iteration equal to 2

Step 6: Go to step 2

3.3.4.1. Mathematical problem

For validation of this technique as realized for the OSMP the same mathematical problem is used, the one presented in subchapter 3.2.2. The same feasible solution presented in fig. 3.10 is chosen when applying the manifold mapping.

- Search for a feasible solution: $\bar{y} = [12.69, 2.05]$ i.e. $\hat{x} = -1.6$

The problem to be solved with MM is the one from eq. 3.28 and is the same problem used with OSMP.

$$\hat{x}_i = \arg_{x \in \mathbb{R}} \min \left\| KoC(x) - \begin{bmatrix} 12.69 \\ 2.05 \end{bmatrix} \right\| \quad (3.28)$$

When calculating with MM the same stopping criteria is set $\varepsilon_1 = \varepsilon_2 = 10^{-4}$ and the band of x is $[-2, 2]$. The main interest when using this technique is to obtain with the coarse model, of course correcting it iteratively, the same results calculated with the fine one.

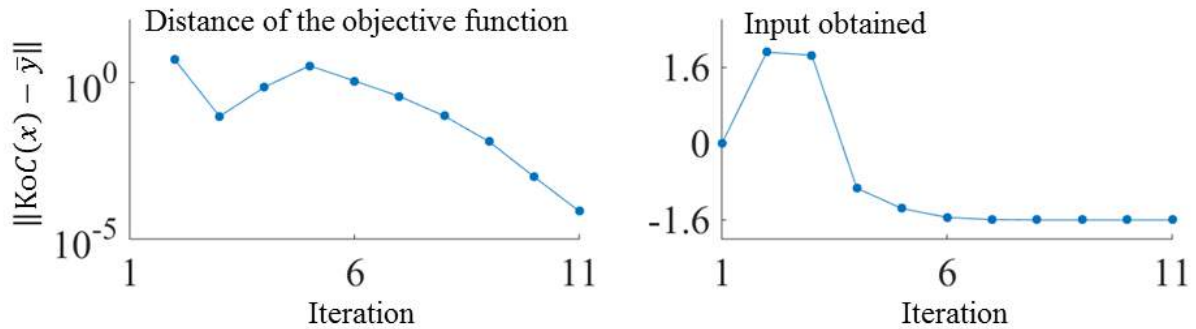


Fig.3.19 Distance of the objective function in respect to target and best input obtained

For this example the optimization is launched on the coarse model and using MM technique this model is iteratively corrected, based on the fine model, in order to minimize the distance between it and a reference point. Fig. 3.19 highlights the distance of the objective function (that has a smooth convergence), but also points the value of x obtained iteratively. As calculated only with the fine model the interest is to obtain with the coarse model $\hat{x} = -1.6$, value that actually is obtained with this type of technique as well.

The objective function variation as a function of the input x is represented in fig. 3.20. This figure emphasizes the evolution of the fine model, the best point obtained when optimizing the fine model and the evolution of the coarse model for different iterations, together with the best point obtained with the coarse model.

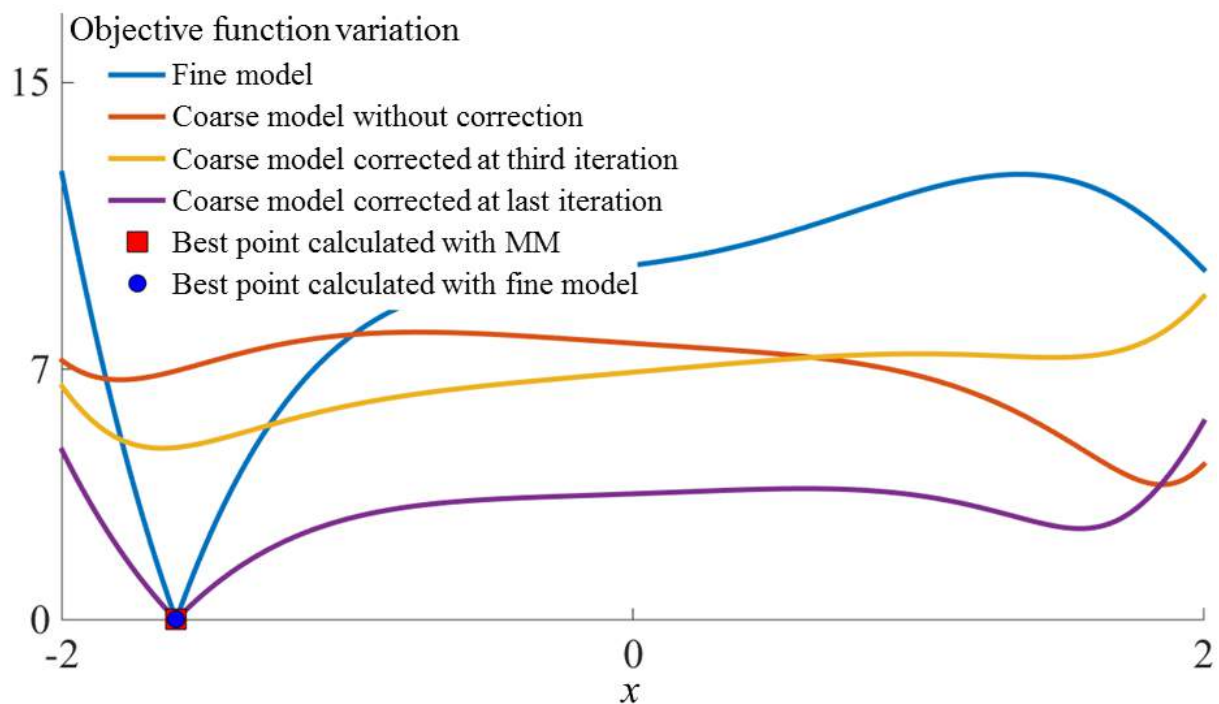


Fig.3.20 Objective function variation as a function of input x for different iterations when considering a feasible point

From the above figures it is clear that, if using the coarse model corrected iteratively based on the fine one, correction obtained by means of MM technique, is possible to achieve the same results, with a much faster model, when compared with an accurate one. The entire Matlab model with the MM implementation applied for the mathematical function presented in subchapter 3.2.2 can be found in *Appendix 3.B*.

3.3.5. Comparison between the OSMP and MM methods applied to the mathematical model

Both methods have something in commune, i.e. both of them correct the outputs of a fast, not so accurate, model based on a fine, very accurate one. The output space mapping

proportional technique is easy to implement, but are cases in which is not working, for instance if the coarse and fine model don't have the same tendency. The manifold mapping technique is much harder to implement, due to the Jacobian calculation, but this technique works properly if the initial starting point is not very far from the solution.

In this subchapter a comparison realized on the mathematical problem is given in terms of OSMP and MM techniques. This comparison has as benchmark the fine model. The objective function is to minimize the distance between the coarse model corrected and a reference target using the both OSMP respectively MM methods.

$$\hat{x}_i = \arg_{x \in \mathbb{R}} \min \|K o C(x) - \bar{y}\| \quad (3.29)$$

where \bar{y} takes 40 feasible values reported in fig. 3.20.

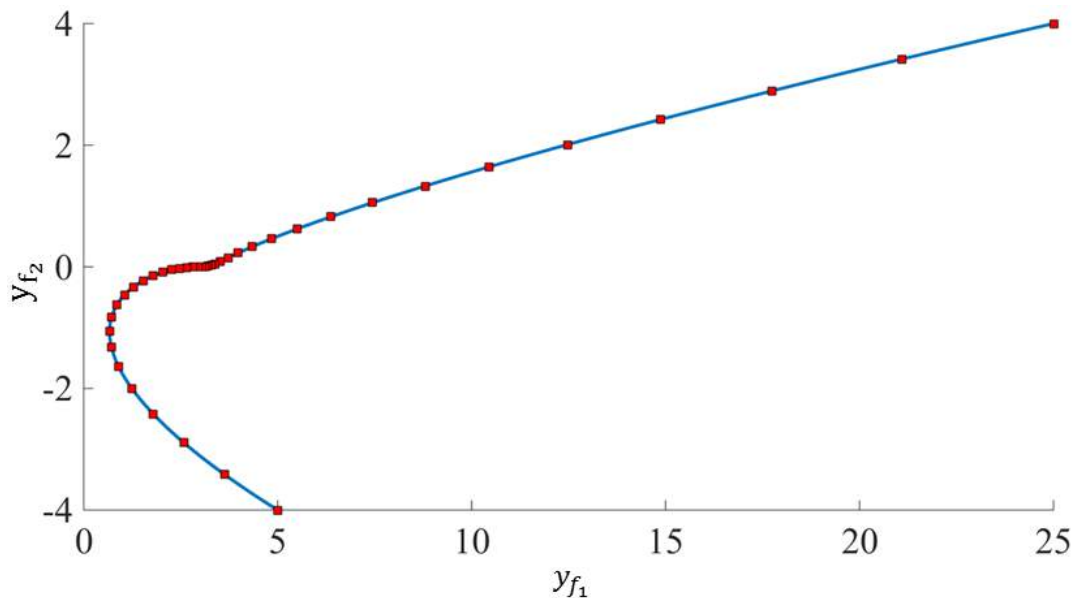


Fig.3.21 Fine model output variation and 40 feasible solutions

The next set of simulations is realized considering all the points presented in fig. 3.21, by using the output SM proportional and manifold mapping techniques. The maximum number of iterations for both techniques is set to 40 and the tolerance to $\varepsilon_1 = \varepsilon_2 = 10^{-4}$, exactly the same stopping criteria used in above tests.

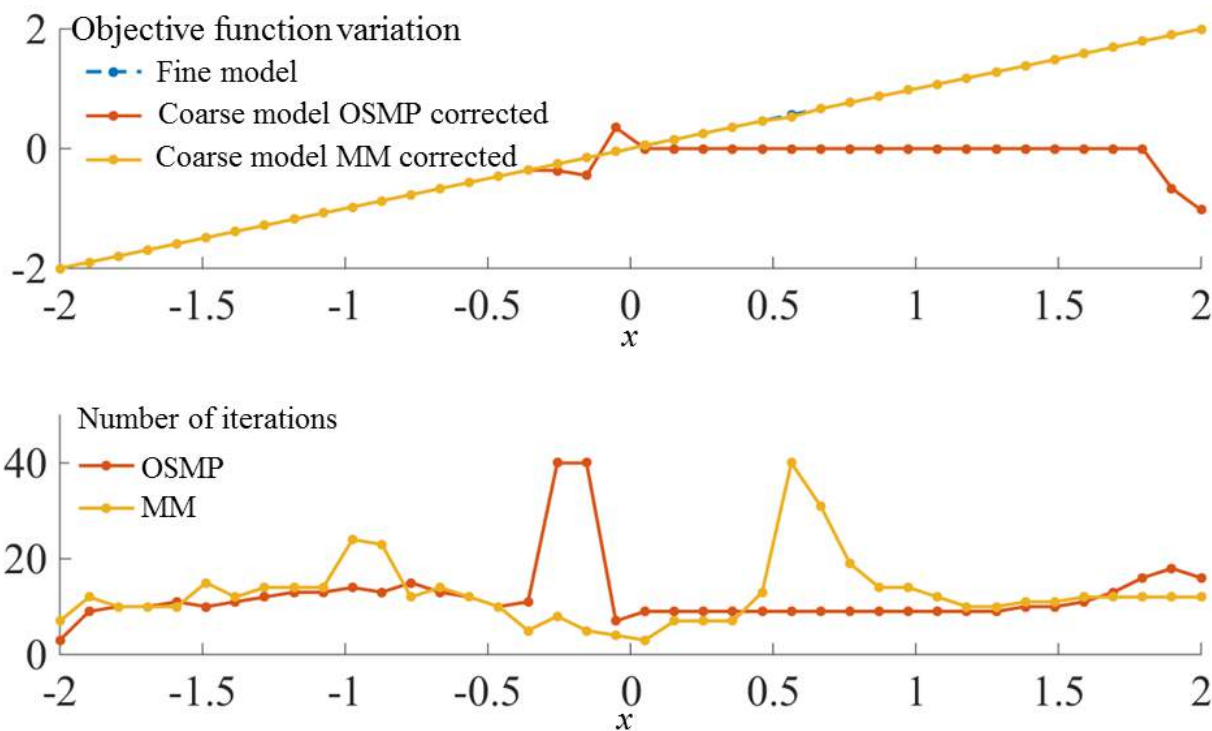


Fig.3.22 Objective function variation of the two models when using OSMP and MM applied to coarse model and the number of iterations for each objective

The values obtained exclusively with the fine model and the values obtained with OSMP and MM are represented in fig. 3.22, together with the number of iterations needed by the coarse model to obtain the solution. From this figure it is clear to affirm that the MM mapping works properly on this mathematical model and the results obtained using this technique are identical to the results obtained using only the fine model. However the OSMP technique works on this mathematical model only in the first part (for the negative values of $x < -0.5$). This may be justified by the fact that only in the first part the models have the same tendency (fig. 3.9 left side) and around $x = -0.5$ this tendency changes. Therefore it is possible to restate that the OSMP works properly if the coarse and fine models have the same tendency.

From the above results it is clear that manifold mapping works properly on this mathematical model for each feasible point. Instead, output space mapping proportional finds the solution only if the fine and coarse models have the same tendency. One can incline to affirm that MM is the best option when using this approach, but this technique as pointed above, is based on a more complicated modality of correcting the coarse model, which can lead to difficulties in implementation. Another aspect is the starting point of the optimization (when iteration is equal to 1), if this point is around the solution the convergence is smooth and the minimum is found, but if this point is far from the solution this technique tends to go in other direction and to provide false results. Hence, in the next paragraph the OSMP and MM are used and compared with the results obtained strictly with the fine model.

3.4. Optimization of the SR machine by using SM technique

As show in the last part of the second chapter, the commutation angles have an influence on the mean electromagnetic torque and on the ripple torque likewise. Therefore in this part of the thesis an optimization is performed on finding the optimum commutation angles and reference current that give the maximum of electromagnetic torque with the minimum of oscillations [17]. But to have accurate results an accurate model is needed. However this model requires an increased amount of time to perform the calculations. Therefore the space mapping technique detailed and tested above can be used in order to also reduce the optimization computation time [18].

3.4.1. Description of the parameter control optimization

For this optimization problem the geometry is fixed [19], the inputs that are changed are the moment when the phase should be supplied (θ_{on}), the moment when the supply should be cut-off (θ_{off}) and the reference current (i_{ref}). A diagram of the optimization problem is presented in fig. 3.23.

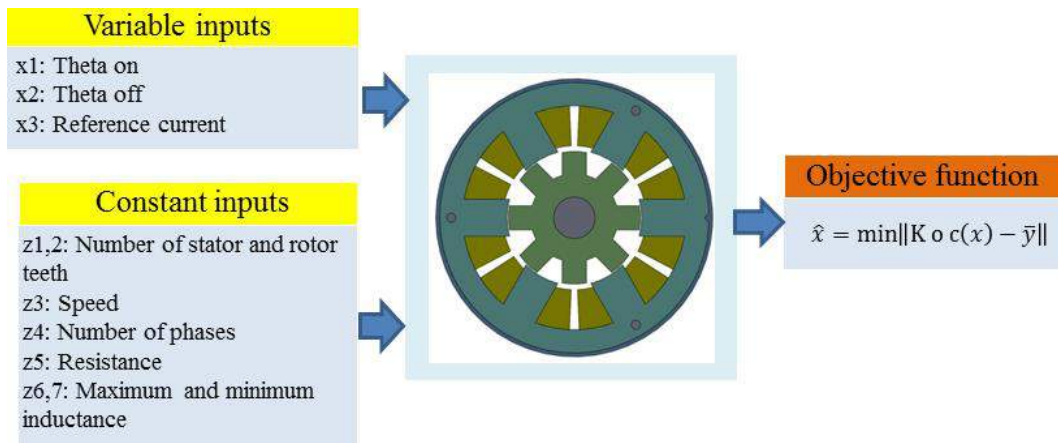


Fig.3.23 Outline of the parameter control optimization problem

In order to compare the two time reducing optimization methods, a mono-objective problem optimization of a switched reluctance machine is considered. The aim is to find the best control parameters with a view to maximize the mean electromagnetic torque, for a certain profile destination, while the torque ripple remains beneath an imposed value.

The objective function defined for the optimization problem to be solved by the coarse model is finding the optimum \hat{x} that minimizes the distance between the coarse model output and a corresponding specification \bar{y} :

$$\hat{x} = \arg_{x \in \mathbb{R}} \min \|K o C(x) - \bar{y}\| \quad (3.30)$$

where:

$$c: x \in \begin{cases} X_n^l \leq X_n \leq X_n^u \\ z_j \end{cases} \rightarrow \begin{cases} y_{c_1} = \langle T_e \rangle \\ y_{c_2} = T_{rip} \end{cases} \quad (3.31)$$

with: $\bar{y} = [y_{c_1}, y_{c_2}]$ $X_n = [x_1, \dots, x_3]$ and $z_j = [z_1, \dots, z_7]$

In eq. 3.31 X_n represents the vector of the design variables that need to be optimized, each variable being between a lower (X_n^l) and an upper (X_n^u) band. The constant inputs are represented by z_j and the average value of electromagnetic torque and the ripple torque by $\langle T_e \rangle$ respectively $T_{rip} = T_{e_{max}} - T_{e_{min}}$.

3.4.2. Approach used in fine and coarse models selection

The choice of the fine and coarse models is an important step because as previously pointed out; the tendency of the models is an issue. Another aspect is the properties of the both models, one to be accurate and the other to be fast. If it is possible to reduce the computation time of the accurate model without reducing the precision is very helpful for global computation time of the optimization. Finally, the selection of the fast model is very important because a poor choice of this model leads to noises in system and SM will not work.

➤ Reference model selection

The reference (fine) model is time dependent; simulations are realized on Matlab/Simulink (Chapter 2 section 2.5). The SR machine model is supplied from a three-phase half-bridge inverter. Current control by hysteresis and position sensor that provides the rotor position information for electronic commutation of stator phase currents are also considered when simulating the fine model. This model takes into account the non-linearity of iron laminations. A finite element model is used to determine the magnetic flux across the airgap and electromagnetic torque for multiple phase current strengths and different rotor positions. A cartography map of the flux and electromagnetic torque is obtained thereafter FE simulations (fig. 3.24 and 3.25), following that, this map to be used inside a Look-Up table in the fine model simulations. Eq. 2.2 is used to compute the voltage for the fine model.

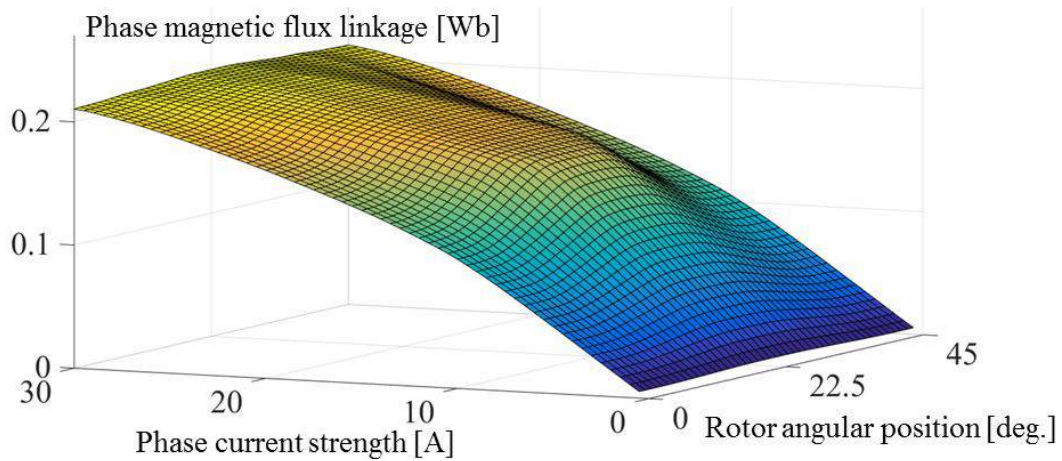


Fig.3.24 FE-computed phase magnetic flux as a function of rotor position and phase current strength

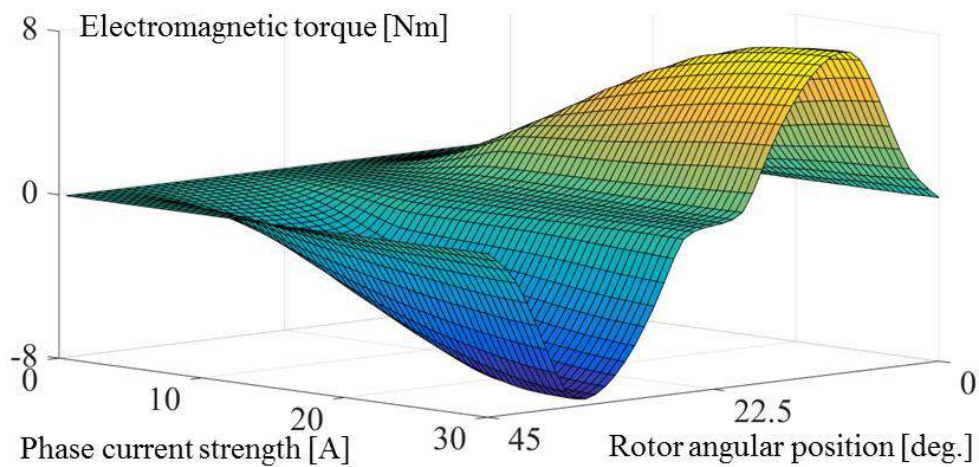


Fig.3.25 FE-computed electromagnetic torque as a function of rotor position and phase current strength

Because the finite element software requires a large amount of time to compute one simulation (40 minutes) when current limitation by hysteresis is used, by means of an interpolation in Matlab/Simulink environment, it is possible to have the same results in almost 4s considering a fine simulation step and current control by hysteresis. The time of FE model to compute one simulation is justified by the increased number of divisions needed in order to maintain the current in the imposed hysteresis band, the mesh discretization and because here the nonlinearity of the material is considered. If the current is not maintained in the imposed hysteresis band an increased amount of noises will appear in the system. Therefore, if the geometry of the machine is fixed the usage of FE software in an optimization process is not justified, even if this model is used only to correct the fast one.

When performing the simulations to compute figs. 3.24 and 3.25, the machine rotor was engaged in motion at constant speed and one phase was supplied with constant current in the band $[0.5,30]A$ with an increased step of $0.5A$. However in practice on the prototype it is not possible to use such high current due to the limitation of the phase, the nominal current being

4A. Therefore not to damage the winding the maximum current in the phase was limited at 6A when optimization was performed.

➤ Coarse model selection

The coarse model is deduced from the fine one. Several numerical and physical simplifications are considered to fasten its calculation. This model should, in a much faster way provide the needed quantities required by the optimization problem.

The first attempt of deducing the coarse model was by taking the fine model and increasing the simulation step (fig. 3.26) in order to increase its speed.

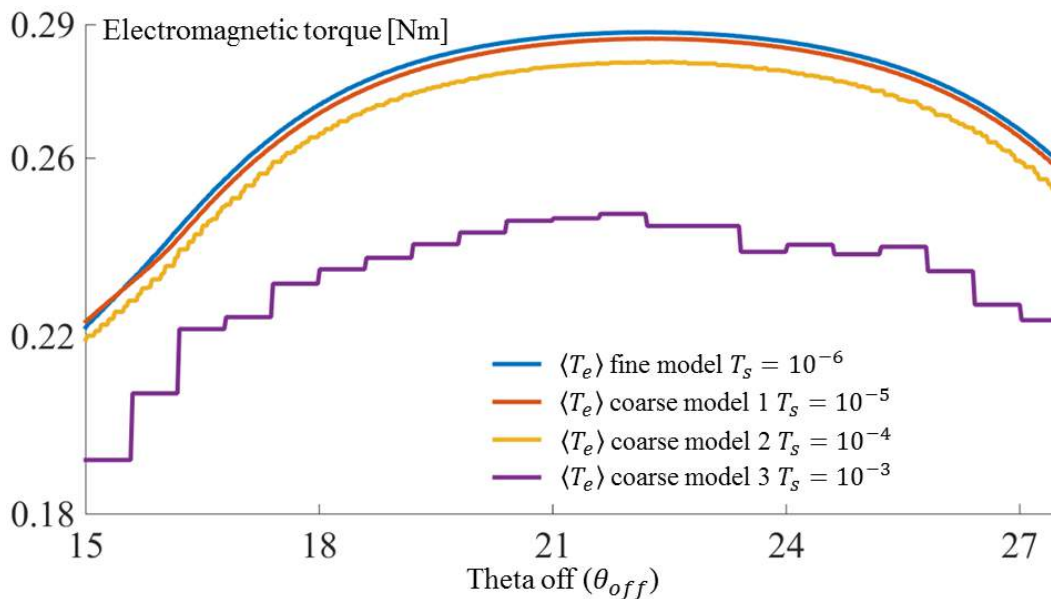


Fig.3.26 Comparison of the fine and three proposed coarse models, when $\theta_{on} = 0^\circ$, $i_{ref} = 4A$ and variable θ_{off}

When one variable (in this particular case θ_{off}) is changing and the rotor is engaged in motion at constant speed, one can obtain the evolution of the mean electromagnetic torque ($\langle T_e \rangle$) in function of the changed variable (θ_{off}), this waveform being represented in fig. 3.26 for different models.

If one simulation performed with the fine model requires 3.7s, for the first coarse model the time needed to compute one simulation is 2.1s, for the second coarse model 1.9s and for the third 1.7s. It is clear that by increasing the simulation step the time needed to realize one simulation decreases, although if we take a look at fig. 3.25 it is noticeable that if the simulation step increases, some noises appear in the system.

Because of the fact that even for the coarse model a time dependent simulation is needed to calculate the torque ripple, for the second attempt of choosing the fast model some assumption have to be done to increase its speed.

First of all, the fine model is implemented in Matlab/Simulink and the optimization is launched in Matlab; as the Matlab software requires time to access the Simulink toolbox the coarse model is created in Matlab environment to diminish this time. When solving the differential equations for phase currents, the software requires a rather large amount of time, hence the currents for the coarse model are considered equal to the reference ones with an evolution as illustrated in fig. 3.27. Thereafter, as an ideal evolution of the current in the phase is considered, their control is no longer required when calculating the electromagnetic torque behavior, the material saturation is not accounted for in the coarse model and the torque waveform is also depicted in fig. 3.27.

Due to the hysteresis current control implementation in the fine model, for less noises (given by the hysteresis band) in the system, a smaller simulation step was necessary, which led to an increased computation time; however, as this type of control was removed in the coarse model, a higher simulation step can be engaged.

Consequently in Matlab environment when modeling the coarse model, the electromagnetic torque of the SR machine is calculated (eq. 2.6), the slope of the inductance is also computed and its evolution is considered sinusoidal. Finally having the evolution of electromagnetic torque determined the ripple torque can be deduced. A brief representation of this new coarse model is presented in fig. 3.27.

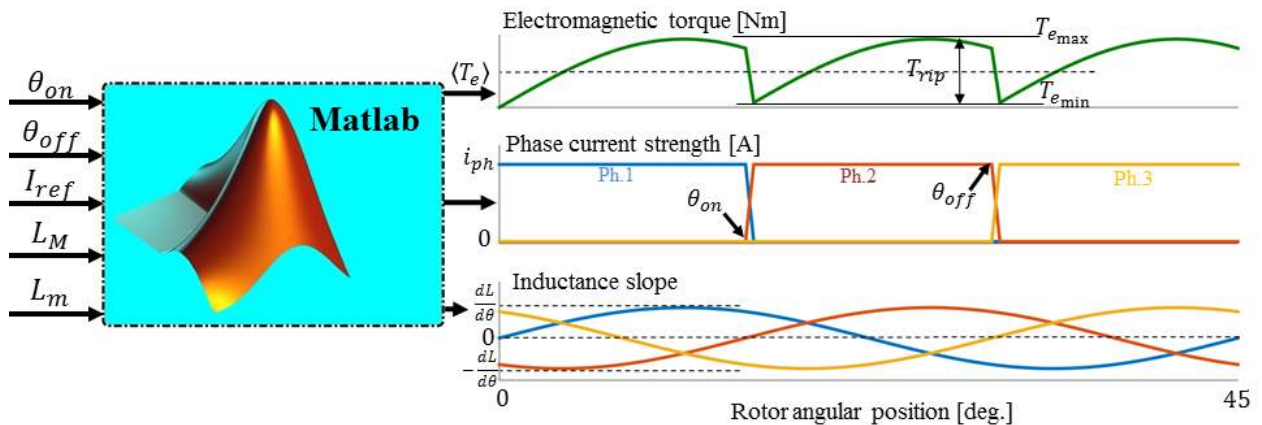


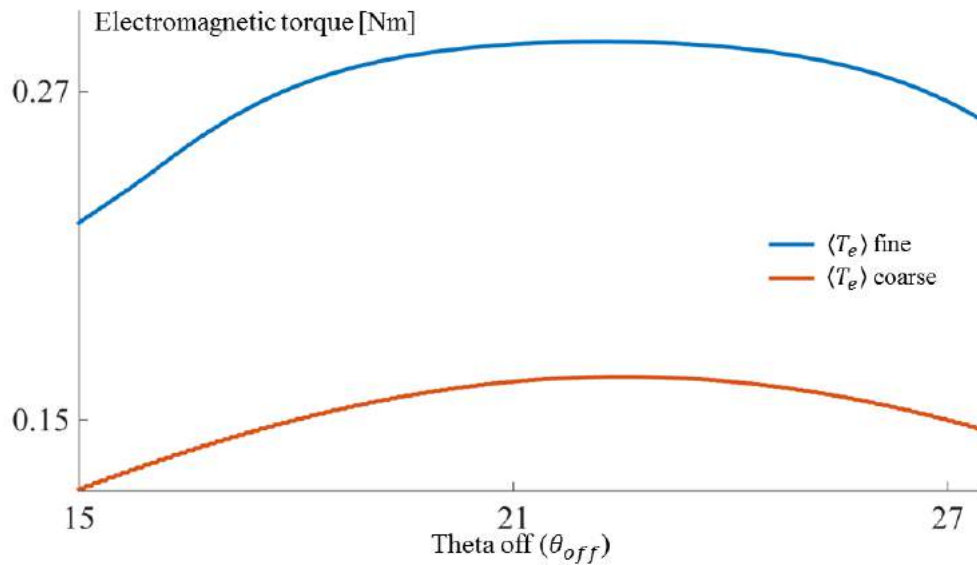
Fig.3.27 Structure and data flow of the coarse model

This new coarse model proves to be even faster than the previous versions, approximately 0.09s for one simulation. But the most important aspect is that this coarse model doesn't have any noises. In table 3.1 one can find the main differences between the proposed coarse model and the fine one.

Table 3.1 Fine and coarse models specifications

<i>Characteristics</i>	<i>Fine model</i>	<i>Coarse model</i>
<i>Saturation effect</i>	Yes	No
<i>Differential equations</i>	Yes	No
<i>Current control</i>	Yes	No
<i>Sampling time (s)</i>	10^{-6}	10^{-3}
<i>Computation time (s)</i>	5	0.09

The same principle as the one used to create fig. 3.26 is applied to realize the waveforms of the fine and the coarse models. Fig. 3.28 highlights the tendencies of the reference model and the fast one when one input variable is changed in an imposed band.

**Fig.3.28** Fine and coarse $\langle T_e \rangle$ in function of θ_{off} , when $\theta_{on} = 0^\circ$ and $i_{ref} = 4A$

Before starting the optimization using the both techniques, an optimization is realized using only the fine model. As pointed in the fine model description, the data obtained after FE-computation is implemented in a look up table in Matlab/Simulink environment. Because the time necessary to simulate one period with the fine model is approximately 4s it is possible to perform an optimization on this model to have a reference for observing the differences between this optimization and the optimization using space mapping.

The optimization performed on all models is based on sequential quadratic programming (SQP) algorithm under the `fmincon` function [20]. For multiple starting points, it searches the constrained minimum of a scalar function of several variables [21].

In order to get an idea of the difference between local minimum solvers i.e. `fmincon` and global minimum solvers i.e. `Multistart`, further some explaining together with an example is provided. The `fmincon` is a gradient-based method that finds the local minimum of a non-linear multi-variable function. It starts from an initial estimate, iterates according to a given update scheme and stops when criteria is satisfied. Instead the `Multistart` runs the `fmincon` for multiple

starting points, as name implies. All minimum obtained for each starting point is saved in a vector and from this vector the best result is taken as minimum global [22]. For the next example the “peaks” function from Matlab is chosen and in the first part a local search is launched, followed afterwards by a global one.

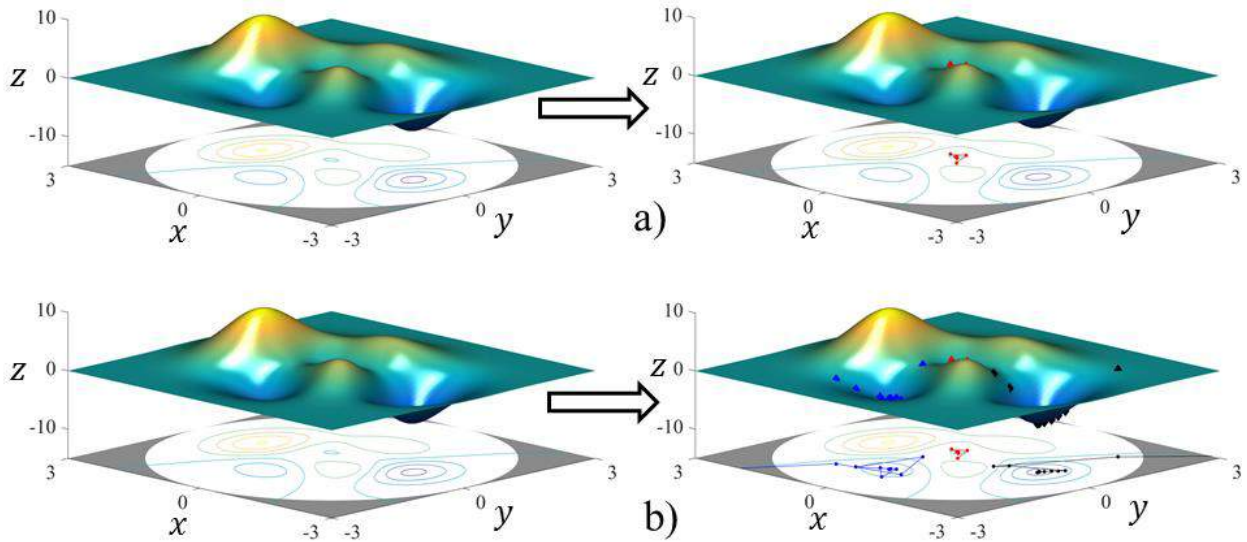


Fig.3.29 Local minimum (a) and global minimum (b) search applied to Matlab peaks function

When using `fmincon` the algorithm finds the best value $x = 0.2964$, $y = 0.3202$ and $z = -0.0649$. These values don't represent the global minimum but are normal because the initial point x_0 is set to be $x_0 = [0,0]$, that is why the algorithm finds one of the local minimum that is around the initial points. However when Multistart is used the algorithm finds all minimum whether they are local or global and in the end the global minimum is chosen. In fig. 3.29a the minimum found is represented with red and in fig. 3.29b the two local minimum are represented with blue respectively red and the global minimum with black. The Multistart finds $x = 0.2283$, $y = 1.6255$ and $z = -6.5511$, values that correspond to the global minimum.

3.4.3. Output space mapping proportional applied to machine optimization

The main interest of this subchapter is to determine the optimal control parameters of the switched reluctance machine in order to minimize the distance between the output fine model and an imposed reference. In this part both the motor and generator operation modes are targeted. For this approach the coarse model presented above is used to optimize the input parameters, this model being corrected iteratively respect to the fine one. For the optimization process Multistart under the `fmincon` function is used, with the number of runs set to 100.

➤ Motor operation mode

The main principle of the machine for working as a motor is to excite the phase when the rotor teeth are unaligned with the stator ones, so that the nearest rotor teeth to be attracted into alignment. The optimization problem is the one presented in fig. 3.22 and the interested is to achieve an average electromagnetic torque of $\langle T_e \rangle = 0.5$ [Nm] for a maximum ripple torque of $T_{rip} = 0.34$ [Nm].

The optimization using the SQP algorithm is launched on the coarse model presented above and the best inputs obtained after optimization are used as inputs for evaluating the fine model. Thereafter, their outputs are compared; if the difference between them is smaller than an imposed tolerance, $\varepsilon = 10^{-3}$, the optimization stops and the results are considered to be the best ones.

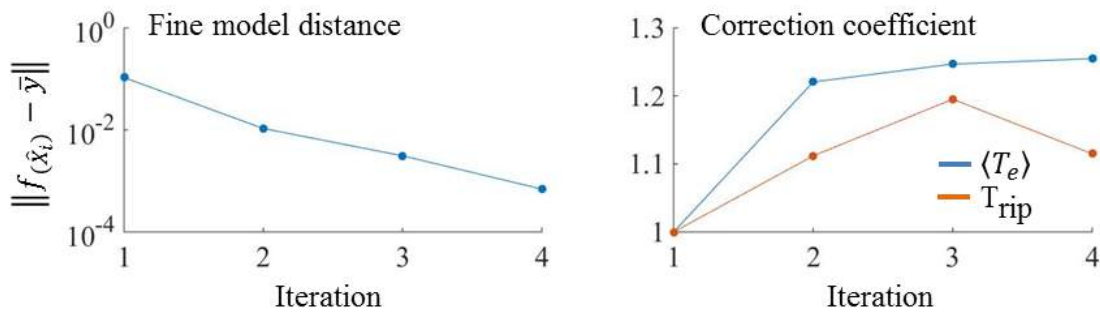


Fig.3.30 Distance with the target and correction coefficient using OSMP technique, in motor operation mode

Fig. 3.30 represents the evolution of the objective function and the correction coefficient progression for each iteration. The output SM proportional requires four iterations to obtain a feasible solution.

➤ Generator operation mode

The principle of the machine working in generator operation mode is to energize the stator phase in the negative slope of the inductance, which means the instant when the rotor teeth depart from the aligned position, in the rotation direction. For the generating mode the commutation angles need to be shifted in order to have a continuous conversion of mechanical energy. Because the machine is generating, the electromagnetic torque value results as negative for this operation mode. For this case we are interested to obtain an average electromagnetic torque of $\langle T_e \rangle = -0.5$ [Nm] for a maximum ripple torque of $|T_{rip}| = 0.34$ [Nm].

As in motor, a stopping criterion has to be implemented also for the generator case, i.e. when the difference between the fine output and the target is smaller than $\varepsilon = 10^{-4}$ the optimization stops.

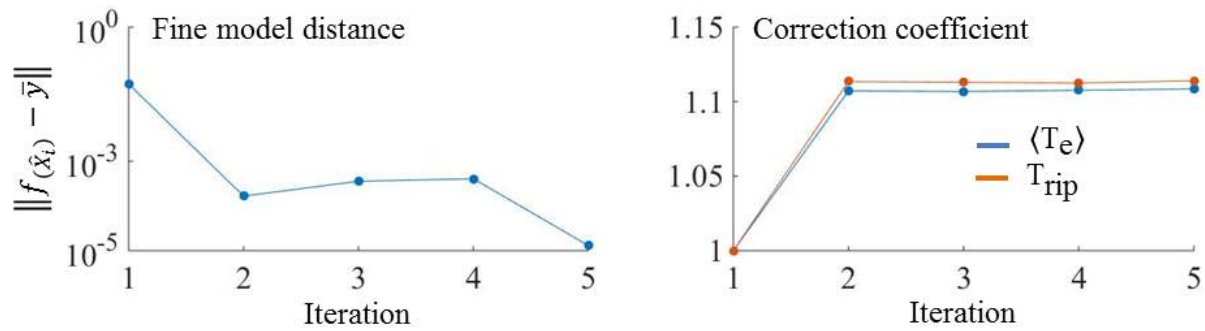


Fig.3.31 Distance with the target and correction coefficient using OSMP technique, in generator operation mode

The optimization using OSMP in generator operation mode requires only five evaluations of the fine model. Fig. 3.31 illustrates the correction coefficient for all corrected outputs and the convergence of the model.

3.4.4. Manifold mapping applied to SR machine optimization

When using manifold mapping the same objective function is used as for output SM proportional and when optimization is launched on the coarse model the algorithm and its parameters are still the ones used previously. Because of the fact that in this thesis the aim is to study the both operation modes of the SR machine, when using the MM technique the optimization is launched to determine the optimal control parameters both in motor and generator operation mode.

➤ Motor operation mode

In order to be able to see a comparison between both techniques and the fine model is necessary to maintain the same initialization parameters as for the previous technique, i.e. output SM proportional. Here also the aim is to achieve an average electromagnetic torque of $\langle T_e \rangle = 0.5$ [Nm] for a maximum ripple torque of $T_{rip} = 0.34$ [Nm]. The model stops when the tolerance is smaller then $\varepsilon = 10^{-3}$.

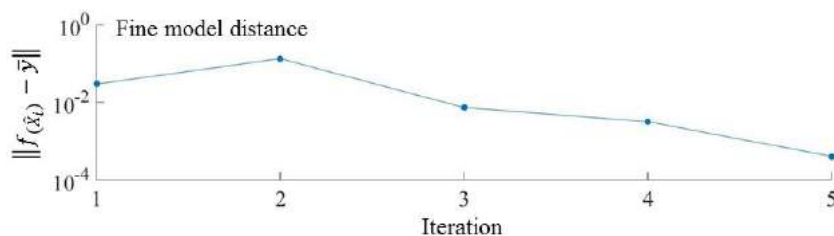


Fig.3.32 Distance with the target using MM in motor operation mode

The distance between the fine model and the imposed target is represented in fig. 3.32. This technique requires five evaluations of the fine model to satisfy the tolerance.

➤ Generator operation mode

Because the both operation modes are studied equally, a comparison in terms of best results obtained with both techniques is required in this case also. Consequently the parameter initialization has to be the same as the ones used for the OSMP technique; the same aim applies for this case also, i.e. to achieve an average electromagnetic torque of $\langle T_e \rangle = -0.5$ [Nm] for a maximum ripple torque of $T_{rip} = 0.34$ [Nm]. The tolerance that the model should satisfy in order to stop is $\varepsilon = 10^{-4}$.

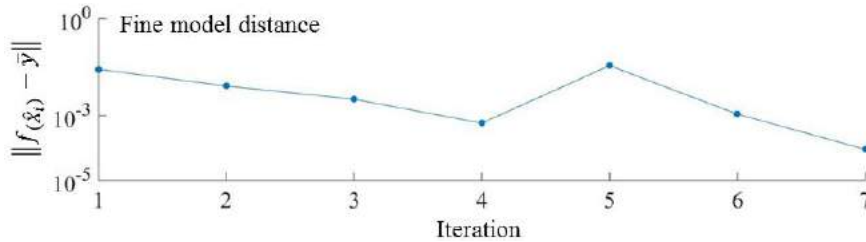


Fig.3.33 Distance with the target using MM in generator operation mode

When using MM to determine the control parameters of the SR machine in generator operation mode, the distance between the fine model and the imposed target is pointed in fig. 3.33. This technique requires seven iterations to obtain the desired results.

3.4.5. Comparative optimal results

The comparison is realized in terms of best inputs and outputs as well the number of evaluations of the fine model and the time required by the optimization process to compute these results. The reference result is the one achieved after optimizing strictly the fine model.

➤ Motor operation mode

First of all the comparison is realized for the case in which the machine is functioning as motor i.e. realizes the energy conversion from electrical into mechanical.

Table 3.2 Best inputs and outputs obtained with both techniques in motor operation mode

Best results obtained with:	Fine model	OSMP	MM
Theta on [deg.]	0	0	0
Theta off [deg.]	20	19.82	19.8
Reference current [A]	5.33	5.32	5.33
Mean electromagnetic torque [Nm]	0.50	0.497	0.499
Ripple torque [Nm]	0.34	0.34	0.34
Speed [rpm]	100	100	100
Number of fine model evaluations	3340	4	5
Optimization time [s]	$6.14 \cdot 10^3$	$0.498 \cdot 10^3$	$0.564 \cdot 10^3$

In order to find the best parameters when using strictly the fine model the optimization algorithm needs more than 3000 evaluations. Because this model is accurate the necessary time to compute the optimization is almost two hours, a big amount of time when compared with the time spent by the OSMP and MM to finish the same optimization (less than 9 minutes). As it

can be remarked from the table 3.2 the OSMP and MM techniques give almost the same results as if the simulation would have been launched on the fine model itself.

Thanks to the low time necessary to perform an optimization it is possible to calculate the best computation angles (θ_{on} and θ_{off}) for different values of speed and for multiple phase current strengths. Figs. 3.34 and 3.35 show a cartography map of the best commutation angles for different values of speed and for multiple phase currents. These values can be used in terms of an interpolation when simulations or tests are performed in order to have the best computation angles that maximize the mean electromagnetic torque with the lowest ripple torque regardless the speed and current changes in the machine.

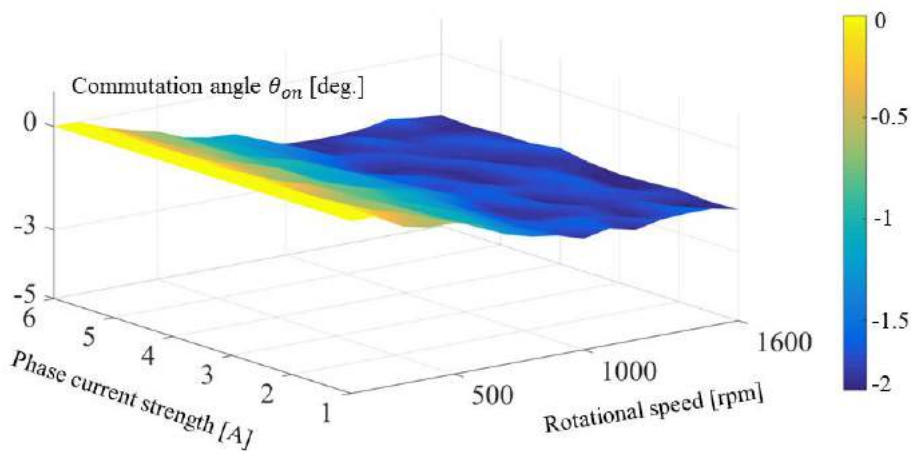


Fig.3.34 Best θ_{on} for different rotational speed and phase current strength

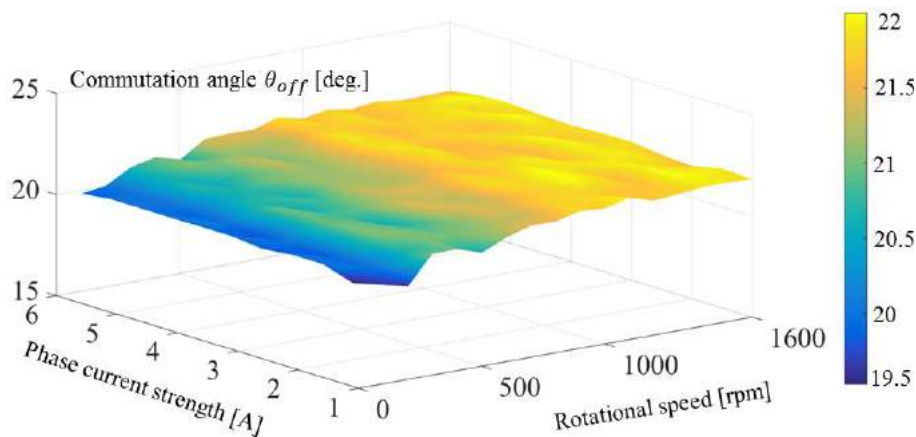


Fig.3.35 Best θ_{off} for different rotational speed and phase current strength

The above figures provide the values of the commutation angles that maximize the electromagnetic torque for each speed in the band [100 ÷ 1600]rpm with an increased step of 100rpm and for each phase current in the band [1 ÷ 6]A with an increased step of 0.5A.

➤ Generator operation mode

For the case in which the machine is generating, that means the mechanical energy is converted into electrical one, a comparison in terms of best inputs and outputs is detailed in table 3.3.

Table 3.3 Best inputs and outputs obtained with both techniques in generator operation mode

Best results obtained with:	Fine model	OSMP	MM
Theta on [deg.]	23.46	23.24	23.48
Theta off [deg.]	45	45	45
Reference current [A]	5.31	5.31	5.34
Mean electromagnetic torque [Nm]	-0.499	-0.499	-0.5
Ripple torque [Nm]	0.34	0.34	0.34
Speed [rpm]	100	100	100
Number of fine model evaluations	3427	5	7
Optimization time [s]	$6.3 \cdot 10^3$	$0.616 \cdot 10^3$	$0.701 \cdot 10^3$

From table 3.3 it is clear that even in generator operation mode when using both techniques the obtained results are near the ones calculated strictly with the fine model, but not only, the computation time decreases with more than 80%.

3.5. Space mapping technique applied to design and control optimization of SR machine for ISA applications

Having two optimization techniques presented and tested first on a mathematical function and afterwards applied to a SR machine prototype to optimize the input parameters, techniques that decrease considerably the optimization time, it is possible to increase the optimization problem. Because the OSMP and MM proved that they can work when calculating the best inputs of a three-phase six stator and eight rotor teeth SR machine further on the idea is to add some sizing parameters besides the control parameters in order to determine the best geometry and control of a SR machine to be used in ISA applications.

The objective is to maximize the average electromagnetic torque towards 150 Nm at 200 rpm rotor speed [23], in motor operation mode by taking into account some imposed constraints. The SR machine topology for the design optimization is $N_S = 6$ and $N_R = 8$.

3.5.1. Optimization problem description

The proposed optimization is a mono-objective problem with the aim of finding the best size and control of a SR machine to be used in ISA applications. The definition of the optimization problem to be solved with the coarse model can be expressed in terms of finding the optimum \hat{x} that minimizes the distance between the fast model output and a corresponding specification \bar{y} .

$$\hat{x} = \arg_{x \in \mathbb{R}} \min \|K_oC(x) - \bar{y}\| \quad (3.32)$$

where:

$$c: x \in \begin{cases} X_n^l \leq X_n \leq X_n^u \\ z_j \end{cases} \rightarrow \begin{cases} y_{c_1} = \langle T_e \rangle \\ y_{c_2} = T_{rip} \\ y_{c_3} = \eta \end{cases} \quad (3.33)$$

with: $\bar{y} = [y_{c_1}, \dots, y_{c_3}]$ $X_n = [x_1, \dots, x_{11}]$ and $z_j = [z_1, \dots, z_6]$

In eq. 3.33 X_n represents the vector of the design and control variables that needs to be optimized, each variable being between a lower (X_n^l) and an upper (X_n^u) band. The constant inputs are represented by z_j and the average value of electromagnetic torque, the ripple torque and machine efficiency, $\langle T_e \rangle$, $T_{rip} = T_{e_{max}} - T_{e_{min}}/T_{av}$ respectively η .

The entire problem presented above can be synthetized as shown in fig. 3.36.

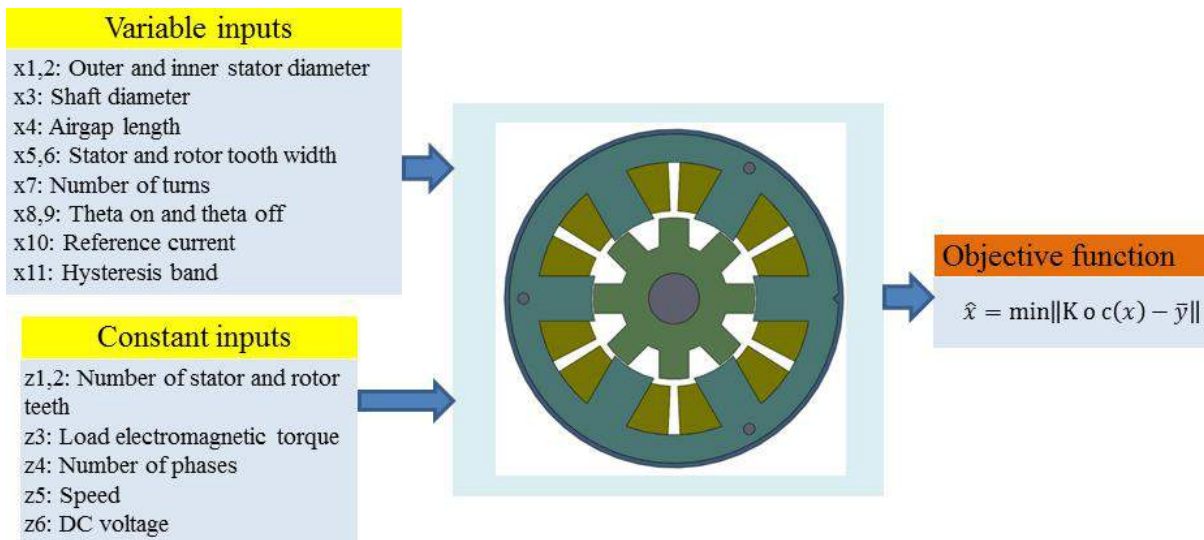


Fig.3.36 Optimization problem applied to parameter design and control optimization

This mono-objective optimization problem has eleven input variables; these are control and design variables. The interest is to obtain after the optimization $\langle T_e \rangle = 150\text{Nm}$, $T_{rip} \leq 0.55$ and $\eta \geq 85\%$ for an imposed constant speed of 200rpm.

3.5.2. Selection of the fine and coarse models

For this optimization problem the reference fine model is a finite element model, the geometry design provided by the fast coarse model is implemented in the FE software that is JMAG Designer. Because of the fact that a certain number of fine model evaluations are required and for each evaluation the geometry changes, an automatic script was performed for escaping the discomfort of drawing each geometry. However the optimization is launched in Matlab and the computation of the fine model is realized in JMAG Designer and due to that a link between the both software's was done. This link was realized as follows: first the automatic

script that constructs the machine geometry, imposes conditions, materials, generates mesh and runs simulation was made in VBScript. This script can be simulated directly from CMD and Matlab software can access CMD through a code line, therefore having this information it is possible to command the VBScript directly from Matlab. A workflow of the entire link between Matlab and JMAG designer is represented in fig. 3.37.

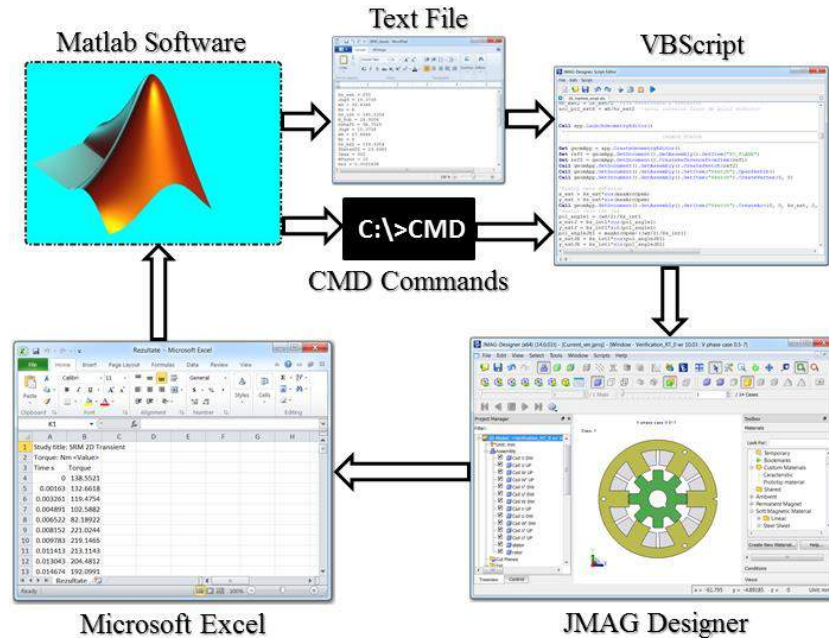


Fig.3.37 Structure and data flow for the link between Matlab and JMAG Designer

It is possible to explain fig. 3.37 as follows: at first the coarse model that is implemented in Matlab is optimized to provide the optimal geometric parameters of the machine. These parameters together with the initialization ones needed by JMAG Designer are saved in a text file. Through CMD command, Matlab software accesses VBScript and gives the run command, afterwards the VBScript takes all the initialization parameters from the text file, builds the model, according to the dimensions saved in this file, imposes the materials, together with the conditions, generates the mesh, runs the transient simulation and saves all results in a CSV file. Finally when all this process is finalized Matlab loads the CSV file that contains the simulation results which are further compared with the ones given by the coarse model. The entire VBScript used to draw the machine can be found in *Appendix 3.C*.

The coarse model is the one represented in fig. 3.27 with the difference that here the maximum and minimum inductance are calculated from the machine geometry as detailed in chapter 2.

3.5.3. Output space mapping proportional applied to SR machine optimization

In this part the output SM proportional is used to determine in a fast manner the optimal design and control parameters of the SR machine to be used in integrated starter alternator system. When launching the simulation the target is considered as the one presented in subchapter 3.5.1, i.e. $\langle T_e \rangle = 150\text{Nm}$, $T_{rip} \leq 0.55$ and $\eta \geq 85\%$ for an imposed constant speed of 200rpm.

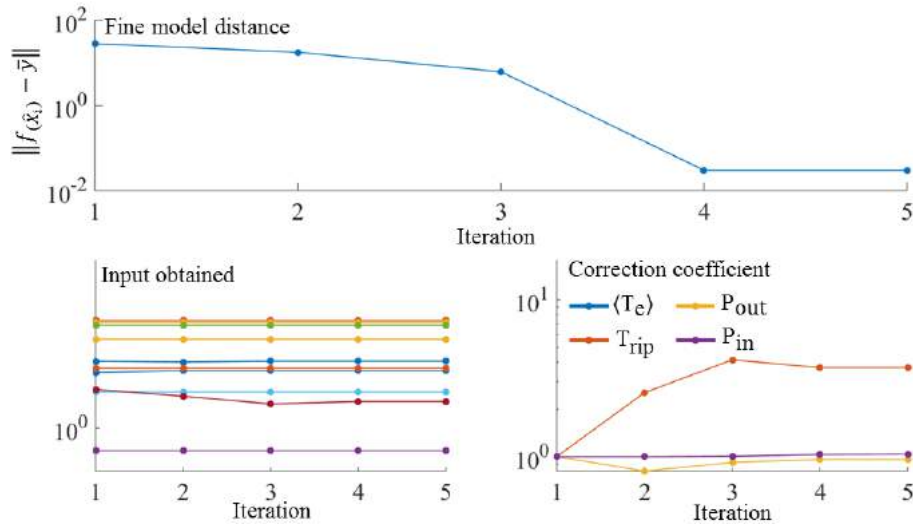


Fig.3.38 Distance with the target, obtained input and correction coefficient using OSMP technique in SR machine for ISA applications

Fig. 3.38 represents the distance between the output of the fine model and the corresponding imposed target. Also in this figure is represented the best input obtained after each iteration and the correction calculated for each corrected component.

3.5.4. Manifold mapping applied to SR machine optimization

When using the manifold mapping to correct the fast model the same objective function is used as in OSMP case. By keeping the same problem only changing the correction methodology the idea is to verify if it is possible to obtain the same results. As mentioned here the target is $\langle T_e \rangle = 150\text{Nm}$, $T_{rip} \leq 0.55$ and $\eta \geq 85\%$ for an imposed constant speed of 200rpm

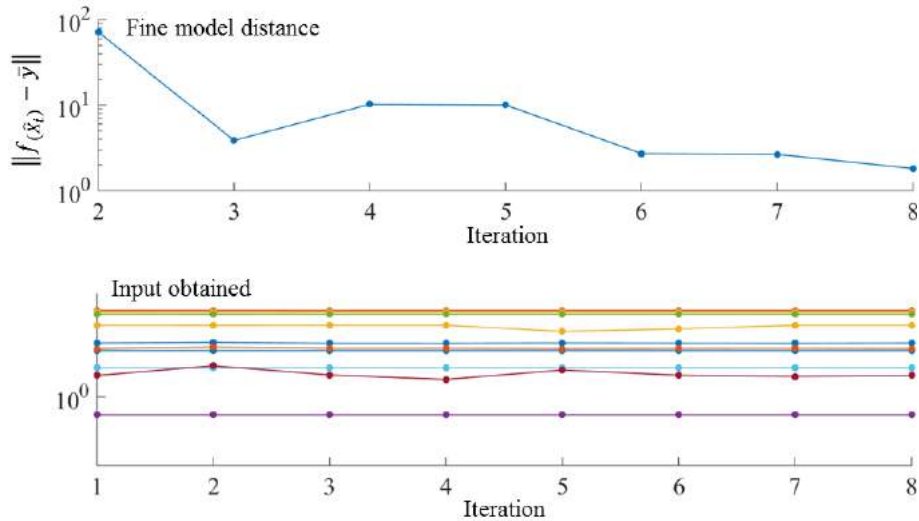


Fig.3.39 Distance with the target and input obtained using MM technique in SR machine for ISA applications

In fig. 3.39 is represented the distance between the output of the fine model and the imposed target and the values of the input obtained after each iteration. Further a comparison in terms of best input and associated output obtained with each model is provided.

3.5.5. Comparative optimal design

Because of the fact that the optimization problem is not changed and the target is always the same for the comparison the interest is to have after the optimization process almost the same inputs for both cases. Table 3.4 presents the inputs and outputs obtained with each technique.

Table 3.4 Best inputs and outputs obtained with both techniques

Design parameters:	Optimal value found using OSMP	Optimal value found using MM
θ_{on} angle for motor operation [deg.]	0	0
θ_{off} angle for motor operation [deg.]	22	22
Hysteresis band [A]	0.05	0.05
Stator outer diameter [mm]	255	254.99
Stator inner diameter [mm]	160.4	160.4
Shaft diameter [mm]	90.7	90.7
Stator pole width [mm]	36.60	36.61
Rotor pole width [mm]	25	24.9
Air-gap [mm]	0.3	0.3
Axial length [mm]	300	299
Number of turns per phase	7	7
Efficiency, at 200 rpm [%]	86	86
Mean electromagnetic torque [Nm]	149.7	148.3
Torque ripple	0.51	0.52
Machine speed [rpm]	200	200
Number of stator teeth	6	6
Number of rotor teeth	8	8
Number of phases	3	3

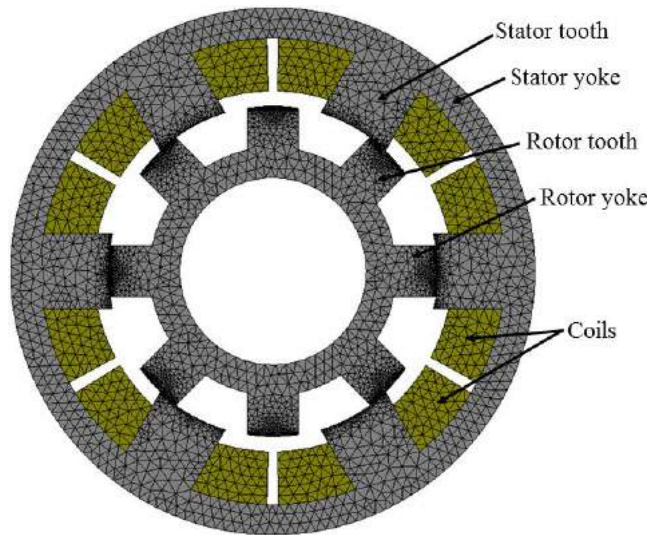


Fig.3.40 FE-discretized cross-section geometry of the optimally-designed three-phase 6/8 SR machine for ISA applications

After five iterations in OSMP case and eight in MM case, computing more than 3000 evaluations for each iteration, one obtains the main design optimization results listed in Table 3.4 and the cross-section geometry presented in fig. 3.40.

3.6. Simulation of the optimally-designed SR machine used in ISA application

Since during optimization process the magnetic saturation effect is not accounted for, and the phase self-inductance profile is considered linear, the optimized three-phase 6/8 SR machine configuration is imported in the FE-based software and simulated for different values of phase current strengths. The data obtained by several FE field analyses are then used to build the simulation model of the SR machine, in both motor and generator operating modes.

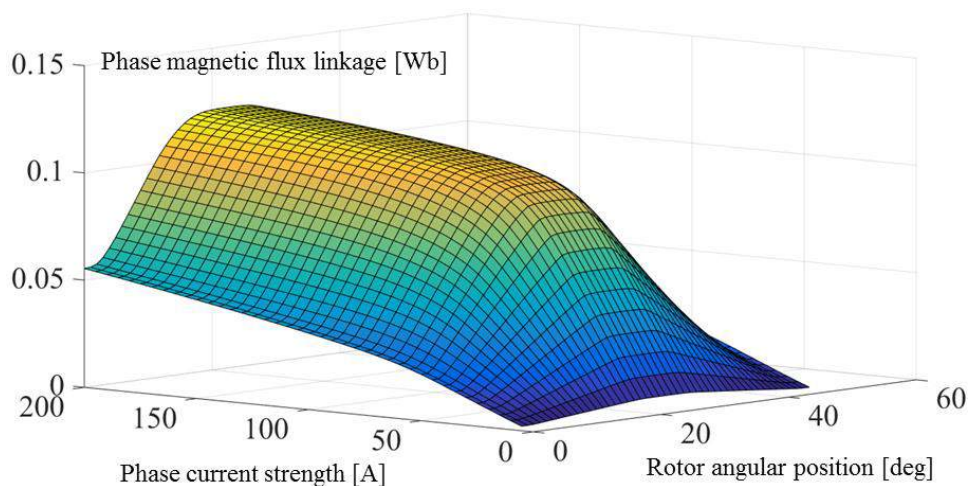


Fig.3.41 FE-computed phase magnetic flux linkage as a function of rotor position and phase current strength.

The response surface of the phase magnetic flux linkage as nonlinear function of the phase current strength and rotor angular position, shown in fig. 3.41, is obtained for a

mechanical period of $2\pi/N_R$ and for phase current strength values in the range of $0.5 \rightarrow 200$ [A]. The software used for FE simulations is again JMAG-Designer.

The data from table 3.4 is implemented in MATLAB/ Simulink environment using a look-up table. Hysteresis current control and PI speed/torque control are considered in the simulations of the three-phase 6/8 SR machine under study.

The SR machine, in motor operation mode, has to develop an electromagnetic torque of 150 Nm, at a rotor speed of 200 rpm, for the ICE start-up. PI speed control is used to determine the reference phase current strength. Figs. 3.42 displays the current, speed, electromagnetic torque and power responses of the three-phase 6/8 SR machine operating as a motor (starter).

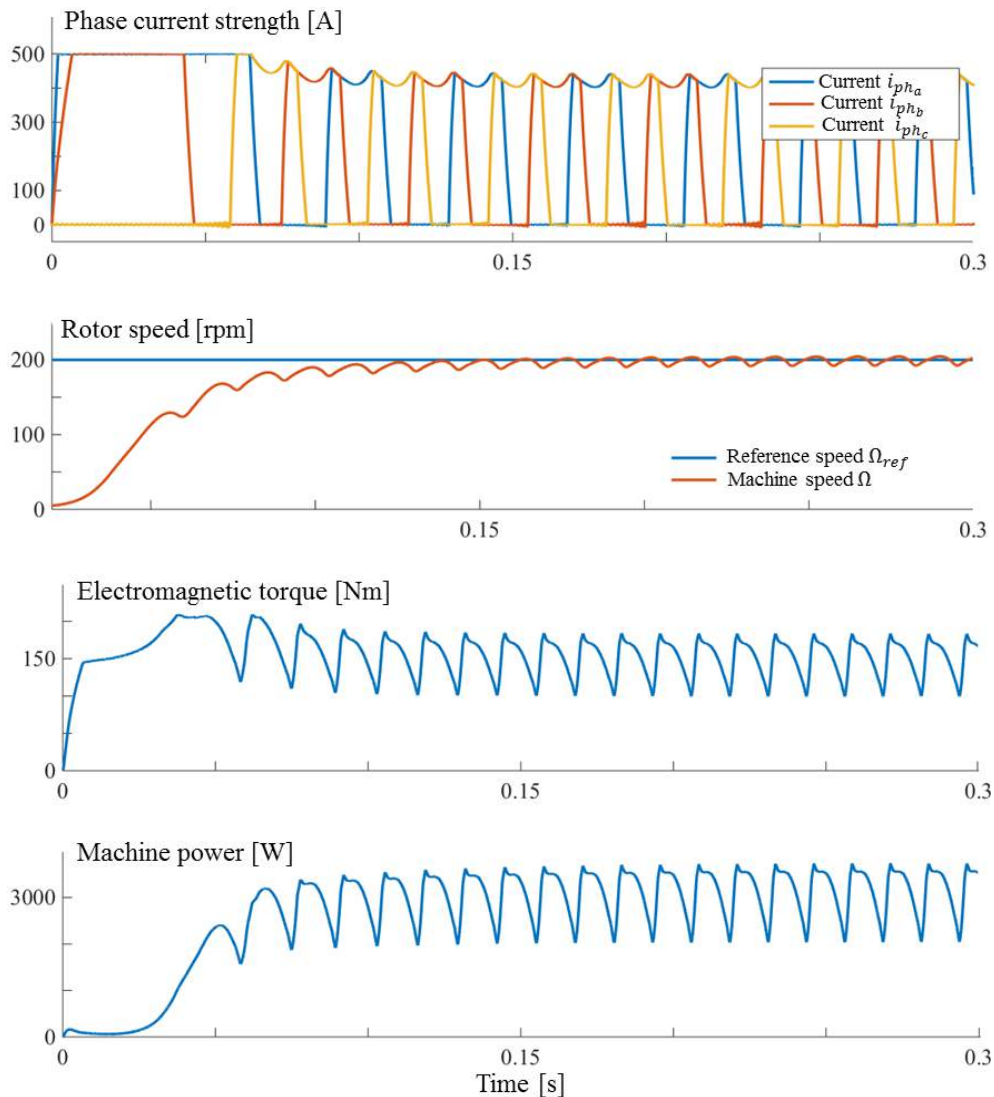


Fig.3.42 Simulated steady-state responses in current, speed, electromagnetic torque and output power of the three-phase 6/8 SR machine, in motor operating mode during ICE start-up.

The SR machine in generating operation mode is driven by the ICE, at certain speed. The developed electromagnetic torque should be negative by convention, so that the stator-phase energization must correspond to the decreasing slope of the phase self-inductance, when

the rotor teeth are just leaving the aligned position in the direction of rotation. PI torque control is used for reference phase current strength determination in hysteresis current control.

For the generating mode of the SR machine, optimized θ_{on} and θ_{off} commutation angles have been determined for operation at constant high-speed of 3000 rpm. In its turn, the reference torque is calculated so that the power is kept constant regardless the rotor speed change.

Fig. 3.43 displays the current, electromagnetic torque and power responses of the SR machine in generator operation, for $\theta_{on} = 24^\circ$ and $\theta_{off} = 45^\circ$.

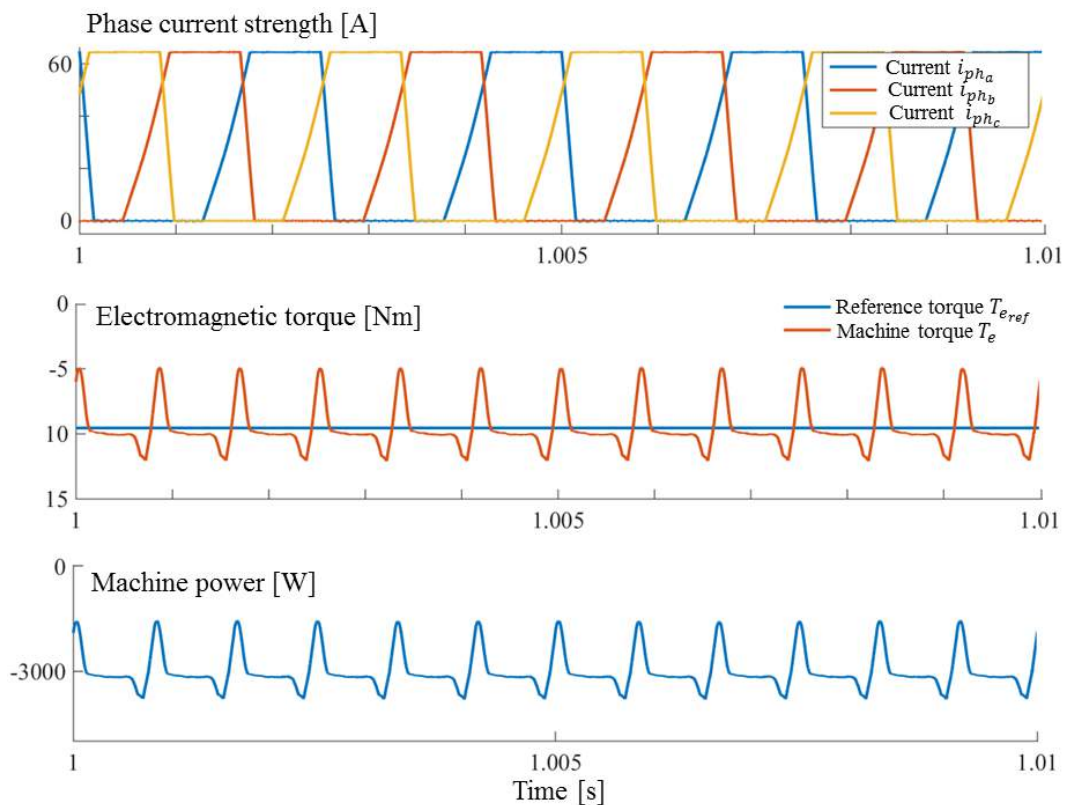


Fig.3.43 Simulated steady-state responses in current, electromagnetic torque and output power of the three-phase 6/8 SR machine, in generator operating mode, at 3000 rpm rotor speed.

In fig. 3.44, simulations are carried out for a small part of the SR-machine operation cycle in automotive ISA application, as follows: for the first two seconds the SR machine starts in motor operation mode, and the reference speed is set to 200 rpm; during this period the ICE is started; at the instant $t_1 = 2$ s, SR machine changes to generator operation mode, the machine being driven by the ICE, and the rotor speed is set to 900 rpm; once the speed reaches 3000 rpm, it is decreased back to 900 rpm, before stopping the machine, at the instant $t_2 = 10$ s.

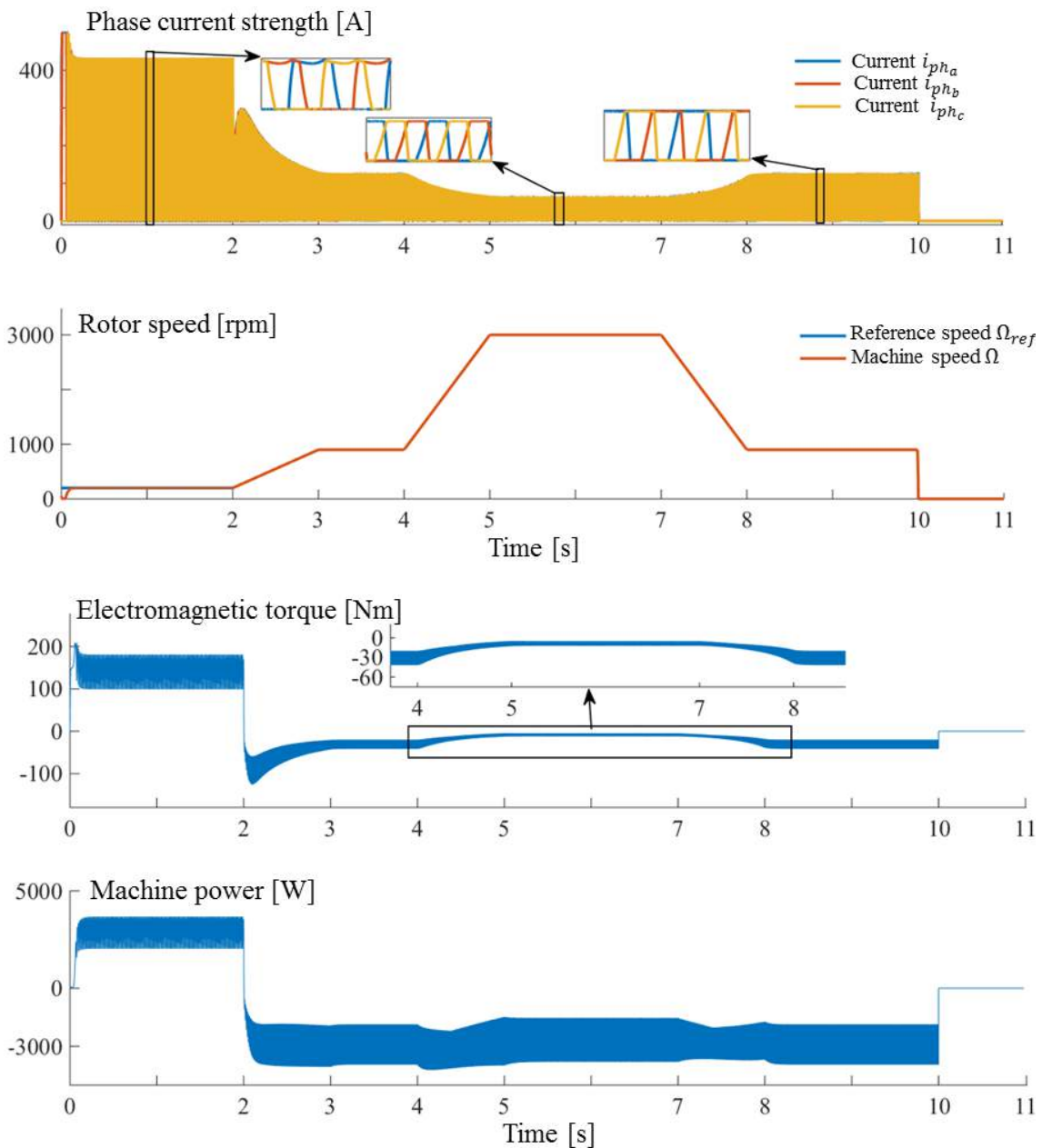


Fig.3.44 Simulated dynamic responses in phase current, rotor speed, electromagnetic torque and output power of the three-phase 6/8 SR machine for a part of its operation cycle in automotive ISA application.

In the dynamic simulations for the machine operating in motor mode, the commutation angles are constant, corresponding to their values of table 3.4, whereas for the generator mode, the commutation angles are $\theta_{on} = 24^\circ$ and $\theta_{off} = 45^\circ$. The simulated driving cycle in fig. 3.44 consists of start-up of the ICE (for SRM operation mode) and then charging of the car battery (for SRG operation mode) at different speeds of the ICE.

The dynamic simulation results prove that three-phase 6/8 SR machine with proper SRM/G control is suitable for automotive ISA applications.

3.7. Conclusions

The optimization progressively becomes an important feature when designing an electrical machine. Even though until now the design of the electrical machine was based on the engineer experience accumulated over the years, this design could not guaranty that their solution was the best one for the specific application. If correctly used the optimization can conduct to a design that satisfies the requirements, but not only, the obtained design can be optimal in a certain sense depending on the application for which the machine was build.

The third chapter of this thesis is dedicated to the optimization process of a three-phase six stator and eight rotor teeth SR machine. In the first part of this chapter the general aspects of the optimization is presented together with the comparison between a minimum local and a minimum global.

Because of the fact that when designing an electrical machine a lot of aspects should be considered and due to the fact that the optimization problem increases and becomes “heavy” to be computed, sometimes one optimization process requires a big amount of time to be finished.

This thesis aims to present step by step, to compare and validate two techniques of reducing the optimization computation time. The two techniques presented in this chapter are output space mapping proportional and manifold mapping, the theoretical approach of these techniques is provided in this chapter, but not only, a test is realized in terms of a mathematical function to verify when the models have a smooth convergence and when the models cannot converge. Besides is possible to draw a general idea of the required tendency of the fast model respect to the accurate one (for the techniques to have a smoot convergence the tendency of the models should be the same) in order to derive the fast model from the accurate one so that the coarse model to have the same tendency as the fine one.

Having knowledge about the requirements of the both techniques to work it is possible to gradually increase the optimization problem. But before that a proper selection of the models is required, therefore in the second part of this chapter a detailed selection process of the fine accurate model and the deduction of the fast coarse model is described. In the first instance the both techniques are used to define the best control of a SR machine prototype. A comparison in terms of best inputs and outputs calculated with these techniques is also provided and discussed in this chapter, following that these results to be FEM and experimentally validated in the fourth chapter. Further on this optimization problem is increased, besides control, size parameters are added. Likewise a comparison of the models is again provided.

Finally, steady-state and dynamic simulations have been performed for the optimally-designed three-phase 6/8 SR machine functioning in SR motor and generator mode, as part of automotive ISA operation cycle.

Selected references

- [1] Kiranyaz S. Ince T. Gabbouj M., *Multidimensional particle swarm optimization for machine learning and pattern recognition.*: Springer, 2014.
- [2] Wikipedia. [Online]. https://en.wikipedia.org/wiki/Mathematical_optimization
- [3] Matlab. [Online]. <https://www.mathworks.com>
- [4] Ilea D. Radulescu M. M., Gillon F. Brochet P., "Multi-objective optimization of a switched reluctance motor for light electric traction applications," in *IEEE Vehicle Power and Propulsion Conference*, 2010.
- [5] Lei G. Wang T., Zhu J., Guo Y. Wang S., "System-Level Design Optimization Method for Electrical Drive Systems—Robust Approach," *IEEE Transactions on Industrial Electronics*, vol. 62, pp. 4702-4713, 2015.
- [6] Stipetić S. Miebach W. Žarko D., "Optimization in design of electric machines: Methodology and workflow," in *ACEMP-OPTIM-ELECTROMOTION*, 2015.
- [7] Bandler J. W. Biernacki R. M., Chen S. H., Grobelny P. A. Hemmers R. H., "Space mapping technique for electromagnetic optimization," *IEEE Transactions on Microwave Theory and Techniques*, vol. 42(12), pp. 2536-2544, 1994.
- [8] Bandler J. W. Cheng Q. S., Dakrouy S. A., Mohamed A. S., Bakr M. H., Madsen K. Sondergaard J., "Space Mapping: The State of the Art," *IEEE Transactions on Microwave theory and techniques*, vol. 52(1), pp. 337-361, 2004.
- [9] Khlissa R., *Contribution à la définition des méthodes d'optimisation rapides et économiques pour le dimensionnement d'actionneurs électriques*, Doctoral dissertation, Compiègne ed., 2015.
- [10] Rayas-Sánchez J. E. Vargas-Chávez N., "A linear regression inverse space mapping algorithm for EM-based design optimization of microwave circuits," *Microwave Symposium Digest (MTT), IEEE MTT-S International*, pp. 1-4, 2011.
- [11] Cheng Q. S. Bandler J. W., "An implicit space mapping technique for component modeling," in *European Microwave Conference*, 2006, pp. 458-461.

- [12] Khliissa R. Vivier S., Vargas L. O. Friedric G., "Application of output space mapping method for fast optimization using multi-physical modeling," in *IEEE Energy Conversion Congress and Exposition*, 2012, pp. 1306-1313.
- [13] Wikipedia. Jacobian matrix and determinant. [Online]. https://en.wikipedia.org/wiki/Jacobian_matrix_and_determinant
- [14] S. Vivier D. Lemoine G. Friedrich, "Fast Optimization of an IPMSM with Space Mapping Technique," in *978-1-4577-0541-0/11/IEEE*, 2011.
- [15] Echeverria D. Lahaye D., Encica L. Lomonova E., "Manifold-mapping optimization applied to linear actuator design," *IEEE transactions on magnetics*, vol. 42(4), pp. 1183-1186, 2006.
- [16] Echeverría D. Hemker P. W., "Manifold mapping: a two-level optimization technique," *Computing and Visualization in Science*, vol. 11(4-6), pp. 193-206, 2008.
- [17] **Zaharia M. V.** Laczko A. A., Pop A. A. Radulescu M.M, "Optimal commutation angles of a switched reluctance motor/generator.," *Ecological Vehicles and Renewable Energies (EVER)*, pp. 1-8, 2015.
- [18] **M. V. ZAHARIA** F. GILLON M.M. RADULESCU, "Fast determination of the optimal control parameters of a switched reluctance machine using space mapping technique," *Optimization and inverse problems in electromagnetism*, 2016.
- [19] Ilea Dan, *Conception optimale des moteurs à réluctance variable à commutation électronique pour la.*: Doctoral dissertation, Ecole Centrale de Lille; Technical University of Cluj-Napoca, 2013.
- [20] Agnarsson J. Sunde M. Ermilova I., "Parallel optimization in matlab," Project to Computational Science: Report. 2013.
- [21] F. Gillon, "Méthodologies de conception optimale des composants electromagnétiques ," Université des Sciences et Technologie de Lille-Lille I, Lille, L'Habilitation à diriger des Recherches 2009.
- [22] Ugray Z. Lasdon L., Plummer J., Glover F. Marti R., "Scatter search and local NLP solvers: A multistart framework for global optimization," *INFORMS Journal on Computing*, vol. 19(3), pp. 328-340, 2007.
- [23] **M.V. Zaharia** F. Gillon M.M. Radulescu, "Design optimization of a switched reluctance machine-based integrated starter/alternator for automotive applications," in *21th International conference on electrical machines*, Lausanne-Switzerland, 2016.

Chapter 4

Experimental study and control of a three-phase 6/8 SR machine

4.1. Introduction

This thesis deals with the optimization of a three-phase 6 stator and 8 rotor teeth SR machine. The optimization is performed to define the best commutation angles and reference current for this machine in order to have the maximum of mean electromagnetic torque with the minimum of torque oscillations. But in order to see the accuracy of the results, FE and experimentally validations of the obtained results after the optimization process is mandatory. This chapter presents in detailed mode the experimental test bench together with the control applied to the SR machine prototype used to partially validate the commutation angles obtained after the optimization.

4.2. Experimental test bench

Validation of the three-phase 6/8 SR machine [1] optimization results by FE simulations and experimental tests is mandatory. This chapter presents in detail the experimental test bench together with the control applied to the studied SR machine prototype.

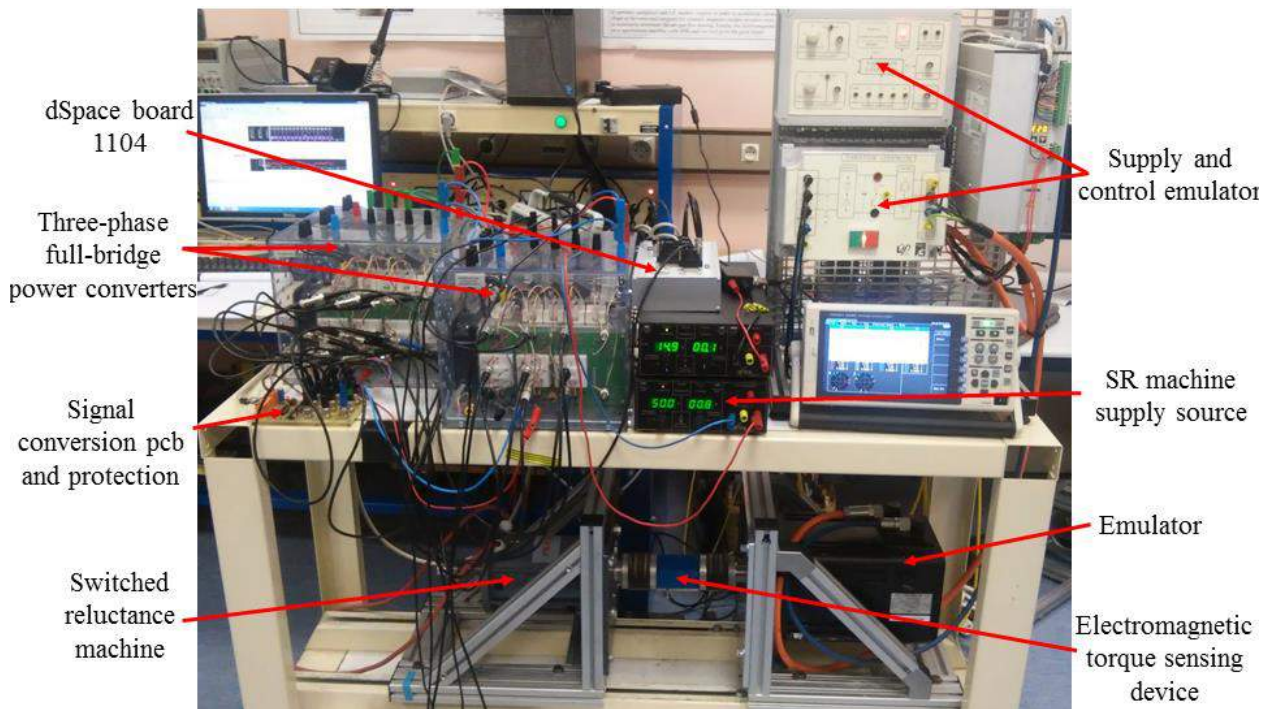


Fig.4.1 Experimental test bench

The laboratory set-up on which the experimental tests were carried out is presented in fig.4.1. It is composed of the power electronic converters used to supply the SR machine, the DC voltage source, the dSPACE board 1104 for real-time simulations and the electromagnetic torque sensing device. A more detailed description of hardware and software components of the experimental test bench is presented in the next sections.

4.2.1. Hardware components

In this part a description for each of the components used for the experimental test is presented.

4.2.1.1. Three-phase half-bridge inverter

For the SR machine the supply modality are discussed in chapter 2 of this thesis. Because in the simulations the supply is realized through a three-phase half-bridge inverter, for the tests the same supply has to be done to be able to compare the simulation results with those experimentally obtained. However, in the laboratory this type of inverter was not available, instead the three-phase full-bridge type inverter was accessible. This type consists of a three-phase diode rectifier plus inverter with brake chopper Semikron Semiteach –IGBT, having the representation from fig.4.2. The entire Semikron equipment includes the rectifier, the three-phase inverter bridge and the arm used for regenerative braking. From the datasheet of this inverter (*Appendix 4.A*), it results that its rated current strength is 30A for a voltage of 440V.

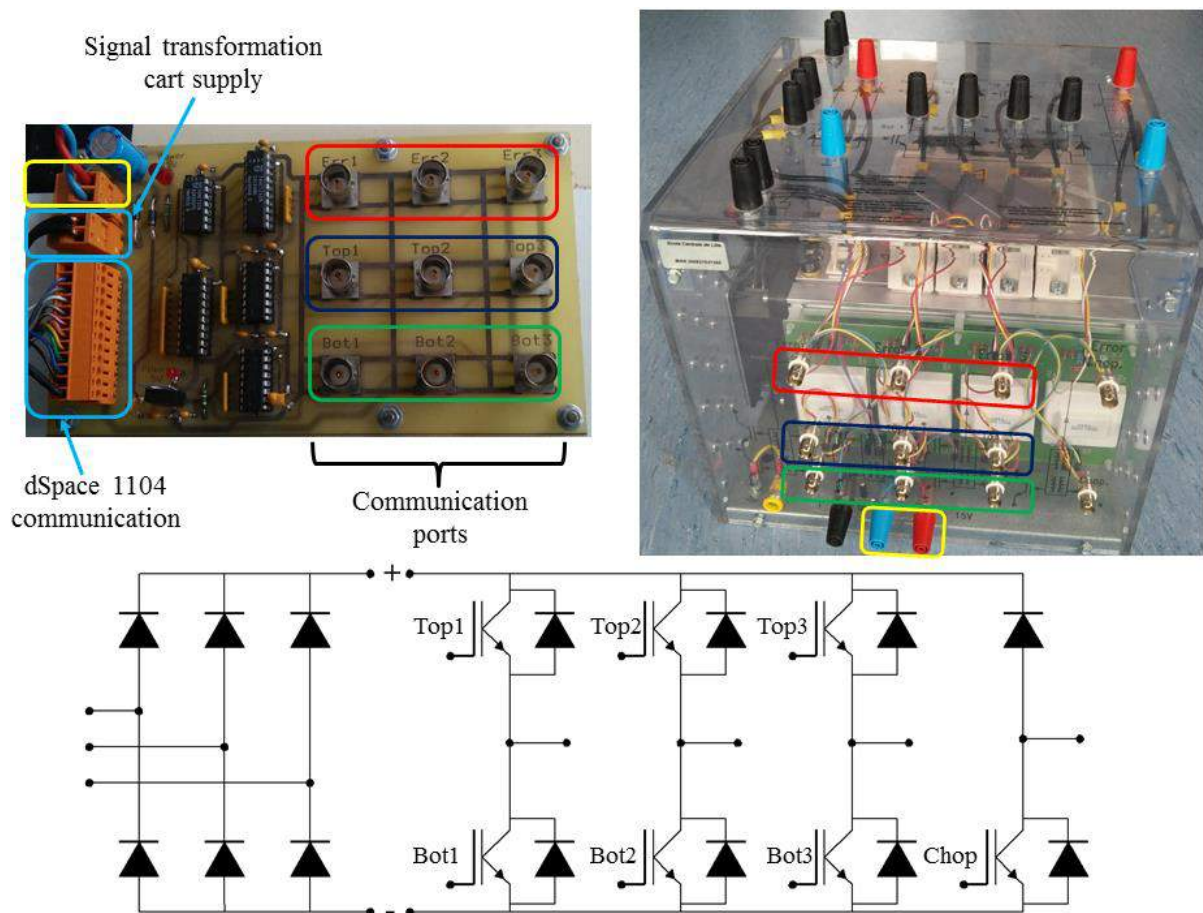


Fig.4.2 Three-phase rectifier and inverter assembly with braking chopper Semikron Semiteach –IGBT and signal transformation cart

Fig.4.2 shows the signal transformation cart, the Semikron inverter and its schematic representation. The accessibility of the six switches is possible through six BNC ports that are

interconnected with the signal transformation and protection cart. Other three BNC ports are used to recover the signal error given by the converter.

The control signals of the inverter are implemented in the range $0 \div 15\text{V}$. The cart used for the transformation of the signals from the range $0 \div 5\text{V}$ to $0 \div 15\text{V}$, represented in fig.4.2 (upper left), has also short-circuit protection and achieves the link between the Semikron and the dSPACE board.

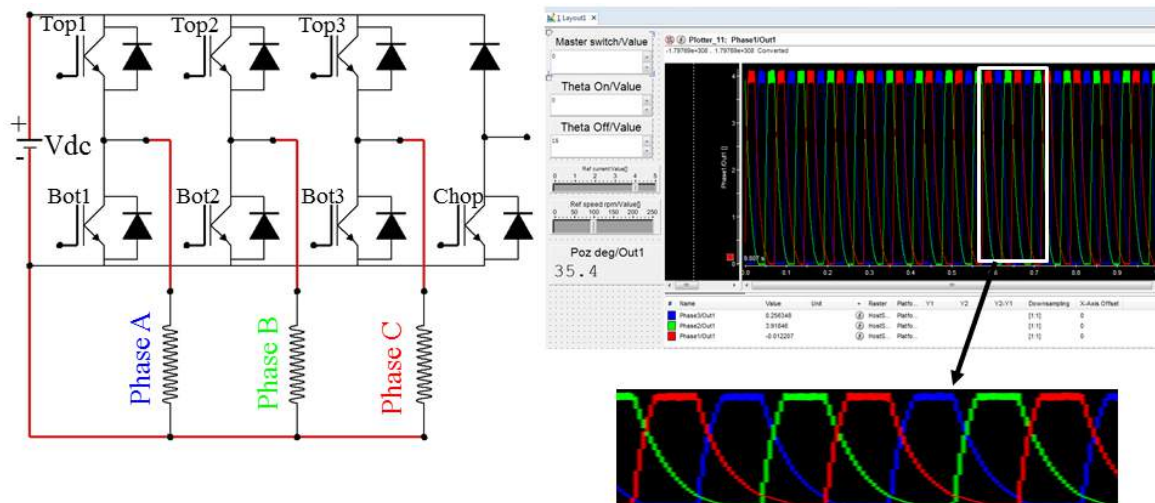


Fig.4.3 Three-phase full-bridge inverter and control desk SR machine waveforms

For the first case, the voltage supply shown in fig.4.3 is done through a Semikron inverter. A DC source is used to feed the machine with constant voltage and each of the three phases is powered for a specific amount of time. To avoid damaging the inverter, if the top IGBT is “ON”, automatically the bottom one will be “OFF”. Therefore, based on the measurements visualized through the ControlDesk interface and depicted in fig.4.3, it is obvious that when the supply of phase A is cut-off the current in that phase has a slow decrease through the diodes. The task to decrease this current in a much faster way is done by injecting negative voltage into phase A when the supply of this specific phase is off. This negative supply ends when the current in the phase is null.

As mentioned before, because a three-phase half-bridge inverter was not available when the tests were performed, two inverters of three-phase full-bridge type were used to act like a half-bridge one. Fig.4.4 represents the phase connections of the SR machine with the two Semikron inverters, together with the phase current evolution read from ControlDesk. The connection of phase A is realized as follows: top1 of the signal conversion cart (fig.4.2, upper left) is connected to top1 of the first inverter and with bottom4 of the second inverter (fig. 4.4) and bottom1 of the cart is connected with bottom1 of the first inverter and top4 of the second inverter. The same principle is used for phase B and phase C as well.

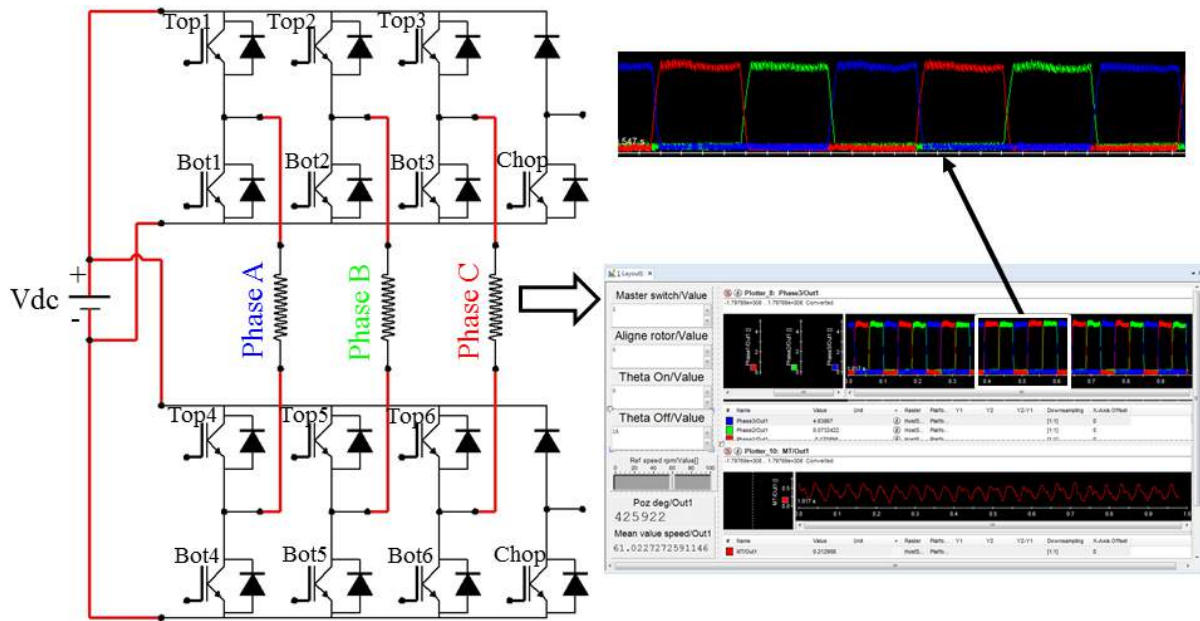


Fig.4.4 Three-phase half-bridge inverter and SR machine waveforms visualized using ControlDesk interface

As specified above, not to damage the inverters when the top IGBTs are “ON” the bottom ones are in opposite state, i.e. “OFF”. On this basis, when controlling the SR machine by considering the conduction of phase A, the top1 IGBTs from the first inverter and bottom4 from the second one are open to current passing and bottom1 and top4 are closed. It is clear that the decrease of current in the phase is faster than in previous case, therefore it is possible to affirm that if necessary two full-bridges can act like a conventional SR machine inverter, if connected as shown in fig. 4.4.

4.2.1.2. Testing equipment dSpace 1104

The controller board dSpace 1104 realizes the interface between the program created to control the SR machine and the motor-inverter assembly. The dSpace cart, compatible with the Simulink block diagrams, uses the real-time interface (RTI) and the software ControlDesk. The library RTI contains real time communication blocks.

This cart receives signals from the speed and position transducer, interprets these signals and sends impulses to the inverter based on the readings. From the inverter the three errors can be read by the dSpace and further can be used as a protection when the control program is realized.

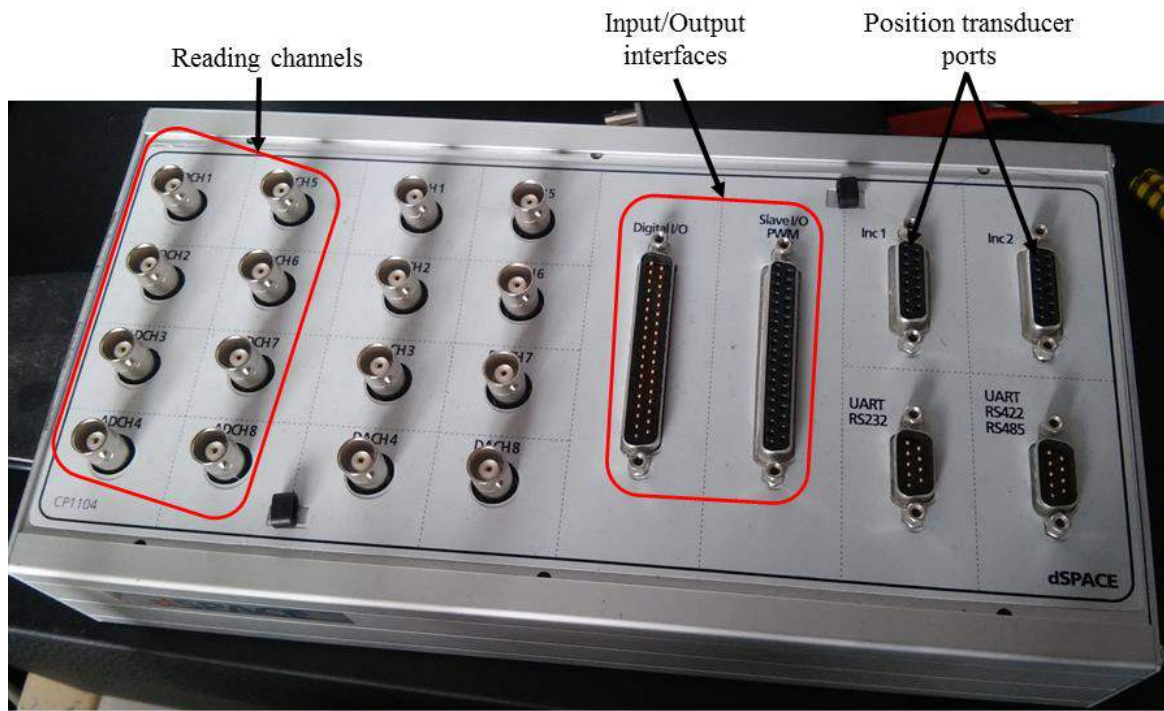


Fig.4.5 Controller board dSpace 1104

Fig. 4.5 represents the view of the controller board dSpace 1104 used when conducting the tests on SR machine in both motor and generator operation modes. The BNC connectors “ADCH” are used for current and electromagnetic torque readings and to port “Inc” is connected the speed transducer.

4.2.1.3. Auxiliary equipment

In order to perform the tests on the bench some auxiliary equipment is needed. The additional equipment used when testing the SR machine is listed below:

- Position sensor type BaumerIVO GI321 which has a maximum resolution of 1024 per turn (*Appendix 4.A*). This encoder provides signals of type transistor-transistor logic (TTL) and it is used to give the SR machine rotor position and speed.
- The torque transducer is a rotating torque sensor with non-contact transmission, being supplied as an active sensor with integrating measuring amplifiers. The measured data is transmitted maintenance-free and without signals distortion between stator and rotor. *Appendix 4.C* provides the datasheet for this component.
- Digital oscilloscope Tektronix DPO2014 with five acquiring channels is used to real-time visualize the shaft electromagnetic torque. Thanks to the USB output

it is possible to save the visualized data on an external USB key. A detailed user manual of this oscilloscope can be found in [2].

- Supply sources
- Computer with MATLAB/Simulink software installed, containing RTI library and real time software ControlDesk.
- A permanent-magnet synchronous machine used to emulate the primary mover for SR machine working in generator operation mode

All the auxiliary equipment are presented in fig. 4.6.

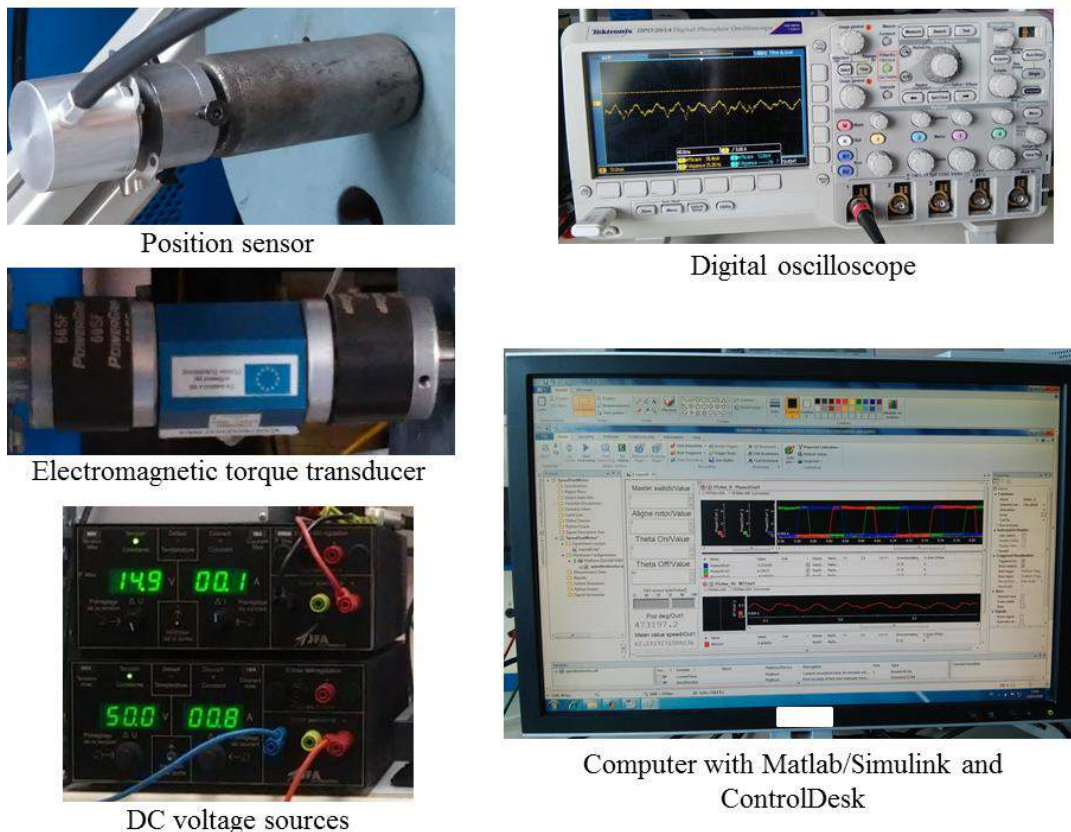


Fig.4.6 Auxiliary equipment

4.2.2. Software components

For the command strategy of the SR machine functioning in motor and generator operation modes the Simulink toolbox from Matlab software is used. Through the dSpace 1104 board the control of the SR machine is achieved. The real time interface software has all the necessary blocks to link the created control software with the dSpace board. In order to see in real time the evolution of the SR machine output quantities the ControlDesk software is used.

The required data from the machine (torque, speed, rotor position, etc.) are provided always through the dSpace board.

4.2.2.1. *Real-time control software*

The software used to command the SR machine is realized in Matlab/Simulink environment. The general structure of the program can be found in fig. 4.7. The simulation step is fixed and is set to $T_s = 10^{-4}$ s and the name of the solver used is Runge-Kutta.

An overall description of the control presented in fig. 4.7 is pointed in the following lines, but a more detailed description of each component can be found in the next section. When master switch is “1” the entire program is active and when is “0” the control program is unavailable and the PWM is deactivated. The “Machine Current and Torque” blocks provide information on the phase current and electromagnetic torque, read directly from the machine. The “Rotor position reset” block performs the reset of the rotor position after the rotor alignment is accomplished. The blocks “Motor run” and “Generator run” contain the PI speed/torque controls together with the current control and the commutation sequence.

The command program from fig. 4.7 realizes the automatically pass between motor and generator modes. This is possible thanks to the switch “Motor to Generator”. The principle is that when the switch notices that the machine speed is below 60 rpm the “Motor run” block is active and when the speed increases above 60 rpm the “Generator run” block becomes active. The above speed of 60 rpm is a low speed because the prototype used is of low power, the voltage used to supply the machine is $V_{dc} = 50V$ and the load of the emulator together with the stress given by the machines coupling reach the maximum load that can be achieved by this prototype for this supply and for 5.3A current in the phase.

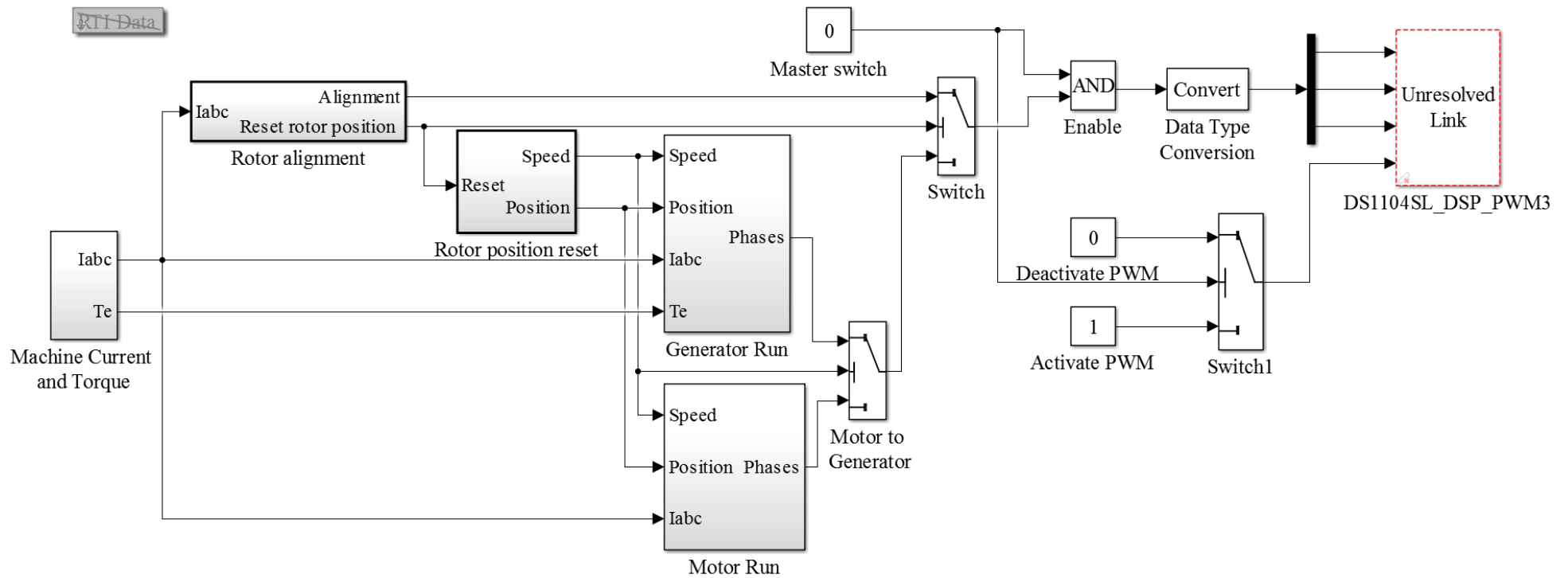


Fig.4.7 Block diagram of the software implemented in MATLAB/Simulink environment for controlling the SR machine in motor and generator operation modes

With the help of the BNC connectors ADCH from the dSpace cart it is possible to read directly from the machine the phase currents through the ports 5, 6 and 7 and the electromagnetic torque, the eighth port. Fig. 4.8 represents in more detailed mode the data acquisition and the principle of aligning the rotor and the stator teeth.

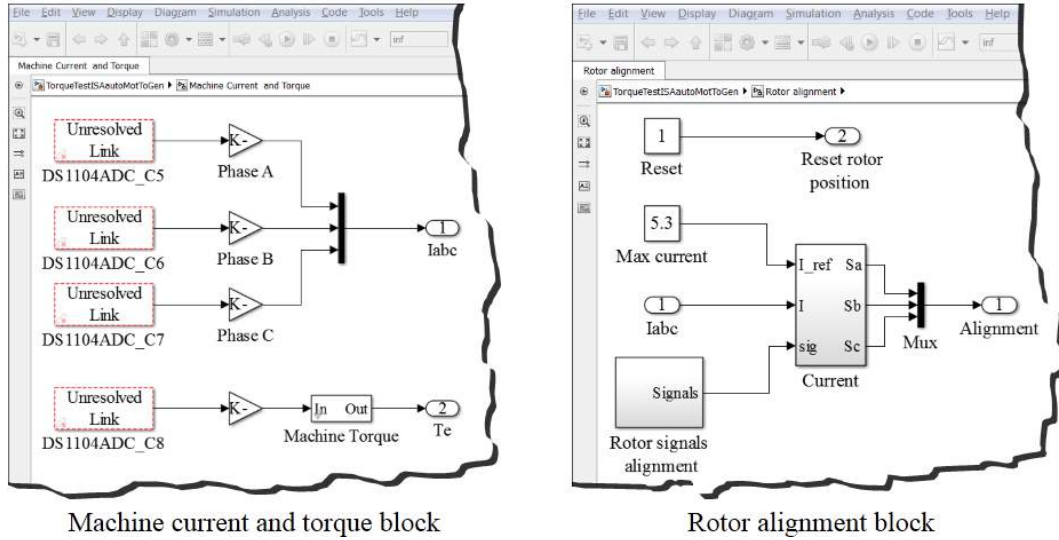


Fig.4.8 Detailed view of the “Machine current and torque” block and “Rotor alignment” block

From the “Rotor alignment” block when the “Reset” is 1 phase C is supplied with a maximum of current 5.3A and the rotor is aligned with this phase. For all this period only the alignment command is active. After the rotor is aligned this rotor displacement, detected by the position sensor must be cancelled in order for the program to start from the new rotor position and to consider 0 degrees of rotor motion. Therefore, for this operation the “Rotor position reset” block intervenes (fig. 4.9).

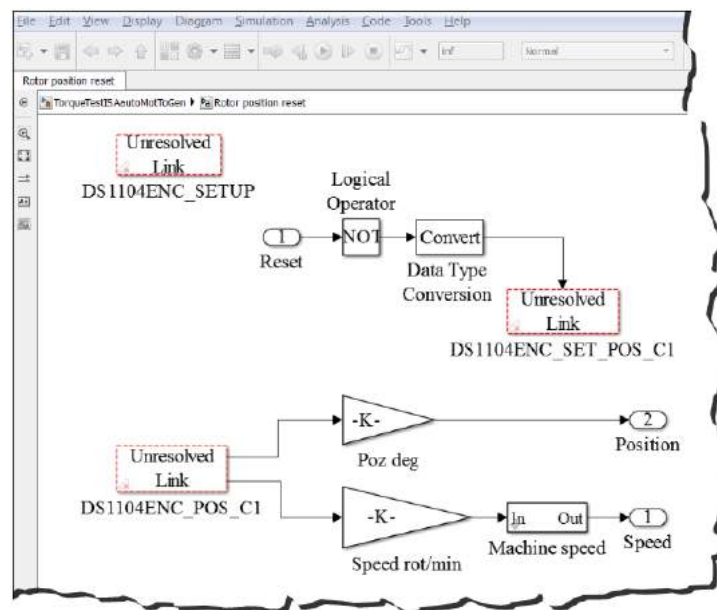


Fig.4.9 Detailed view of the “Rotor position reset” block

When the “Reset” from the aligned rotor position becomes 0 the rotor position is reset and that position is considered the starting point, following that the control program to start the imposed switching sequence.

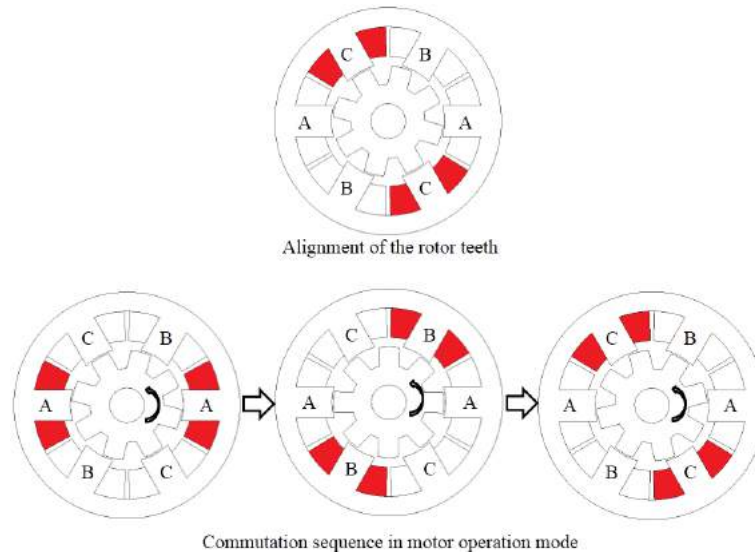


Fig.4.10 Alignment of the rotor teeth and commutation sequence in motor operation mode of the studied SR machine

Fig. 4.10 synthesizes the alignment operation as well as the commutation sequence. It is possible to explain the above figure as follows: when the rotor completes the aligned process and the motion is kept the one presented in fig. 4.10, at first, phase A is supplied until the rotor is aligned with the excited phase, i.e. from 0° to 15° mechanical degrees, followed by the phase B from 15° to 30° and phase C from 30° to 45° . All these rotor positions are calculated with eq. 2.113 from chapter 2. The motion continuity is linked to a continuum excitation sequence.

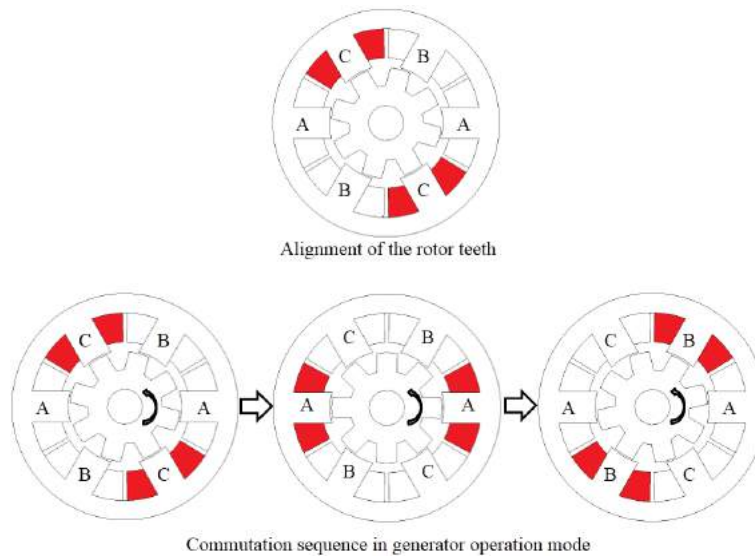


Fig.4.11 Alignment of the rotor teeth and commutation sequence in generator operation mode of the studied SR machine

For the generator operation mode the main idea of the machine to be able to realize the energy conversion from mechanical to electrical is to excite the phase in the moment in which the rotor is perfectly aligned with the stator excited one. Fig. 4.11 exemplifies the aligned rotor position and the commutation sequence of the generator operation mode. For this operation from 0° to 15° mechanical degrees phase C is excited, followed by phase A from 15° to 30° and phase B from 30° to 45° , when the motion direction is kept the one from fig. 4.11.

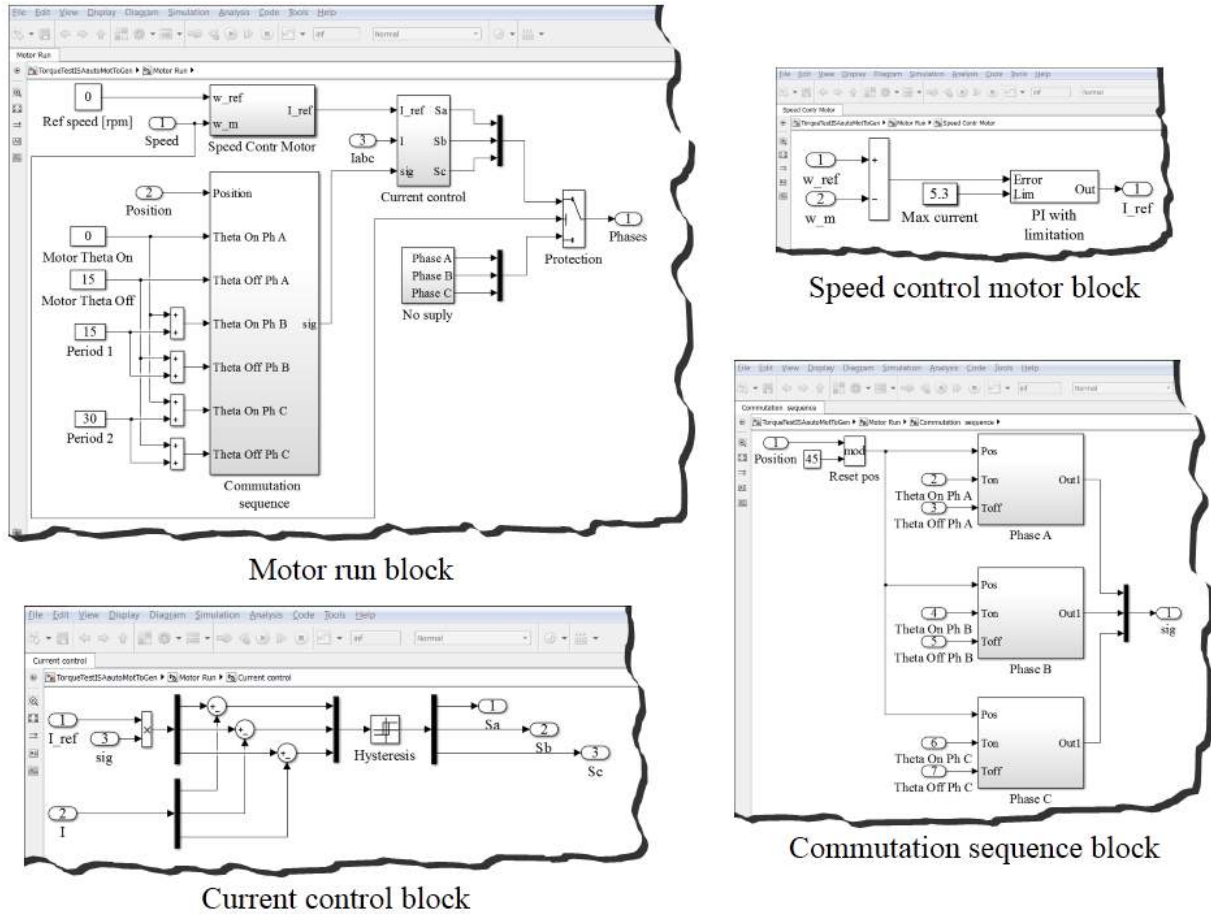


Fig.4.12 Detailed view of the “Motor run” block and its containing blocks

Fig. 4.12 exemplifies a detailed view of the “Motor run” block with all of its containing blocks. In this part a PI speed control is implemented, which is used to provide the reference current. A limitation of the PI is realized in order not to have an increased current that can damage the phase. A current control by hysteresis is also implemented in this part together with the commutation sequence.

The “No supply” block is used to cut-off the supply if the machine is starting to rotate in the opposite direction of the imposed rotation. This is used as a caution measure not to have uncontrollable speeds in the machine. Therefore, if the machine starts to rotate contrary whit a speed greater than 5 rpm the phase supply is interrupted.

The implementation of the phase excitation in generator operation mode is detailed in fig. 4.13. For this part a PI torque control is realized and as in the motor case a current limitation is implemented not to damage the phase. Current control by hysteresis is also performed for this operation mode together with the commutation sequence.

As in motor case the “No supply” block exists in this case as well, because if the rotation of the machine is in opposite direction respect to the imposed one the excitation sequence will not be good as it will not supply the phase when the rotor is perfectly aligned with the stator one.

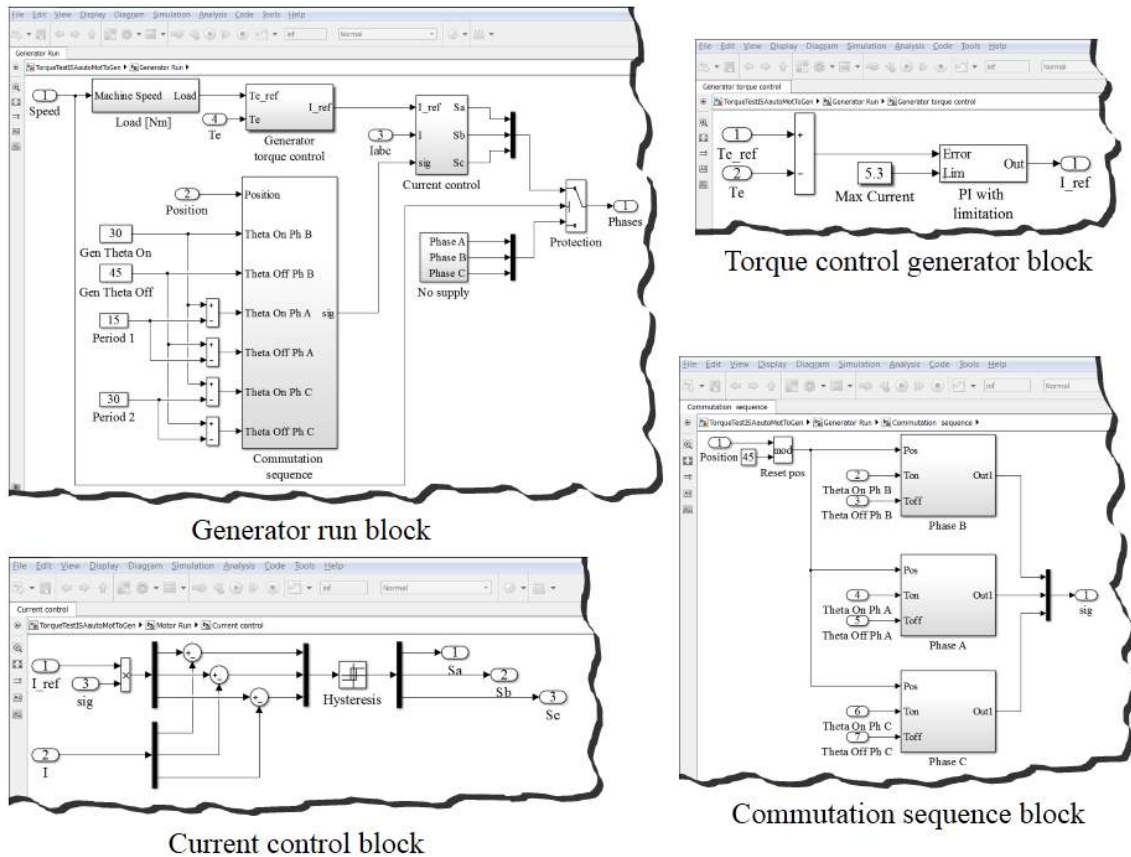


Fig.4.13 Detailed view of the “Generator run” block and its containing blocks

4.2.2.2. Real-time software

The real time software used is called ControlDesk. The real time interface is built here based on the desired variable inputs and on the outputs that are visualized. During the experiments thanks to this software it is possible to interact with the machine and also to establish a communication between the dSpace board and ControlDesk.

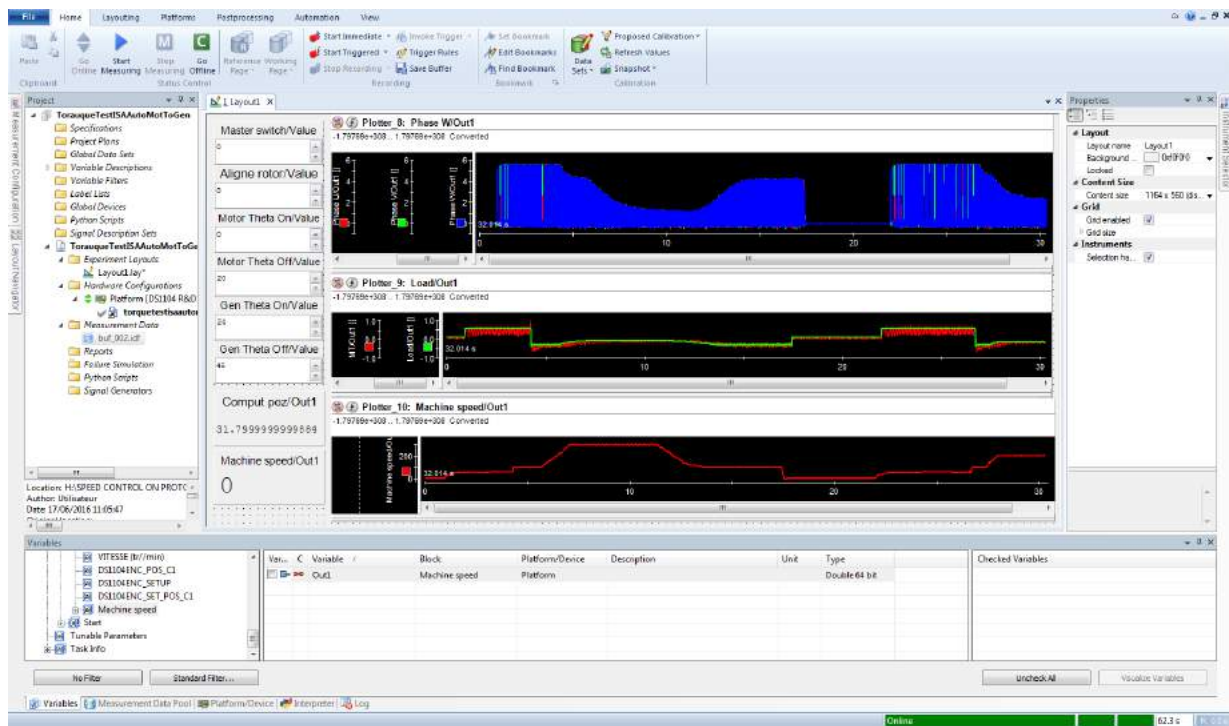


Fig.4.14 View of the ControlDesk interface

Fig. 4.13 shows the ControlDesk program used for controlling in motor and generator operation modes the SR machine. When master switch is active the entire system is active. When realizing the experimental test the first step is to align the rotor, therefore the align rotor is set to 1. Next the master switch is activated and one phase is supplied, during which period the rotor is aligned with the stator excited phase. After that the computed rotor angle appears in the computation position display. Thereafter the master switch is deactivate and the aligned rotor is set to 0 and when this command is performed the position is reset back to 0° , meaning that in the computation position display will appear 0. After this alignment process is completed if the master switch is activated the machine is starting to rotate in the imposed direction (fig. 4.10 for the motor operation mode).

Numerical inputs are used for the computation angles i.e. motor theta on, motor theta off, generator theta on and generator theta off. The imposed values are in degrees and symbolize the moment when the excitation should be applied to the phase (theta on) and the moment when this excitation should be cut-off (theta off).

For visualizing the data the software has incorporated displays that give the instant value at each time and plotters that exemplify the time evolution of the visualized data. For the tests, the phase current, electromagnetic torque along with the reference torque and speed are plotted and the rotor position is displayed.

4.3. Steady-state tests for motor and generator operation modes of the studied SR machine and dynamic tests for a part of ISA driving cycle

4.3.1. Phase inductance measurement

Due to the double salient configuration of this machine, the phase inductance varies as function of rotor position. Hence, when the rotor tooth is perfectly aligned with the stator one the inductance has the maximum value, and when the poles are perfectly unaligned the inductance is at its minimum value. Not only the rotor position gives a variation of the inductance, phase current also allows inductance variation.

The measurements of the inductance on the SR machine prototype is realized by applying a sinusoidal supply on one phase. During this supply the rotor is blocked first in the aligned position and afterwards in unaligned position. The supply is realized from an autotransformer and the frequency is 50Hz. The voltage and current are read following that the inductance to be computed with the help of eq. 4.1.

$$L_{eff} = \frac{1}{2\pi f} \sqrt{\left(\frac{U}{I}\right)^2 - R^2} \quad (4.1)$$

The measurements are performed for different phase current strengths and for the aligned and unaligned rotor position. The phase resistance is measured $R = 3.5\Omega$. Fig. 4.15 shows the evolution of the phase inductance for different values of phase current and for three distinct computation modalities i.e. FE computed, analytically calculated and measured on the prototype.

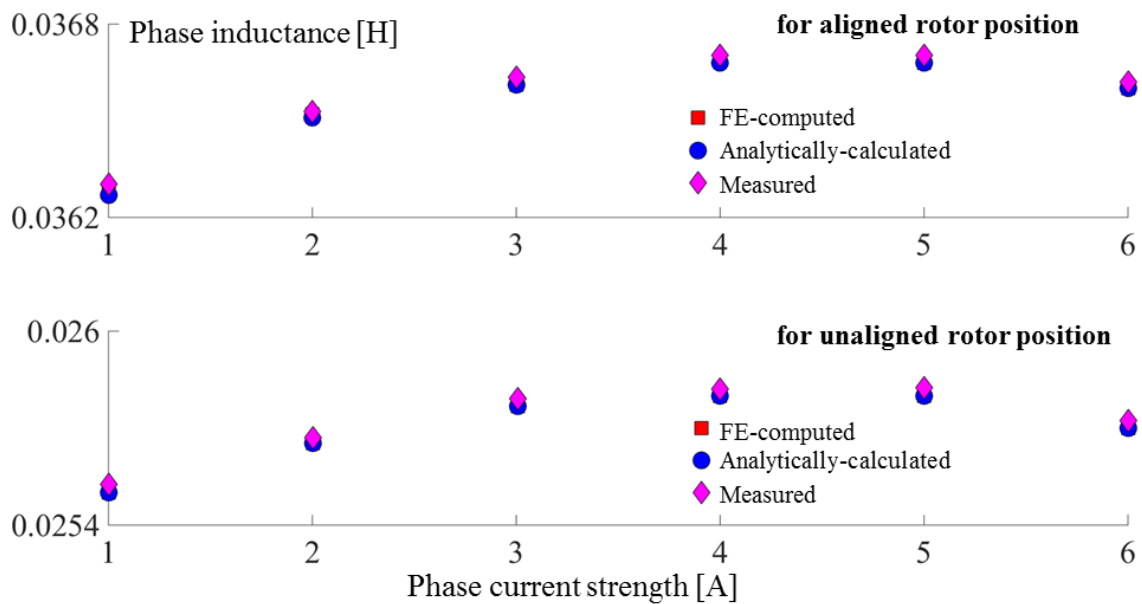


Fig.4.15 Comparative FE-computed, analytically-calculated and measured maximum and minimum values of the stator-phase self-inductance of the three-phase 6/8 SR machine.

4.3.2. Commutation angles validation for motor operation mode

In the third chapter an optimization was performed using OSMP and MM, in order to determinate the best commutation angles that lead to the maximization of the mean electromagnetic torque with the condition that the ripple torque not to exceed an imposed value. In this part simulations are carried out to validate the obtained commutation angles by means of FE computation, analytically calculated and measurements on the existing prototype.

For the finite element validation the geometry of the studied machine was implemented in JMAG Designer software and hysteresis current regulation was employed. The supply voltage in all cases was set to $V_{dc} = 50V$ and the rotor was engaged in motion at constant speed of 60 rpm.

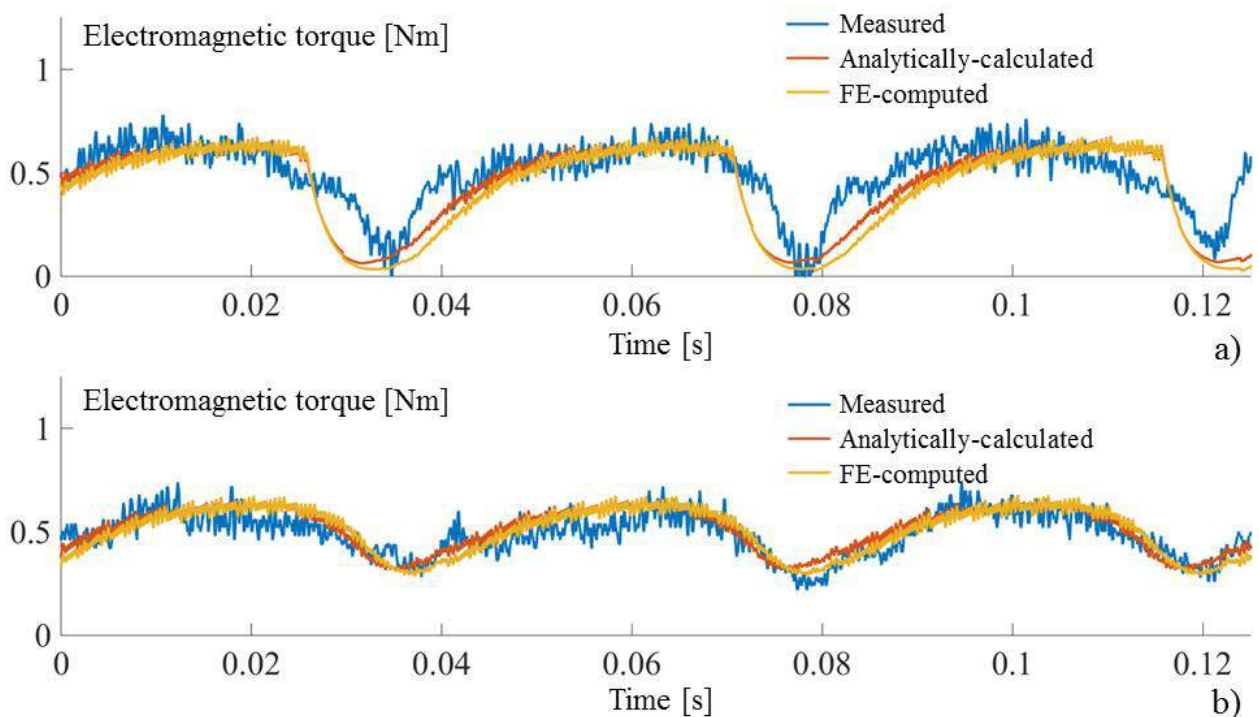


Fig.4.16 Electromagnetic torque computed by simulations and measured on the prototype; a) theoretical parameters, b) optimal found parameters for motor operation mode

When measurements were performed on the prototype a current control by hysteresis was implemented as well as a PI speed control. The load of the machine was given by the cogging torque of the emulator and the friction resulted due to the coupling between the motors. The evolution of the electromagnetic torque was visualized on the above presented oscilloscope and the data could be saved on an external flash drive. Fig. 4.16 shows the evolution of the electromagnetic torque measured on the prototype, computed by means of FE computation and analytically calculated. In fig. 4.16a for the commutation angles was used the theoretical angles i.e. $\theta_{on} = 0^\circ$ and $\theta_{off} = 15^\circ$, however in fig. 4.16b the commutation angles used are the ones obtained after the optimization process is completed ($\theta_{on} = 0^\circ$ and $\theta_{off} = 20^\circ$). From the figure it is noticeable a reduction of the torque oscillations, therefore if a mean value of the

electromagnetic torque evolution is realized and a calculation of the ripple torque is performed for both sets of commutation angles one can obtain the results presented in table 4.1.

Table 4.1 Measurement, FE computed and analytically calculated electromagnetic torque comparison function of two sets of commutation angles

Commutation angles	Measured	FEM computed	Analytically calculated
$\theta_{on} = 0^\circ$	$\langle T_e \rangle = 0.46$	$\langle T_e \rangle = 0.39$	$\langle T_e \rangle = 0.36$
$\theta_{off} = 15^\circ$	$T_{rip} = 0.64$	$T_{rip} = 0.64$	$T_{rip} = 0.64$
$\theta_{on} = 0^\circ$	$\langle T_e \rangle = 0.5$	$\langle T_e \rangle = 0.5$	$\langle T_e \rangle = 0.49$
$\theta_{off} = 20^\circ$	$T_{rip} = 0.37$	$T_{rip} = 0.34$	$T_{rip} = 0.35$

When computing the torque oscillation eq. 4.2 was used.

$$T_{rip} = T_{\max} - T_{\min} \quad (4.2)$$

4.3.3. Steady-state tests under motor and generator operation mode

4.3.3.1. Motor operation mode

For the next set of tests the motor operation mode was targeted. When tests were performed PI speed control was realized together with hysteresis current control and the reference speed was set to 60rpm.

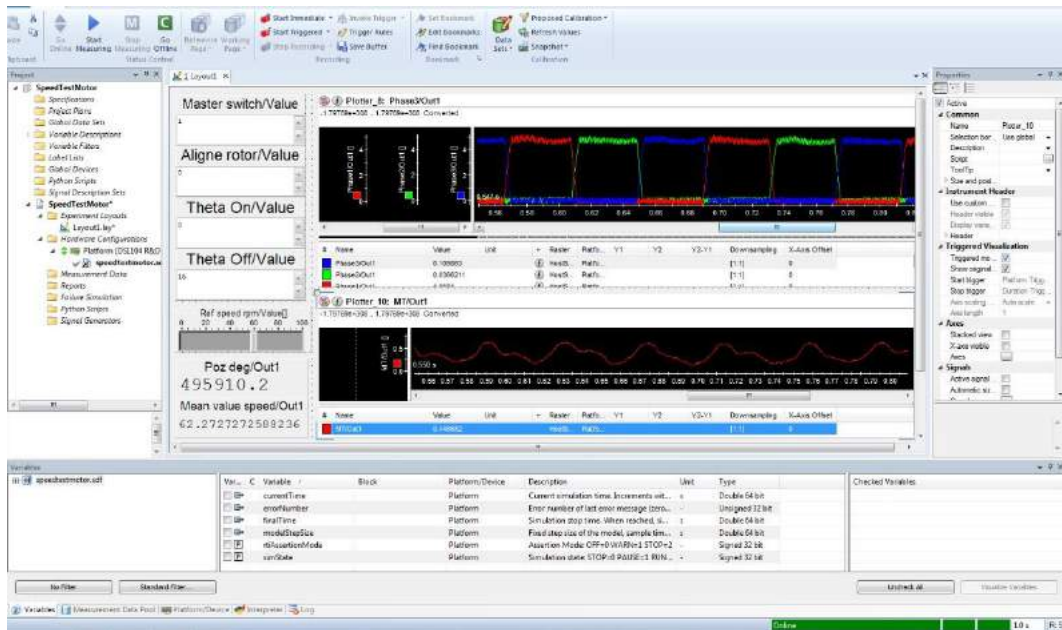


Fig.4.17 ControlDesk interface of the phase current and machine torque for $\theta_{on} = 0^\circ$ and $\theta_{off} = 15^\circ$

Figs. 4.17 and 4.18 represent the evolution of the current in the phase for the case in which theta off is 15° respectively 20° . As it can be remarked from fig. 4.18 when theta off is 20° a prolongation of the excitation period and an overlap of the phase currents is noticeable. On this superpose of the phase currents it is based the limitation of the torque ripples, because the

electromagnetic torque does not have time to decrease due to the decrease of the current in the phase, thanks to the excitation of the second phase in that same time.

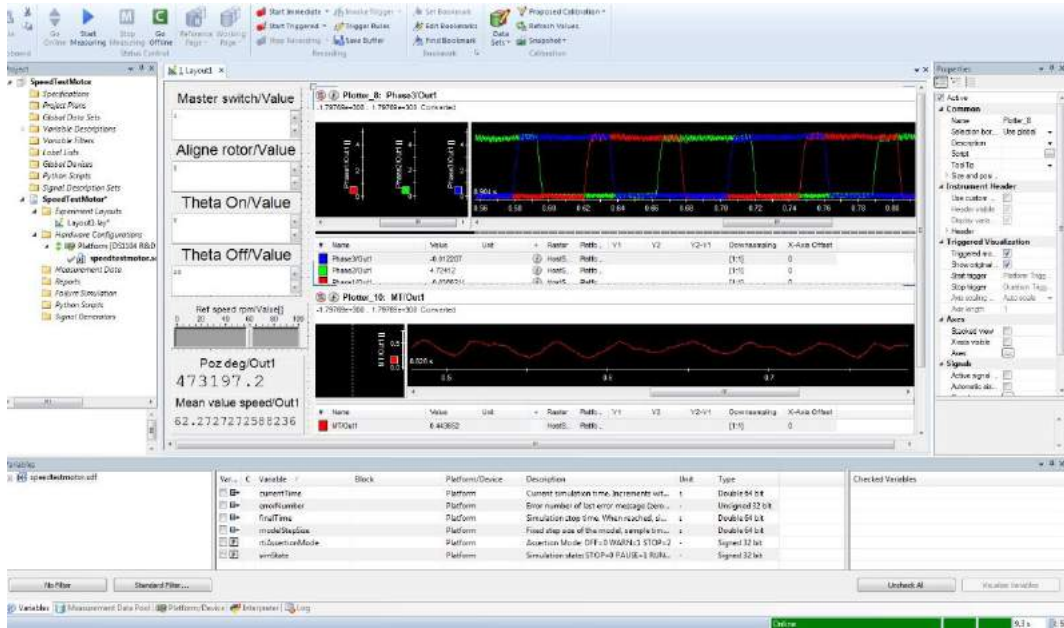


Fig.4.18 ControlDesk interface of the phase current and machine torque for $\theta_{on} = 0^\circ$ and $\theta_{off} = 20^\circ$

4.3.3.2. Generator operation mode

In the generator operation mode the SR machine is engaged in motion by a permanent magnet synchronous machine. The excitation is realized on the negative slope of the inductance in order for the machine to function in generator mode.

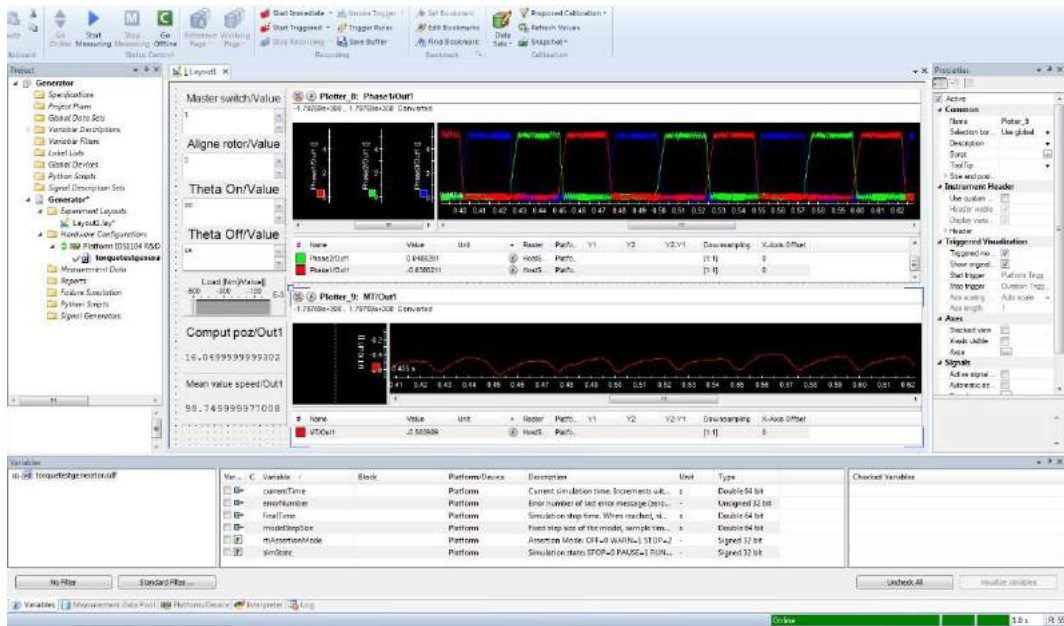


Fig.4.19 ControlDesk interface of the phase current and machine torque for $\theta_{on} = 30^\circ$ and $\theta_{off} = 45^\circ$

When tests were performed the rotor was engaged in motion from an external source at a constant speed of 100 rpm. A PI torque control was implemented and the reference torque was provided as a variable input. Likewise a hysteresis current control was also realized for these tests.

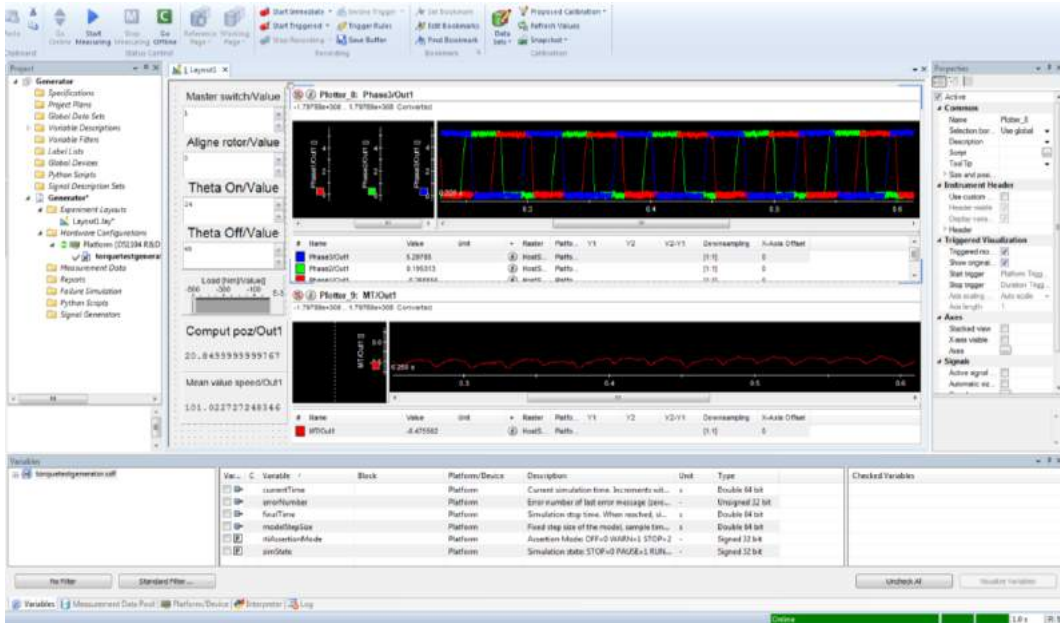


Fig.4.20 ControlDesk interface of the phase current and machine torque for $\theta_{on} = 24^\circ$ and $\theta_{off} = 45^\circ$

In fig. 4.19 and 4.20 the reference load torque is set to $T_l = -0.5\text{Nm}$ and two sets of commutation angles are used $\theta_{on} = 30^\circ$ and $\theta_{off} = 45^\circ$ respectively $\theta_{on} = 24^\circ$ and $\theta_{off} = 45^\circ$. As in motor operation mode the second set of angles cause a phase current overlap as pointed in fig. 4.20. The electromagnetic torque in the phase is negative by convention, due to the fact that the machine functions in generator mode.

4.3.4. SR machine tests as part of automotive ISA operation cycle

For the next tests a small driving cycle was implemented. This cycle contains the motor operation mode (starting of the ICE) and generator operation mode (battery supply). For these tests the control was the one presented in this chapter in section 4.1.2.

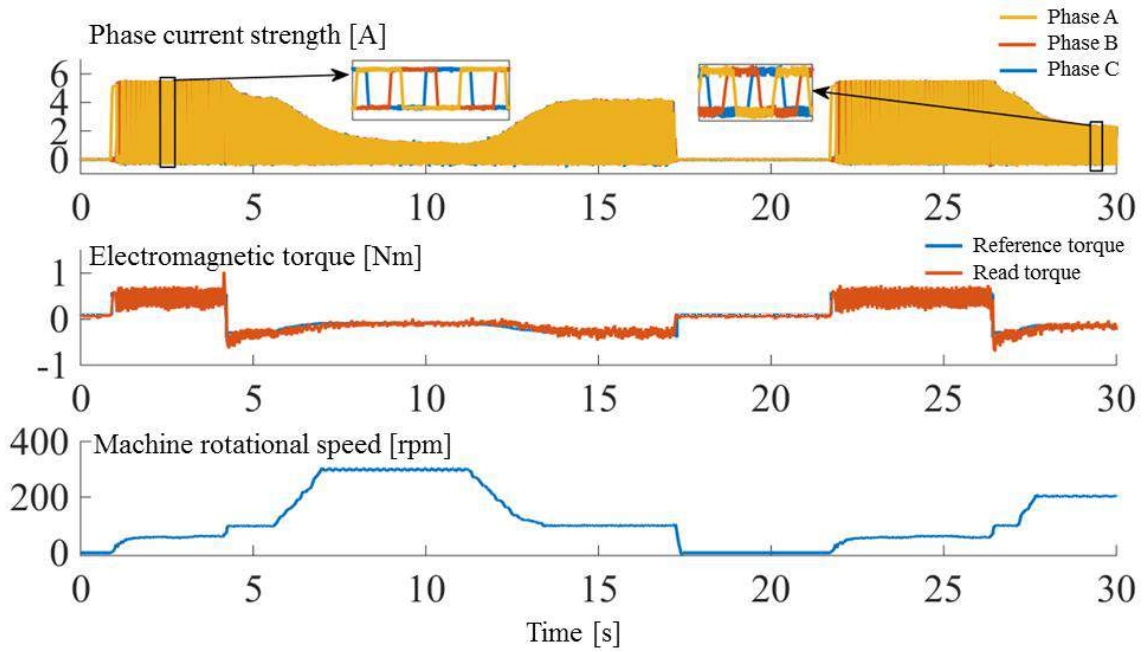


Fig.4.21 Experimentally dynamic responses in phase current, rotor speed, electromagnetic torque and output power of the three-phase 6/8 SR machine for a part of its operation cycle in automotive ISA application.

In fig. 4.21, tests are carried out for a small part of the SR-machine operation cycle in automotive ISA application, as follows: for the first second the SR machine is in stationary mode following that at time instant $t_1 = 1$ s to start in motor operation mode, and the reference speed is set to 60 rpm; during this period the ICE is started; at the instant $t_2 = 2.1$ s, SR machine changes to generator operation mode, the machine being driven by the ICE, and the rotor speed is set to 70 rpm; once the speed reaches 300 rpm, it is decreased back to 70 rpm, before stopping the machine, at the instant $t_2 = 17.2$ s. Afterwards for a period of 4.5s the electrical machine is stopped, this is considered the stopping at traffic lights of the vehicle, after which the SR machine starts in motor operation mode to restart the ICE, following that at time instant $t_3 = 26$ s to change to generator operation mode where the speed increases from 70 rpm to 200 rpm before ending the cycle.

The above presented cycle is a fictive one because the SR machine used to perform this tests is a small machine that is not able to start an ICE, this is used to point the ability of this machine to change the functioning mode by changing the commutation angles and also the smooth transition from motor to generator operation mode.

For the entire driving cycle for the motor operation mode the commutation angles were chosen to be: $\theta_{on} = 0^\circ$ and $\theta_{off} = 20^\circ$ and for generator operation mode $\theta_{on} = 24^\circ$ and $\theta_{off} = 45^\circ$. Another possibility of choosing the best commutation angles when tests are performed is to implement in the control program realized in Matlab/Simulink a LookUpTable that based on the speed and reference current to choose the best theta on and theta off from an imposed set of values

(as showed in chapter 3 figs. 3.34 and 3.35) that give the best control of the SR machine regardless the speed and phase current.

4.4. Conclusions

After performing optimization on any kind of device the most important aspect is to validate the results obtained. In the majority of cases validation by means of finite element computation is performed, but the most important validation is by experimental tests. This chapter deals with the experimental tests performed on the prototype of a three-phase 6 stator and 8 rotor teeth SR machine.

In the first part of this chapter is presented the entire test bench used to realize the tests. Another modality of supplying this type of machine from two full bridge inverters connected so that they can operate like a half bridge is also presented in this chapter. This is followed by a detailed presentation of the entire control implemented in Matlab/Simulink environment used to test the machine in motor and generator modes, but also in a part of a small driving cycle for automotive ISA applications.

Also in this chapter comparison between analytically calculated, FE- computed and measured, maximum and minimum phase inductance is performed, as well as validations in terms of best commutation angles obtained after optimization, by means of tests executed on the prototype and also compared with the simulation results.

Finally, steady-state tests in motor and generator operation modes with two different sets of commutation angles are realized in the last part, before ending with tests carried out for a small driving cycle for automotive ISA applications

Selected references

- [1] D. Ilea, *Conception optimale des moteurs à réductance variable à commutation électronique pour la traction des véhicules électriques légers.*: Doctoral dissertation, Ecole Centrale de Lille; Technical university of Cluj-Napoca, Roumanie, 2011.
- [2] User Manual. DPO2000 and MSO2000 Series. [Online].
http://instrumentationlab.berkeley.edu/sites/default/files/BSC01/Scope_Manual_MSO-2024web.pdf
- [3] M. Ruba, *Design and study of a modular switched reluctance machine.*: Doctoral dissertation, 2010.
- [4] Petrus V. Gyselinck J. Iancu V., *Switched reluctance motors for electric vehicle propulsion: comparative numerical and experimental study of control schemes.*: Doctoral dissertation, 2012.

General conclusions, original contributions and prospects

The objective of this research was to study a three-phase six stator and eight rotor SR machine for automotive ISA usage. The entire work starts from defining the analytical model for this type of machine to be simulated in motor and generator operation mode. The intention for this analytical model is to use it in an optimization process, but to be certain that the results obtained with this model are the right ones, validations by means of FE computation or measurements on an existing machine are required.

In the first chapter the importance of reducing the CO₂ emission is pointed out, followed by the functioning principle of the SR machine in both motor and generator operation modes. A state of the art of the hybridization and different types of hybridization is also presented in this chapter, before concluding with a comparison in terms of cost for three types of electrical machines (internal permanent magnet machine, induction machine and switched reluctance machine).

The second chapter is focused on the analytical modeling of the SR machine. In this part some conventional and nonconventional topologies are presented, with an increased number of stator teeth and with an increased number of rotor teeth, respectively. Comparison in terms of advantages and disadvantages for each configuration is also provided in this chapter.

The SR machine is simple and cheap in construction due to its simple rotor construction (only laminated steel without permanent magnets), the component that increases the price of this machine being the converter by means of which the machine must be supplied. Also, in the second chapter with a detailed functioning principle are presented some possibilities of supplying this machine. The voltage and electromagnetic torque equations are written in this chapter for the case in which the saturation is accounted for and for when is neglected.

By reason of the double saliency of this machine the inductance can evolve in function of rotor position and also depending on the phase current. And because for this thesis the topology of the machine is chosen with an increased number of rotor teeth an overlap between stator and rotor will always appear regardless the rotor position. Hence, an ideal evolution of the inductance and the equations necessary to compute the rotor position for each point of this inductance are given in the second chapter. But not only, starting from the analytical calculation of the maximum and minimum inductance presented in the literature for a configuration with 8 stator and 6 rotor poles SR machine, this thesis presents the computation of the aligned and unaligned inductance for the configuration with 6 stator and 8 rotor teeth SR machine. In order to see the accuracy of this new calculations, validation on the SR machine prototype, in terms of FE computation of the inductance for the two rotor positions (aligned and

unaligned) is also provided in this chapter together with the detailed computing of the aligned and unaligned inductance for the nominal phase current strength of 4A.

This thesis points out that an increased number of rotor poles can provide a decrease in the torque oscillations, but in order to increase the mean electromagnetic torque with constraint on the torque ripple an optimization process must be launched. The second chapter presents the impact of the commutation angles on the value of mean electromagnetic torque and on the torque oscillations and the necessity of the optimization process.

The third chapter is entirely dedicated to the optimization process. Here the difference between a local minimum and a global minimum is explained together with the difference between the algorithms that determine the local and global minimum. The optimization sequence is also detailed. But the most important aspect is the modality of computing the problem to be optimized, because in most of the time a complex problem can lead to an increased number of evaluations and automatically to a rather large amount of time to obtain accurate results.

This thesis presents two models upon which optimization can be performed, one accurate but long in computation time and one fast but under the penalty of precision. Also in this work one can find the modality of linking the two models by using space mapping technique in order to have accurate results in a short time.

The space mapping technique studied in this thesis is based on a local correction of the coarse model output using OSMP and a much sophisticated correction modality using Jacobian matrix under MM approach. The functioning steps of these two techniques (OSMP and MM) are detailed in the third chapter together with an application on a mathematical model. Comparison in terms of obtained results strictly with the fine model and the ones obtained with the coarse model corrected by means of both techniques are provided in this chapter.

Having knowledge of the functioning principle of this two techniques it was possible to apply them to determine the best commutation angles and reference current that give the maximum mean electromagnetic torque with the ripple not exceeding an imposed value, for a three-phase 6 stator and 8 rotor poles SR machine, configuration that is available in the L2EP laboratory. But a proper determination of right fine and coarse models is a crucial step on which this optimization is based, therefore in this chapter the determination of this two models is also presented. Comparison between the results obtained with the fine model and the ones obtained with the coarse corrected model are provided in this chapter together with the necessary time required to finalize the optimization on the fine respectively on the coarse iteratively corrected model. It is possible to affirm that by applying these techniques the computation time has decreased with more than 80% and the results are almost the same.

The previous obtained results show that applied to the control optimization of the SR machine these strategies work properly, therefore the next step was to increase the optimization problem and besides control to add also the design of the SR machine to be used in ISA applications. But in this case the previous fine model was not usable and in order to have accurate results a FE model was required, hence the modality of using FE computation in the optimization process is also detailed in this chapter. This chapter ends with comparison in terms of obtained results and simulations in both motor and generator operation modes together with simulation of a small driving cycle.

Each optimization requires validation either by FE method or by experimental measurements. These validations are mandatory to be realized in order to see the accuracy of the results. On this basis, the fourth chapter of the thesis is dedicated to tests validation compared with FE computation and analytically calculated results. In the first part of this chapter a modality of linking two full-bridge inverters to act like a half-bridge is detailed followed by the command program performed in Matlab/Simulink used to perform the tests on the SR machine. It is possible to conclude that after the experimental tests the measured results match the simulated ones.

The contributions brought by the author on this thesis are described below:

- Implementation in Matlab/Simulink environment of an analytical model that is able to be simulated in motor and generator operation mode by adjusting the commutation angles in the positive or negative slope of the inductance
- Realization of the equations used to calculate rotor position based on an ideal evolution of the inductance, applied for a three-phase 6 stator and 8 rotor teeth SR machine
- Adaptation to an increased number of rotor teeth SR machine topology for calculation of the maximum and minimum inductance, based on a previous analytical calculation applied for a configuration with an increased number of stator poles
- Implementing and mathematically testing of two time reducing methods for further usage in SR machine optimization
- Perform time dependent optimization on a SR machine to determine first the optimal control and afterwards the optimal design and control
- Development of a coarse model, that has the benefit of speed, to be used in the optimization process and iteratively correcting this model based on a fine model to obtain the optimal desired design in a faster way

- Realization of a link between Matlab and JMAG Designer to use this FE model in the correction process when searching for the optimal design and control of a three-phase 6 stator and 8 rotor teeth SR machine to be used in automotive ISA applications
- Experimental tests and FE computation performed to validate the obtained results

As future prospects for the presented work the following can be suggested:

- Topology optimization using three components i.e. air, iron and magnet, focused on the rotor, to determine the best shape of this machine part in order to increase its performances. But not only on the rotor, but also on the stator with 4 components (air, iron, coil and magnets), to determine the best stator shape.
- Thermal and vibration analyses to be performed on the SR machine

Appendix 2.A

Detailed voltage calculation

The voltage equation written from the flux-linkage point of view can be expressed as follows:

$$u_{ph} = R \cdot i_{ph} + \frac{d}{dt} \Psi_{ph}(\theta) \quad (\text{A.1})$$

$$\Psi_{ph}(\theta) = L(\theta) \cdot i_{ph} \quad (\text{A.2})$$

Changing eq. A.2 into A.1 one can obtain:

$$u_{ph} = R \cdot i_{ph} + \frac{d}{dt} L(\theta) \cdot i_{ph} \quad (\text{A.3})$$

$$u_{ph} = R \cdot i_{ph} + \frac{di_{ph}}{dt} L(\theta) + \frac{dL(\theta)}{dt} i_{ph} \quad (\text{A.4})$$

Considering that $\Omega = d\theta/dt$, eq. A.4 can be reformulated as:

$$u_{ph} = R \cdot i_{ph} + L(\theta) \frac{di_{ph}}{dt} + \frac{\partial L(\theta)}{\partial \theta} i_{ph} \cdot \Omega \quad (\text{A.5})$$

When saturation is considered the voltage equation becomes:

$$u_{ph} = R \cdot i_{ph} + \left(L(i_{ph}, \theta) + i_{ph} \frac{\partial (L(i_{ph}, \theta))}{\partial i_{ph}} \right) \frac{di_{ph}}{dt} + \frac{\partial (L(i_{ph}, \theta))}{\partial \theta} i_{ph} \cdot \Omega \quad (\text{A.6})$$

Appendix 2.B

Analytical calculation of the phase inductance for aligned and unaligned rotor position

Starting from the analytical equations presented in this chapter, the following appendix reveals, based on a predefined machine size, the computation of the aligned and unaligned inductances for a phase current strength of 4A.

The following table discloses values of machine parameters used in the analytical computation.

Machine axial length [mm]	$l_a = 118$	Air-gap [mm]	$g = 0.85$
Number of stator teeth	$N_S = 6$	Number of rotor teeth	$N_R = 8$
Stator pole arc [deg.]	$\beta_S = 31.4$	Rotor pole arc [deg.]	$\beta_R = 21.3$
Stator inner diameter [mm]	$D_{Sint} = 58.25$	Stator outer diameter [mm]	$D_{Sext} = 116.6$
Stator pole thickness [mm]	$w_S = 16$	Rotor pole thickness [mm]	$w_R = 10.5$
Stator yoke thickness [mm]	$w_{Sy} = 10$	Rotor yoke thickness [mm]	$w_{Ry} = 10$
Height of stator teeth [mm]	$h_S = 19.175$	Height of rotor teeth [mm]	$h_R = 9.275$
Rotor outer diameter [mm]	$D_{Rext} = 56.55$	Rotor inner diameter [mm]	$D_{Rint} = 18$
Maximum inductance calculated by FE analyze for a current of 4A [H]	$L_{MFEM} = 0.03668$	Minimum inductance calculated by FE analyze for a current of 4A [H]	$L_{mFEM} = 0.02575$

Aligned inductance

- *Air-gap path1*

$$l_{g1} = g = 0.85 \cdot 10^{-3} \quad (B.1)$$

$$A_{g1} = \frac{\beta_S \frac{D_{Sint}}{2} l_a + \beta_R \left(\frac{D_{Sint}}{2} - g \right) l_a}{2} = 1.6 \cdot 10^{-3} \quad (B.2)$$

- *Stator tooth path1*

$$l_{Sp1} = h_S = 0.0192 \quad (B.3)$$

$$A_{Sp1} = \beta_S \frac{D_{Sint}}{2} l_a = 0.0019 \quad (B.4)$$

- *Rotor tooth path1*

$$l_{Rp1} = h_R = 0.0093 \quad (B.5)$$

$$A_{Rp1} = \beta_R \left(\frac{D_{Sint}}{2} - g \right) l_a = 0.0012 \quad (B.6)$$

- *Stator yoke path1*

$$l_{Sy1} = \frac{\pi}{2} (D_{Sint} + h_S + w_{Sy}) = 0.1373 \quad (B.7)$$

$$A_{Sy1} = w_{Sy} \cdot l_a = 0.1280 \quad (\text{B.8})$$

- *Rotor yoke path1*

$$l_{Ry1} = \frac{\pi}{2} \left(\frac{D_{Sint}}{4} - g - h_R + \frac{D_{Rint}}{2} \right) = 0.0211 \quad (\text{B.9})$$

$$A_{Ry1} = \left(\frac{D_{Sint}}{2} - g - h_R \right) l_a = 0.0022 \quad (\text{B.10})$$

$$\Psi_{a1} = \frac{N_{sp} \cdot i_{ph}}{2(R_{Sp1} + R_{g1} + 2R_{Rp1}) + \frac{1}{2}R_{Ry1} + \frac{1}{2}R_{Sy1}} = 1.8878 \cdot 10^{-4} \quad (\text{B.11})$$

$$L_{a1} = \frac{N_{sp} \Psi_{a1}}{i_{ph}} = 0.0310 \quad (\text{B.12})$$

- *Air-gap path2*

$$l_{g2} = \frac{3h_s \pi}{4} \frac{\pi}{2} = 0.022 \quad (\text{B.13})$$

$$A_{g2} = \frac{3h_s}{4} l_a = 0.0017 \quad (\text{B.14})$$

- *Stator tooth path2*

$$l_{Sp2} = \frac{1}{2} \frac{3h_s}{4} + \frac{w_{Sy}}{2} = 0.0122 \quad (\text{B.15})$$

$$A_{Sp2} = \frac{1}{2} \left(\frac{3h_s}{4} l_a \right) = 8.48 \cdot 10^{-4} \quad (\text{B.16})$$

- *Stator yoke path2*

$$l_{Sy2} \cong l_{Sp2} = 0.0122 \quad (\text{B.17})$$

$$A_{Sy2} = w_{Sy} \cdot l_a = 0.0012 \quad (\text{B.18})$$

$$\Psi_{a2} = \frac{\frac{3}{4} N_{sp} \cdot i_{ph}}{R_{Sp2} + R_{g2} + R_{Sy2}} = 1.1607 \cdot 10^{-5} \quad (\text{B.19})$$

$$L_{a2} = \frac{3N_{sp} \Psi_{a2}}{i_{ph}} = 0.0057 \quad (\text{B.20})$$

$$L_M = L_{a1} + L_{a2} = 0.0367 \text{ [H]} \quad (\text{B.21})$$

Unaligned inductance

- *Air-gap path1*

$$l_{g1} = \frac{D_{Sint}}{2} - g - h_R = 0.019 \quad (\text{B.22})$$

$$A_{g1} = 2 \cdot \theta_3 \left(\frac{D_{Sint}}{2} - g - h_R \right) l_a = 5.207 \cdot 10^{-4} \quad (\text{B.23})$$

- *Stator tooth path1*

$$l_{sp1} = h_S = 0.019 \quad (\text{B.24})$$

$$A_{sp1} = \frac{1}{4} \left(\frac{D_{Sint}}{2} \beta_S \cdot l_a \right) = 4.708 \cdot 10^{-4} \quad (\text{B.25})$$

- *Stator yoke path1*

$$l_{sy1} = \frac{\pi(D_{Sint} + 2h_S + w_{Sy})}{2} = 0.1674 \quad (\text{B.26})$$

$$A_{sy1} = w_{Sy} \cdot l_a = 0.00118 \quad (\text{B.27})$$

- *Rotor yoke path1*

$$l_{ry1} = \pi \left(\frac{D_{Rint}}{4} + \frac{D_{Sint}}{4} - \frac{g}{2} - \frac{h_R}{2} \right) = 0.04399 \quad (\text{B.28})$$

$$A_{ry1} = \left(\frac{D_{Sint}}{2} - g - h_R - \frac{D_{Rint}}{2} \right) l_a = 0.00118 \quad (\text{B.29})$$

$$\Psi_{u1} = \frac{N_{sp} \cdot i_{ph}}{2R_{sp1} + 2R_{g1} + \frac{R_{sy1}}{2} + \frac{R_{ry1}}{2}} = 2.822 \cdot 10^{-6} \quad (\text{B.30})$$

$$L_{u1} = \frac{N_{sp} \Psi_{u1}}{i_{ph}} = 9.257 \cdot 10^{-4} \quad (\text{B.31})$$

- *Air-gap path2*

$$l_{g2} = BC \left(\frac{\pi}{3} \right) = 0.0106 \quad (\text{B.32})$$

$$A_{g2} = \frac{1}{2} (A_{Rp2} + A_{sp2}) = 1.9566 \cdot 10^{-4} \quad (\text{B.33})$$

- *Stator tooth path2*

$$l_{sp2} \cong h_S = 0.019175 \quad (\text{B.34})$$

$$A_{sp2} = \frac{3}{48} \beta_S \frac{D_{Sint}}{2} l_a = 1.177 \cdot 10^{-4} \quad (\text{B.35})$$

- *Rotor tooth path2*

$$l_{Rp2} \cong \frac{3}{4} h_R = 0.0069562 \quad (\text{B.36})$$

$$A_{Rp2} = \frac{h_R}{4} l_a = 2.736 \cdot 10^{-4} \quad (\text{B.37})$$

$$\Psi_{u2} = \frac{N_{sp} \cdot i_{ph}}{2(R_{Sp2} + R_{g2} + R_{Rp2}) + R_{Sy2} + R_{Ry2}} = 1.899 \cdot 10^{-6} \quad (\text{B.38})$$

$$L_{u2} = 2 \frac{N_{sp} \Psi_{u2}}{i_{ph}} = 6.229 \cdot 10^{-4} \quad (\text{B.39})$$

- *Air-gap path3*

$$l_{g3} = g = 8.5 \cdot 10^{-5} \quad (\text{B.40})$$

$$A_{g3} = \frac{\theta_1 \frac{D_{Sint}}{2} l_a + \theta_1 \left(\frac{D_{Sint}}{2} - g \right) l_a}{2} = 3.397 \cdot 10^{-4} \quad (\text{B.41})$$

- *Stator tooth path3*

$$l_{Sp3} = h_S = 0.019175 \quad (\text{B.42})$$

$$A_{Sp3} = \theta_1 \frac{D_{Sint}}{2} l_a = 2.3 \cdot 10^{-4} \quad (\text{B.43})$$

- *Rotor tooth path3*

$$l_{Rp3} = h_R = 0.0093 \quad (\text{B.44})$$

$$A_{Rp3} = \theta_1 \left(\frac{D_{Sint}}{2} - g \right) l_a = 4.48 \cdot 10^{-4} \quad (\text{B.45})$$

$$\Psi_{u3} = \frac{N_{sp} \cdot i_{ph}}{2(R_{Sp3} + R_{g3} + R_{Rp3}) + R_{Sy3} + R_{Ry3}} = 4.087 \cdot 10^{-5} \quad (\text{B.46})$$

$$L_{u3} = 2 \frac{N_{sp} \Psi_{u3}}{i_{ph}} = 0.0134 \quad (\text{B.47})$$

- *Air-gap path4*

$$l_{g4} = \frac{1}{2} (DB + DC) \theta_4 = 0.0138 \quad (\text{B.48})$$

$$A_{g4} = \frac{1}{2} (A_{Sp4} + A_{Rp4}) = 2.897 \cdot 10^{-4} \quad (\text{B.49})$$

- *Stator tooth path4*

$$l_{Sp4} = h_S = 0.0192 \quad (\text{B.50})$$

$$A_{Sp4} = \frac{3}{4} \frac{h_S}{4} l_a = 4.24 \cdot 10^{-4} \quad (\text{B.51})$$

- *Rotor tooth path4*

$$l_{Rp4} = h_R = 0.0093 \quad (\text{B.52})$$

$$A_{Rp4} = \left(\frac{D_{Sint}}{2} - g \right) \frac{\beta_R}{8} l_a = 1.551 \cdot 10^{-4} \quad (\text{B.53})$$

$$\Psi_{u4} = \frac{N_{sp} \cdot i_{ph}}{2(R_{Sp4} + R_{g4} + R_{Rp4}) + R_{Sy4} + R_{Ry4}} = 2.15 \cdot 10^{-6} \quad (\text{B.54})$$

$$L_{u4} = 2 \frac{N_{sp} \Psi_{u4}}{i_{ph}} = 7.068 \cdot 10^{-4} \quad (\text{B.55})$$

- *Air-gap path5*

$$l_{g5} = \frac{h_S \pi}{4 \cdot 2} = 0.0075 \quad (\text{B.56})$$

$$A_{g5} = A_{Sp5} = 0.0011 \quad (\text{B.57})$$

- *Stator tooth path5*

$$l_{Sp5} = \frac{h_S}{4} = 0.0048 \quad (\text{B.58})$$

$$A_{Sp5} = \frac{h_S}{2} l_a = 0.0011 \quad (\text{B.59})$$

- *Stator yoke path5*

$$l_{Sy5} \cong \frac{h_S}{4} + \frac{w_{Sy}}{4} = 0.0073 \quad (\text{B.60})$$

$$A_{Sy5} = A_{Sy1} = 0.0012 \quad (\text{B.61})$$

$$\Psi_{u5} = \frac{N_{sp} \cdot i_{ph}}{2R_{Sp5} + R_{g5} + R_{Sy5}} = 3.095 \cdot 10^{-5} \quad (\text{B.62})$$

$$L_{u5} = 2 \frac{N_{sp} \Psi_{u5}}{i_{ph}} = 0.010 \quad (\text{B.63})$$

$$L_m = \sum_{j=1}^5 L_{uj} = 0.0258 [H] \quad (\text{B.64})$$

For each step of the ideal inductance, the values of angles calculated for the three-phase 6/8 SR machine are presented below.

$$\beta_{Ropen} = \frac{2\pi - N_R \cdot \beta_R}{N_R} = 23.7^\circ \quad (\text{B.65})$$

$$\theta_1 = \frac{\beta_S - \beta_{Ropen}}{2} = 3.85^\circ \quad (\text{B.66 a})$$

$$\theta_2 = \beta_R - \theta_1 = 17.45^\circ \quad (\text{B.66 b})$$

$$\theta_3 = \theta_2 + (\beta_S - \beta_R) = 27.55^\circ \quad (\text{B.66 c})$$

$$\theta_4 = \theta_3 + (\beta_{Ropen} + \beta_R - \beta_S) = 41.15^\circ \quad (\text{B.66 d})$$

$$\theta_5 = \theta_4 + \theta_1 = \frac{2\pi}{N_R} = 45^\circ \quad (\text{B.66 e})$$

Appendix 3.A

Matlab implementation of the OSM technique

```
function OSM = OutputSpaceMapping()
warning off
%-----INITIALIZATION VALURS-----
NrSim = 1e5;           % Number of simulation
iterMax = 40;         % Number of iteration to be used in optimization
lb = -2;              % Low band of Input
ub = 2;               % Upper bund for Input
k = [1;1];           % Initial correction coefficient for output
Ref_Pct = -1.6;       % Reference point for OSM calculation
Pct = 1;              % Feasible or not-feasible point 1=Feasible, 2=Non-feasible
xBand = lb:(ub-lb)/(NrSim-1):ub;
%-----END-----
%%
function fOSM = fineOSM(x)
    f1 = x.^4-x.^3-x.^2-x+3;
    f2 = -1/2*x.^3;
    fOSM = [f1; f2];
end
function f = fine(x,yg)
    f1 = fineOSM(x);
    f2 = (f1(1,:)-yg(1,:)).^2;
    f3 = (f1(2,:)-yg(2,:)).^2;
    f = sqrt(f2+f3);
end
%%
function cOSM = coarseOSM(x,k)
    c11 = x.^4./2+1/2;
    c22 = 4./5.*x+2;
    c1 = c11.*k(1,:);
    c2 = c22.*k(2,:);
    cOSM=[c1; c2];
end
function c = coarse(x,k,yg)
    c1 = coarseOSM(x,k);
    c2 = (c1(1,:)-yg(1,:)).^2;
    c3 = (c1(2,:)-yg(2,:)).^2;
    c = sqrt(c2+c3);
end
%%

if Ref_Pct>=lb && Ref_Pct<=ub
else
    error('Please select a reference point ("Ref_Pct") between upper ("ub") and lower ("lb")
value')
end
if Pct == 1
    yg = fineOSM(Ref_Pct);
elseif Pct == 0
```



```

    yg = [12;1.6];
else
    error('Please select point ("Pct") to be Feasible ("1") or Non-Feasible ("0")')
end

%---Fine model optimization -----
[finRef,dist_fin] = min(fine(xBand,yg)); % Best value of input of the fine model
x_ref = xBand(dist_fin); % Best value of output of the fine model
%---end-----
%%
%--CALCULATION OF THE OUTPUT CORRECTION COEFICIENT-----
for iter = 1:iterMax
    %---Coarse model optimization -----
    [minobj_dist,dist_coarse] = min(coarse(xBand,k,yg)); % Best value of input for the coarse
    model
    x = xBand(dist_coarse); % Best value of output for the coarse
    model
    %---end-----

    %--- Ajustement----
    yf = fineOSM(x); % Simulation of fine model with best value find after optimization
    yc = coarseOSM(x,[1;1]); % Simulation of coarse model with best value find after
    optimization
    obj_dist = minobj_dist;
    k1(iter) = k(1,:); % Hold each value of correction for each iteration
    k2(iter) = k(2,:);
    Inp(iter) = x; % Hold each value of best input for each iteration
    Fine1(iter) = yf(1,:); % Hold each value of output of fine model for each iteration
    Fine2(iter) = yf(2,:);
    Coarse_corect1(iter) = yc(1,:); % Hold each value of output of coarse model for each iteration
    Coarse_corect2(iter) = yc(2,:);
    Dist_cors_fine(iter) = obj_dist; % Hold each value of distance between fine and coarse
    models
    %---end-----

    %---Calculate correction coefficient-----
    k =yf./yc; % Calculation of correction coefficient
    %---end-----

    % ---Stopping criteria-----
    tolerance = 1e-4; % Value of tolerance imposed
    if obj_dist<tolerance
        disp('Space mapping terminated: Objective function exceed tolerance')
        break
    elseif iter>=iterMax
        disp('Space mapping terminated: Iterations reach maximum imposed')
        break
    elseif iter>2
        dist = abs(Dist_cors_fine(iter-1)-Dist_cors_fine(iter));
        if dist<=tolerance^2
            disp('Space mapping terminated: Distance not changing')
            break

```

```

    end
end
%---end-----
end
[l stepk] = size(k1);
%%
%-----PLOT FUNCTION-----
i = 1:length(k1);
figure('Name','Output Space Mapping Proportional','NumberTitle','off')
subplot(2,2,1)
semilogy(i,Dist_cors_fine,'-', 'MarkerSize',20)
title('Distance of coarse model (yf-k*yc)'),xlabel('Iteration'),ylabel('Distance')
set(gca,'FontSize',20,'FontName','Times New Roman')
subplot(2,2,2)
plot(i,Inp,'-', 'MarkerSize',20)
title('Input obtained from coarse model'),xlabel('Iteration'),ylabel('Input obtained')
set(gca,'FontSize',20,'FontName','Times New Roman')
subplot(2,2,[3,4])
hold on
plot(i,k1,'-', 'MarkerSize',20)
plot(i,k2,'-', 'MarkerSize',20)
title('Correction coefficient'),xlabel('Iteration'),ylabel('k1 and k2'),legend('k1','k2')
set(gca,'FontSize',20,'FontName','Times New Roman')
hold off
xBand = (lb):(ub)-(lb)/(NrSim-1):(ub);
MT_fine = fine(xBand,yg);
Length = length(xBand);
M_coarse = coarse(xBand,[1;1],yg);
kk = ones(Length,1);
CoarseIter1 = M_coarse;
if stepk>3
    M_coarse = coarse(xBand,[k1(:,3);k2(:,3)],yg);
    CoarseIter3 = M_coarse;
else
end
M_coarse = coarse(xBand,[k1(:,stepk);k2(:,stepk)],yg);
CoarseIterLast = M_coarse;

x_plot = lb:(ub-lb)/(Length-1):ub;
figure('Name','Objective function evaluation','NumberTitle','off')
hold on
plot(x_plot,MT_fine,'-')
plot(x_plot,CoarseIter1,'-')
if stepk>3
    plot(x_plot,CoarseIter3,'-')
else
end
plot(x_plot,CoarseIterLast,'-')
[minobj_dist,step_dist] = min(Dist_cors_fine(:,2:end));
plot(Inp(step_dist+1),minobj_dist,'square','MarkerEdgeColor','k','MarkerFaceColor','r','Marker
Size',15)
plot(x_ref,finRef,'o','MarkerEdgeColor','k','MarkerFaceColor','b','MarkerSize',10)

```

```

if stepk>3
    legend('Fine model', 'Coarse without correction', 'Coarse with correction 3 iter','Coarse with
correction last iter', 'Best Point OSM', 'Best Point of fine model', 'Location', 'North')
else
    legend('Fine model', 'Coarse without correction', 'Coarse with correction last iter', 'Best
Point OSM', 'Best Point of fine model', 'Location', 'North')
end
xlabel('Input'), ylabel('Output'), title('Variation of objective function')
set(gca,'FontSize',20,'FontName','Times New Roman')
figure('Name','Fine and coarse mathematical models','NumberTitle','off')
fOSM = fineOSM(x_plot);
cOSM = coarseOSM(x_plot,[1;1]);
subplot(2,2,1)
hold on
plot(x_plot,fOSM(1,:),'-'),plot(x_plot,fOSM(2,:),'-')
hold off
legend('yf1','yf2')
xlabel('Input'), ylabel('Output Fine'), title('Fine model')
set(gca,'FontSize',20,'FontName','Times New Roman')
subplot(2,2,2)
hold on
plot(x_plot,cOSM(1,:),'-'),plot(x_plot,cOSM(2,:),'-')
hold off
legend('yc1','yc2')
xlabel('Input'), ylabel('Output Coarse'), title('Coarse model')
set(gca,'FontSize',20,'FontName','Times New Roman')
subplot(2,2,3)
hold on
plot(x_plot,fOSM(1,:),'-'),plot(x_plot,cOSM(1,:),'-')
hold off
legend('yf1','yc1')
xlabel('Input'), ylabel('Output Fine and Coarse'), title('Coarse and Fine model')
set(gca,'FontSize',20,'FontName','Times New Roman')
subplot(2,2,4)
hold on
plot(x_plot,fOSM(2,:),'-'),plot(x_plot,cOSM(2,:),'-')
hold off
legend('yf2','yc2','Location','southwest')
xlabel('Input'), ylabel('Output Fine and Coarse'), title('Coarse and Fine model')
set(gca,'FontSize',20,'FontName','Times New Roman')
a1 = fineOSM(Ref_Pct);
a2 = [12;1.6];
figure('Name', 'Fine models and searched solutions','NumberTitle','off')
hold on
plot(fOSM(1,:),fOSM(2,:),'-')
plot(a1(1,:),a1(2:),'square','MarkerEdgeColor','k','MarkerFaceColor','r','MarkerSize',5)
plot(a2(1,:),a2(2:),'o','MarkerEdgeColor','k','MarkerFaceColor','g','MarkerSize',5)
xlabel('yf1'), ylabel('yf2')
hold off
set(gca,'FontSize',20,'FontName','Times New Roman')
end

```

Appendix 3.B

Matlab implementation of the MM technique

```
function MM = ManifoldsMapping()
warning off
%-----INITIALIZATION VALURS-----
NrSim = 1e5;           % Number of simulation
iterMax = 40;         % Number of iteration to be used in optimization
lb = -2;              % Low band of Input
ub = 2;               % Upper bund for Input
k = [1;1]*pinv([1;1]); % Initial correction coefficient for output
Ref_Pct = -1.6;       % Reference point for OSM calculation
Pct = 1;              % Feasible point 1=Feasible
x0 = 0.6;             % First starting point for optimization
xBand = lb:(ub-lb)/(NrSim-1):ub;
%%
function fOSM = fineOSM(x)
    f1 = x.^4-x.^3-x.^2-x+3;
    f2 = -1/2*x.^3;
    fOSM = [f1; f2];
end
function f = fine(x,yg)
    f1 = fineOSM(x);
    f2 = (f1(1,:)-yg(1,:)).^2;
    f3 = (f1(2,:)-yg(2,:)).^2;
    f = sqrt(f2+f3);
end
%%
function cOSM = coarseOSM(x)
    c1 = x.^4./2+1/2;
    c2 = 4./5.*x+2;
    cOSM=[c1; c2];
end
function c = coarse(x,yi)
    c1 = coarseOSM(x);
    c2 = (c1(1,:)-yi(1,:)).^2;
    c3 = (c1(2,:)-yi(2,:)).^2;
    c = sqrt(c2+c3);
end
%%
%-----END-----
if Ref_Pct>=lb && Ref_Pct<=ub
else
    error('Please select a reference point ("Ref_Pct") between upper ("ub") and lower ("lb")
value')
end
if Pct == 1
    yg = fineOSM(Ref_Pct);
else
    error('Please select point ("Pct") to be Feasible ("1")')
end
%---Fine model optimization -----
```

```

[finRef,dist_fin] = min(fine(xBand,yg)); % Best value of input of the fine model
x_ref = xBand(dist_fin); % Best value of output of the fine model
%---end-----
%%
%--CALCULATION OF THE OUTPUT CORRECTION COEFICIENT-----
for iter = 1:iterMax

    if iter>=2
        %---Coarse model optimization -----
        [minobj_dist_i,dist_coarse] = min(coarse(xBand,yi)); % Best value of input for the
coarse model
        x = xBand(dist_coarse); % Best value of output for the coarse model
        x0 = x;
        %---end-----
        Dist_cors_fine_i(iter) = minobj_dist_i;
        Inpl1(iter) = x; % Input obtained after optimization
        yf = fineOSM(x); % Simulation of the fine model
        yc = coarseOSM(x); % Simulation of the coarse model
        Log_Plot_yf = fine(x,yg); % Sim of fine norm of fine model
        Log_Plot_yf1i(iter) = (Log_Plot_yf); % Norm distance
        Fine(:,iter) = yf; % Fine results for each iteration
        Coarse(:,iter) = yc; % Coarse results for each iteration
        % ----- Calculation of the Jacobian matrix-----
        for p = 1:iter-1
            dyf = Fine(:,iter)-Fine(:,p);
            dyc = Coarse(:,iter)-Coarse(:,p);
            dyf11(:,p) = dyf;
            Dyf = dyf11;
            dyc11(:,p) = dyc;
            Dyc = dyc11;
        end
        %---end-----
        k = Dyc*pinv(Dyf); % Correction
        yi = Ci(:,iter-1)-(k*(Fi(:,iter-1)-yg)); % Calculation of the new target

    else
        yf = fineOSM(x0);
        yc = coarseOSM(x0);
        yi = yc-(k*(yf-yg));
        Fine(:,iter) = yf;
        Coarse(:,iter) = yc;
        minobj_dist_i = 1;
    end
    Fi = Fine;
    Ci = Coarse;

    Y(:,iter) = yi; % The new target for each iteration

    % ---Stopping criteria-----
    tolerance = 1e-4; % Value of tolerance imposed
    if minobj_dist_i<tolerance
        disp('Space mapping terminated: Objective function exceed tolerance')
    end

```

```

    break
elseif iter>=iterMax
    disp('Space mapping terminated: Iterations reach maximum imposed')
    break
elseif iter>2
    dist = abs(Dist_cors_fine_i(iter-1)-Dist_cors_fine_i(iter));
    if dist<=tolerance^2
        disp('Space mapping terminated: Distance not changing')
        break
    end
end
end
%---end-----
end
%%
[l stepk] = size(Y);
%-----PLOT FUNCTION-----
i = 1:length(Y);
figure('Name', ' MM objective function and input obtained ', 'NumberTitle','off')
subplot(2,1,1)
semilogy(i,Dist_cors_fine_i,'-', 'MarkerSize',20)
title('Logarithmic variation of objective function'),xlabel('Iteration'),ylabel(' ')
set(gca,'FontSize',20,'FontName','Times New Roman')
subplot(2,1,2)
plot(i,Inp1i,'-', 'MarkerSize',20)
title('Input obtained from coarse model x'),xlabel('Iteration'),ylabel('Input obtained x')
set(gca,'FontSize',20,'FontName','Times New Roman')
xBand = (lb):((ub)-(lb))/(NrSim-1):(ub);
MT_fine = fine(xBand,yg);
Length = length(xBand);
M_coarse = coarse(xBand,Y(:,1));
kk = ones(Length,1);
CoarseIter1 = M_coarse;
if stepk>3
    M_coarse = coarse(xBand,Y(:,3));
    CoarseIter3 = M_coarse;
else
end
M_coarse = coarse(xBand,Y(:,stepk));
CoarseIterLast = M_coarse;
x_plot = lb:(ub-lb)/(Length-1):ub;
figure('Name', ' MM variation of the objective in function of input x', 'NumberTitle','off')
hold on
plot(x_plot,MT_fine,'-')
plot(x_plot,CoarseIter1,'-')
if stepk>3
    plot(x_plot,CoarseIter3,'-')
else
end
plot(x_plot,CoarseIterLast,'-')
minobj_dist = Dist_cors_fine_i(:,iter);
plot(Inp1i(iter),minobj_dist,'square', 'MarkerEdgeColor','k', 'MarkerFaceColor','r', 'MarkerSize',
15)

```

```
plot(x_ref,finRef,'o','MarkerEdgeColor','k','MarkerFaceColor','b','MarkerSize',10)
if stepk>3
    legend('Fine model', 'Coarse without correction', 'Coarse with correction 3 iteration',
'Coarse with correction last iteration', 'Best Point OSM', 'Best Point of fine model', 'Location',
'North')
else
    legend('Fine model', 'Coarse without correction', 'Coarse with correction last iteration',
'Best Point OSM', 'Best Point of fine model', 'Location', 'North')
end
xlabel('Input'), ylabel('Output'), title('Variation of objective function')
set(gca,'FontSize',20,'FontName','Times New Roman')
end
```

Appendix 3.C

VBScript used to automatically draw the SR machine

```
' JMAG-Designer Script for SR-machine  
' Created by Zaharia Valentin  
' Copyright 2015 V. Zaharia, EC-LILLE, L2EP and Technical University of Cluj Napoca  
' $ Date: 2015/07/14 $
```

```
' -----  
' Draw complete motor in 2D
```

```
' =====  
' D_Shaft - external diameter of Stator (mm)  
' JugS      - stator yoke length (mm)  
' wS        - length of stator tooth (mm)  
' Ns        - number of stator poles  
' Ds_int    - inner stator diameter (mm)  
' H_bob     - high of coils (mm)  
' Dshaft    - Shaft diameter (mm)  
' JugR      - rotor yoke length (mm)  
' wR        - length of rotor tooth (mm)  
' Nr        - number of rotor poles  
' Dr_ext    - external diameter of rotor (mm)  
' ThetaOff  - end of excitation (deg)  
' Imax      - maximum value of current (A)  
' NTurns    - number of turns per coil  
' Rez       - coil resistance (ohm)  
' SpeedRpm  - machine speed (rpm)  
' InitPozDeg - initial rotor position for rotor to start (deg)  
' MeshPartSize - size of mesh in machine parts  
' MeshGapSize - size of mesh in machine air-gap  
' RadialDiv  - radial divisions in mesh properties  
' CircDiv    - circumferential divisions in mesh properties  
' AirRegScale - scale of air region  
' AxialLength - machine axial length (mm)  
' Paralel    - parallel computation  
' Procesors  - number of processor to be used  
' NrSteps    - number of steps  
' EndTime    - simulation end time (s)  
' NrDivizons - number of divisions in simulation
```

```
' =====  
' INITIALIZATION  
' =====
```

```
pi = 3.141592653589793  
maxArcOpem = (2*pi)/Ns      'maximum opening of the stator pole (the upper part) in rad  
Rs_ext=Ds_ext/2             'stator external radius  
Rs_int1 = Rs_ext-JugS       'the inner radius below yoke  
Rbob_int = Rs_int1-H_bob    'the inner stator radius  
arc_bob_int = wS/Rbob_int   'the inner arc realized by the stator pole  
arc_polS = wS/Rs_int1       'the arc of the stator pole  
Rs_int2 = Ds_int/2          'inner radius of the stator  
arc_pol_intS = wS/Rs_int2   'inner arc realized by the stator pole
```



```

maxArcOpemRot = (2*pi)/Nr 'shaft maximum opening in rad
Rshaft=Dshaft/2          'shaft radius
Rr_ext1 = Rshaft+JugR    'the upper radius above the yoke
arc_polR = wR/Rr_ext1    'the arc realized by the rotor pole
Rr_ext2 = Dr_ext/2      'the external radius of the rotor
arc_pol_extR = wR/Rr_ext2 'inner arc realized by the stator pole
'=====
' END INITIALIZATION
'=====
Call app.LaunchGeometryEditor()
'=====
' CREATE STATOR
'=====
Set geomApp = app.CreateGeometryEditor()
Set ref1 = geomApp.GetDocument().GetAssembly().GetItem("XY_PLANE")
Set ref2 = geomApp.GetDocument().CreateReferenceFromItem(ref1)
Call geomApp.GetDocument().GetAssembly().CreateSketch(ref2)
Call geomApp.GetDocument().GetAssembly().GetItem("Sketch").OpenSketch()
Call geomApp.GetDocument().GetAssembly().GetItem("Sketch").CreateVertex(0, 0)
'Srator cerc exterior
x_ext = Rs_ext*cos(maxArcOpem)
y_ext = Rs_ext*sin(maxArcOpem)
Call geomApp.GetDocument().GetAssembly().GetItem("Sketch").CreateArc(0, 0, Rs_ext, 0,
x_ext, y_ext)
'Srator cerc int jug
pol_angle1 = (wS/2)/Rs_int1
x_extJ = Rs_int1*cos(pol_angle1)
y_extJ = Rs_int1*sin(pol_angle1)
pol_angleJE1 = maxArcOpem-((wS/2)/Rs_int1)
x_extJE = Rs_int1*cos(pol_angleJE1)
y_extJE = Rs_int1*sin(pol_angleJE1)
Call geomApp.GetDocument().GetAssembly().GetItem("Sketch").CreateArc(0, 0, x_extJ,
y_extJ, x_extJE, y_extJE)
'Srator cerc int pol inf
pol_angle2 = (wS/2)/Rs_int2
x_intP1 = Rs_int2*cos(pol_angle2)
y_intP1 = Rs_int2*sin(pol_angle2)
Call geomApp.GetDocument().GetAssembly().GetItem("Sketch").CreateArc(0, 0, Rs_int2, 0,
x_intP1, y_intP1)
'Srator cerc int pol sup
pol_anglePsup1 = maxArcOpem-((wS/2)/Rs_int2)
x_extPsup1 = Rs_int2*cos(pol_anglePsup1)
y_extPsup1 = Rs_int2*sin(pol_anglePsup1)
x_extPsup2 = Rs_int2*cos(maxArcOpem)
y_extPsup2 = Rs_int2*sin(maxArcOpem)
Call geomApp.GetDocument().GetAssembly().GetItem("Sketch").CreateArc(0, 0,
x_extPsup1, y_extPsup1, x_extPsup2, y_extPsup2)
'Line inf pol inf
Call geomApp.GetDocument().GetAssembly().GetItem("Sketch").CreateLine(Rs_int2, 0,
Rs_ext, 0)
'Line sup pol inf

```

```

Call geomApp.GetDocument().GetAssembly().GetItem("Sketch").CreateLine(x_intP1,
y_intP1, x_extJ, y_extJ)
'Line inf pol sup
Call geomApp.GetDocument().GetAssembly().GetItem("Sketch").CreateLine(x_extPsup1,
y_extPsup1, x_extJE, y_extJE)
'Line sup pol sup
Call geomApp.GetDocument().GetAssembly().GetItem("Sketch").CreateLine(x_extPsup2,
y_extPsup2, x_ext, y_ext)
'Select draw with a rectangle
Call geomApp.View().SelectByRectangleWorldPos(-10, -10, 0, Ds_ext, Ds_ext, 0, 0)
'Create region
Call geomApp.GetDocument().GetAssembly().GetItem("Sketch").CreateRegions()
Call
geomApp.GetDocument().GetAssembly().GetItem("Sketch").CreateRegionRadialPattern()
Call geomApp.GetDocument().GetAssembly().GetItem("Sketch").GetItem("Region Radial
Pattern").SetProperty("Merge", 1)
Set ref1 = geomApp.GetDocument().GetAssembly().GetItem("Sketch").GetItem("Vertex")
Set ref2 = geomApp.GetDocument().CreateReferenceFromItem(ref1)
Call geomApp.GetDocument().GetAssembly().GetItem("Sketch").GetItem("Region Radial
Pattern").SetPropertyByReference("Center", ref2)
ReDim refarray(0)
refarray(0) = "faceregion(TRegionItem23)"
Call geomApp.GetDocument().GetAssembly().GetItem("Sketch").GetItem("Region Radial
Pattern").SetProperty("Region", refarray)
Call geomApp.GetDocument().GetAssembly().GetItem("Sketch").GetItem("Region Radial
Pattern").SetProperty("Angle", (360/Ns))
Call geomApp.GetDocument().GetAssembly().GetItem("Sketch").GetItem("Region Radial
Pattern").SetProperty("Instance", Ns)
' End snetch and change name and color
Call geomApp.GetDocument().GetAssembly().GetItem("Sketch").SetProperty("Name",
"Stator core")
Call geomApp.GetDocument().GetAssembly().GetItem("Stator core").SetProperty("Color",
"darkgreen")
Call geomApp.GetDocument().GetAssembly().GetItem("Stator core").CloseSketch()
'=====
' END STATOR
'=====
'=====
' CREATE COILS
'=====
Set geomApp = app.CreateGeometryEditor()
Set ref1 = geomApp.GetDocument().GetAssembly().GetItem("XY_PLANE")
Set ref2 = geomApp.GetDocument().CreateReferenceFromItem(ref1)
Call geomApp.GetDocument().GetAssembly().CreateSketch(ref2)
Call geomApp.GetDocument().GetAssembly().GetItem("Sketch.2").OpenSketch()
Call geomApp.GetDocument().GetAssembly().GetItem("Sketch.2").CreateVertex(0, 0)
'Coil cerc ext bob inf Jug
ArcCoilOpem = (maxArcOpem/2)*0.95
coil_angle1 = ArcCoilOpem
x_extCoil1 = Rs_int1*cos(coil_angle1)
y_extCoil1 = Rs_int1*sin(coil_angle1)

```

```

Call geomApp.GetDocument().GetAssembly().GetItem("Sketch.2").CreateArc(0, 0, x_extJ,
y_extJ, x_extCoil1, y_extCoil1)
'Coil cerc ext bob sup Jug
diff_arcPol = ArcCoilOpem+(maxArcOpem-ArcCoilOpem*2)
coil_angle2 = diff_arcPol
x_extCoil2 = Rs_int1*cos(coil_angle2)
y_extCoil2 = Rs_int1*sin(coil_angle2)
Call geomApp.GetDocument().GetAssembly().GetItem("Sketch.2").CreateArc(0, 0,
x_extCoil2, y_extCoil2, x_extJE, y_extJE)
'Coil cerc int bob inf
coil_angleInt1 = (wS/2)/Rbob_int
x_intCoil1 = Rbob_int*cos(coil_angleInt1)
y_intCoil1 = Rbob_int*sin(coil_angleInt1)
x_intCoilEnd1 = Rbob_int*cos(coil_angle1)
y_intCoilEnd1 = Rbob_int*sin(coil_angle1)
Call geomApp.GetDocument().GetAssembly().GetItem("Sketch.2").CreateArc(0, 0,
x_intCoil1, y_intCoil1, x_intCoilEnd1, y_intCoilEnd1)
'Coil cerc int bob sup
x_intCoil2 = Rbob_int*cos(coil_angle2)
y_intCoil2 = Rbob_int*sin(coil_angle2)
coil_angleSup = maxArcOpem-((wS/2)/Rbob_int)
x_intCoilEnd2 = Rbob_int*cos(coil_angleSup)
y_intCoilEnd2 = Rbob_int*sin(coil_angleSup)
Call geomApp.GetDocument().GetAssembly().GetItem("Sketch.2").CreateArc(0, 0,
x_intCoil2, y_intCoil2, x_intCoilEnd2, y_intCoilEnd2)
'Line inf coil inf
Call geomApp.GetDocument().GetAssembly().GetItem("Sketch.2").CreateLine(x_intCoil1,
y_intCoil1, x_extJ, y_extJ)
'Line sup coil inf
Call
geomApp.GetDocument().GetAssembly().GetItem("Sketch.2").CreateLine(x_intCoilEnd1,
y_intCoilEnd1, x_extCoil1, y_extCoil1)
'Line inf coil sup
Call geomApp.GetDocument().GetAssembly().GetItem("Sketch.2").CreateLine(x_intCoil2,
y_intCoil2, x_extCoil2, y_extCoil2)
'Line sup coil sup
Call
geomApp.GetDocument().GetAssembly().GetItem("Sketch.2").CreateLine(x_intCoilEnd2,
y_intCoilEnd2, x_extJE, y_extJE)
'Select draw with a rectangle
Call geomApp.View().SelectByRectangleWorldPos(-10, -10, 0, Ds_ext, Ds_ext, 0, 0)
'Create region
Call geomApp.GetDocument().GetAssembly().GetItem("Sketch.2").CreateRegions()
'Multiplie
Call
geomApp.GetDocument().GetAssembly().GetItem("Sketch.2").CreateRegionRadialPattern()
Set ref1 = geomApp.GetDocument().GetAssembly().GetItem("Sketch.2").GetItem("Vertex")
Set ref2 = geomApp.GetDocument().CreateReferenceFromItem(ref1)
Call geomApp.GetDocument().GetAssembly().GetItem("Sketch.2").GetItem("Region Radial
Pattern").SetPropertyByReference("Center", ref2)
ReDim refarray(1)
refarray(0) = "faceregion(TRegionItem43)"

```

```

refarray(1) = "faceregion(TRegionItem44)"
Call geomApp.GetDocument().GetAssembly().GetItem("Sketch.2").GetItem("Region Radial
Pattern").SetProperty("Region", refarray)
Call geomApp.GetDocument().GetAssembly().GetItem("Sketch.2").GetItem("Region Radial
Pattern").SetProperty("Angle", (360/Ns))
Call geomApp.GetDocument().GetAssembly().GetItem("Sketch.2").GetItem("Region Radial
Pattern").SetProperty("Instance", Ns)
' End snetch and change name and color
Call geomApp.GetDocument().GetAssembly().GetItem("Sketch.2").SetProperty("Name",
"Coil")
Call geomApp.GetDocument().GetAssembly().GetItem("Coil").SetProperty("Color", "gray")
Call geomApp.GetDocument().GetAssembly().GetItem("Coil").CloseSketch()
'=====
' END COIL
'=====
'=====
' CREATE ROTOR
'=====
Set geomApp = app.CreateGeometryEditor()
Set ref1 = geomApp.GetDocument().GetAssembly().GetItem("XY_PLANE")
Set ref2 = geomApp.GetDocument().CreateReferenceFromItem(ref1)
Call geomApp.GetDocument().GetAssembly().CreateSketch(ref2)
Call geomApp.GetDocument().GetAssembly().GetItem("Sketch.3").OpenSketch()
Call geomApp.GetDocument().GetAssembly().GetItem("Sketch.3").CreateVertex(0, 0)
'Rotor shaft arc open
x_shaftR = Rshaft*cos(maxArcOpemRot)
y_shaftR = Rshaft*sin(maxArcOpemRot)
Call geomApp.GetDocument().GetAssembly().GetItem("Sketch.3").CreateArc(0, 0, Rshaft, 0,
x_shaftR, y_shaftR)
'Rotor pol int Jug
pol_angleRot1 = (wR/2)/Rr_ext1
x_intJugR = Rr_ext1*cos(pol_angleRot1)
y_intJugR = Rr_ext1*sin(pol_angleRot1)
pol_angleRot2 = maxArcOpemRot-((wR/2)/Rr_ext1)
x_intJugRend = Rr_ext1*cos(pol_angleRot2)
y_intJugRend = Rr_ext1*sin(pol_angleRot2)
Call geomApp.GetDocument().GetAssembly().GetItem("Sketch.3").CreateArc(0, 0,
x_intJugR, y_intJugR, x_intJugRend, y_intJugRend)
'Rotor pol inf ext
pol_angleRot2 = (wR/2)/Rr_ext2
x_extPolInf = Rr_ext2*cos(pol_angleRot2)
y_extPolInf = Rr_ext2*sin(pol_angleRot2)
Call geomApp.GetDocument().GetAssembly().GetItem("Sketch.3").CreateArc(0, 0, Rr_ext2,
0, x_extPolInf, y_extPolInf)
'Rotor pol sup ext
pol_angleRot3 = maxArcOpemRot-((wR/2)/Rr_ext2)
x_extPolSup = Rr_ext2*cos(pol_angleRot3)
y_extPolSup = Rr_ext2*sin(pol_angleRot3)
x_extPolSupEnd = Rr_ext2*cos(maxArcOpemRot)
y_extPolSupEnd = Rr_ext2*sin(maxArcOpemRot)
Call geomApp.GetDocument().GetAssembly().GetItem("Sketch.3").CreateArc(0, 0,
x_extPolSup, y_extPolSup, x_extPolSupEnd, y_extPolSupEnd)

```

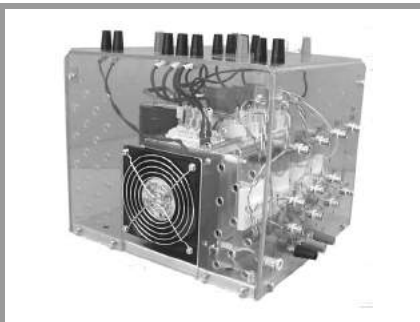
```

'Line inf pol inf
Call geomApp.GetDocument().GetAssembly().GetItem("Sketch.3").CreateLine(Rshaft, 0,
Rr_ext2, 0)
'Line sup pol inf
Call geomApp.GetDocument().GetAssembly().GetItem("Sketch.3").CreateLine(x_intJugR,
y_intJugR, x_extPolInf, y_extPolInf)
'Line inf pol sup
Call
geomApp.GetDocument().GetAssembly().GetItem("Sketch.3").CreateLine(x_intJugRend,
y_intJugRend, x_extPolSup, y_extPolSup)
'Line sup pol sup
Call geomApp.GetDocument().GetAssembly().GetItem("Sketch.3").CreateLine(x_shaftR,
y_shaftR, x_extPolSupEnd, y_extPolSupEnd)
'Select draw with a rectangle
Call geomApp.View().SelectByRectangleWorldPos(-10, -10, 0, Ds_ext, Ds_ext, 0, 0)
'Create region
Call geomApp.GetDocument().GetAssembly().GetItem("Sketch.3").CreateRegions()
'Multiple
Call
geomApp.GetDocument().GetAssembly().GetItem("Sketch.3").CreateRegionRadialPattern()
Call geomApp.GetDocument().GetAssembly().GetItem("Sketch.3").GetItem("Region Radial
Pattern").SetProperty("Merge", 1)
Set ref1 = geomApp.GetDocument().GetAssembly().GetItem("Sketch.3").GetItem("Vertex")
Set ref2 = geomApp.GetDocument().CreateReferenceFromItem(ref1)
Call geomApp.GetDocument().GetAssembly().GetItem("Sketch.3").GetItem("Region Radial
Pattern").SetPropertyByReference("Center", ref2)
ReDim refarray(0)
refarray(0) = "faceregion(TRegionItem64)"
Call geomApp.GetDocument().GetAssembly().GetItem("Sketch.3").GetItem("Region Radial
Pattern").SetProperty("Region", refarray)
Call geomApp.GetDocument().GetAssembly().GetItem("Sketch.3").GetItem("Region Radial
Pattern").SetProperty("Angle", (360/Nr))
Call geomApp.GetDocument().GetAssembly().GetItem("Sketch.3").GetItem("Region Radial
Pattern").SetProperty("Instance", Nr)
' End snetch and change name and color
Call geomApp.GetDocument().GetAssembly().GetItem("Sketch.3").SetProperty("Name",
"Rotor core")
Call geomApp.GetDocument().GetAssembly().GetItem("Rotor core").SetProperty("Color",
"blue")
Call geomApp.GetDocument().GetAssembly().GetItem("Rotor core").CloseSketch()
'=====
' END ROTOR
'=====

'Import geometry
Call app.ImportDataFromGeometryEditor()
Call geomApp.Quit()

```

SEMISTACK - IGBT



SEMITRANS Stack¹⁾

Three-phase rectifier + inverter with brake chopper

**SEMITEACH - IGBT
SKM 50 GB 123D
SKD 51
P3/250F**

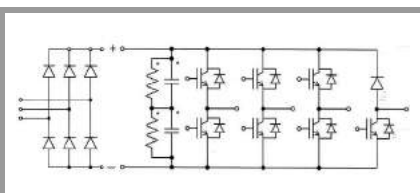
Features

- Multi-function IGBT converter
- Transparent enclosure to allow visualization of every part
- IP2x protection to minimize safety hazards
- External banana/BNC type connectors for all devices
- Integrated drive unit offering short-circuit detection/cut-off, power supply failure detection, interlock of IGBTs + galvanic isolation of the user
- Forced-air cooled heatsink

Typical Applications

- Education: One stack can simulate almost all existing industrial applications:
 - 3-phase inverter+brake chopper
 - Buck or boost converter
 - Single phase inverter
 - Single or 3-phase rectifier

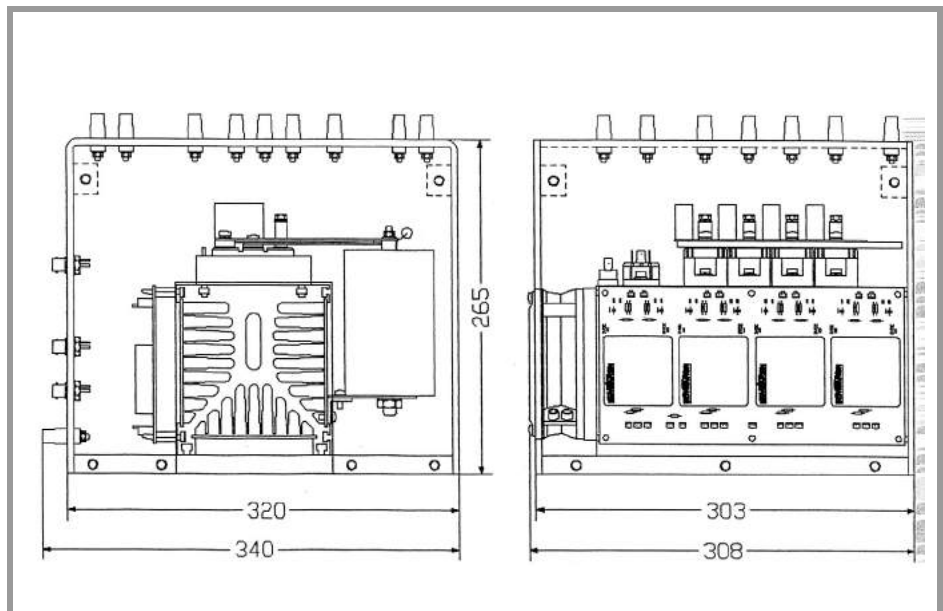
¹⁾ Photo non-contractual



B6U + B6CI + E1CIKF

Circuit	I_{rms} (A)	V_{ac} / V_{dcmax}	Types
B6CI	30	440 / 750	SEMITEACH - IGBT

Symbol	Conditions	Values	Units
I_{rms}	no overload	30	A
V_{CES}	IGBT - 4x SKM 50 GB 123D	1200	V
$V_{CE(SAT)}$	$I_c = 50A, V_{GE} = 15V, \text{chip level}; T_j = 25(125)^\circ C$	2,7 (3,5)	V
V_{GES}		± 20	V
I_c	$T_{case} = 25 (80)^\circ C$	50 (40)	A
I_{CM}	$T_{case} = 25 (80)^\circ C; t_p = 1ms$	100 (80)	A
$V_{in(max)}$	Rectifier - 1x SKD 51/14		
	without filter	3 x 480	V
C_{eqvl}	DC Capacitor bank - Electrolytic 2x 2200 μF /400V total equivalent capacitance	1100 / 800	$\mu F / V$
		V_{DCmax} max. DC voltage applied to the capacitor bank	750
Power supply	Driver - 4x SKHI 22	0 / 15	V
Current consumption	max; per driver	16	mA
Thermal trip	Normally Open type (NO)	71	$^\circ C$



General dimensions

This technical information specifies semiconductor devices but promises no characteristics. No warranty or guarantee expressed or implied is made regarding delivery, performance or suitability.

Incremental encoders

Micro series, with end shaft

Resolution 30...1024 pulses

GI321



GI321 with end shaft

Features

- Micro encoder with end shaft $\varnothing 4$ mm
- Resolution max. 1024 ppr
- Housing $\varnothing 24$ mm
- High rotation speed max. 10000 rpm
- Operating temperature range -20...+85°C
- Integrated spring washer
- Cost-efficient mounting

Technical data - electrical ratings

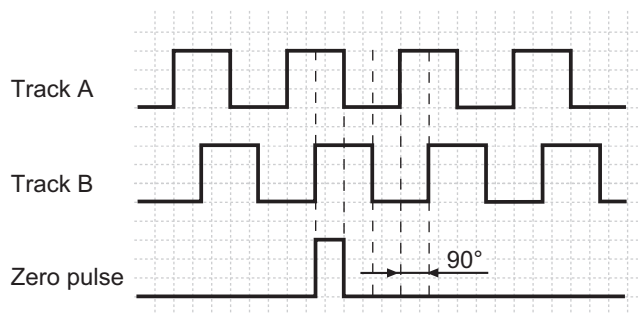
Voltage supply	5 VDC ± 5 % 8...30 VDC
Reverse polarity protection	Yes (8...30 VDC)
Consumption w/o load	≤ 25 mA
Resolution (steps/turn)	30...1024
Reference signal	Zero pulse, width 90°
Sensing method	Optical
Output frequency	≤ 100 kHz
Output signals	A 90° B + N
Output circuit	TTL linedriver final stage Push-pull short-circuit proof
Interference immunity	DIN EN 61000-6-2
Emitted interference	DIN EN 61000-6-4

Technical data - mechanical design

Housing	$\varnothing 24$ mm
Shaft	$\varnothing 4$ mm end shaft
Protection DIN EN 60529	IP 54
Operating speed	≤ 10000 rpm
Starting torque	≤ 0.007 Nm
Material	Aluminium, bare
Operating temperature	-20...+85 °C
Relative humidity	90 % non-condensing
Resistance	DIN EN 60068-2-6 Vibration 10 g, 55-2000 Hz DIN EN 60068-2-27 Shock 30 g, 11 ms
Weight approx.	50 g
E-connection	Cable 1 m

Output signals

Clockwise rotating direction when looking at flange.



Incremental encoders

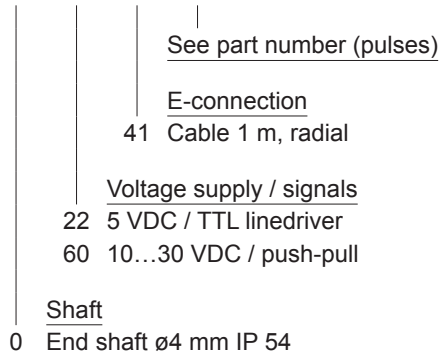
Micro series, with end shaft

Resolution 30...1024 pulses

GI321

Part number

GI321. 0 41



Terminal assignment

Core colour	Assignment
green	Track A
yellow	Track B
grey	Track N (zero pulse)
brown	UB
white	GND
transparent	Shield/Housing

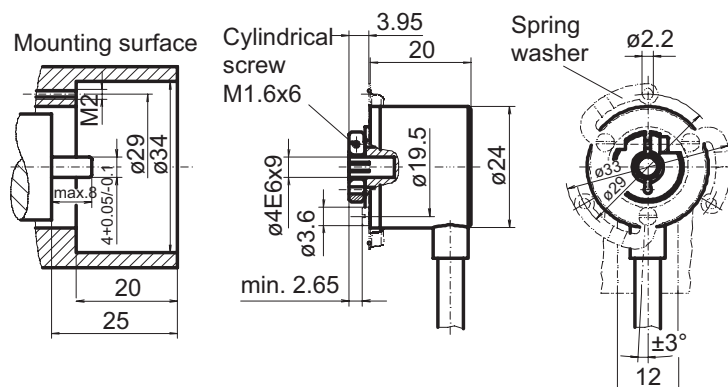
Part number (pulses)

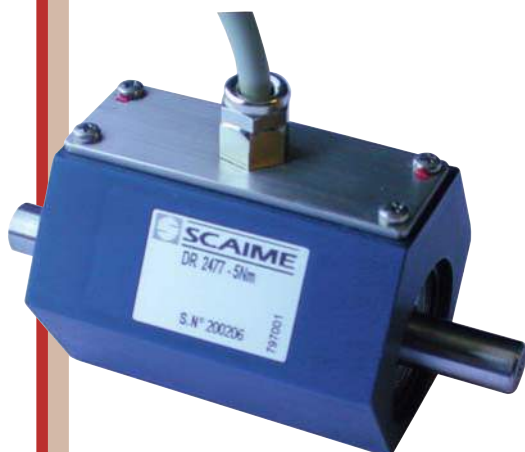
38 (30)	06 (200)	17 (600)
40 (60)	11 (300)	22 (1000)
41 (100)	13 (360)	23 (1024)

Other pulse numbers upon request.

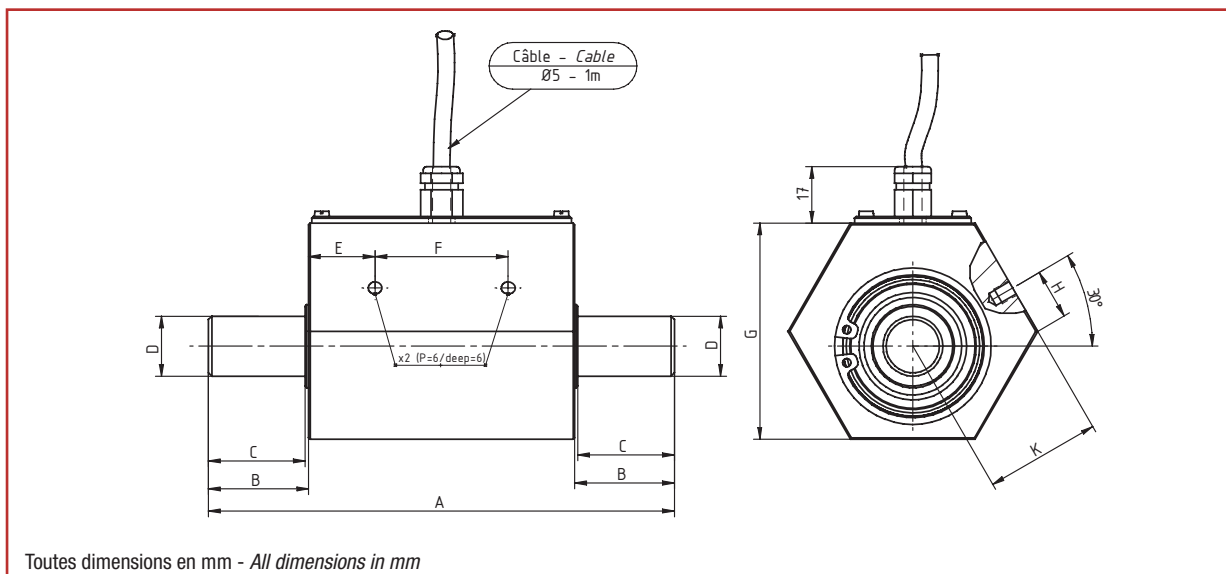
Example: ordering key 23 = 1024 pulses

Dimensions





- Transmission digitale du signal, sans contact
- Maintenance réduite (pas de balais)
- Bande passante : 1 KHz
- Signal de sortie haut niveau (± 5 V)
- Axes lisses
- Contactless digital signal transmission
- Maintenance free
- Cut off frequency : 1 KHz
- Active output signal (± 5 V)
- Shaft without keyway



Couple Nominal Nominal Torque [Nm]	Dimensions Dimensions [mm]									
	A	B	C	ØD	E	F	G	H	K	Ø trous taraudés Threaded holes
0.2 ... 2	100	18	17	8 g6	14.5	35	46	8	26	M4
5 ... 15	100	18	17	10 g6	14.5	35	46	8	26	M4
20 ... 50	140	30	29	18 g6	20	40	65	15	34.8	M5
100 ... 200	160	40	39	22 g6	20	40	65	15	34.8	M5

Nota : l'utilisation de deux accouplements est indispensable, ceux proposés par SCAIME vous assurent fiabilité et performance - The use of two couplings is essential, those proposed by SCAIME ensure you reliability and performance.

Caractéristiques Techniques - Technical specifications

Couple Nominal (C.N.) Nominal Torque [Nm]	Vitesse de rotation max. Max. Speed [tr/min]	Raideur Springrate [Nm/rad]	Moment d'inertie Moment of inertia J en [kg m ²]		Charge axiale max. Max. thrust load [N]
			Côté entraînant Drive side	Côté résistant Test side	
0.2	8 000*	76	1.6×10^{-6}	1.0×10^{-6}	20
0.5	8 000*	1.7×10^2	1.6×10^{-6}	1.0×10^{-6}	30
1	8 000*	3.6×10^2	1.6×10^{-6}	1.1×10^{-6}	40
2	8 000*	3.5×10^2	1.6×10^{-6}	1.1×10^{-6}	40
5	8 000*	8.9×10^2	1.7×10^{-6}	1.1×10^{-6}	50
10	8 000*	8.9×10^2	1.7×10^{-6}	1.1×10^{-6}	50
15	8 000*	8.9×10^2	1.7×10^{-6}	1.1×10^{-6}	50
20	6 000*	8.4×10^3	4.2×10^{-5}	2.1×10^{-5}	1 600
50	6 000*	8.4×10^3	4.2×10^{-5}	2.1×10^{-5}	1 600
100	6 000*	2.0×10^4	4.7×10^{-5}	2.7×10^{-5}	3 000
200	6 000*	2.0×10^4	4.7×10^{-5}	2.7×10^{-5}	3 000

* Option : Possibilité de vitesse supérieure sur demande - Increased number of revolutions on request

Connexion électrique - Electric Connection

+ alim.	+ signal	- signal	- alim.	Masse
+ excit.	+ signal	- signal	- excit.	Shield
marron	jaune	blanc	vert	-
brown	yellow	white	green	-

Caractéristiques - Specifications

MÉCANIQUES		MECHANICAL	
Couple Nominal (C.N.)	Nominal Torque (C.N.)	Voir page - See page 2	Nm
Couple de travail admissible	Service torque*	150	% C.N.
Couple ultime avant rupture	Ultimate torque	> 250	% C.N.
PRÉCISIONS		ACCURACY	
Classe de précision	Accuracy class	0.25	% C.N.
Répétabilité	Repeatability	±0.05	% C.N.
Fréquence de rafraîchissement	Refresh rate	-	KHz
Bande passante (-3 dB)	Cut off frequency (-3 dB)	1	KHz
ÉLECTRIQUES		ELECTRICAL	
Tension d'alimentation	Supply voltage	12 ... 28	Vcc
Courant d'alimentation	Supply current	< 90	mA
Signal de sortie	Output signal	±0 ... 5	V
Courant de sortie max.	Output current max	5	mA
Principe de connexion	Connection type	câble - cable 1	m
GÉNÉRALES		GENERAL	
Plage de température compensée	Nominal temperature range	+5 ... +45	°C
Plage de température opérationnelle	Service temperature range	0 ... +60	°C
Dérive thermique de sensibilité	Temperature coefficient of sensitivity	±0.02	% C.N./°C
Dérive thermique de zéro	Temperature coefficient of zero signal	±0.04	% C.N./°C
Degré de protection (DIN 40 050)	Level of protection (DIN 40 050)	IP50	
Temps de réponse	Response time	< 1	ms

* Attention : le signal de sortie sera en saturation en dessus de 110 %
the output signal will be saturated above 110 %

Options - Options

Signal de sortie	Output signal	±10	V
C.N. spéciales	Special ranges		

Accessoires - Accessories



Accouplement



GM80-PA



PAX-D



BP501 - F 74105 Annemasse Cedex
Tél. : (+33) 4 50 87 78 64
Fax : (+33) 4 50 87 78 42
E.mail : info@scaime.com



Téléchargez tous
nos documents sur :
Download all
our documents from :
www.scaime.com

Agent



Europass Curriculum Vitae



Personal information

First name(s) / Surname(s)	ZAHARIA Mihai Valentin
Address(es)	70-72 Mehedinti Street, Bloc D2, Sc.2, Ap.47, Cluj-Napoca, Romania
Telephone(s)	+40755878615
E-mail	m_valentin.zaharia@yahoo.com , Valentin.Zaharia@mae.utcluj.ro , mihai_valentin.zaharia@ec-lille.fr
Nationality	Romanian
Date of birth	18 th November 1985
Gender	Male

Work experience

Dates	November 2012 –June 2016
Occupation or position held	Research Assistant
Main activities and responsibilities	Research project: <i>'Innovative wind energy conversion micro-system with direct-driven electric generator for residential uses'</i>
Name and address of employer	Technical University of Cluj-Napoca, Romania
Type of business or sector	Engineering
Dates	June 2011 - February 2012
Occupation or position held	Engineer
Main activities and responsibilities	Responsible of service of video cameras and BMS access systems for hotels
Name and address of employer	SC Caliom SRL, Cluj-Napoca, Romania
Type of business or sector	Engineering

Education and training

Dates	2013- 2016
Occupation or position held	Full time PhD student in co-tutelle under the co-supervision of MdC HdR Frédéric Gillon
PhD research activity	<i>"Contributions to the study of switched reluctance machine for automotive integrated starter-alternator application"</i> (<i>"Contributions à l'étude des machines a reluctance variable pour application alerno-démarrreur automobile"</i>)
Name and type of organisation providing education and training	Ecole Centrale de Lille, France, Faculty of Electrical Engineering and Power Electronics Member of Optimization team "Laboratoire d'électrotechnique et d'électronique de puissance de Lille" – L2EP (Research Laboratory of Electrical Engineering and Power Electronics)
Dates	2012- 2016
Occupation or position held	Full time PhD student under the co-supervision of Prof. Dr. Ing. Mircea M. Radulescu
PhD research activity	<i>"Contributions to the study of switched reluctance machine for automotive integrated starter-alternator application"</i>

Name and type of organisation providing education and training	Technical University of Cluj-Napoca, Faculty of Electrical Engineering, Department of Electrical Machines
	Member of The Special Electric Machines and Light Electric Traction (SEMLET) Research Laboratory Faculty of Electrical Engineering, Technical University of Cluj-Napoca, Romania
Dates	February 2012 – June 2012
Occupation or position held	Erasmus student under the co-supervision of Prof. Domenico Casadei
Title of qualification awarded	Realization of the dissertation thesis on electric machine profile; thesis name: “Implementation of an Induction Machine Vector Control for Both Sensored and Sensorless Schemes” .
Name and type of organisation providing education and training	Universita Degli Studi Di Bologna, Italy
Dates	2010-2012
Title of qualification awarded	Master engineer Field of study: Engineering Applied Sciences
Name and type of organisation providing education and training	Technical University of Cluj-Napoca, Romania Faculty of Electrical Engineering
Dates	2007 - 2010
Title of qualification awarded	Engineer Field of study: Engineering Applied Sciences
Name and type of organisation providing education and training	Technical University of Cluj-Napoca, Romania Faculty of Electrical Engineering
Dates	2004 -2007
Title of qualification awarded	College engineer Field of study: Electromechanics
Name and type of organisation providing education and training	Technical University of Cluj-Napoca, Romania Technical, Economic and Administrative College

Publications

2016

- Full paper **Mihai Valentin Zaharia, F. Gillon, M.M. Radulescu, “Design optimization of a switched reluctance machine-based integrated starter-alternator for automotive applications”, XXIIth International Conference on Electrical Machines (ICEM'2016), Lausanne, Switzerland.**
- Full paper **Mihai Valentin Zaharia, F. Gillon, M.M. Radulescu, R. Khliissa, “Fast determination of the optimal control parameters of a switched reluctance machine using space mapping technique”, Optimization and inverse problems in electromagnetism 2016 (OIPE 2016), Rome, Italy.**

2015

- Full paper **Valentin Zaharia, F. Gillon, A. Laczko (Zaharia), A.A. Pop and M.M. Radulescu, „Optimal commutation angles of a switched reluctance motor/generator”, International Conference on Ecological Vehicles and Renewable Energies (EVER 2015), Monaco.**
- Full paper **Andreea Laczko, V. Zaharia, S. Brisset and M.M. Radulescu, „Modelling and simulation of a brushless DC permanent-magnet generator-based wind energy conversion system”, International Conference on Ecological Vehicles and Renewable Energies (EVER 2015), Monaco.**

2014

- Full paper **A. A. Pop, Mircea M. Radulescu, H.Balan, M. Chirca, Valentin Zaharia, „ Electromagnetic Design and Finite-Element Analysis of an Axial-Flux Permanent-Magnet Machine” ,International Conference on Applied and Theoretical Electricity (ICATE 2014), Craiova, Romania**

Languages

<i>Romanian</i>	Native
<i>English</i>	Proficient user (C1)
<i>Italian</i>	Proficient user (C1)
<i>French</i>	Basic user (A2)

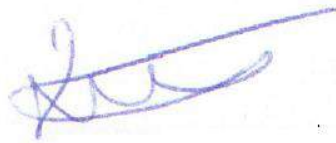
Awards

Dates 15 April – 15 June 2016

Type of scholarship	International mobility of academic study
Name and type of organization providing the scholarship	Agence Universitaire de la Francophonie (AUF), Bureau Europe Centrale et Orientale, Bucuresti, Romania

Competences

Computer skills	MS Office (Word, Excel, PowerPoint), Mathcad, AutoCAD, Matlab, Matlab/Simulink, dSpace, ControlDesk, JMag Designer, JMag Script (VBScript), SolidWorks.
Driving licence	I am the holder of a Romanian drivers licence. Category B vehicle



Mihai Valentin ZAHARIA

Publications

Journal article

- [1] **Mihai Valentin ZAHARIA**, F. Gillon, M.M. Radulescu and R. Khliissa, “Fast determination of the optimal control parameters of a switched reluctance machine using space mapping technique”, *The International Journal of Applied Electromagnetics and Mechanics (IJAEM)*, 10 pp., 2016. **(under review)**
- [2] Dranca M., **Mihai Valentin ZAHARIA**, Chirca M., Radulescu M. M., and Gillon F., “Design and Numerical Magnetic Field Analysis of Switched Reluctance Generators”, *Acta Electrotehnica*, 56(3), (pp. 1-4), 2012

International conferences publications

- [1] **Mihai Valentin ZAHARIA**, F. Gillon, M.M. Radulescu and R. Khliissa, “Fast determination of the optimal control parameters of a switched reluctance machine using space mapping technique”, *The 14th International Workshop on Optimization and Inverse Problems in Electromagnetism (OIPE)*, Rome, Italy, 13-15 September 2016, 10 pp. **(Oral presentation)**
- [2] **Mihai Valentin ZAHARIA**, F. Gillon, M.M. Radulescu, “Design optimization of a switched reluctance machine-based integrated starter/alternator for automotive applications”, *The 22th International Conference on Electrical Machines (ICEM)*, (pp. 1577-1583) Lausanne, Switzerland, 4-7 September 2016. **(Oral presentation)**
- [3] **Mihai Valentin ZAHARIA**, Laczko Andreea Adriana, Pop Adrian Augustin, Radulescu M. Mircea, Frédéric Gillon, “Optimal commutation angles of a switched reluctance motor/generator”, *2015 Tenth International Conference on Ecological Vehicles and Renewable Energies (EVER)*, (pp. 1-8), IEEE, 2015. **(Oral presentation)**
- [4] Laczko Andreea Adriana, **Mihai Valentin ZAHARIA**, Mircea M. Radulescu, Stéphane Brisset, “Modeling and simulation of a brushless DC permanent-magnet generator-based wind energy conversion system”, (pp. 1-7), *2015 Tenth International Conference on Ecological Vehicles and Renewable Energies (EVER)*, IEEE, 2015.
- [5] Pop Adrian Augustin, Radulescu M. Mircea, Horia Balan, Mihai Chirca, **Mihai Valentin ZAHARIA**, “Electromagnetic design and finite-element analysis of an axial-flux permanent-magnet machine”, *2014 International Conference on Applied and Theoretical Electricity (ICATE)*, (pp. 1-4), IEEE, 2014.

Design optimization of a switched reluctance machine-based integrated starter/alternator for automotive applications

M.V. Zaharia, F. Gillon and M.M. Radulescu

Abstract – This paper presents findings from an optimal design study on a switched reluctance machine operating in both motoring and generating modes as automotive integrated starter/alternator. The design optimization approach employs an analytical lumped-parameter modelling of the switched reluctance machine in motor and generator operations, which is refined by finite-element magnetic field analysis of the machine and then implemented in MATLAB/Simulink environment. The objective function of the design optimization problem is the maximization of the average electromagnetic torque of the machine for motor operating mode under constraints on rotor speed, energy efficiency and torque ripple. Steady-state and dynamic simulation results for the optimally-designed switched reluctance machine in motoring and generating modes, as part of automotive integrated starter/alternator operation cycle, are also provided.

Index Terms—design by optimization, integrated starter/alternator, motor and generator operation modes, optimal control, switched reluctance machine

I. INTRODUCTION

Switched reluctance (SR) machine is able to operate either as a motor or generator by adjusting the commutation angles, and thus changing the direction of the electro-mechanical conversion power flow [1], [2]. In SR motor (SRM) operating mode, the electronic power converter regulates the magnitude of the stator phase currents to meet the torque and speed requirements of the mechanical load, while in SR generator (SRG) operation, the power converter energizes the stator phases to support continuous conversion from mechanical energy extracted from the prime mover to electric energy.

In recent years, there has been growing interest of car manufacturers in automotive integrated starter/alternator (ISA) system, which combines into a single electric machine traditionally separate internal-combustion-engine (ICE) crankshaft-mounted starting motor and battery-charging generator. ISA system can also provide stop/start operation and regenerative braking to reduce fuel consumption and exhaust emissions. [3], [4].

SR machine represents a strong contender for automotive ISA applications due to its favorable attributes, like structural simplicity with no magnetic sources on the rotor, cost-effective manufacturing, robustness, high torque

density, fault-tolerant and wide-speed-range capabilities. However, torque ripples, vibrations and acoustic noise are main concern issues with regards to SR machine operation, and shall be adequately addressed [5], [6].

In ISA system, the SR machine has to be optimally designed as SR motor (SRM), for high starting torque during cold-cranking of the ICE, at low speeds, and as SR generator (SRG), for high-efficiency recharging the car battery and providing the electric power for on-board equipment, at high speeds.

The present paper reports on the design optimization approach to three-phase SR machines for SRM/G operation in the context of automotive ISA application. The SRM/G analytical modelling with finite-element magnetic field computation refinement and implementation in MATLAB/Simulink environment is developed in Section II of the paper. Section III addresses the mono-objective constrained design optimization problem of the SR machine for SRM/G proper operation in automotive ISA system. In Section IV, steady-state and dynamic simulations are carried out for the optimally-designed SR machine functioning in SRM/G modes, as part of automotive ISA operation cycle. Some concluding remarks are finally made in Section V.

II. MODELLING OF SR MACHINE IN SRM/G OPERATION

In what follows, by fitly combining the electrical and mechanical lumped-parameter modelling with the finite-element (FE) magnetic field analysis of the SR machine, a simulation model is developed and implemented in MATLAB/Simulink environment for the SRM/G operation of the machine.

The three-phase SR machine considered for study is of 6/8 topology, i.e. having $N_S = 6$ stator poles and $N_R = 8$ rotor poles, with the expedient features of more machine-sizing flexibility, larger available stator-winding space, lesser mass for stator and rotor laminations, higher average electromagnetic torque and lower torque ripple due to increased number of strokes and hence faster rate of change of the stator phase-winding inductance, when compared to conventional 6/4 and 12/8 SR machine topologies with similar volume constraints [7].

The general stator phase-winding voltage equation of the three-phase 6/8 SR machine under study can be written as

$$u_{ph} = Ri_{ph} + \frac{d\psi_{ph}(i_{ph}, \theta)}{dt} = Ri_{ph} + \frac{d(L(i_{ph}, \theta)i_{ph})}{dt}$$

M.V. Zaharia is with the Technical University of Cluj-Napoca, Cluj-Napoca, Romania and with the Ecole Centrale de Lille, Villeneuve d'Ascq / Lille, France (e-mail: Valentin.Zaharia@mae.utcluj.ro)

F. Gillon is with the Ecole Centrale de Lille, Villeneuve d'Ascq / Lille, France (e-mail: frederic.gillon@ec-lille.fr)

M.M. Radulescu is with the Technical University of Cluj-Napoca, Cluj-Napoca, Romania (e-mail: Mircea.Radulescu@emd.utcluj.ro)

$$= Ri_{ph} + \left(L(i_{ph}, \theta) + i_{ph} \frac{\partial(L(i_{ph}, \theta))}{\partial i_{ph}} \right) \frac{di_{ph}}{dt} + i_{ph} \Omega \frac{\partial(L(i_{ph}, \theta))}{\partial \theta}, \quad (1)$$

where u_{ph} , i_{ph} and ψ_{ph} stand for instantaneous values of stator phase-winding voltage, current strength and magnetic flux-linkage, respectively; R and L denote the stator phase-winding resistance and self-inductance, respectively; θ and Ω , are the rotor angular position and speed, respectively. The phase-winding voltage u_{ph} is considered as the (positive) energizing DC-link voltage, for SRM operation, while as the (negative) generated DC-link voltage, for SRG operation.

The SR machine being always driven into magnetic saturation to enhance the utilization of its magnetic circuit, the stator-phase flux-linkage and inductance are non-linear functions of stator-phase current strength and rotor position.

By using the JMAG-Designer software [8], several magnetic field FE analyses in the cross-section of the three-phase 6/8 SR machine (Fig. 1) have been carried out in order to plot the stator phase-winding self-inductance variation in respect of rotor angular position for different phase current strengths (Fig. 2).

By neglecting the nonlinear effects of saturation, i.e. assuming magnetic linearity, the SRM/G voltage equation (1) can be simplified as

$$u_{ph} = Ri_{ph} + L(\theta) \frac{di_{ph}}{dt} + i_{ph} \Omega \frac{\partial L(\theta)}{\partial \theta} \quad (2)$$

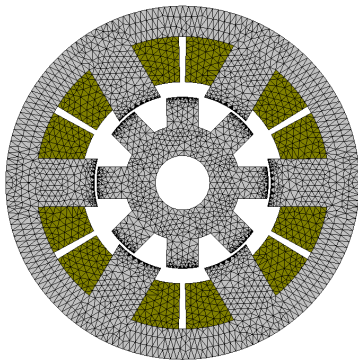


Fig. 1. FE-discretized cross-section geometry of the three-phase 6/8 SR machine under study.

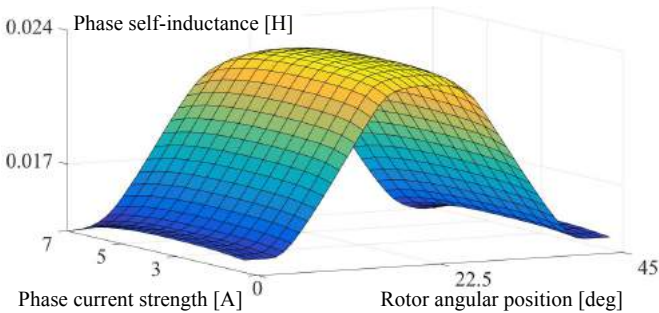


Fig. 2. Stator-phase self-inductance of the three-phase 6/8 SR machine as a function of stator-phase current strength and rotor angular position.

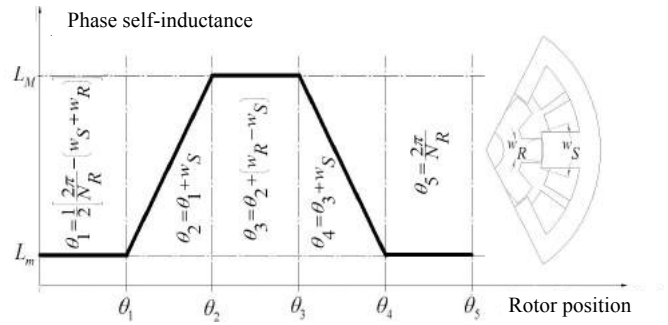


Fig. 3. Ideal stator-phase self-inductance profile with reference to rotor position for the three-phase 6/8 SR machine.

The last term in the above equation is the motional phase back-emf developed in the SR machine, which opposes the increase of stator-phase current during motoring, whereas contributes to the increase of stator-phase current in generating mode of operation. The motional phase back-emf depends on the slope of the phase-winding self-inductance profile with reference to rotor position, which has the ideal shape shown in Fig. 3.

FE-computed and analytically-calculated, maximum L_M and minimum L_m values of the stator-phase self-inductance of the three-phase 6/8 SR machine under study are compared in Fig. 4, showing good agreement. It is to be noted that the maximum L_M value of the phase self-inductance corresponds to the minimum reluctance pole-aligned position.

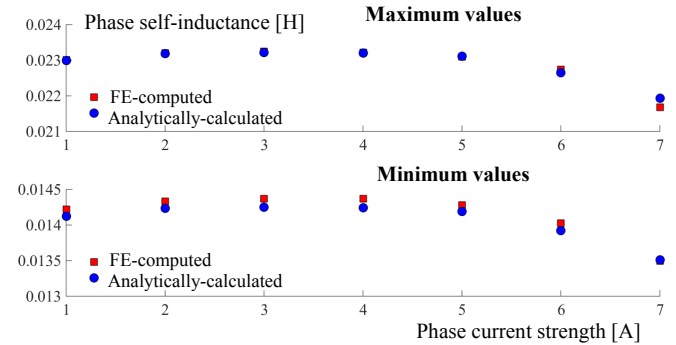


Fig. 4. Comparative FE-computed and analytically-calculated maximum and minimum values of the stator-phase self-inductance of the three-phase 6/8 SR machine.

By solving the SRM/G phase-voltage equation (2), one obtains the time-variation of the phase current strength in motoring and generating operation modes. Fig. 5 displays comparative FE-computed, analytically-calculated and experimental results for the time-variation of the stator-phase current strength in the steady-state motoring operation of the three-phase 6/8 SR machine under study, at constant rotor speed and for two values of the energizing DC-link voltage, i.e. 8 V and 15 V, respectively. As assessed outcome of this comparison, the average value of the phase current strength obtained from experimental results is with 4.4% and 4.5% lower than that determined from FE-computed and analytically-calculated results, respectively, for the case of 15 V energizing DC-link voltage.

It is to be noted that the phase-winding current strength profiles for the motoring and generating modes of the SR machine are the mirror image of each other with reference to

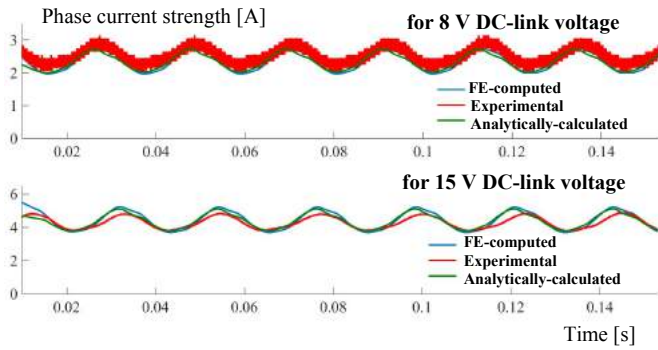


Fig. 5. Comparative FE-computed, analytically-calculated and experimental results for the time-variation of the stator-phase current strength in the steady-state motoring operation of the three-phase 6/8 SR machine, for constant rotor speed and two values of DC-link voltage.

the aligned pole position, for the same speed and symmetrical turn-on and turn-off angles [6].

The phase electromagnetic torque developed by the three-phase 6/8 SR machine can be expressed in terms of phase magnetic co-energy as

$$T_{e,ph}(i_{ph}, \theta) = \left. \frac{\partial W'_{mag,ph}}{\partial \theta} \right|_{i_{ph}=cte} = \left. \frac{\partial \int_0^{i_{ph}} L(i, \theta) i_{ph} di}{\partial \theta} \right|_{i_{ph}=cte} \quad (3)$$

During motoring operation, the SR machine produces positive phase electromagnetic torque for the positive phase self-inductance slope at rotor angles between unaligned and the next aligned pole position in the direction of rotation. In generating mode, due to the negative slope of the phase-winding inductance from aligned to unaligned pole position in the direction of rotation, negative phase electromagnetic torque is produced.

The SRM/G simulation model has been developed and implemented in MATLAB/Simulink environment with the block diagram shown in Fig. 6.

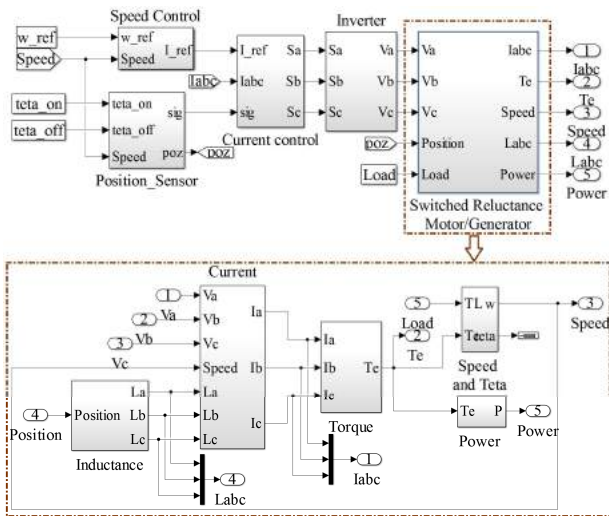


Fig. 6. MATLAB/Simulink model of the three-phase 6/8 SR machine in SRM/G operation.

The simulation modules are the three-phase 6/8 SR machine model, the controller block for hysteresis stator-current control and PI rotor-speed regulation, the power converter with three-phase half-bridge asymmetrical topology and the position sensor block providing the rotor position information for electronic commutation of stator phase currents.

The outputs of the SR machine simulation block are the stator phase currents, the developed electromagnetic torque, the rotor speed and the generated power.

Further application of dynamic simulations using MATLAB/Simulink model together with FE magnetic field analyses enables the design of the three-phase 6/8 SR machine to be optimized for motoring and generating operation.

III. DESIGN OPTIMIZATION OF SR MACHINE FOR AUTOMOTIVE ISA APPLICATION

Having the analytical model implemented in MATLAB/Simulink and the validation by FE method for each step followed in analytical computation, this model can further be used in design optimization process.

The mathematical formulation of the mono-objective constrained optimization problem is

$$\max T_e(x_i, y_j) \quad (4)$$

Subject to $g_k(x_i, y_j), k = 1, \dots, 3$

with $x_i = [x_1, \dots, x_{11}]$, $x_i^l \leq x_i \leq x_i^u$

$y_j = [y_1, \dots, y_6]$,

$g_k = [g_1, \dots, g_3]$, $g_k^l \leq g_k \leq g_k^u$

where x_i represents the vector of the design variables, each variable being between lower and upper limits, x_i^l and x_i^u , respectively, y_j represents the constant inputs, and g_k defines the constraints function, each constraint being between lower g_k^l and upper g_k^u limits.

Fig. 7 shows the design optimization problem with all variable and constant inputs.

The objective function is the average electromagnetic torque maximization towards 150 Nm at 200 rpm rotor speed, in motor operation mode [12] by taking into account the imposed constraints. The SR machine topology for the design optimization is that used before in the FE magnetic field analyses with the rotor speed set as constraint.

Because the FE method is very slow in computation time (about 20 minutes for one simulation) and obtaining one design optimization solution requires rather large number of evaluations, a much faster model is required. The proposed methodology relies on performing the optimization process on the MATLAB/Simulink model shown by the block diagram of Fig.6 (about 10 seconds for one simulation) and then evaluating the obtained optimal configuration by FE magnetic field analysis, made outside the optimization loop.

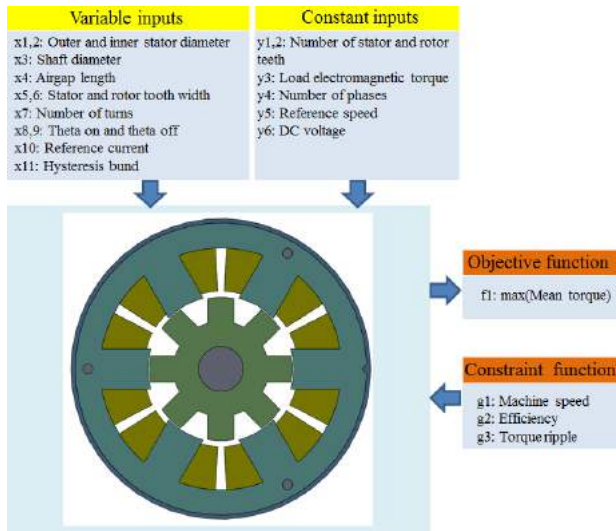


Fig. 7. Design optimization problem of the three-phase 6/8 SR machine.

Output results of both models are confronted, and correction of MATLAB/Simulink model is made, if there is no satisfactory agreement between results. This technique is called the ‘output space mapping technique’, and fully described in [13].

The design optimization is based on sequential quadratic programming (SQP) algorithm under the *fmincon* function. For multiple starting points, it searches the constrained minimum of a scalar function of several variables [14]. After four iterations with more than 5000 evaluations per iteration, one obtains the main design optimization results listed in Table I.

Since during optimization process the magnetic saturation effect is not accounted for, and the phase self-inductance profile is considered linear, the optimized three-phase 6/8 SR machine configuration is imported in the FE-based software and simulated for different values of phase current strength. The data obtained by several FE field analyses are then used

TABLE I
DESIGN OPTIMIZATION RESULTS

Design parameters	Optimal values	Unit
Theta-On commutation angle for motor operation	0	[deg.]
Theta-Off commutation angle for motor operation	20	[deg.]
Hysteresis band	0.05	[A]
Stator outer diameter	255	[mm]
Stator inner diameter	160.4	[mm]
Shaft diameter	96.7	[mm]
Stator pole width	38.4	[mm]
Rotor pole width	27.7	[mm]
Air-gap	0.3	[mm]
Axial length	330	[mm]
Number of turns per phase	14	
Efficiency, at 200 rpm	75	[%]
Torque ripple	45	[%]
Reference speed	200	[rpm]
Number of stator teeth	6	
Number of rotor teeth	8	
Number of phases	3	

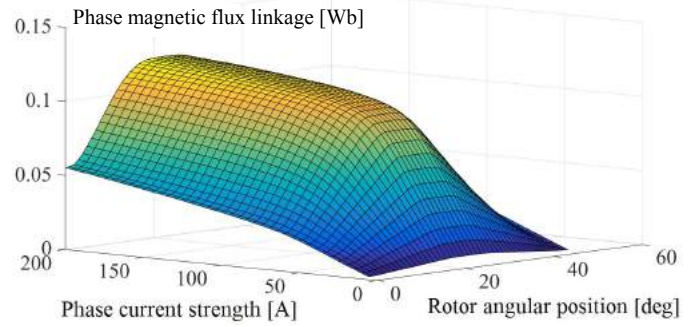


Fig. 8. FE-computed phase magnetic flux linkage as a function of rotor position and phase current strength.

to build the simulation model of the SR machine, in both motor and generator operating modes.

The response surface of the phase magnetic flux linkage as nonlinear function of the phase current strength and rotor angular position, shown in Fig. 8, is obtained for mechanical period of $2\pi/N_R$ and for phase current strength values in the range of 0.5 – 200 [A]. The software used for FE simulations is again JMAG-Designer.

IV. SIMULATION RESULTS FOR THE OPTIMALLY-DESIGNED SR MACHINE

Data from Table I are implemented in MATLAB/Simulink environment using a look-up table. Hysteresis current control and PI speed control are considered in simulations of the three-phase 6/8 SR machine under study.

A. Motor operation mode

The SR machine, in motor operation mode, has to develop an electromagnetic torque of 150 Nm, at a rotor speed of 200 rpm, for the ICE start-up.

Fig. 9 displays the current, speed, electromagnetic torque and power responses of the three-phase 6/8 SR machine operating as a motor (starter).

B. Generator operation mode

The SR machine in generating operation mode is driven by the ICE, at certain speed. The developed electromagnetic torque should be negative, so that the stator-phase energization must correspond to the decreasing slope of the phase self-inductance, when the rotor teeth are just leaving the aligned position in the direction of rotation. PI speed control is used for reference phase current strength determination in hysteresis current control

For the generating mode of the SR machine, optimized θ_{on} and θ_{off} commutation angles have been determined for operation at constant high-speed of 3000 rpm. PI torque control is used to determine the reference phase current strength. In its turn, the reference torque is calculated so that the power is kept constant regardless the rotor speed change.

Fig. 10 displays the current, electromagnetic torque and power responses of the SR machine in generator operation, for $\theta_{on} = 23.5^\circ$ and $\theta_{off} = 45^\circ$.

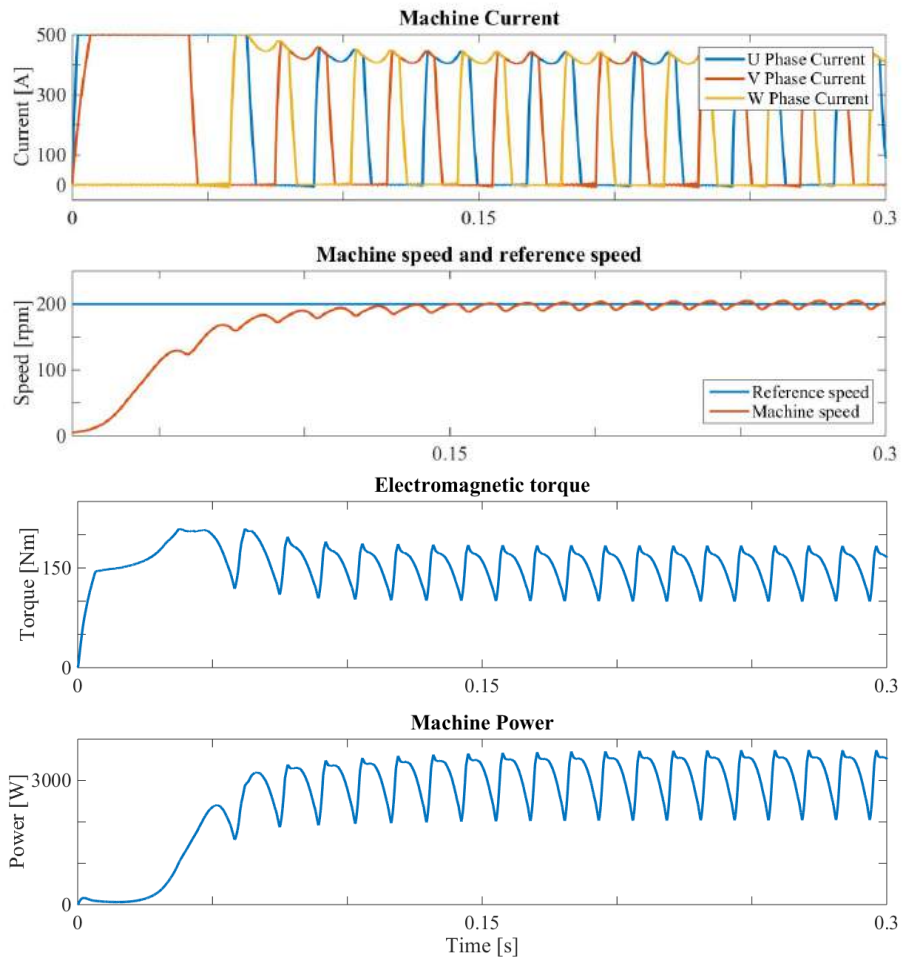


Fig. 9. Simulated steady-state responses in current, speed, electromagnetic torque and output power of the three-phase 6/8 SR machine, in motor operating mode during ICE start-up.

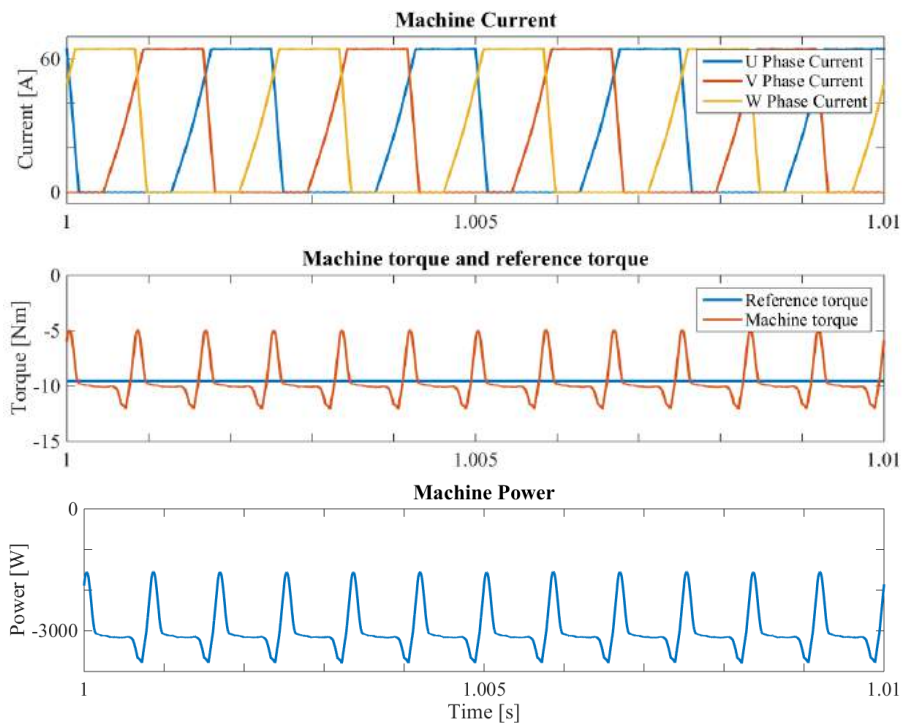


Fig. 10. Simulated steady-state responses in current, electromagnetic torque and output power of the three-phase 6/8 SR machine, in generator operating mode, at 3000 rpm rotor speed.

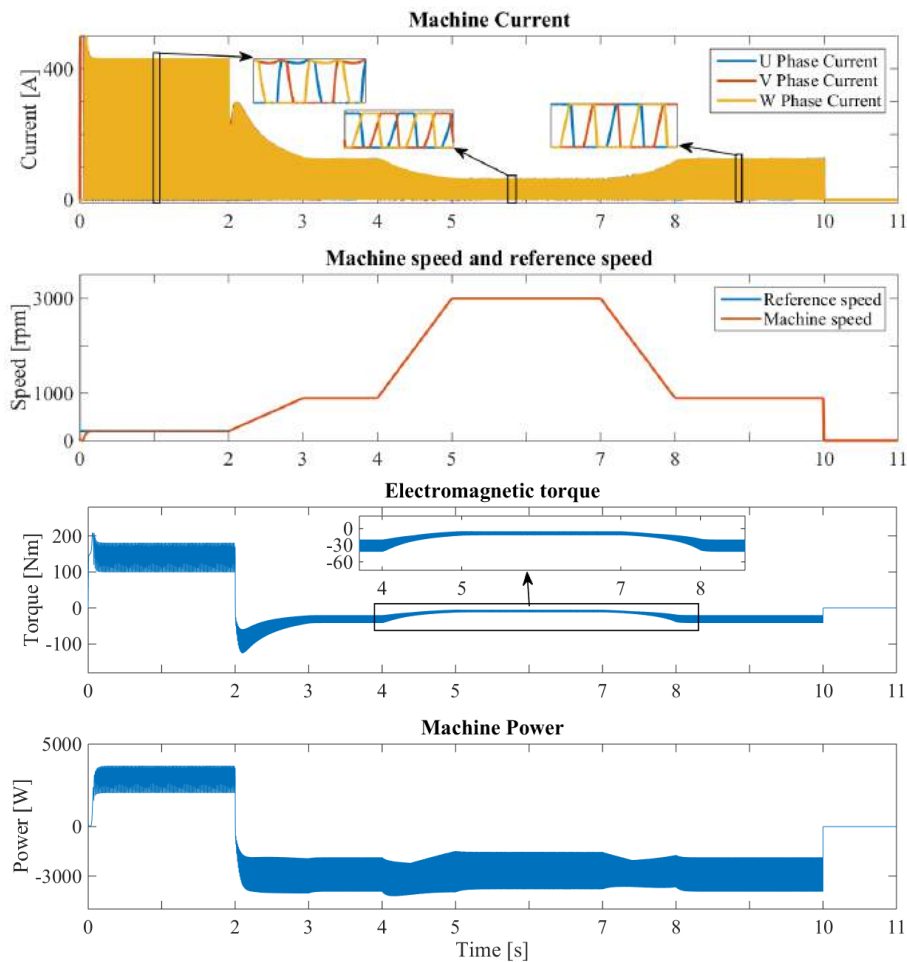


Fig. 11. Simulated dynamic responses in phase current, rotor speed, electromagnetic torque and output power of the three-phase 6/8 SR machine for a part of its operation cycle in automotive ISA application.

C. Integrated starter/alternator

In Fig. 11, simulations are carried out for a small part of the SR-machine operation cycle in automotive ISA application, as follows: for the first two seconds the SR machine starts in motor operation mode, and the reference speed is set to 200 rpm; during this period the ICE is started; at the instant $t_1 = 2$ s, SR machine changes to generator operation mode, the machine being driven by the ICE, and the rotor speed is set to 900 rpm; one the speed reaches 3000 rpm, it is decreased back to 900 rpm, before stopping the machine, at the instant $t_2 = 10$ s.

In the dynamic simulations for the machine operating in motor mode, the commutation angles are constant, corresponding to their values of Table I, whereas for the generator mode, the commutation angles are $\theta_{on} = 23.5^\circ$ and $\theta_{off} = 45^\circ$. The simulated driving cycle in Fig. 11 consists of start-up of the ICE (for SRM operation mode) and then charging of the car battery (for SRG operation mode) at different speeds of the ICE.

The dynamic simulation results prove that three-phase 6/8 SR machine with proper SRM/G control is suitable for automotive ISA applications.

V. CONCLUSIONS

In this paper, the design optimization of three-phase 6/8 SR machines for SRM/G operation for automotive ISA application has been studied.

The SRM/G analytical modelling with FE magnetic field computation refinement and implementation in MATLAB/Simulink environment has been developed.

The mono-objective constrained design optimization problem of the three-phase 6/8 SR machine for SRM/G operation in automotive ISA system has been addressed.

Finally, steady-state and dynamic simulations have been performed for the optimally-designed three-phase 6/8 SR machine functioning in SRM/G mode, as part of automotive ISA operation cycle.

VI. REFERENCES

- [1] R. Krishnan, *Switched Reluctance Motor Drives: Modeling, Simulation, Analysis, Design and Applications*. Boca Raton, FL, USA: CRC Press, 2001.
- [2] H. Chen, J.J. Gu, "Implementation of three-phase switched reluctance machine system for motors and generators", *IEEE/ASME Trans. Mechatron.*, vol.15, no.3, pp.421-432, 2010.
- [3] W. Cai, "Comparison and review of electric machines for integrated starter alternator applications," in *Proc. IEEE Ind. Applicat. Soc. Conf. - IAS 2004*, vol. 1, pp. 386-393, 2004.

VII. BIOGRAPHIES

- [4] P. Zhang, S.S. Williamson, "Recent status and future prospects of integrated starter-generator based hybrid electric vehicles", *IEEE Veh. Power Propuls. Conf. – VPPC 2008*, 8 pp., 2008.
- [5] A. de Vries Y. Bonnassieux, M. Gabsi, F. d'Oliveira, C. Plasse, "A switched reluctance machine for a car starter-alternator system", *Proc. IEEE Int. Conf. Electr. Mach. Drives – IEMDC 2001*, pp. 323–328, 2001.
- [6] B. Fahimi, A. Emadi, R.B. Sepe, Jr., "A switched reluctance machine-based starter/alternator for more electric cars", *IEEE Trans. Energy Convers.*, vol. 19, no. 1, pp. 116–124, 2004.
- [7] P.C. Desai, M. Krishnamurthy, N. Schofield, A. Emadi, "Novel switched reluctance machine configuration with higher number of rotor poles than stator poles: Concept of implementation", *IEEE Trans. Ind. Electron.*, vol. 57, no. 2, pp. 649–659, 2010.
- [8] JMAG–Designer, "<https://www.jmag-international.com>".
- [9] W. Ding, D. Liang, "A fast analytical model for an integrated switched reluctance starter/generator", *IEEE Trans. Energy Convers.*, vol. 25, no. 4, pp. 948–956, Dec. 2010.
- [10] J. Faiz, K. Moayed-Zadeh, "Design of switched reluctance machine for starter/generator of hybrid electric vehicle", *Elect. Power Syst. Res.*, vol. 75, pp. 153–160, 2005.
- [11] M.V. Zaharia, Andreea-Adriana Laczko, A.A. Pop, M.M. Radulescu, F. Gillon, "Optimal commutation angles of a switched reluctance motor/generator", *10th Int. Conf. Ecol. Veh. Renew. Energ. – EVER 2015*, 8 pp., 2015.
- [12] R. Khliissa, S. Vivier, L. A. Ospina Vargas, G. Friedrich, "Application of output Space Mapping method for fast optimization using multi-physical modeling", *Energy Conversion Congress and Exposition (ECCE)*, 2012.
- [13] J.W. Bandler, Q.S. Cheng, S.A. Dakroury, A.S. Mohamed, M.H. Bakr, K. Madsen, J. Sondergaard, "Space mapping: the state of the art", *IEEE Trans. Microwave Theory Techn.*, vol. 52, no. 1, pp. 337–361, 2004.
- [14] J. Agnarsson, M. Sunde, Inna Ermilova, "Parallel optimization in MATLAB", *Project in Computational Science: Report*, January 2013.

Valentin Zaharia was born in Romania in 1985. He received the M.Sc. degree from the Faculty of Electrical Engineering, Technical University of Cluj-Napoca, Cluj-Napoca, Romania, in 2012. Since October 2012, he pursues a full-time Ph.D. study program in Electrical Engineering at the Technical University of Cluj-Napoca under international co-supervision of Ecole Centrale de Lille, Villeneuve d'Ascq/Lille, France. His research interests are in special electric machines for automotive applications.

Frédéric Gillon obtained Engineer Diploma, in 1992 and Ph.D. degree in 1997, both in electrical engineering, from Université des Sciences et Technologies de Lille, Lille, France. Since 1999, he has been Associate Professor with Ecole Centrale de Lille, Villeneuve d'Ascq/Lille, France. His main research subjects are optimization design of electromechanical systems and special electric machines, such as linear, axial- and radial-flux synchronous motors as well as electric railway propulsion systems.

Mircea M. Radulescu received the Dipl.-Ing. degree with honors from the Technical University of Cluj-Napoca, Cluj-Napoca, Romania, in 1978 and the Ph.D. degree from the Polytechnic University of Timisoara, Timisoara, Romania, in 1993, both in electrical engineering. Since 1983, he has been with the Faculty of Electrical Engineering, Technical University of Cluj-Napoca, Romania, where he is currently Full Professor in the Department of Electric Machines and Drives, as well as Head of the Special Electric Machines and Light Electric Traction (SEMLET) Research Laboratory. He is author or co-author of more than 150 published scientific papers in refereed technical journals and international conference and symposium proceedings. His teaching and research activities include classical and special electric machines, computer-aided design of electromechanical devices, design and control of small electronically-commutated motors, actuators and mechatronic drives, light electric traction systems.

Optimal commutation angles of a switched reluctance motor/generator

M.V. Zaharia^{1,2}, Andreea Adriana Laczko (Zaharia)^{1,2}
A.A. Pop¹, M.M. Radulescu¹

¹Technical University of Cluj-Napoca
Cluj-Napoca, Romania
(Valentin.Zaharia@mae.utcluj.ro)

F. Gillon²

²L2EP, Ecole Centrale de Lille
Villeneuve d'Ascq, France
(frederic.gillon@ec-lille.fr)

Abstract — For switched reluctance machines, a major problem is the torque ripple, which causes increased and undesirable acoustic noise and possible irregular speed. This paper aims at determining optimal turn-on and turn-off angles for torque ripple reduction of a three-phase 6/8 switched reluctance motor/generator. A commutation-angle optimization technique is therefore implemented for both motoring and generating operation modes over an extended speed range.

Keywords — switched reluctance motor/generator, torque ripple, turn-on and turn-off angles, optimization

I. INTRODUCTION

Switched reluctance machine is capable of operating as motor and also as generator (SRM/G) by adjusting the commutation angles, and thus changing the direction of the conversion power flow [1, 2]. In SRM operation mode, the electronic power converter regulates the magnitude of the stator current to meet the torque and speed requirements of the mechanical load. In SRG operation, the power converter energizes the stator phases to support continuous conversion from mechanical energy to electrical energy by extracting it from the prime mover. Belonging to the class of doubly-salient reluctance machines, SRM/G together with its electronic power converter and controller has the advantages of simple and rugged brushless machine structure, no high switching frequency of the power converter, good reliability of the machine and power converter, as well as low inertia and fault tolerance capability. All these issues conspire to favour SRM/G in high-speed applications.

In recent years, there has been an increasing interest in using SRM/G as integrated starter-alternator for more-electric-aircraft or more-electric-car engines, to generate electric power and also to provide engine starting [3, 4]. This is because SRM/G has the potential of higher

reliability, less manufacturing cost and faster dynamic response than its permanent-magnet machine contender. However, SRM/G exhibits noticeable torque ripple and acoustic noise. The torque ripple is due to highly nonlinear and discrete nature of the torque production mechanism, which is significant at the commutation instants. Besides, traditional closed-loop current control scheme for SRM/G brings large acoustic noise due to variable switching frequency [5]. The control key in SRM/G operation is to precisely synchronize the stator-phase current pulses with the rotor position, in order to accomplish maximum machine efficiency with reduced torque ripple.

In this context, the aim of the present work is to determine the optimal turn-on and turn-off angles for torque ripple reduction of a three-phase SRM/G in 6 stator poles/ 8 rotor poles configuration (Fig.1).

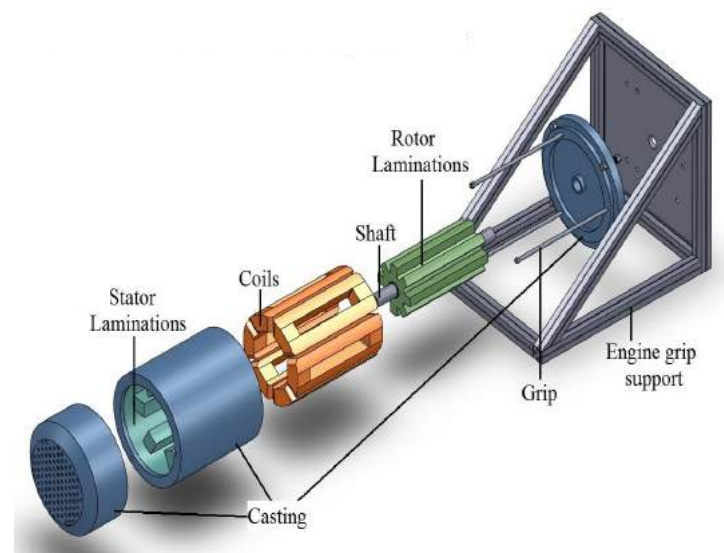


Fig. 1. Exploded view of the SRM/G under study

II. SRM/G SIMULATION MODEL

To solve the problem regarding torque ripple, an analytical model of SRM/G is implemented in MATLAB/Simulink environment, comprising calculus relations for the stator-phase voltages, inductances, electromagnetic torque and torque ripple.

A. Voltage computation

The applied voltage on the stator phase equals the sum of resistive voltage drop and time-derivative of the linkage flux:

$$V_1 = r_1 \cdot i_1 + \frac{d\phi_1}{dt}, \quad (1)$$

where ϕ_1 and i_1 are the magnetic flux and the current of phase 1, respectively.

If the mutual inductance between windings is neglected, the matrix form of stator-voltage equations for the considered three-phase SRM/G can be written as

$$\begin{bmatrix} v_1 \\ v_2 \\ v_3 \end{bmatrix} = [R_1 \quad R_2 \quad R_3] \cdot \begin{bmatrix} i_1 \\ i_2 \\ i_3 \end{bmatrix} + \begin{bmatrix} L_1 & 0 & 0 \\ 0 & L_2 & 0 \\ 0 & 0 & L_3 \end{bmatrix} \cdot \frac{d}{dt} \begin{bmatrix} i_1 \\ i_2 \\ i_3 \end{bmatrix} + \frac{d}{d\theta} \begin{bmatrix} L_1 & 0 & 0 \\ 0 & L_2 & 0 \\ 0 & 0 & L_3 \end{bmatrix} \cdot \begin{bmatrix} i_1 \\ i_2 \\ i_3 \end{bmatrix} \cdot \begin{bmatrix} \frac{d\theta_1}{dt} & \frac{d\theta_2}{dt} & \frac{d\theta_3}{dt} \end{bmatrix} \quad (2)$$

where $\frac{d\theta}{dt}$ is the rotor angular speed (rad/s), R the electrical resistance of each stator phase and $\frac{dL}{d\theta}$ the inductance slope.

B. Inductance computation.

An important step in writing the analytical model of the SRM/G is to compute the magnetic flux of one phase function of the current and the rotor position. By taking into consideration a perfectly aligned position between the stator and the rotor teeth (Fig.2a) the maximum inductance expression can be easily found below [7]:

$$L_M = \mu_0 \cdot \frac{N^2 \cdot l_a \cdot w_R \cdot D_{oR}}{2g}, \quad (3)$$

where N is the number of turns per phase winding, l_a the machine axial length, g is the air-gap, D_{oR} the outer diameter of the rotor and w_R the rotor pole-arc. The fringing and the end effects are neglected in (3).

For determining the value of the minimum inductance, L_m , corresponding to the unaligned position between stator and rotor teeth, the design parameters of a prototype

SRM/G were introduced in *JMAG-Designer* software, in order to build a finite-element (FE) field-analysis model (Fig.2). The rotor was gradually rotated until the rotor teeth reached the unaligned position of Fig.2, *b*. Further, the overlapped surface between stator and rotor teeth was measured, and using equation (3), but with the measured overlapping surface, the minimum inductance value was determined.

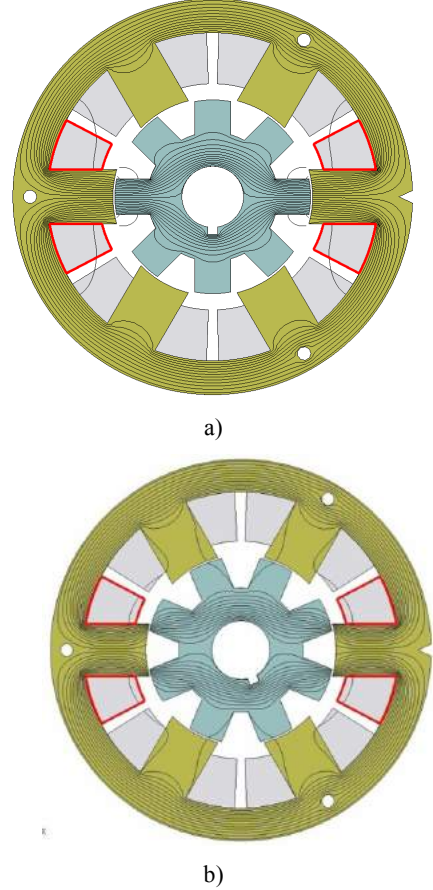


Fig.2. Magnetic flux distribution in the 6/8 SRM/G for aligned position (a) and unaligned position (b)

In Fig.3, inductance characteristics of the prototype three-phase SRM/G are represented for different current values, i.e. FE-computed inductance characteristics are marked by (red) squares, and experimentally-obtained (on prototype SRM/G) inductance characteristics are marked by (blue) triangles. The experimental determination of the maximum and minimum inductances of the SRM/G prototype has been performed by supplying one stator phase with different voltages, measuring the applied voltage, current and resistance values, and computing the inductance values by the following formula [10]:

$$L = \frac{1}{2\pi f} \sqrt{\left(\frac{U}{I}\right)^2 - R^2} \quad (4)$$

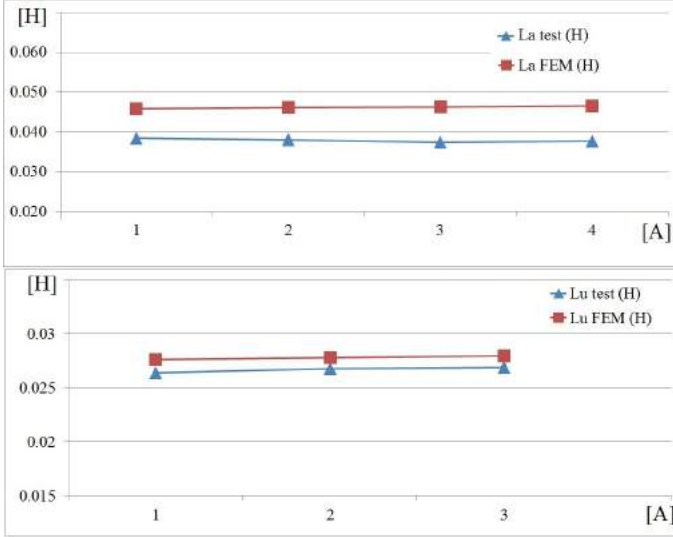


Fig.3. FE-computed and experimentally-obtained inductance characteristics of the prototype three-phase SRM/G, for aligned position (upper) and unaligned position (lower).

with the frequency of the power supply of 50 Hz and the value of the measured resistance of $R = 2.98 \Omega$ per phase. In Fig.4 is represented the ideal waveform of the inductance as function of rotor angular position [1].

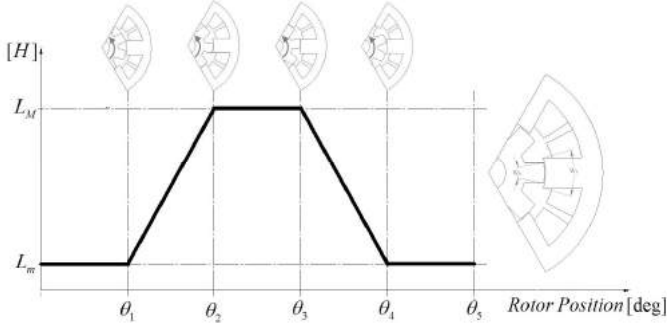


Fig.4. Idealized phase-inductance characteristic of the three-phase SRM/G as a function of rotor angular position

$$\theta_1 = \frac{1}{2} \left[\frac{2\pi}{N_R} - (w_S + w_R) \right] \quad (5)$$

$$\theta_2 = \theta_1 + w_R \quad (6)$$

$$\theta_3 = \theta_2 + (w_S - w_R) \quad (7)$$

$$\theta_4 = \theta_3 + w_R \quad (8)$$

$$\theta_5 = \frac{2\pi}{N_R}, \quad (9)$$

where N_R is the number of rotor teeth, w_S the stator-tooth width and w_R the rotor-tooth width.

To determine the θ_{on} angle (eq.5) for the SRM operating mode, the instant when the inductance starts to increase (when the rotor tooth starts to overlap the stator pole) must be known. The θ_{off} angle (eq.6) corresponds to the instant when the rotor tooth is perfectly aligned with the corresponding stator pole, i.e. when the proper stator-phase energizing must end.

For the SRG operation mode, the θ_{on} angle (eq.6) corresponds to the instant when the excitation of the proper stator-phase must occur, while the θ_{off} angle (eq.7) corresponds to the instant when the rotor exits the aligned position.

C. Electromagnetic torque computation

The calculus expression of the electromagnetic torque for a three phase machine can be written as

$$T_e = \frac{1}{2} \left\{ i_1^2 \frac{dL_1}{d\theta} + i_2^2 \frac{dL_2}{d\theta} + i_3^2 \frac{dL_3}{d\theta} \right\} \quad (10)$$

In the above relation, the SRM/G magnetic circuit saturation effect and the mutual inductances were neglected.

D. Torque ripple computation

The torque ripple is calculated by the following formula [10]:

$$T_{rip} = \frac{T_{max} - T_{min}}{T_{av}} \quad (11)$$

where T_{max} , T_{min} and T_{av} are the maximum, minimum and average values of the SRM/G developed torque, respectively.

The MATLAB/Simulink model for determination of SRM/G optimal commutation angles is presented in Fig.5.

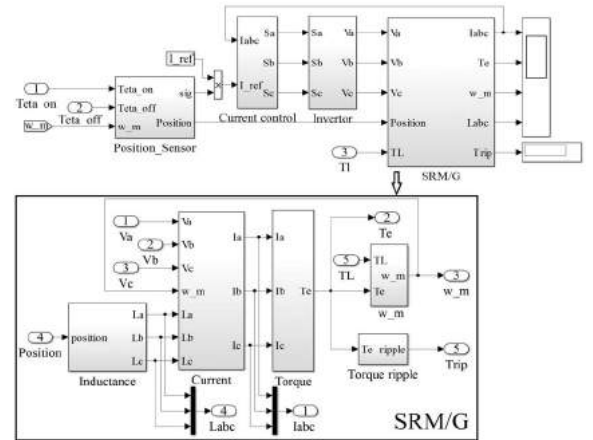


Fig.5. MATLAB/Simulink model of the SRM/G

In the SRM/G simulation model, hysteresis current control was implemented, sampling time of $\tau_s = 2 \cdot 10^{-5}$ s was used, and DC-source supply of 130 V was considered.

The outputs of the SRM/G simulation block are the current, torque and torque ripple, speed and inductance. The position-sensor block yields the rotor position (computed from rotor speed) for electronic switching of SRM/G and energizing its right stator phase at right time via the three-phase half-bridge asymmetrical inverter with the topology and power switches signals shown in Fig.6.

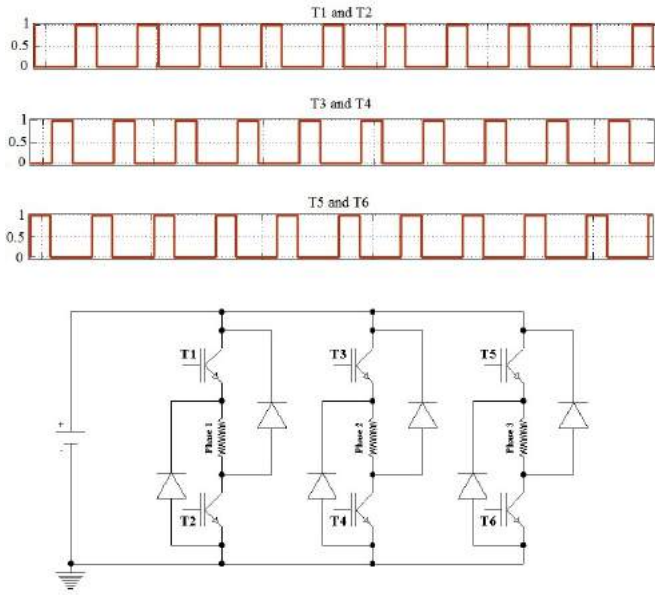


Fig.6. Three-phase half-bridge asymmetrical inverter

III. SRM/G OPTIMAL COMMUTATION ANGLES

In this section, SRM/G optimal commutation angles are determined for both motoring and generating operation modes.

The reference current is set to 4 A value, and theta-on and theta-off angles are chosen using equations (5) – (9).

To obtain the best switching angles 5 different rotor speeds/loads were used in order to get more accurate values of these angles. If we choose to use a smaller number of rotor speeds/loads (i.e. only two) other values for these angles are obtained, less accurate ones.

A. SRM optimal commutation angles

For the SRM operation mode, torque-ripple characteristics as a function of both theta-on and theta-off commutation angles are computed (Figs.7 and 8) at constant speed and constant mechanical load, respectively. For the turn-on angle, the band values are chosen between -1° and 2° with an increasing step of 0.2° ,

whereas for the turn-off angle, the band values are chosen from 17° to 24° with an increasing step of 0.5° .

In Fig.7, the surface characteristics of SRM torque ripple for 5 different constant values of the rotor speed (700, 1000, 1300, 1600 and 2000 rpm) are represented.

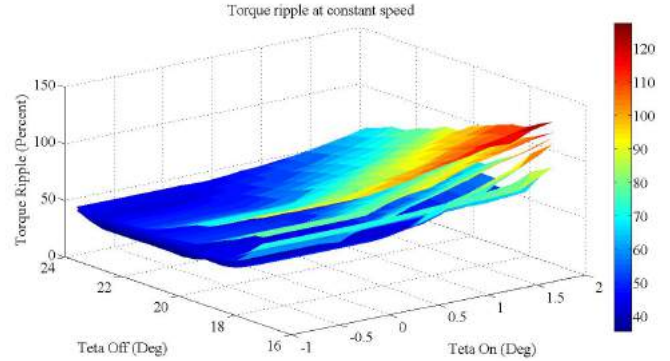


Fig.7. SRM torque-ripple characteristics as a function of both theta-on and theta-off commutation angles, at constant speed

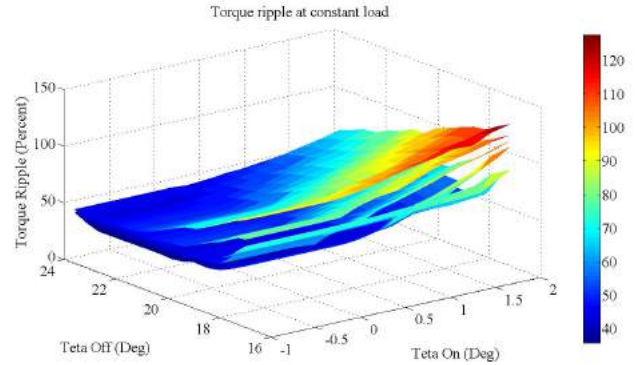


Fig.8. SRM torque-ripple surface characteristics as a function of both theta-on and theta-off commutation angles, at constant load torque

Fig.8 represents the surface characteristics of SRM torque ripple for 5 different mechanical loads, chosen so that the corresponding rotor speed is around of 700, 1000, 1300, 1600 and 2000 rpm, respectively.

To determine the SRM optimal commutation angles, that ensure the lowest torque ripple, the mean-value computation method was used: for each rotor speed and load torque value, respectively, the commutation angles were determined, such that the lowest torque ripple was obtained for each case; hence, 5 pairs of values for theta-on and theta-off angles were obtained, as recorded in Table 1; from these 5 paired-values for theta-on and theta-off angles, an average paired-value was obtained and considered as the best one, i.e. $\theta_{on} = 0.04^\circ$ and $\theta_{off} = 21.692^\circ$, for constant rotor speed and $\theta_{on} = -0.118^\circ$ and $\theta_{off} = 21.7^\circ$, for constant load torque, respectively (Table 3).

TABLE 1. SRM OPTIMAL THETA-ON AND THETA-OFF ANGLES FOR DIFFERENT VALUES OF ROTOR SPEED AND LOAD TORQUE

Speed	Theta -On	Theta -Off	Ripple Torque	Load Torque	Theta -On	Theta -Off	Ripple Torque
700	0	22.06	34.67	0.2	-0.16	19.82	35.66
1000	0	21.14	38.46	0.15	-0.16	22.64	39.6
1300	0	22.06	40.3	0.11	0.05	20.76	41.77
1600	0	20.22	43.03	0.06	-0.16	22.64	43.92
2000	0.2	22.98	42.47	0.001	-0.16	22.64	43.04

B. SRG optimal commutation angles

For the SRG operation mode, a prime mover is needed and the commutation angles must be shifted, so that the excitation stage occurs when the rotor tooth is perfectly aligned with the corresponding stator pole. If the prime mover displaces the SRG rotor from this aligned position, an opposite (negative) electromagnetic torque is developed by the machine, which thus operates as a generator.

Similarly to the motoring operation case, SRG torque-ripple characteristics are computed (using MATLAB) as a function of both theta-on and theta-off commutation angles (Figs.9 and 10) at constant speed and constant mechanical load, respectively. For the turn-on angle, the band values are chosen between 10° and 15°, whereas for the turn-off angle, the band values are chosen from 35° to 40° (with an increasing step of 0.25° in both cases).

In Fig.9, the surface characteristics of SRG torque ripple for 5 different constant values of the rotor speed (700, 1000, 1300, 1600 and 2000 rpm) are represented. Fig.10 represents the surface characteristics of SRG torque ripple for 5 different electromagnetic torques, chosen so that the corresponding rotor speed is around of 700, 1000, 1300, 1600 and 2000 rpm, respectively.

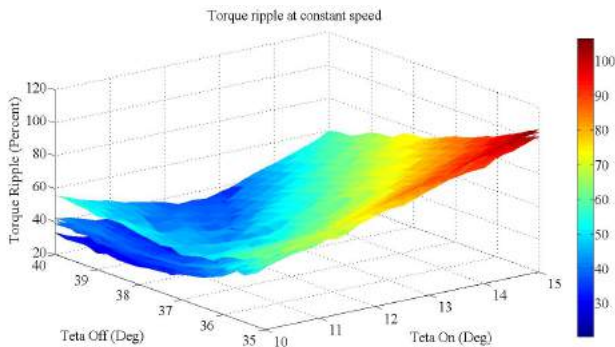


Fig.9. SRG torque-ripple characteristics as a function of both theta-on and theta-off commutation angles, at constant speed

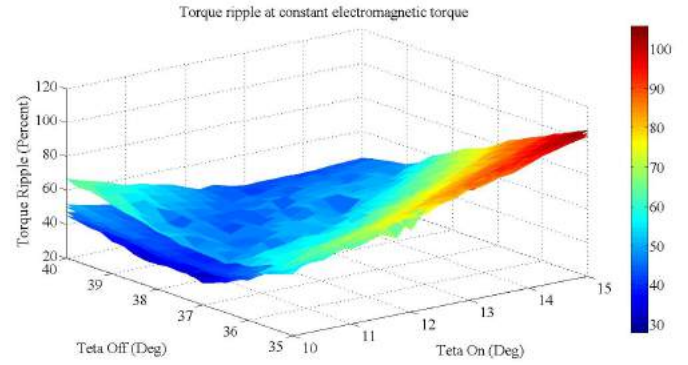


Fig.10. SRG torque-ripple surface characteristics as a function of both theta-on and theta-off commutation angles, at constant electromagnetic torque

Similarly to the SRM case, the mean-values computing method is used for determining the best commutation angles of SRG operation mode, from the 5 pairs of values for theta-on and theta-off angles recorded in Table 2. The obtained average paired-values, considered as the best ones, were $\theta_{on} = 12.25^\circ$ and $\theta_{off} = 40^\circ$, for constant speed and $\theta_{on} = 13.05^\circ$ and $\theta_{off} = 39.7^\circ$, for constant electrical load, respectively (Table 4).

TABLE 2. SRG OPTIMAL THETA-ON AND THETA-OFF ANGLES FOR DIFFERENT VALUES OF ROTOR SPEED AND LOAD TORQUE

Rotor Speed	Theta -On	Theta -Off	Ripple Torque	Elmag Torque	Theta -On	Theta -Off	Ripple Torque
700	12.75	40	21	-0.29	12	39.75	37.72
1000	12.25	40	20.81	-0.32	12.25	39.75	33.01
1300	12.25	40	21.03	-0.36	14.75	39.75	33
1600	11.5	40	20.29	-0.39	13.5	39.75	27.92
2000	13.75	40	30.34	-0.41	12.75	39.5	41.34

IV. SIMULATION RESULTS

A. Simulation results for SRM operation mode

Table 3 presents the SRM torque ripple values for the optimal commutation angles determined above by the average-values computation method, in comparison with the torque ripple values obtained for theoretical commutation angles. It can be found, that SRM torque ripple values

- are reduced (in average) by 22.07% for optimal commutation angles determined by the average-values computation method as compared to torque ripple values obtained for theoretical commutation angles, at constant rotor speed.

- are reduced (in average) by 23.18% for optimal commutation angles determined by the average-values

computation method as compared to torque ripple values obtained for theoretical commutation angles, at constant load torque.

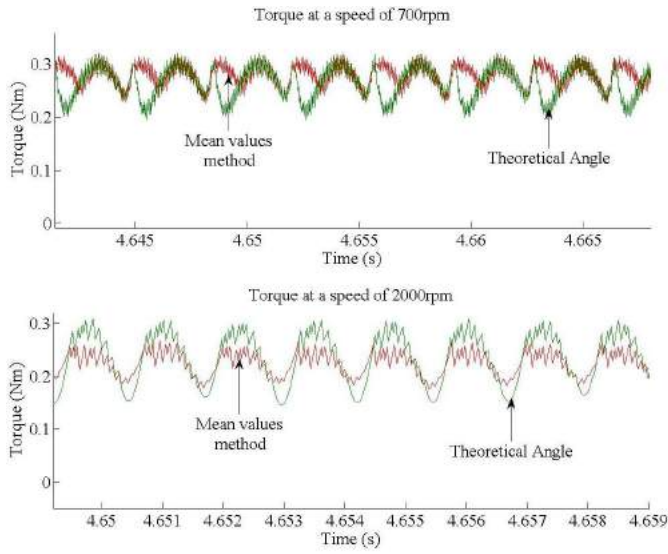


Fig.11. Torque behavior depending on the commutation angles at two different speeds.

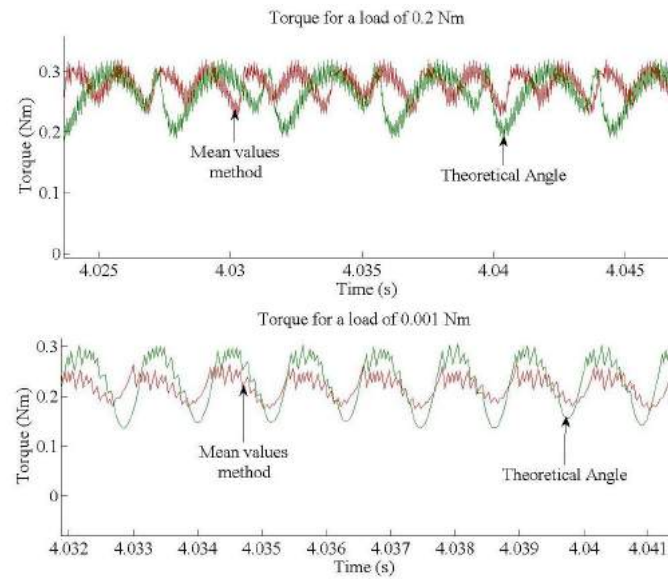


Fig.12. Torque behavior depending on the commutation angles for two different loads.

TABLE 3. COMPARATIVE SIMULATION RESULTS FOR SRM OPERATION MODE

Speed (rpm)	Ripple Torque (%)	Average Torque (Nm)	Commutation Angles (Deg)	Percentage reduction (%)
700	36.22	0.2794	Computed values by the average-value computation method	26.67
1000	40.17	0.2726		4.27
1300	43.49	0.262		12.30

1600	44.28	0.2472	$\theta_{on} = 0.04^\circ$	28.81
2000	47.17	0.2247	$\theta_{off} = 21.692^\circ$	38.28
700	49.39	0.2655	Theoretical values $\theta_{on} = -0.17^\circ$ $\theta_{off} = 17.94^\circ$	
1000	41.96	0.2648		
1300	49.59	0.2592		
1600	62.2	0.2513		
2000	76.43	0.2371		

Load Torque (Nm)	Ripple Torque (%)	Average Torque (Nm)	Commutation Angles (Deg)	Percentage reduction (%)
0.2	35.99	0.2786	Computed values by the average-value computation method $\theta_{on} = -0.118^\circ$ $\theta_{off} = 21.7^\circ$	31.59
0.15	40.75	0.2706		3.37
0.11	44.03	0.2587		5.19
0.06	44.9	0.2418		33.20
0.001	47.85	0.2183		42.56
0.2	52.61	0.2647	Theoretical values $\theta_{on} = -0.17^\circ$ $\theta_{off} = 17.94^\circ$	
0.15	42.17	0.2649		
0.11	46.44	0.2576		
0.06	67.22	0.2448		
0.001	83.31	0.2279		

In Fig.11 and 12 is represented the waveform of the electromagnetic torque for the smallest and the biggest load torque (Fig.12) and for the lowest and highest speed (Fig.11). For each case, the angles used were those obtained through the mean values method and the results were compared to the results obtained with the theoretical angle. The exact values of the used angles (Figs.11 and 12), of electromagnetic torque and ripple torque can be found in Table 3.

B. Simulation results for SRG operation mode

Table 4 presents the SRG torque ripple values for the optimal commutation angles determined above by the average-value computation method, in comparison with the torque ripple values obtained for theoretical commutation angles. It can be found, that SRG torque ripple values

- are reduced (in average) by 46.1% for optimal commutation angles determined by the average-values computation method as compared to torque ripple values obtained for theoretical commutation angles, at constant rotor speed.

- are reduced (in average) by 19.7% for optimal commutation angles determined by the average-values computation method as compared to torque ripple values obtained for theoretical commutation angles, at constant (negative) electromagnetic torque.

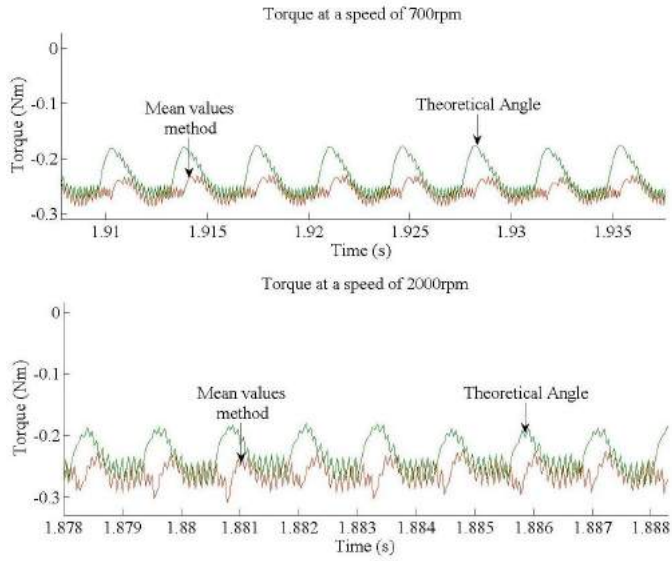


Fig.13. Torque behavior depending on the commutation angles at two different speeds

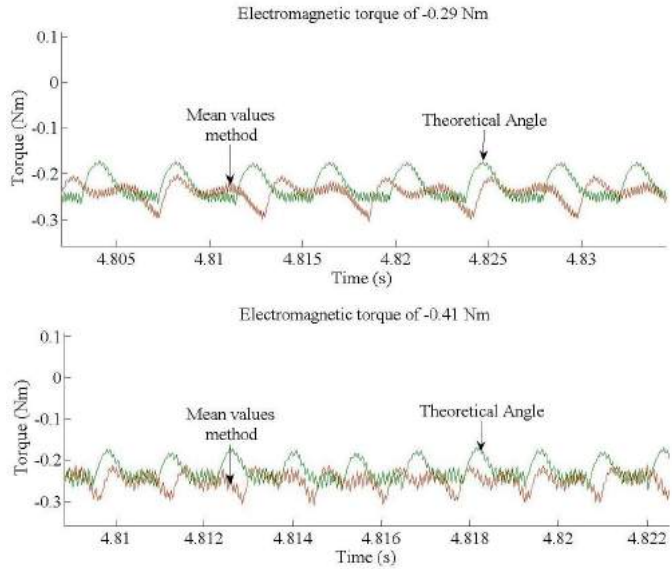


Fig.14. Torque behavior depending on the commutation angles at two different electromagnetic torque

Fig.13 and Fig.14 illustrate the waveforms of the electromagnetic torque for the generator mode. For the realization of Fig.13 the speed of the generator was chosen to be constant for the smallest value (700rpm) and the biggest value (2000rpm). In Fig.14 the electromagnetic torque was chosen to be constant for a value of -0.29 Nm and -0.41 Nm. In both figures (13 and 14) the chosen angles were the ones calculated with the method of mean values and the theoretical angle. The exact values of ripple torque and electromagnetic torque are shown in Table 4. As it can be noticed from Table 4, Fig.13 and Fig.14 the value of the electromagnetic torque varies with the angles, therefore not only the ripple torque

depends on the commutation angles but also the electromagnetic torque.

TABLE 4. COMPARATIVE SIMULATION RESULTS FOR SRG OPERATION MODE

Speed (rpm)	Ripple Torque (%)	Average Torque (Nm)	Commutation Angles (Deg)	Percentage reduction (%)
700	24.15	-0.258	Computed values by the average-value computation method $\theta_{on} = 12.25^\circ$ $\theta_{off} = 40^\circ$	48.98
1000	20.81	-0.258		57.00
1300	21.03	-0.259		57.06
1600	28.39	-0.258		45.62
2000	34.47	-0.259		22.00
700	47.33	-0.238	Theoretical values $\theta_{on} = 12.05^\circ$ $\theta_{off} = 37.15^\circ$	
1000	48.4	-0.236		
1300	48.98	-0.236		
1600	52.21	-0.2401		
2000	44.19	-0.2317		

Elmag Torque (Nm)	Ripple Torque (%)	Average Torque (Nm)	Commutation Angles (Deg)	Percentage reduction (%)
-0.29	40.54	-0.242	Computed values by the average-value computation method $\theta_{on} = 13.05^\circ$ $\theta_{off} = 39.7^\circ$	10.82
-0.32	35.69	-0.249		15.21
-0.36	35.3	-0.255		19.94
-0.39	29.12	-0.258		33.65
-0.41	43.38	-0.249		16.22
-0.29	45.46	-0.225	Theoretical values $\theta_{on} = 12.05^\circ$ $\theta_{off} = 37.15^\circ$	
-0.32	42.09	-0.23		
-0.36	44.09	-0.235		
-0.39	43.89	-0.2385		
-0.41	51.78	-0.2237		

V. CONCLUSION

The aim of this paper was the determination of optimal turn-on and turn-off angles for torque ripple reduction of a three-phase 6/8 SRM/G. An analytical model of SRM/G and a commutation-angle optimization technique for reducing the torque ripple were implemented in MATLAB /Simulink environment, for both motoring and generating operation modes over an extended speed range. Simulation-based performance analysis results for SRM/G with hysteresis current-control and commutation angles optimized to reduce torque ripple have been also provided and discussed.

REFERENCES

- [1] R. Krishnan, *Switched reluctance motor drives: modeling, simulation, analysis, design and applications*, CRC Press, Boca Raton, USA, 2001.
- [2] H. Chen, J.J. Gu, "Implementation of three-phase switched reluctance machine system for motors and generators," *IEEE/ASME Trans. Mechatron.*, vol.15, no.3, pp.421-432, 2010.
- [3] R. Hall *et al.*, "Design and initial testing of an outer rotating segmented rotor switched reluctance machine for an aero-engine shaft-line-embedded starter/generator", *Proc. IEEE Int. Electr. Mach. Drives Conf. – IEMDC 2005*, pp. 1870–1877.
- [4] B. Fahimi, A. Emadi, R.B. Sepe, Jr., "A switched reluctance machine-based starter/alternator for more electric cars", *IEEE Trans. Energy Convers.*, vol. 19, no. 1, pp. 116–124, 2004.
- [5] J. Sun *et al.*, "Implementation of a high-speed switched reluctance starter/generator system", *Proc. IEEE 15th Int. Conf. Electr. Mach. Syst. – ICEMS 2012*, 5 pp.
- [6] J. Sun *et al.*, "Torque ripple comparison of short-pitched and fully-pitched winding switched reluctance machine", *Proc. IEEE 15th Int. Conf. Electr. Mach. Syst. – ICEMS 2012*, 6 pp.
- [7] Muhammet Garip Yusuf Ozoglu Erkan Mese, "Static analysis of mutually coupled switched reluctance motor with finite element method", *UCTEA The Chamber Of Electrical Engineer.*
- [8] V.V. Prabhu, K.S. Mahesh, C. Renuka, "Simulation of switched reluctance motor/generator with optimum turn-on and turn-off control for the application of variable speed drives", *Proc. IEEE Int. Conf. Sustainable Energy Intell. Syst. – SEISCON 2011*, pp. 501-506.
- [9] C. Mademlis, I. Kioskeridis. "Optimizing performance in current-controlled switched reluctance generators". *IEEE Trans. Energy Convers.*, vol. 20, no. 3, pp. 556-565, 2005.
- [10] D. Ilea, F. Gillon, P. Brochet, M.M. Radulescu, "Comparative finite-element and permeance-network analysis for design optimization of switched reluctance motors", in: *"Computational methods for the innovative design of electrical devices"*, Springer-Verlag, Berlin, Germany, 2011, pp. 304-310.

Contributions à l'étude des machines à reluctance variable et à auto-commutation électronique pour application alterno-démarrreur intégré automobile

Ce travail de recherche est réalisé dans le cadre d'une collaboration internationale entre l'Université Technique de Cluj-Napoca, en Roumanie et Centrale Lille, en France. La thèse présentée porte sur l'optimisation d'une machine triphasée 6/8 à reluctance variable et à auto-commutation électronique (RVAE) en fonctionnement moteur et générateur.

La machine RVAE a une construction simple, ce qui permet une fabrication à faible coût. Toutefois, la machine RVAE a un inconvénient majeur, elle possède intrinsèquement une forte ondulation de couple électromagnétique développé.

Cette thèse a comme premier objectif, de réduire l'ondulation de couple grâce aux paramètres de contrôle dans le mode de fonctionnement moteur, mais également dans le mode de fonctionnement générateur. Par conséquent, un modèle analytique a été développé et mis en œuvre dans un environnement de calcul numérique. Ce modèle tient compte de la géométrie de la machine et peut être simulé dans les deux modes de fonctionnement, en ajustant les angles de commutation des phases. Un outil d'optimisation permettant de trouver les meilleurs paramètres de contrôle a été utilisé. Toutefois, le processus d'optimisation est très lent.

En conséquence, le second objectif de ce travail est de trouver une stratégie pour réduire le temps du processus d'optimisation sans abaisser la précision des résultats. Pour cela, une stratégie de 'mapping' est proposée entre un modèle grossier, mais rapide, et un modèle fin, mais lent. Au cours du travail, il a été démontré que pour avoir une bonne convergence de la stratégie de 'mapping' il est important que les deux modèles aient des tendances similaires. Le choix du modèle grossier impacte fortement la convergence et la précision. Un travail est mené sur le choix du modèle grossier, dans le cadre d'un modèle fournissant des valeurs en fonction du temps. Deux stratégies de 'mapping' ont été utilisées dans cette thèse : 'Output Space Mapping Proportional'(OSMP) et 'Manifold Mapping' (MM). Tout d'abord, ces deux stratégies sont testées sur un modèle mathématique afin de valider le développement réalisé et de comparer sur cet exemple rapide les performances. Ensuite, ces stratégies sont utilisées pour déterminer les paramètres de contrôle optimaux de la machine RVAE étudiée. Le problème d'optimisation est ensuite complété en ajoutant des variables géométriques au processus d'optimisation du contrôle, précédemment traité. Les outils développés sont ensuite utilisés dans le cadre du dimensionnement par optimisation d'un alterno-démarrreur intégré automobile.

Finalement, des expériences et des essais sur un prototype de machine RVAE sont menés afin de valider les résultats du processus d'optimisation du contrôle en mode moteur et générateur.

Chapitre 1

Machine à réluctance variable et à auto-commutation électronique comme alerno-démarrreur intégré

Ce chapitre examine brièvement l'importance de la diminution de la consommation de carburant pour la minimisation des émissions de dioxyde de carbone. Le principe de fonctionnement de la machine RVAE, en moteur et en générateur, est décrit.

Deux possibilités de connexion des systèmes alerno-démarrreur intégré (ADI) dans l'industrie automobile existent. La première possibilité consiste à relier par une courroie la machine électrique au moteur à combustion interne (MCI). La deuxième possibilité consiste à placer la machine électrique entre le MCI et la boîte de vitesses.

A la fin du chapitre, une comparaison en terme de coût et de poids entre les machines RVAE, asynchrones et synchrones à aimants permanents est fourni, permettant de justifier le choix de la machine RVAE pour les applications ADI, notamment grâce à la simplicité de construction du rotor de cette machine avec un coût de fabrication réduit.

Chapitre 2

Modélisation et simulation de la machine à réluctance variable et à auto-commutation électronique

Le deuxième chapitre est consacré à l'approche analytique de la machine triphasée à réluctance variable à six dents au stator et huit dents au rotor. Le comportement électrique et électromagnétique de cette machine est étudié dans ce chapitre. Ensuite, ce modèle analytique sera utilisé dans un processus d'optimisation permettant d'obtenir les grandeurs de contrôle optimales, c'est-à-dire : les angles de commutation et le courant de référence. Ensuite, la complexité du problème d'optimisation est augmentée en ajoutant des variables de dimensionnement aux variables de contrôle. Ainsi, le processus d'optimisation fournit simultanément la meilleure taille et le meilleur contrôle associé.

Dans le deuxième chapitre, certaines topologies classiques et nouvelles de MRV sont fournies. Pour pouvoir démarrer de n'importe quelle position et être capable de changer de sens de rotation, la machine RVAE doit avoir au moins trois phases.

Différentes topologies de convertisseur pour la machine RVAE sont présentées. Le convertisseur classique en demi-pont asymétrique est présenté. Les modes de fonctionnement

moteur et générateur sont présentés. Deux autres possibilités de convertisseurs sont détaillées, à savoir le convertisseur Miller et le convertisseur triphasé à pont complet.

La machine RVAE étudiée dans cette thèse est triphasée, à 6 dents au stator et 8 dents au rotor. Cette structure a plusieurs avantages : une grande flexibilité de dimensionnement, un espace de bobinage du stator plus grand, une masse réduite des tôles stator et de rotor, un couple électromagnétique élevé et des ondulations de couple plus faible. En effet, l'ondulation de couple est réduite en raison d'un plus grand nombre de dents et donc un taux de changement plus rapide de l'inductance, en comparaison aux topologies de machine RVAE 6/4 et 12/8 plus conventionnelles et ceci pour des contraintes de volume similaires.

Le modèle analytique est développé pour le cas où la saturation est considérée et lorsque la saturation est négligée. L'équation de tension de phase du stator de la machine est écrite et le calcul mathématique pour obtenir cette équation est détaillé dans l'Annexe 2A. Le couple électromagnétique développé par la machine RVAE est exprimé à partir de la co-énergie magnétique.

Le calcul de l'inductance est une étape importante. Cette inductance varie avec la position du rotor et avec le courant. Dans la deuxième partie de ce chapitre, une évolution idéale de l'inductance pour une période ($2\pi/N_R$) est présentée conjointement avec les équations nécessaires pour calculer l'angle de déplacement du rotor pour chaque segment de l'inductance. Comme un objectif de la thèse est de concevoir une machine RVAE pour être utilisée dans des applications ADI et parce qu'un calcul analytique réduit le temps de calcul, un calcul analytique de l'inductance maximale et minimale est présenté pour une configuration avec un nombre accru des dents du rotor par rapport à celles du stator.

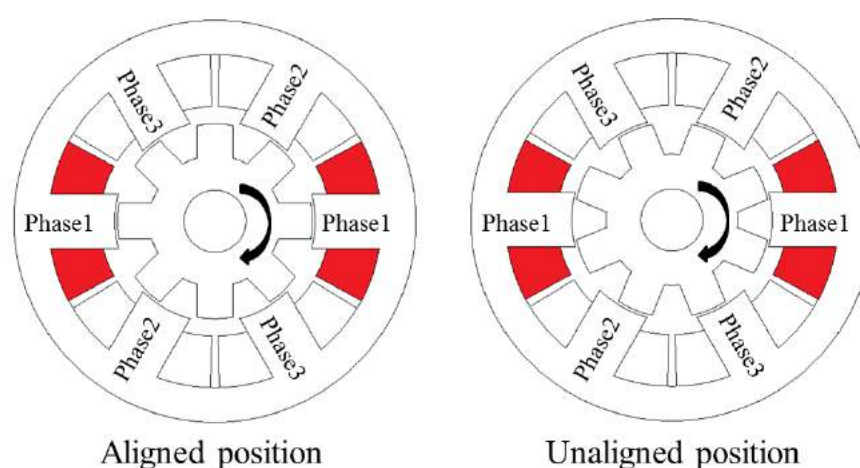


Fig. 1. Différentes positions de rotor pour le prototype de la machine RVAE.

Le calcul de l'inductance pour les deux positions de rotor (aligné et non-aligné) est déduit d'un calcul effectué sur une machine 8/6 RVAE et adapté à une machine 6/8 RVAE. La différence est due au fait que pour une machine 8/6 en position non alignée, les dents du rotor ne chevauchent pas celles du stator, mais dans le cas de la machine 6/8, il existe toujours un chevauchement entre les dents du stator et les dents du rotor (Fig.1, non-alignée).

Le modèle électrique est validé en comparant les résultats de ce modèle à des résultats obtenus par éléments finis. La machine est alimentée par une tension continue 8 V DC ou 15 V DC, et la machine tourne à vitesse constante. A cause de l'effet de réluctance, le courant absorbé varie en fonction du temps. Pour ces deux tensions, la forme et les valeurs du courant sont similaires. Le calcul du couple électromagnétique est vérifié pour différentes valeurs de courant de phase avec les deux modèles. Afin d'estimer la précision du modèle analytique, une comparaison entre le calcul par éléments finis (EF) et le calcul analytique pour l'inductance maximale et minimale est fournie dans ce chapitre.

La dernière partie de ce chapitre présente l'influence des angles de commutation, θ_{on} et θ_{off} , sur le couple électromagnétique moyen et sur les oscillations de couple.

Chapitre 3

Optimisation de la machine à réluctance variable à reluctance variable et à auto-commutation électronique en utilisant une technique 'Output Space Mapping'

Dans le chapitre précédent, le modèle analytique de la machine RVAE a été détaillé. L'objectif du chapitre 3 est d'utiliser le modèle analytique dans un processus d'optimisation rapide et fiable. La difficulté est l'utilisation du modèle analytique développé dans un processus d'optimisation. Cette difficulté est due au nombre important d'évaluations du modèle nécessaire dans le cadre d'une optimisation.

Le modèle analytique en lui-même est assez rapide. Mais la vitesse de ce modèle diminue à cause de l'effet combiné du temps de résolution des équations différentielles utilisées pour le calcul des courants et des boucles de contrôles utilisées pour les asservissements de couple ou de vitesse. Par conséquent, le processus d'optimisation est long. Ce chapitre propose des stratégies permettant de réduire le temps utilisé par le processus d'optimisation.

Habituellement, l'optimisation consiste à la minimisation d'un objectif en respectant certaines contraintes. Le problème d'optimisation peut avoir plusieurs minimums locaux.

Un minimum local est la valeur minimale autour de laquelle toutes les valeurs de la fonction sont supérieures ou égales à la valeur dans un voisinage donné. Dans de nombreuses circonstances, les minimums locaux ne sont pas des minimums globaux. Par conséquent, un minimum local est la meilleure solution dans un voisinage proche, mais un minimum global est la meilleure solution sur l'ensemble du domaine d'étude. Un problème d'optimisation peut être mono-objectif ou multi-objectif. Dans le cadre de cette thèse, l'optimisation mono-objectif est retenue en termes de minimisation d'une distance aux objectifs.

Lors de la conception d'une machine électrique de nombreux aspects doivent être envisagées et le problème d'optimisation peut nécessiter une grande quantité de temps pour être achevé. Dans le cadre de cette thèse, la technique de 'space mapping' (SM) est utilisée pour réduire le temps d'optimisation. Cette technique, nécessite l'utilisation de deux modèles: un modèle rapide en temps de calcul sur lequel l'optimisation sera lancée mais grossier en précision (modèle grossier) et un modèle lent en temps de calcul mais précis (modèle fin). Le modèle grossier est corrigé à chaque itération par le modèle fin avant chaque nouvelle optimisation. Les deux techniques utilisées dans ce chapitre sont : 'Output Space Mapping Proportional' (OSMP) et 'Manifold Mapping' (MM).

La technique OSMP est utilisée pour obtenir un résultat précis de manière rapide avec un minimum d'évaluations du modèle fin. Cette technique est basée sur l'utilisation du modèle grossier dans la boucle d'optimisation, tandis que le modèle fin est utilisé pour corriger progressivement les résultats du modèle grossier. Il est important que le modèle grossier ait un temps de calcul faible car il est fortement sollicité. Une forte différence en temps de calcul entre le modèle fin et le modèle grossier est primordiale. Mais, le modèle grossier doit toujours être capable de fournir les bonnes tendances si l'on veut que la technique fonctionne correctement. A la fin du processus, le modèle grossier corrigé donne la solution optimale \hat{x} .

La technique OSMP est très simple à mettre en œuvre. Le principe de cette technique est de corriger localement les sorties du modèle rapide par des coefficients en prenant comme référence les sorties du modèle fin au point courant. Les coefficients de correction sont calculés sur la base des sorties du modèle grossier par rapport aux sorties du modèle fin.

Comme la technique précédente, la technique MM corrige les sorties du modèle grossier. Cependant, la technique MM utilise une relation plus compliquée pour corriger le modèle grossier. Cette technique transforme le modèle grossier avec deux actions: une translation permettant d'aligner le modèle grossier sur le modèle fin et une rotation permettant d'ajuster la dérivée du modèle grossier sur la dérivée du- modèle fin.

Ces deux techniques sont validées au moyen d'un modèle mathématique. Les fonctions mathématiques ont été choisies de manière à avoir une différence entre le modèle fin et grossier. La fonction objectif est écrite en termes de minimisation de la distance. Grâce aux fonctions mathématiques la validation est rapide et permet de tester facilement le comportement des deux techniques. Tout d'abord, une optimisation sur le modèle fin est réalisée afin d'avoir une référence. Deux problèmes sont traités, le premier problème consiste à définir un objectif réalisable $\bar{y} = [12.69, 2.05]$, puis le second problème consiste à définir un objectif non réalisable $\bar{y} = [12, 1.6]$ mais proche d'une solution réalisable. Ces deux problèmes sont ensuite utilisés avec les deux techniques d'accélération du processus d'optimisation (OSMP et MM). Finalement, le comportement des deux techniques est étudié sur l'ensemble du domaine. La technique MM semble plus robuste sur l'exemple mathématique et OSMP n'a pas toujours de bonnes propriétés de convergence.

Comme montré dans la dernière partie du deuxième chapitre, les angles de commutation des phases ont une forte influence sur le couple électromagnétique moyen et sur l'ondulation du couple. Dans cette partie de la thèse, une optimisation est effectuée pour déterminer les valeurs optimales des angles de commutation et du courant de référence permettant d'atteindre un couple électromagnétique et une ondulation de référence. Avant de procéder à l'optimisation, le choix du modèle grossier est un point crucial. Le modèle de référence (le modèle fin) est fonction du temps; les simulations sont réalisées avec MATLAB/ Simulink. Le courant des phases de la machine à RV est régulé par une commande par hystérésis. Les consignes de ces courants dépendent également d'un capteur de position qui fournit la position du rotor. Le modèle fin prend en compte la non-linéarité des tôles magnétiques. Un modèle éléments finis a été utilisé pour déterminer le flux et le couple électromagnétique pour de multiples courants de phases et pour différentes positions du rotor.

Le modèle grossier (Fig.2) dépend également du temps. Afin de réduire son temps d'évaluation, ce modèle doit être simplifié au maximum. Les hypothèses et approches suivantes sont considérées:

- le modèle fin est mis en œuvre dans Matlab / Simulink et l'optimisation est lancée sous Matlab. Comme le Matlab nécessite du temps pour accéder à la boîte à outils Simulink, le modèle grossier est créé directement dans l'environnement Matlab.
- Le temps de résolution des équations différentielles pour déterminer l'évolution du courant de phase est relativement important. Les courants pour le modèle grossier sont considérés égaux en permanence à la consigne.

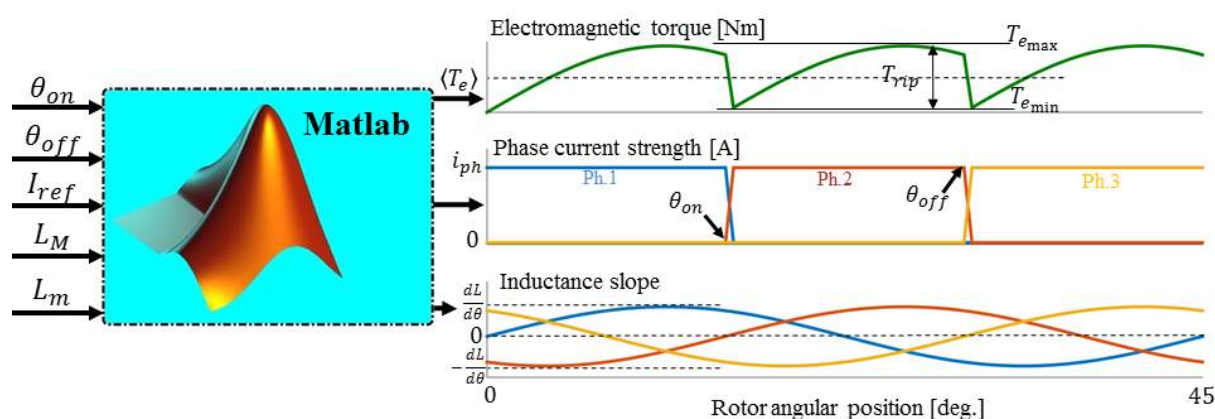


Fig. 2. Structure du modèle grossier.

- Une évolution idéale du courant dans la phase est considérée, donc leur contrôle n'est plus nécessaire.
- Pour le calcul du couple électromagnétique dans le modèle grossier, la saturation du matériau n'est pas prise en compte.
- En raison de l'implémentation de la commande de courant par hystérésis dans le modèle fin, un petit pas de simulation a dû être utilisé, ce qui conduit à un temps de calcul assez important. Comme ce type de contrôle a été éliminé dans le modèle grossier, un pas de simulation plus élevé peut être utilisé.

Une comparaison entre le modèle fin et grossier est réalisée par rapport aux objectifs et aux variables. Les temps de calcul sont également comparés. L'optimisation est réalisée avec l'OSMP et le MM sur la machine RVAE à la fois sur le mode de fonctionnement moteur et générateur. Les résultats de référence sont ceux obtenus après optimisation avec le modèle fin seul. Les deux techniques d'accélération fonctionnent correctement et convergent en quelques itérations (maximum 5). Un facteur 10 est gagné sur le temps de calcul.

Le problème d'optimisation sur les grandeurs de contrôle est complété avec l'ajout de variables de dimensionnement. Ainsi le contrôle et les dimensions de la machine seront déterminés simultanément pour trouver la meilleure machine RVAE répondant au problème formulé en intégrant intrinsèquement l'influence de la commande dans le dimensionnement de la machine.

Pour ce problème d'optimisation, le modèle fin est un modèle éléments finis. JMAG Designer est utilisé comme outil de modélisation par éléments finis. Le modèle grossier est celui présenté précédemment (Fig.2) avec comme différence que l'inductance maximale et l'inductance minimale sont calculées analytiquement à partir de la géométrie de la machine

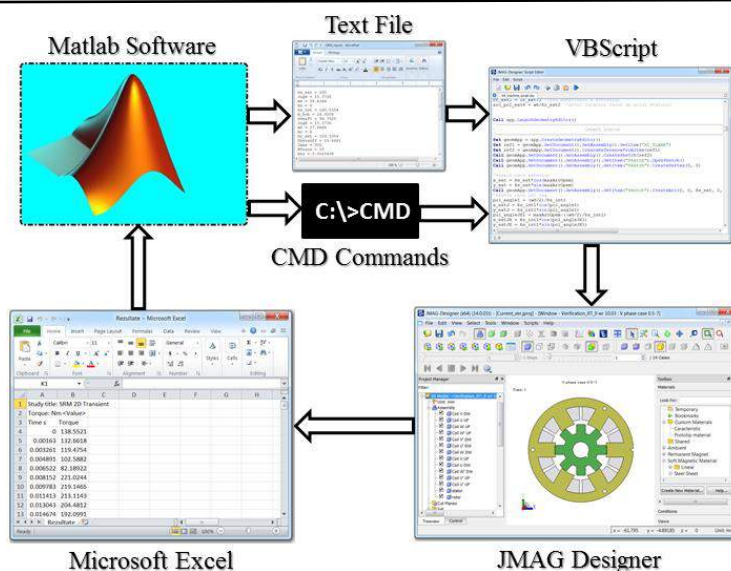


Fig. 3. Structure de la connexion entre MATLAB et JMAG Designer.

comme détaillé dans le deuxième chapitre. Le modèle éléments finis est paramétré pour faire évoluer ces dimensions en fonction des géométries trouvées par le modèle grossier. La structure d'échange entre Matlab et JMAG Designer est présentée sur la figure .3. L'optimisation est lancée sur un cahier des charges moteur avec les 2 techniques d'optimisation. La structure et la commande obtenues avec les 2 techniques sont très proches.

La machine obtenue est testée en mode moteur et générateur pour analyser ses performances. Ensuite, des simulations sont effectuées sur cycle de fonctionnement. Dans un premier temps, la machine à RV démarre en mode moteur et la vitesse de référence est réglée à 200 tr/min ; à la fin de cette période le moteur thermique a démarré. Ensuite, la machine à RV passe en mode générateur ; la machine est entraînée par le moteur thermique, la vitesse est imposée à 900 tr/min puis à 3000 tr/min et de nouveau à 900 tr/min. Le comportement de l'ADI est analysé en condition.

Chapitre 4

Étude expérimentale et contrôle d'une machine triphasée 6/8 à reluctance variable et à auto-commutation électronique

Dans le chapitre précédent, des optimisations ont été réalisées afin de trouver les meilleurs angles de commutation et le courant de référence afin d'avoir le maximum de couple électromagnétique moyen avec le minimum d'oscillations de couple. Ce travail a été réalisé avec des modèles numériques. Ce chapitre propose de valider sur banc d'essai les résultats

obtenus par modélisation et optimisation. Le banc d'essai avec un prototype de machine à RV avec ses convertisseurs et sa carte de commande est présenté sur la Fig. 4.

Dans la première partie de ce chapitre, l'ensemble du banc d'essai est présenté. Une solution pratique avec des onduleurs triphasés classiques à pont complet est présenté afin d'alimenter la machine à RV de façon classique.

La stratégie de commande de la machine à RV est réalisée avec Simulink. Une carte dSPACE 1104, permet d'appliquer cette commande au prototype. Le logiciel temps-réel dispose de toutes les fonctions nécessaires pour relier le logiciel de contrôle à la carte dSPACE. Finalement, pour visualiser en temps réel l'évolution des sorties de la machine, le logiciel ControlDesk est utilisé. Grâce à cet outil, la machine peut être commandée pour fonctionner en moteur ou en générateur.

En raison de la configuration à double saillance de cette machine, l'inductance de phase varie en fonction de la position et du courant du rotor. Le banc d'essai est donc utilisé pour mesurer l'évolution de l'inductance de phase. L'inductance est mesurée grâce à une alimentation sinusoïdale. L'inductance en fonction du courant est mesurée pour une position alignée des dents rotor et stator et pour une position non alignée. Les valeurs obtenues sont comparées avec les différents modèles développés (EF et analytique). Les valeurs obtenues sont suffisamment proches.

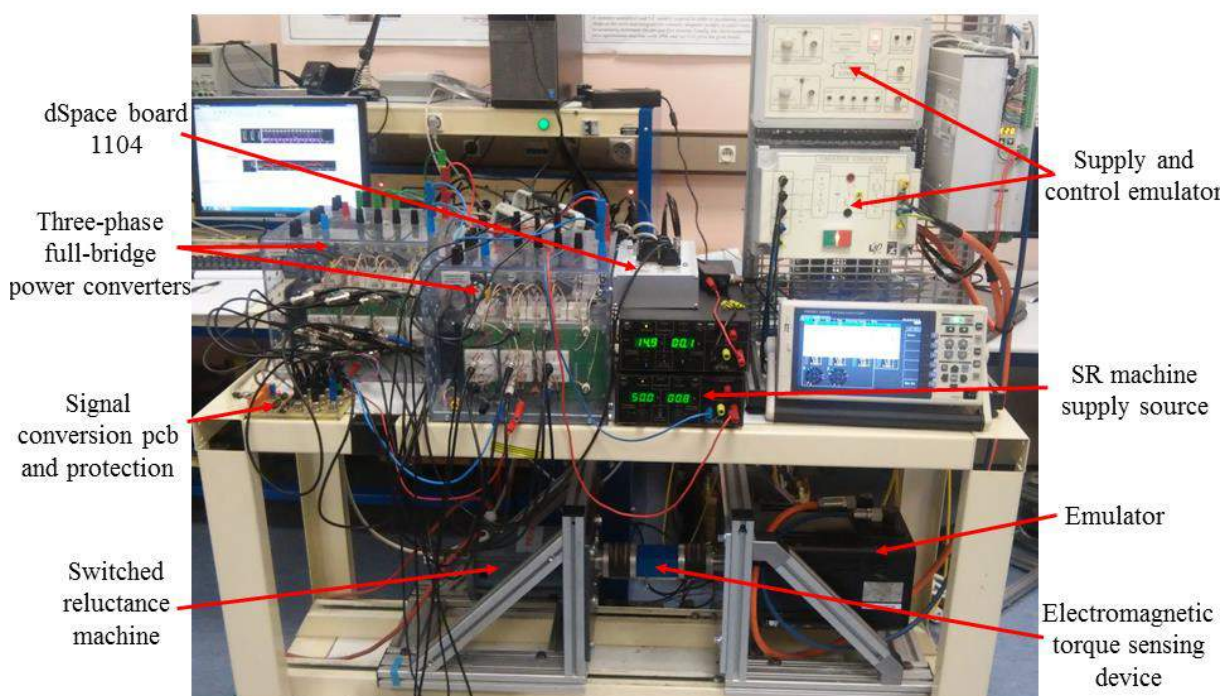


Fig. 4. Banc d'essai expérimental.

Dans le troisième chapitre, une optimisation a été effectuée en utilisant OSMP et MM, afin de déterminer les meilleurs angles de commutation qui conduisent à la maximisation du couple électromagnétique moyen à condition que le couple d'ondulation ne dépasse pas une valeur imposée. Grâce au banc d'essai, le contrôle trouvé par optimisation est testé en pratique. Les résultats de modélisation par éléments finis et les essais sont présentés. Les formes d'ondes obtenues par modélisation et par mesures sont proches.

Des essais pour différents régimes permanents en mode moteur et générateur avec les angles théoriques et optimaux sont effectués. Des essais avec un cycle réduit de fonctionnement sont également réalisés.

Contributions à l'étude des machines à reluctance variable pour application alternateur-démarrateur automobile

Résumé: Ce travail de recherche est réalisé dans le cadre d'une collaboration internationale entre l'Université Technique de Cluj-Napoca en Roumanie et Centrale Lille en France. Cette thèse a comme premier objectif, de réduire l'ondulation de couple d'une machine triphasée 6/8 à reluctance variable grâce aux paramètres de contrôle dans le mode de fonctionnement moteur et générateur. Par conséquent, un modèle analytique a été développé et mis en œuvre dans un environnement de calcul numérique. Un outil d'optimisation permettant de trouver les meilleurs paramètres de contrôle a été utilisé. Toutefois, le processus d'optimisation est très lent. En conséquence, une stratégie pour réduire le temps du processus d'optimisation sans abaisser la précision des résultats est proposée. Une stratégie de 'mapping' est utilisée entre un modèle grossier mais rapide et un modèle fin mais lent. Un travail est mené sur le choix du modèle grossier, dans le cadre d'un modèle fournissant des valeurs en fonction du temps. Deux stratégies de 'mapping' ont été utilisées dans cette thèse : l' 'Output Space Mapping Proportional' (OSMP) et le Manifold Mapping (MM). Ces deux stratégies sont utilisées pour déterminer les paramètres de contrôle optimaux. Le problème d'optimisation est ensuite complété en ajoutant des variables géométriques au processus d'optimisation du contrôle. Les outils développés sont ensuite utilisés dans le cadre du dimensionnement par optimisation d'un alternateur-démarrateur automobile. Finalement, des expériences et des essais sur un prototype de Machine à RV sont menés afin de valider les résultats du processus d'optimisation en mode moteur et générateur.

Mots clés: conception et contrôle par optimisation, éléments finis, manifold mapping, output space mapping proportional, moteur/générateur à reluctance variable

Contributions to the study of Switched reluctance machine for automotive integrated starter-alternator application

Abstract: The switched reluctance machine has a simple construction making it cheaper in execution but one of the drawbacks of this machine is the torque ripple. This thesis had as first target, the usage of an optimization tool to calculate the best control parameters to correct this major drawback in motor and generator operation modes. Hence, an analytical model that takes into account the machine geometry and that is able to be simulated in both operation modes by adjusting the commutation angles was provided and implemented in a calculation environment. The second target of this work is to investigate a method to reduce the optimization time without lowering the accuracy of the results. The strategy used in the optimization process is known in literature as the space mapping technique, more precisely for this thesis output space mapping proportional and manifold mapping were studied. After testing them on a mathematical model it was possible to continue the investigation on defining the optimal control parameters of a three-phases 6/8 SR machine prototype, being able that further to use this strategy in a much complicated process, i.e. defining the right geometry and control of a SR machine to be used in automotive integrated starter alternator systems. The final target of the thesis was to conduct experiments and tests on the existing prototype in order to partially validate the results of the optimization process.

Keywords: design and control optimization, finite element, manifold mapping, output space mapping proportional, switched reluctance motor/generator.

Contribuții la studiul mașinii cu reluctanță variabilă și autocomutație electronică pentru aplicații de starter-alternator integrat la autovehicule

Rezumat: Mașina cu reluctanță variabilă și autocomutație electronică (MRVAE) are o construcție simplă, acest lucru făcând-o ieftină în execuție, însă unul din marile dezavantaje ale acestei mașini sunt riplul cuplului de forțe electromagnetice. Această teză are ca și prim obiectiv folosirea optimizării pentru a calcula cei mai buni parametri de control pentru a corecta acest mare defect al mașinii MRVAE pentru funcționarea în regim de motor cât și în cel de generator. Prin urmare, un model analitic care ia în considerare geometria mașinii, dar care poate fi simulat în ambele regimuri de operare prin ajustarea unghiurilor de comandă, este implementat într-un mediu de calcul. Mai departe, o optimizare matematică este lansată pentru calculul parametrilor de control ai mașinii, însă pentru a avea rezultate bune, optimizarea trebuie să fie foarte acurată, drept urmare va fi foarte lentă. Așadar, al doilea obiectiv al acestei cercetări a fost determinarea unei metode de reducere a timpului de calcul în procesul de optimizare, fără a diminua însă precizia rezultatelor. În timpul procesului de investigare al strategiei de optimizare, s-a descoperit că un rol important pentru obținerea unor rezultate optime îl are modelul rapid, deoarece pentru a avea o convergență liniară, acest model trebuie să aibă o tendință asemănătoare cu modelul fin. Drept urmare, modalitatea de deducere a celor două modele este de asemenea descrisă în această teză. Strategia utilizată în procesul de optimizare este cunoscută în literatură sub denumirea de “space mapping technique”, mai precis pentru această teză tehnicile “output space mapping” și “manifold mapping” au fost studiate. După testarea lor pe o funcție matematică, a fost posibilă continuarea investigației pe MRVAE trifazată cu 6 poli pe stator și 8 poli pe rotor pentru a obține cel mai bun control al acestui prototip, pentru a putea fi posibil mai apoi să se folosească aceasta tehnică într-un proces de optimizare mai complicat, acela de a obține cel mai bun control și design pentru această mașină urmând a fi utilizată într-un sistem de starter alternator pentru autovehicule. Ultimul obiectiv al acestei teze este acela de a realiza teste experimentale pe prototipul existent, pentru a valida parțial rezultatele obținute în urma procesului de optimizare.

Cuvinte cheie: optimizare pe geometrie și control, element finit, manifold mapping, output space mapping proportional, motorul/generatorul cu reluctanță variabilă